Final Report

PNNL-34408 Rev. 1

Impacts of Climate Change on Human Health and the Environment in the Enewetak Atoll

Phase 2 Report

February 2024

R Prasad
S Ghosh
TA Ikenberry
S Taraphdar
BA Napier
MRL Premathilake
T Wang
LR Leung

Pacific Northwest
NATIONAL LABORATORY

U.S. DEPARTMENT OF ENERGY

Prepared for the U.S. Department of Energy
under Contract DE-AC05-76RL01830

PACIFIC NORTHWEST NATIONAL LABORATORY
operated by
BATTELLE
for the
UNITED STATES DEPARTMENT OF ENERGY
under Contract DE-AC05-76RL01830

Printed in the United States of America

Available to DOE and DOE contractors from
the Office of Scientific and Technical Information,
P.O. Box 62, Oak Ridge, TN 37831-0062
www.osti.gov
ph: (865) 576-8401
fox: (865) 576-5728
email: reports@osti.gov

Available to the public from the National Technical Information Service
5301 Shawnee Rd., Alexandria, VA 22312
ph: (800) 553-NTIS (6847)
or (703) 605-6000
email: info@ntis.gov
Online ordering: http://www.ntis.gov

PNNL-34408 Rev. 1

Impacts of Climate Change on Human Health and the Environment in the Enewetak Atoll

Phase 2 Report

February 2024

R Prasad	BA Napier
S Ghosh	MRL Premathilake
TA Ikenberry	T Wang
S Taraphdar	LR Leung

Prepared for
the U.S. Department of Energy
under Contract DE-AC05-76RL01830

Pacific Northwest National Laboratory
Richland, Washington

Summary

The Department of Energy was directed by the U.S. Congress in Section 3140 of the National Defense Authorization Act of 2022 to conduct a study of the impacts of climate change on the Runit Dome nuclear waste disposal site on the Enewetak Atoll, which is part of the Republic of the Marshall Islands (RMI). The Congress directed this study to also address other environmental hazards resulting from nuclear weapons testing. The current study only addressed the effects of contaminants from nuclear weapons testing on human health and the environment. While other nonradioactive contaminants may be present at the Enewetak Atoll, past surveys have primarily focused on characterizing radioactive contaminants. No data were available for nonradioactive toxins at the Enewetak Atoll. Because new data collection was not within the scope, this study primarily focused on characterizing radioactive contaminants under the effects of climate change using available data.

The United States conducted 43 nuclear weapon tests at the Enewetak Atoll between 1948 and 1958. Most of the tests were conducted on island surfaces, on barges near the islands, or underwater. Fallout and deposition from these tests occurred on the islands, the lagoon, and the ocean. In the 1970s, a cleanup effort collected radioactive waste and placed it in the Cactus Crater on Runit Island. The waste pile was covered with a concrete cap. The Runit Island waste containment structure is also called the Runit Dome. The following sources are important to assess human and environmental effects at the Enewetak Atoll:

- Radionuclides on the land surface of the islands
- Radionuclides in the sediments of the lagoon
- Radionuclides in the waters of the lagoon and nearby ocean
- Radionuclides emplaced in the Cactus Crater (Runit Dome).

The primary source of information for radionuclides in the soils of the Enewetak Atoll is the RMI *Nationwide Radiological Study* (NWRS). NWRS Volume 1 includes information for 31 different islands in the Enewetak Atoll. The most comprehensive survey of lagoon sediment samples is described in a 1973 Atomic Energy Commission (AEC) report that described distributions of ^{152}Eu, ^{207}Bi, ^{90}Sr, ^{137}Cs, ^{241}Am, and $^{239+240}$Pu. Radionuclide concentrations in the lagoon and adjacent ocean waters were also included in the 1973 AEC report, and selected areas were resampled by Woods Hole Oceanographic Institution in 2017. The radioactive contents of the Cactus Crater were described in a 1981 Defense Nuclear Agency report. It was found that radioactivity associated with lagoon sediments remains the largest long-term repository of radioactive contamination at the Enewetak Atoll.

Therefore, PNNL's approach to assessing impacts on human health and the environment from climate change was focused on how lagoon sediments could be mobilized and transported to receptor locations adjacent to atoll islands. PNNL considered several mechanisms including sea-level rise, extreme precipitation, storm surge, and tsunamis. While each of these mechanisms could potentially elevate radiation dose, storm surges both under current and future climates were judged to have the most influence on contaminant mobilization and transport, particularly those in the lagoon sediment. Therefore, PNNL evaluated how current and future storm scenarios could change existing radioactive dose to humans and biota. PNNL's study included (1) estimating the radionuclide source term, (2) estimating effects of climate change on severe storms, (3) estimating mobilization and transport of radionuclides, and (4) estimating radiation dose to humans and biota. A future, hypothetical release of the

radioactive material in the Runit Dome was also postulated. The mobilization and transport of radioactive material hypothetically released from Runit Dome was simulated to assess its effect on humans and biota.

Studies of changes in regional climate of the Pacific Ocean where RMI is located are limited; therefore, estimating the impacts of climate change within the RMI and the Enewetak Atoll is challenging. PNNL performed a limited assessment of historically severe Pacific storms and hurricanes, both in present climate (approximately 2015) and in a future climate (approximately 2090). From the historical storm database, PNNL selected three storms that were among the strongest to pass near Enewetak Atoll. Using these three storms, PNNL generated six plausible storm scenarios—three in the present climate and three in the future climate. These storm scenarios were generated using the Advanced Research Weather Research and Forecasting (WRF-ARW) model. Based on evaluation of 11 global climate models used in the sixth coupled model intercomparison project (CMIP6), PNNL selected the climate model configuration that best reproduced the historical storms. Although warming of the western and central Pacific is predicted by the CMIP6 models, the climate changes were found to strengthen storms in western Pacific more than in the central Pacific, where the Enewetak Atoll is located. The meteorological variables generated by WRF-ARW simulations were used to drive a PNNL-developed ocean hydrodynamic model for the RMI.

PNNL developed the ocean model for RMI using the Finite Volume Community Ocean Circulation Model (FVCOM). The ocean model was used to simulate ocean hydrodynamics during present and future storm scenarios. The hydrodynamics of the modeled domain was used to drive a radionuclide fate and transport model. PNNL developed this model using FVCOM Integrated Compartment Model. The fate and transport model was used for simulating radionuclide mobilization and transport for present and future storm scenarios. In addition, a hypothetical failure of the Runit Dome and subsequent release of radioactive material was evaluated for the future storm scenarios. Therefore, nine storm scenarios were used—three storm scenarios in the present climate, three storm scenarios in the future climate, and three storm scenarios with radioactive release from Runit Dome in the future climate.

PNNL identified receptor locations for 31 islands of the Enewetak Atoll. Humans and biota doses were estimated for the simulated radionuclide mobilization and transport scenarios at each receptor location. PNNL compared the radiation doses for the storm period to that for a normal, without storm condition. Under current climate conditions, annual radiation exposures were below the current U.S. standards for radiation dose limits to the public in the southern islands including Enewetak (Fred) and Medren (Elmer). Radiation doses were somewhat elevated starting at Runit Island northward and westward to Enjebi Island (Janet). The islands in the northwest quadrant, particularly Bokoluo (Alice) and Bokombako (Belle) remain relatively contaminated. The islands in the southwestern quadrant have low contamination. Highest contribution to radiation doses comes from consumption of locally grown foods. Two radionuclides, ^{90}Sr and ^{137}Cs contributed the greatest fraction for most terrestrial foods.

In current climate conditions, the storms temporarily increased radionuclide concentrations in the lagoon waters. Small increases in dose contributions from swimming and boating and consumption of locally caught seafood was found. The inhalation dose from sea spray was increased, but by a negligible amount. Dose to lagoon biota was also slightly increased. In future conditions, doses are expected to be smaller, primarily because of the radioactive decay of the shorter-lived radioisotopes of ^{90}Sr and ^{137}Cs. This has the potential to make all islands except Bokombako (Belle), and perhaps Bokoluo (Alice), in the far northwest of the atoll suitable for residency based on radiation dose limits to the public. For the future climate, the dominant radionuclide for radiation dose remains ^{90}Sr via the local food ingestion pathway.

The effect of the postulated, hypothetical future Runit Dome failure and subsequent release of radioactive material resulted in additional contributions to dose—small increases and decreases among islands other than Runit. Larger increases in dose were estimated for Runit Island. Following the hypothetical Runit Dome failure, if the local food pathway was neglected, the incremental human dose was estimated to be about 20 mrem/year (0.2 mSv/year). Considering local food consumption for this hypothetical scenario would increase this dose approximately 20 times (about 400 mrem/year [4 mSv/year]). The following list provides expected radiation dose limits for context (DOE, 2017; National Research Council, 1994):

- U.S. Environmental Protection Agency dose limit for public drinking water systems is 4 mrem/year (0.04 mSv/year)
- U.S. Nuclear Regulatory Commission (NRC) criteria for decommissioning for unrestricted use is 25 mrem/year (0.25 mSv/year)
- DOE and NRC dose limit for the public is 100 mrem/year (1 mSv/year)
- RMI-U.S. memorandum dose limit for the public is 100 mrem/year (1 mSv/year)
- for the U.S. population, the average natural background dose is approximately 310 mrem/year (3.1 mSv/year) and including man-made radiation results in a dose of 620 mrem/year (6.2 mSv/year)
- U.S. Department of Homeland Security emergency guideline for public relocation is 2,000 mrem/year (20 mSv/year).

Acknowledgments

The authors appreciate and acknowledge the funding and background knowledge provided by the Department of Energy’s Office of Environment, Health, Safety and Security. The report benefited from discussions with staff at Lawrence Livermore National Laboratory, the U.S. Geological Survey, and independent researchers. An independent, internal peer review was conducted by scientists outside of the research team that authored this report at the Pacific Northwest National Laboratory. Comments provided by members of the public and U.S. and international institutions are also acknowledged. These comments helped improve this report.

Acronyms and Abbreviations

ACM2	Asymmetrical Convective Model version 2
AEC	Atomic Energy Commission
ASTGTM	Advanced Spaceborne Thermal Emission and Reflection Radiometer Global Digital Terrain Model
CMIP6	Coupled Model Intercomparison Project Phase 6
DOE	Department of Energy
EEZ	Extended Economic Zone
EPA	U.S. Environmental Protection Agency
FVCOM	Finite Volume Coastal Ocean Model
FVCOM-ICM	Finite Volume Coastal Ocean Model-Integrated Compartment Model
GCM	general circulation model
GEBCO	General Bathymetric Chart of the Oceans
IAEA	International Atomic Energy Agency
IBTrACS	International Best Track Archive for Climate Stewardship
MYNN	Mellor-Yamada-Nakanishi-Nino
NAS	National Academy of Sciences
NCAR	National Center for Atmospheric Research
NDBC	National Data Buoy Center
NOAA	National Oceanic and Atmospheric Administration
NWRS	Nationwide Radiological Study
PBL	planetary boundary layer
PGW	pseudo-global-warming
PNNL	Pacific Northwest National Laboratory
PSMSL	Permanent Service for Mean Sea Level
QNSE	Quasi Normal Scale Elimination
RMI	Republic of the Marshall Islands
RMSE	root-mean-square error
SH	Shin-Hong
SPM	suspended particulate matter
SST	sea surface temperatures
TRU	transuranic
TC	tropical cyclone
UNSCEAR	United Nations Scientific Committee on the Effects of Atomic Radiation
UW	University of Washington
WDM6	WRF double moment 6-class microphysics
WRF-ARW	Advanced Research-Weather Research and Forecasting
WNP	western North Pacific Ocean
WSM6	WRF single moment 6-class microphysics
YSU	Yonsei University

Contents

Figures

Tables

1.0 Introduction

In Section 3140 of the National Defense Authorization Act of 2022, the U.S. Congress directed the Department of Energy (DOE) to conduct a study of the impacts of climate change on the Runit Dome nuclear waste disposal site on the Enewetak Atoll, which is part of the Republic of the Marshall Islands (RMI). Congress directed this study to also address other environmental hazards resulting from nuclear weapons testing. While other nonradioactive contaminants may be present at the Enewetak Atoll, past surveys have focused on characterizing radioactive contaminants. Because new data collection was not within the scope, this study primarily focused on characterizing the effects of radioactive contaminants under the effects of climate change using available data.

DOE contracted with Pacific Northwest National Laboratory (PNNL) to conduct this study. This study is to include a scientific analysis of 1) the Runit Dome nuclear waste disposal site, 2) crypts used to contain nuclear waste and other toxins on the Enewetak Atoll, and 3) radionuclides and other toxins present in the lagoon of the Enewetak Atoll.

There are three overall objectives of the PNNL study:

1. Perform a literature review to identify data and assessment gaps
2. Assess environmental and human health impacts under climate change from release of radionuclides and toxins from the Runit Dome, crypts on the Enewetak Atoll, and Enewetak Lagoon
3. If needed, conduct additional analyses and revise the assessment based on public comments.

The three objectives listed above were identified to be addressed in three phases of this project, with the first two phases to be completed in the current scope of work. The work done in Phase 1 of the project was described in PNNL-34082 (Prasad et al., 2023). This report describes the work in Phase 2, including estimation of human and biota radiation dose from the effects of plausible, severe storms in the current and future climates. Following submission of this report to DOE, PNNL obtained public comments. The public comments were carefully considered and responses were prepared. Recommendations of several public comments were incorporated in this final report.

1.1 Background of Enewetak Atoll and Runit Dome

Enewetak Atoll is in the northwest part of the RMI, approximately 4,500 km west of Hawaii (Figure 1). The atoll consisted of 42 islands, of which 39 still exist (Buesseler et al., 2018). The 39 low-lying islands make up a total land area of approximately 6.9 km^2 that are arranged on a roughly elliptical shaped reef. The elliptical barrier reef has an approximate area of 84 km^2 (Noshkin, 1980). The average land elevation is about 3 m above mean sea level. The barrier reef encompasses a lagoon, which has an area of approximately 932 km^2, with average and maximum depths of approximately 47.4 m and 60 m, respectively. The lagoon is mostly surrounded by the reef except for three entrances from the open ocean—an east channel that is approximately 55 m deep, a 9.7 km wide south channel, and a shallow southwest channel (labeled Deep Entrance, Wide Passage, and Southwest Passage, respectively, on Figure 2).

Enewetak Atoll has a tropical marine climate with mean monthly minimum temperatures relatively constant at about 23°C; mean monthly maximum air temperatures vary a little more from 30 to 32°C (DOE, 1987). Mean annual rainfall is about 1,500 mm, a large portion of which occurs during the wet season that lasts from April through November. Prevailing winds are consistently easterly and northeasterly. Most tropical depressions and tropical storms occur between September and December, although they can occur at any time in the year. These systems travel an average of 7° longitude per day (about 32 km/h) and have length scales of 3,500 to 4,000 km. Therefore, any given location may be affected by these systems for 4.5 to 5 days. Typhoons are relatively rare but can reach Saffir-Simpson categories of 3 or 4 near the Enewetak Atoll. Storm surges during the passage of tropical storms and typhoons, especially when combined with high tides, can cause damage at the low-lying islands of the atoll (Hamilton, 2013).

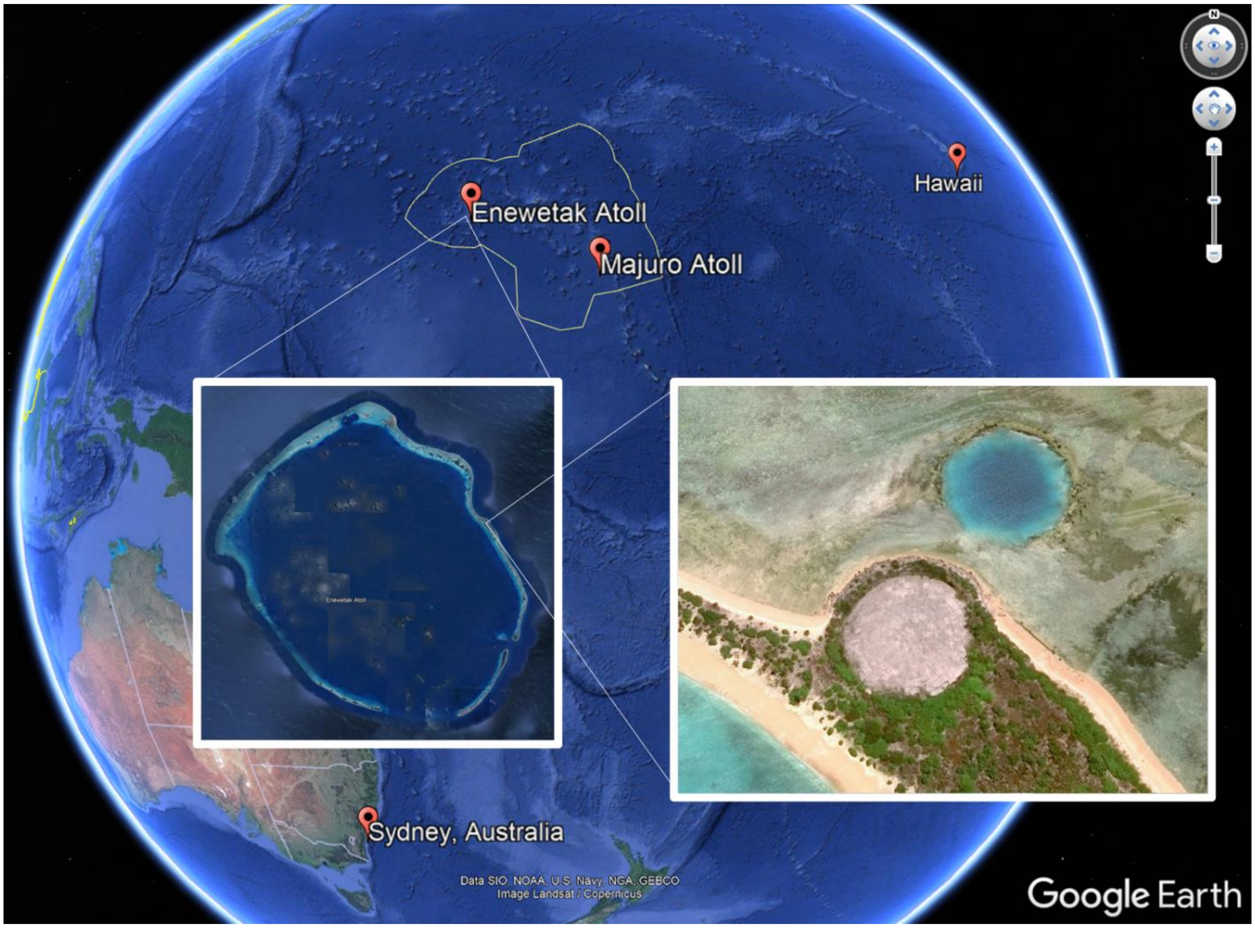

Figure 1. Location of Enewetak Atoll, RMI. The capital of the RMI is located on Majuro Atoll. The outline shows the RMI EEZ. Left inset: Enewetak Atoll and its lagoon. Right inset: Runit Dome capping the Cactus Crater on Runit Island of Enewetak Atoll; the Lacrosse Crater is seen to the northeast.

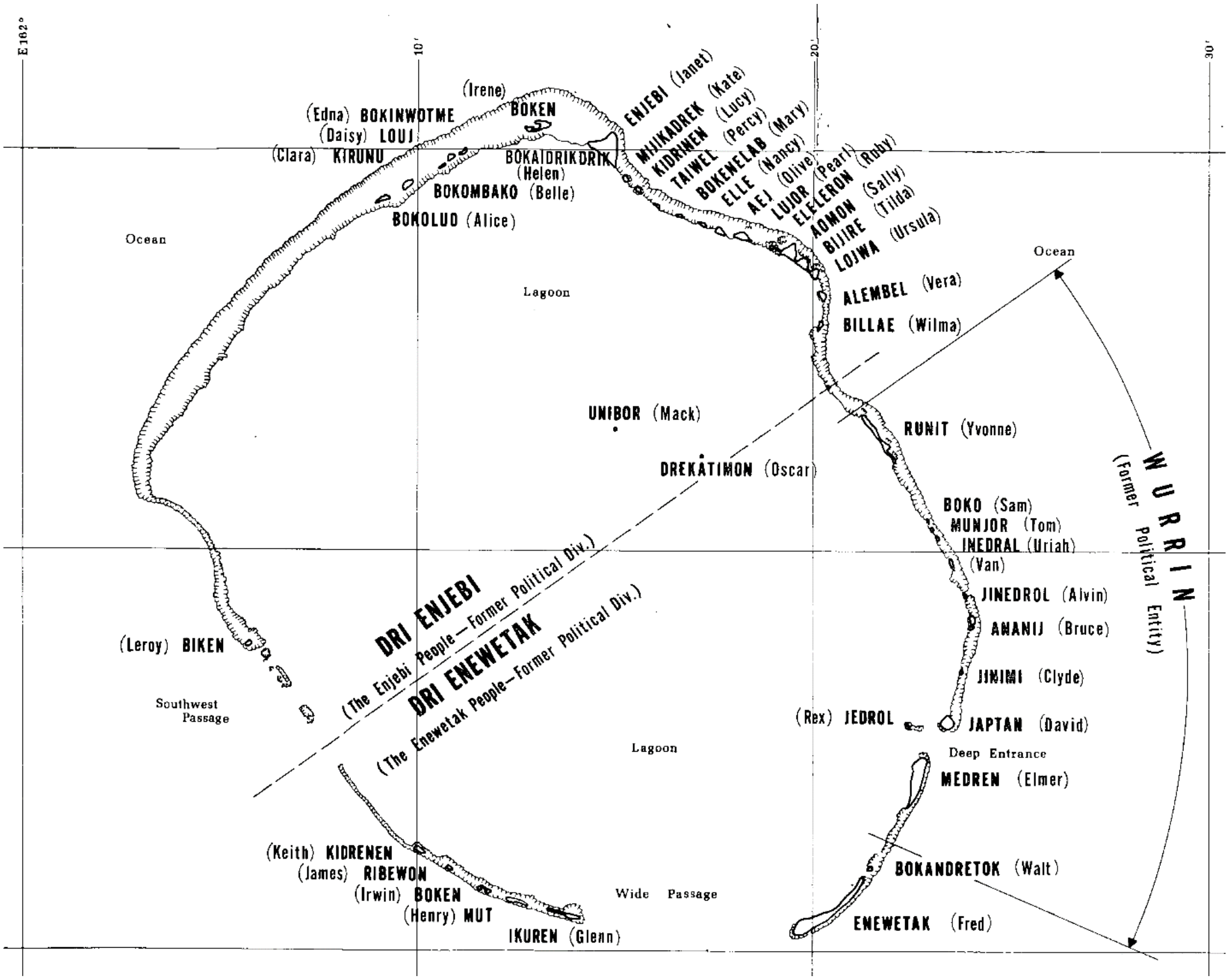

Figure 2. Enewetak Atoll, the lagoon, and the islands comprising the atoll. The island names in bold uppercase are Marshallese names and those in the parentheses are names assigned by the United States military. Source: DNA, 1975.

1.2 Summary of Nuclear Testing at Enewetak Atoll

The United States conducted 43 nuclear weapon tests at Enewetak Atoll between 1948 and 1958. The majority of the tests were conducted either on the islands' surface, on barges near the islands, or underwater. The tests resulted in nearby fallout and deposition to the terrestrial islands and marine environments of the atoll. A list of the tests, with the test type, size, and location, is given in Table 1. Seven tests were performed in the lagoon southwest of Enjebi (Janet) Island, eight in the lagoon west of Runit (Yvonne) Island, and one on the reef southwest of Bokoluo (Alice) Island. All these tests were detonated on barges (surface). Two underwater tests were conducted: one in the lagoon north of Ikuren (Glenn) Island and another in the ocean south of Ribewon (James) Island. Six surface tests were performed. The Mike test destroyed Elugelab island (Gene); Lacrosse and Cactus Craters formed in the north central part of Runit (Yvonne) Island. The Quince and Fig surface tests resulted in spreading of unburned plutonium over a large area of Runit (Yvonne) Island and nearby lagoon waters (DOE, 1982). Figure 3 shows the testing locations throughout the atoll.

Table 1. Details of nuclear tests performed at Enewetak Atoll (DOE 2015).

Test Series	Test Name	Yield (kt)	Latitude (°N)	Longitude (°E)	Date (GMT)	Type	Height of Burst (ft)
Sandstone	X-Ray	37	11.665300	162.234000	April 14, 1948	Tower	200
Sandstone	Yoke	49	11.619410	162.313825	April 30, 1948	Tower	200
Sandstone	Zebra	18	11.551450	162.348100	May 14, 1948	Tower	200
Greenhouse	Dog	81	11.551866	162.347893	April 7, 1951	Tower	300
Greenhouse	Easy	47	11.665400	162.233800	April 20, 1951	Tower	300
Greenhouse	George	225	11.624300	162.303900	May 8, 1951	Tower	200
Greenhouse	Item	45.5	11.669300	162.241500	May 24, 1951	Tower	200
Ivy	Mike	10400	11.667000	162.189900	October 31, 1952	Surface	7
Ivy	King	500	11.558800	162.345400	November 15, 1952	Air drop	1480
Castle	Nectar	1690	11.666600	162.190000	May 13, 1954	Barge	7
Redwing	Lacrosse	40	11.553878	162.348050	May 4, 1956	Surface	0
Redwing	Yuma	0.19	11.618730	162.314125	May 27, 1956	Tower	205
Redwing	Erie	14.9	11.540100	162.357950	May 30, 1956	Tower	300
Redwing	Seminole	13.7	11.672427	162.210365	June 6, 1956	Surface	0
Redwing	Blackfoot	8	11.547200	162.352050	June 12, 1956	Tower	200
Redwing	Kickapoo	1.49	11.623857	162.318780	June 13, 1956	Tower	300
Redwing	Osage	1.7	11.540150	162.356400	June 16, 1956	Air drop	670
Redwing	Inca	15.2	11.629300	162.285000	June 21, 1956	Tower	200
Redwing	Mohawk	360	11.627589	162.295691	July 2, 1956	Tower	300
Redwing	Apache	1850	11.670900	162.199600	July 8, 1956	Barge	10
Redwing	Huron	250	11.677817	162.204974	July 21, 1956	Barge	15
Hardtack 1	Cactus	18	11.552550	162.347270	May 5, 1958	Surface	3
Hardtack 1	Butternut	81	11.542700	162.338600	May 11, 1958	Barge	10
Hardtack 1	Koa	1370	11.670990	162.198652	May 12, 1958	Surface	3
Hardtack 1	Wahoo	9	11.343500	162.174900	May 16, 1958	Underwater	-500
Hardtack 1	Holly	5.9	11.537300	162.347400	May 20, 1958	Barge	13
Hardtack 1	Yellowwood	330	11.659775	162.223408	May 26, 1958	Barge	11
Hardtack 1	Magnolia	57	11.535000	162.345000	May 26, 1958	Barge	14
Hardtack 1	Tobacco	11.6	11.691220	162.214650	May 30, 1958	Barge	10
Hardtack 1	Rose	15	11.532600	162.342600	June 2,1958	Barge	15
Hardtack 1	Umbrella	8	11.378000	162.212000	June 9, 1958	Underwater	-150
Hardtack 1	Walnut	1450	11.684700	162.239850	June 14, 1958	Barge	7
Hardtack 1	Linden	11	11.608900	162.321300	June 18, 1958	Barge	8
Hardtack 1	Elder	880	11.677200	162.185255	June 27, 1958	Barge	9
Hardtack 1	Oak	8900	11.605086	162.100486	June 28, 1958	Barge	6
Hardtack 1	Sequoia	5.2	11.543050	162.347000	July 1, 1958	Barge	6
Hardtack 1	Dogwood	397	11.677570	162.206157	July 5, 1958	Barge	12
Hardtack 1	Scaevola	0	11.550000	162.342500	July 14, 1958	Barge	20
Hardtack 1	Pisonia	255	11.541000	162.320000	July 17, 1958	Barge	6
Hardtack 1	Olive	202	11.678501	162.208073	July 22, 1958	Barge	8
Hardtack 1	Pine	2000	11.651260	162.219650	July 26, 1958	Barge	8
Hardtack 1	Quince	0	11.545500	162.352700	August 6, 1958	Surface	3
Hardtack 1	Fig	0.02	11.545500	162.352700	August 18, 1958	Surface	2

Radionuclides in the environment at the Enewetak Atoll resulted from fission of the weapons material, dispersal of the unfissioned fuel, and activation of materials caught up in the fireballs of the explosions. These processes resulted in large amounts of radioactive fallout, which primarily deposited in the Pacific Ocean (Beck, 2010). The radionuclide fallout on the lagoon surface either settled rapidly to the bottom sediment of the lagoon or remained in the water column as dissolved or particle-bound material, which was eventually discharged to the Pacific Ocean (Robison and Noshkin, 1999).

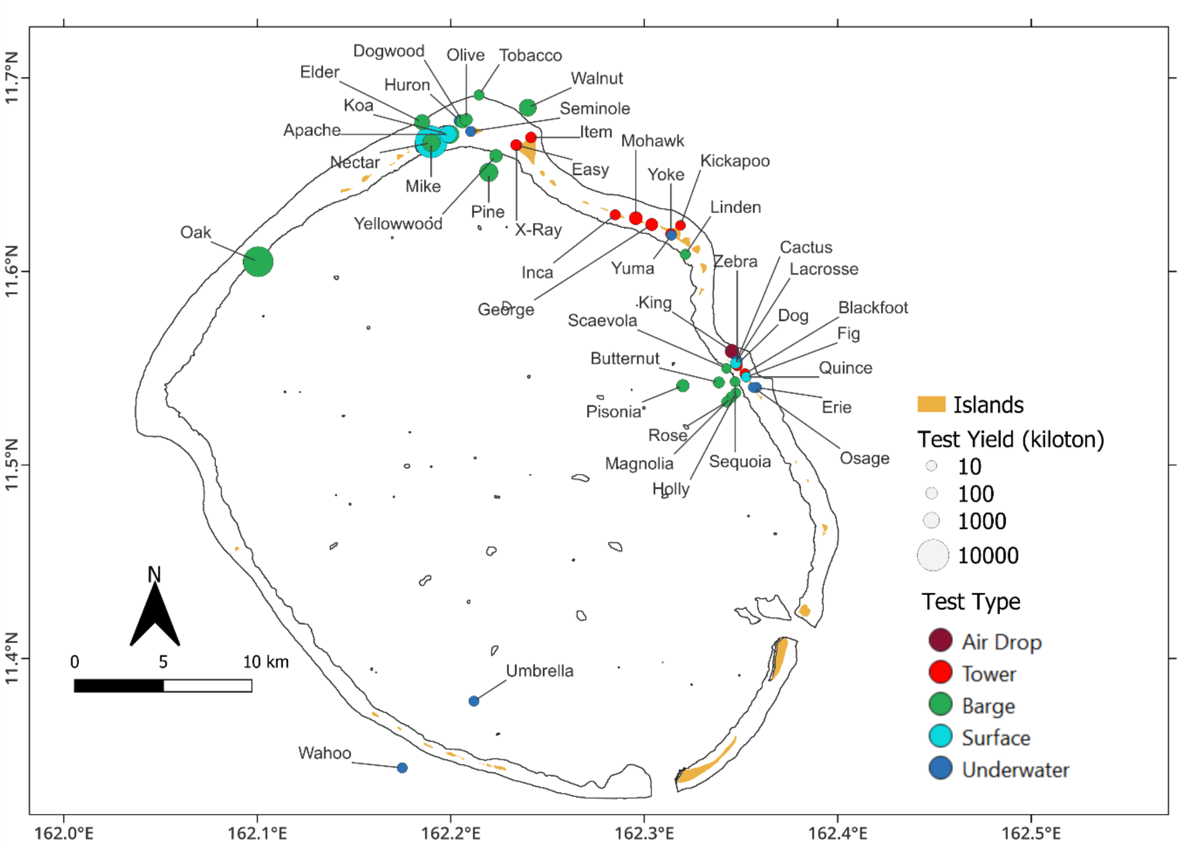

Figure 3. Locations, types, and yields of nuclear tests conducted on and near the Enewetak Atoll.

Radioactive decay and environmental removal mechanisms have reduced the amounts of short-lived radionuclides (e.g., ^{54}Mn, ^{57}Co, ^{65}Zn, ^{144}Ce, ^{110m}Ag, ^{95}Zr, ^{106}Ru). The lagoon sediments contain significant amounts of $^{239+240}$Pu and small amounts of ^{241}Am, ^{238}Pu, ^{137}Cs, ^{90}Sr, and ^{207}Bi (Robison and Noshkin, 1999). Ingestion dose to humans from marine food consumption is estimated to contribute only about 0.1% of the total effective dose for residents of the atoll from all pathways combined (Robison and Noshkin, 1999). As part of the AEC's Enewetak Survey Report during 1973, Robison (1973) assessed that the majority of the ingestion dose for marine food was contributed by ^{137}Cs, ^{60}Co, and ^{90}Sr. However, Robison and Noshkin (1999) reassessed the dose in 1998 and determined ^{137}Cs, ^{207}Bi, $^{239+240}$Pu, ^{60}Co, ^{241}Am, and ^{90}Sr as the major contributors to dose from marine food consumption.

Section 2.0 provides a summary of radionuclide data for island soils, lagoon sediments, lagoon waters, and Runit Dome from various studies performed by the RMI-contracted Nationwide Radiological Survey (Simon and Graham, 1995), Atomic Energy Commission (AEC)/DOE (AEC, 1973; DOE, 1982), Lawrence Livermore National Laboratory (Noshkin in [Hanson, 1980]; Hamilton, 2009), Wood Hole Oceanographic Institution (Buesseler et al., 2018), and the Defense Nuclear Agency (DNA, 1981). The largest studies were performed in the 1970s, major studies were conducted in the 1990s, and some follow-on studies were conducted in 2010s.

1.3 PNNL Approach

The main objective of this work was to assess environmental and human health impacts from potential release or redistribution of existing radionuclides at Enewetak Atoll, within the lagoon, and within the Runit Dome as a result of climate change. To achieve this goal, the work was divided into four major technical tasks:

1. Radionuclide source term estimation
2. Climate scenarios specification
3. Current and future scenario ocean modeling
4. Dose estimation.

These four tasks are discussed in Sections 2.0 to 5.0 of this report.

An extensive volume of literature exists that describes the history of nuclear tests at Enewetak Atoll, cleanup and rehabilitation efforts, and attempts to characterize the extent of radionuclide presence in the environment. PNNL reviewed these historical and contemporary reports to gain an understanding of the location and concentrations of various radionuclides on the islands, within the waters and sediments of the lagoon, and within the Runit Dome. PNNL used data from the RMI Nationwide Radiological Survey (Simon and Graham, 1995), corrected for radioactive decay to 2015 and 2090 to estimate the applicable radionuclide concentration in island soils. PNNL used existing data for radionuclide distributions from the AEC survey (AEC, 1973; Noshkin 1980) in the lagoon sediments to create maps of distributions of radionuclide activity. Because the available data represented the conditions in the early 1970s, PNNL corrected the data for radioactive decay to estimate distributions of radionuclide activities in 2015 and 2090. These radionuclide activities were used as initial conditions for ocean modeling.

Regional climate modeling over the western Pacific Ocean near the RMI is somewhat limited. While global climate models cover the whole region, finer scale regional climate modeling is not readily available; therefore, PNNL performed an independent assessment of severe storms near the Enewetak Atoll. From available historical storms databases, PNNL selected three storms that were strongest in history and/or passed close to the Enewetak Atoll such that they were likely to create the most severe hazards for the atoll. PNNL used the Advanced Research Weather Research and Forecasting (WRF-ARW) Model (Skamarock et al., 2019) to simulate these three plausible severe storms both in the current climate (approximately 2015) and in the future climate (approximately 2090). These plausible severe storms provided meteorological scenarios for subsequent ocean modeling.

To simulate the storm hazards, PNNL developed an ocean model for the RMI region using the Finite Volume Coastal Ocean Model (FVCOM) (Chen et al., 2003; Chen et al., 2013). The model domain covered almost the entire RMI Exclusive Economic Zone (EEZ) including areas within 1,000 km from Enewetak Atoll (Figure 1 and Figure 17 below). The ocean model was driven by the severe storm scenarios simulated by the WRF-ARW model. Six different storm scenarios were used corresponding to each of the three WRF-ARW-simulated plausible severe storms in the current climate and the future climate. The FVCOM simulations provided the ocean hydrodynamic conditions for radionuclide fate and transport modeling.

PNNL developed the FVCOM-Integrated Compartment Model (FVCOM-ICM) (Khangaonkar et al., 2018; Kim and Khangaonkar, 2012) to simulate mobilization and transport of radionuclides in and near the lagoon. Nine different mobilization and transport scenarios were used to represent three storms in the current climate, three storms in the future climate, and three storms in the future climate combined with a postulated, hypothetical release of radioactive material from the Runit Dome. The nine FVCOM-ICM simulations provided radionuclide concentrations in the lagoon waters and bottom sediments. These concentrations and island soil radionuclide concentrations were used to estimate human and biota radiation doses adjacent to all islands of the Enewetak Atoll. PNNL identified receptor locations for all islands of the Enewetak Atoll. Human and biota doses were calculated for several exposure pathways for all storm scenarios. Finally, PNNL compared the estimated doses in the current and future climate with U.S. human health risk standards. Radiation exposure standards for the United States are provided in Appendix F.

Following the publication of the draft report, PNNL solicitated public comments from interested stakeholders. Newspaper notices were published in the U.S. as well as RMI periodicals. The public comment period started on September 28, 2023 and ended on November 15, 2023. The authors of this report carefully considered each comment and responded to them. Several of the comments provided useful insights that were accepted by the authors and incorporated in the final report. The public comments and the authors’ responses are included in Appendix G.

2.0 Radionuclide Sources

Nuclear weapons testing at the Enewetak Atoll resulted in the dispersion of radionuclides across the northern atoll islands, the lagoon, and surrounding ocean. For estimating radiation doses to humans and biota, the following sources are important:

1. Radionuclides deposited on the land surface of the atoll islands and still present
2. Radionuclides deposited in or transported to the lagoon sediment
3. Radionuclides in the water column of the lagoon and the ocean
4. Radionuclides that were emplaced in the Cactus Crater/Runit Dome.

Radionuclides present in these locations at Enewetak Atoll are subject to various environmental and hydrodynamic processes, such as erosion and deposition, suspension and transport, and radioactive decay. Characterizing the present state of these sources, particularly concentrations of the radionuclides, is challenging because only a few radiological surveys have been performed in the last 50 years and only limited data are available to quantify the environmental processes.

2.1 Land and Soils

The primary source of information for radionuclides in the soils of the Enewetak Atoll is the *RMI Nationwide Radiological Study* (NWRS) (Simon and Graham, 1995). Volume 1 of the NWRS includes information on the RMI atolls of Ailinginae, Ailinglaplap, Ailuk, Arno, Aur, Bikar, Bikini, Ebon, Enewetak, Erikub, and Jabat. For Enewetak Atoll, the information was collected for 31 islands and organized in 14 different maps, from southeast to north and back to southwest. The organization of sampling maps for Enewetak Atoll from NWRS Volume 1 is shown in Figure 4.

The NWRS collected a large amount of data for Enewetak Atoll (see Appendix A). There was a total of 176 samples and measurements for the 31 islands. Not all radionuclides were included for analysis in every sample, especially for islands in the southern part of the atoll that had much lower exposure to fallout radionuclides. Fewer samples were taken from smaller islands. Sample types and measurements included soil profiles, surface soil samples and in situ gamma spectrometry measurements. Radionuclides included ^{137}Cs, ^{241}Am, $^{239+240}$Pu, and ^{60}Co.

No analysis was done in the NWRS for ^{90}Sr, a radionuclide of interest in soil for this study. To provide a more comprehensive profile of estimated soil concentrations on all islands, other, earlier sources of soil concentration data were used to supplement the NWRS data. The *Enewetak Radiological Survey*, NVO-140 (AEC, 1973), included measurements of ^{90}Sr as well as ^{137}Cs, ^{239}Pu, and ^{60}Co during late 1972 and early 1973. Mean ^{90}Sr-to-^{239}Pu concentration ratios in the top 15 cm of soil were used to estimate levels of ^{90}Sr at the time of the NWRS. To account for radioactive decay, PNNL assumed that the NWRS measurements were made during 1992. Both Pu and Sr are assumed to be relatively immobile in the soils of Enewetak Atoll, and the levels of ^{90}Sr and ^{239}Pu are affected only by radioactive decay. In Table 2 and Table 3, ^{90}Sr values shown in black were estimated using ^{90}Sr to ^{239}Pu ratio in NVO-140.

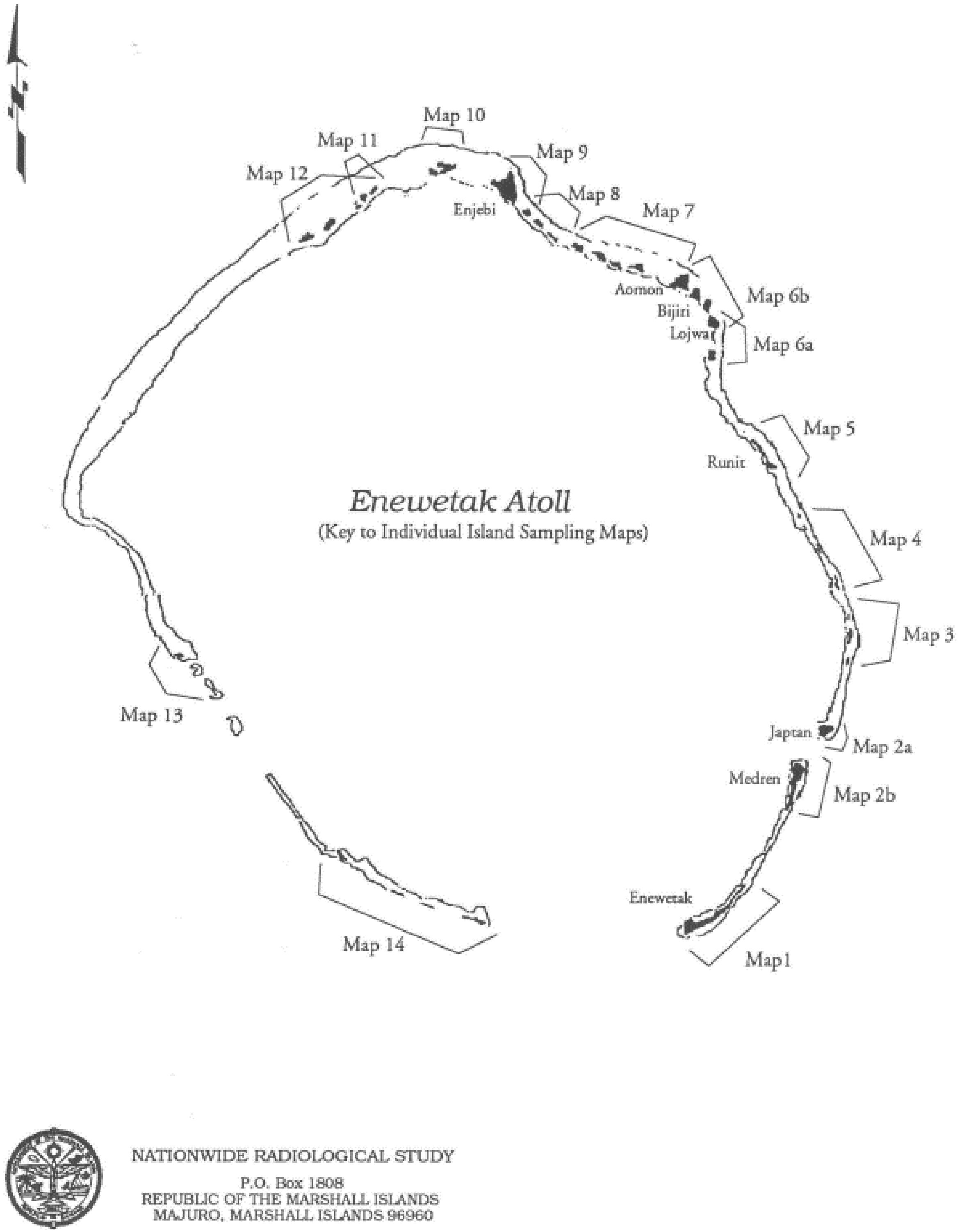

Figure 4. Map key for Enewetak Atoll sampling as part of the NWRS (Simon and Graham, 1995).

Survey information provided in the *Enewetak Radiological Support Project; Final Report*, NVO-213 (DOE, 1982), was used to compare to the NWRS data. For many of the islands with low concentrations of radionuclides, the NWRS analyzed for only ^{137}Cs and sometimes ^{60}Co, with no detection of other radionuclides. For immobile radionuclides, the ratios from NVO-213 were used in conjunction with NWRS data to estimate concentrations of ^{239}Pu and ^{241}Am. In Table 2 and Table 3, ^{90}Sr and ^{239}Pu values shown in blue were taken from NVO-213 (DOE, 1982). Where both 1972 and 1979 data were available, an average of the two values was taken. Values of ^{241}Am in Table 2 and Table 3 were estimated using a ratio of 0.3 of the ^{239}Pu value for that sample, based on ^{241}Am/^{239}Pu ratios rating from 0.11 to 0.5 across all samples.

Table 2 and Table 3 present the estimates of Enewetak Atoll soil concentrations in the years 2015 and 2090, respectively. Radionuclides ^{90}Sr, ^{241}Am, ^{239}Pu, and ^{60}Co are assumed to be relatively immobile in the soils, unlike Cs, and their levels are affected only by radioactive decay. For ^{137}Cs, an effective half-life of 8.5 years has been determined and reported that also accounts for environmental removal from RMI soil (Robison et al., 2003; Hamilton and Robison 2004). For this reason, ^{137}Cs was not used as a basis for estimating other radionuclide concentrations. Highest concentration of ^{137}Cs is on Bokoluo (Alice) and for other radionuclides on Bokombako (Belle), both located in the north-northwest portion of the atoll. These islands and values are bolded in Table 2 and Table 3.

The color key for soil concentrations basis in Table 2 and Table 3 is shown below; the symbol "-" indicates that no activity was detected.

- Black: ^{137}Cs, ^{241}Am, ^{239}Pu, ^{60}Co NWRS (Simon and Graham, 1995)
- Black: ^{90}Sr, ratio of ^{90}Sr/^{239}Pu NVO-140 (AEC, 1973)
- Blue: ^{90}Sr, ^{239}Pu NVO-213 (DOE, 1982)
- Red: ^{241}Am, 0.3 of ^{239}Pu NVO-213 (DOE, 1982)

Table 2. Year 2015 soil concentrations for the Enewetak Atoll.

NWRS Island #	NWRS Map #	Island name	U.S. assigned name	Island location	^{137}Cs (Bq/g)	^{90}Sr (Bq/g)	^{241}Am (Bq/g)	$^{239+240}$Pu (Bq/g)	^{60}Co (Bq/g)
1	1	Enewetak	Fred	SSE	2.0E-04	8.0E-03	8.9E-04	3.0E-03	-
2	2b	Medren	Elmer	SE	2.9E-04	1.0E-02	2.3E-03	7.8E-03	-
3	2a	Japtan	David	SE	8.4E-04	7.2E-03	5.5E-04	1.8E-03	-
4	3	Ananij	Bruce	E	7.4E-04	7.8E-03	1.0E-03	3.3E-03	-
5	4	Inedral	Uriah	E	1.1E-04	5.9E-03	1.0E-03	3.3E-03	1.3E-05
6	4	Van*	Van	E	4.2E-04	5.4E-03	8.9E-04	3.0E-03	-
7	5	Runit	Yvonne+	ENE	1.3E-02	3.0E-02	8.7E-02	5.7E-01	3.3E-04
8	6a	Alembel	Vera	NE	6.7E-03	8.6E-02	5.7E-02	9.6E-02	5.8E-05
9	6a	Billae	Wilma	NE	3.9E-03	1.9E-01	5.8E-02	1.8E-01	8.8E-05
10	6b	Aomon	Sally	NE	1.1E-02	1.6E-01	3.1E-02	2.3E-01	3.3E-05
11	6b	Bijiri	Tilda	NE	6.1E-03	1.7E-01	7.4E-02	1.4E-01	1.0E-04
12	6b	Lojwa	Ursula	NE	5.0E-03	1.3E-01	1.9E-02	7.0E-02	4.6E-05
13	7	Aej	Olive	NE	1.3E-02	2.7E-01	8.2E-02	2.7E-01	-
14	7	Elle	Nancy	NE	3.6E-02	2.8E+00	9.2E-01	2.0E+00	1.0E-03
15	7	Lujor	Pearl	NE	1.5E-02	2.7E-01	3.0E-01	9.9E-01	-
16	8	Bokenelab	Mary	NNE	1.2E-02	3.4E-01	9.6E-02	3.2E-01	-
17	8	Kidrinnenen	Lucy	NNE	1.4E-02	3.7E-01	9.9E-02	3.3E-01	-
18	8	Mijikadrek	Kate	NNE	9.2E-03	2.0E-01	5.2E-02	1.1E-01	-
19	9	Enjebi	Janet	N	3.5E-02	7.4E-01	1.4E-01	4.0E-01	3.0E-04
20	10	Boken–N	Irene	N	8.4E-03	1.1E+00	1.2E-01	1.1E+00	6.6E-04
21	11	Bokinwotme	Edna	NNW	6.4E-03	7.3E-01	1.5E-01	8.0E-01	-
22	11	Louj	Daisy	NNW	9.6E-03	1.2E+00	2.6E-01	7.2E-01	4.9E-04
23	12	**Bokoluo**	Alice	NNW	**1.6E-01**	3.8E+00	8.0E-01	1.6E+00	2.8E-03
24	12	**Bokombako**	Belle	NNW	8.2E-02	**6.9E+00**	**1.1E+00**	**4.1E+00**	**4.9E-03**
25	12	Kirunu	Clara	NNW	4.3E-02	2.9E-01	4.6E-02	2.8E-01	2.7E-04
26	13	Biken	Leroy	WSW	3.6E-03	4.6E-01	1.8E-02	7.4E-02	2.9E-04
27	14	Boken–SSW	Irwin	SSW	6.8E-05	9.1E-03	1.4E-03	4.8E-03	3.8E-05
28	14	Ikuren	Glenn	S	7.9E-04	1.8E-02	1.2E-03	4.1E-03	-
29	14	Kidrenen	Keith	SSW	4.2E-04	1.4E-03	1.2E-03	4.1E-03	-
30	14	Mut	Henry	S	7.8E-04	9.9E-03	1.6E-03	5.2E-03	1.9E-04
31	14	Ribewon	James	SSW	5.2E-05	9.1E-03	8.9E-04	3.0E-03	-

Table 3. Year 2090 soil concentrations for the Enewetak Atoll.

NWRS Island #	NWRS Map #	Island name	U.S. assigned name	Island location	^{137}Cs (Bq/g)	^{90}Sr (Bq/g)	^{241}Am (Bq/g)	$^{239+240}$Pu (Bq/g)	^{60}Co (Bq/g)
1	1	Enewetak	Fred	SSE	4.3E-07	1.3E-03	7.9E-04	2.9E-03	-
2	2b	Medren	Elmer	SE	6.4E-07	1.6E-03	2.1E-03	7.7E-03	-
3	2a	Japtan	David	SE	1.9E-06	1.2E-03	4.9E-04	1.8E-03	-
4	3	Ananij	Bruce	E	1.6E-06	1.3E-03	8.8E-04	3.3E-03	-
5	4	Inedral	Uriah	E	2.4E-07	9.7E-04	8.8E-04	3.3E-03	6.9E-10
6	4	Van*	Van	E	9.2E-07	8.9E-04	7.9E-04	2.9E-03	-
7	5	Runit	Yvonne+	ENE	2.8E-05	5.0E-03	7.7E-02	5.7E-01	1.7E-08
8	6a	Alembel	Vera	NE	1.5E-05	1.4E-02	5.0E-02	9.6E-02	3.0E-09
9	6a	Billae	Wilma	NE	8.7E-06	3.2E-02	5.1E-02	1.8E-01	4.6E-09
10	6b	Aomon	Sally	NE	2.4E-05	2.6E-02	2.8E-02	2.3E-01	1.7E-09
11	6b	Bijiri	Tilda	NE	1.4E-05	2.9E-02	6.5E-02	1.4E-01	5.3E-09
12	6b	Lojwa	Ursula	NE	1.1E-05	2.1E-02	1.6E-02	6.9E-02	2.4E-09
13	7	Aej	Olive	NE	2.9E-05	4.4E-02	7.3E-02	2.7E-01	-
14	7	Elle	Nancy	NE	8.0E-05	4.6E-01	8.1E-01	2.0E+00	5.2E-08
15	7	Lujor	Pearl	NE	3.3E-05	4.5E-02	2.6E-01	9.9E-01	-
16	8	Bokenelab	Mary	NNE	2.7E-05	5.6E-02	8.5E-02	3.2E-01	-
17	8	Kidrinnenen	Lucy	NNE	3.2E-05	6.1E-02	8.7E-02	3.3E-01	-
18	8	Mijikadrek	Kate	NNE	2.0E-05	3.2E-02	4.6E-02	1.1E-01	-
19	9	Enjebi	Janet	N	7.7E-05	1.2E-01	1.2E-01	4.0E-01	1.6E-08
20	10	Boken - N	Irene	N	1.9E-05	1.7E-01	1.1E-01	1.1E+00	3.4E-08
21	11	Bokinwotme	Edna	NNW	1.4E-05	1.2E-01	1.4E-01	8.0E-01	-
22	11	Louj	Daisy	NNW	2.1E-05	1.9E-01	2.3E-01	7.2E-01	2.5E-08
23	12	**Bokoluo**	Alice	NNW	**3.5E-04**	6.2E-01	7.1E-01	1.6E+00	1.5E-07
24	12	**Bokombako**	Belle	NNW	1.8E-04	**1.1E+00**	**9.4E-01**	**4.1E+00**	**2.5E-07**
25	12	Kirunu	Clara	NNW	9.4E-05	4.8E-02	4.1E-02	2.8E-01	1.4E-08
26	13	Biken	Leroy	WSW	7.9E-06	7.5E-02	1.6E-02	7.4E-02	1.5E-08
27	14	Boken - SSW	Irwin	SSW	1.5E-07	1.5E-03	1.3E-03	4.8E-03	2.0E-09
28	14	Ikuren	Glenn	S	1.7E-06	3.0E-03	1.1E-03	4.1E-03	-
29	14	Kidrenen	Keith	SSW	9.2E-07	2.4E-04	1.1E-03	4.1E-03	-
30	14	Mut	Henry	S	1.7E-06	1.6E-03	1.4E-03	5.2E-03	9.9E-09
31	14	Ribewon	James	SSW	1.2E-07	1.5E-03	7.9E-04	2.9E-03	-

2.2 Lagoon Sediments

AEC (1973) described the most comprehensive survey of lagoon sediment samples. Noshkin (in Hanson, 1980) also published lagoon sediment activity results for $^{239+240}$Pu and ^{241}Am based on data from AEC (1973). Similarly, Robison and Noshkin (1999) provided decay corrected estimates of the 1973 and 1979 survey results. However, all these data were not available in detailed raw format as they were published only as isopleth maps. Table 4 shows the average values based on the total inventory estimates and the ranges of values in the isopleth maps.

Table 4. Summarized data for lagoon sediments from three reports at different times

	AEC (1973)		Noshkin (in Hanson, 1980)[a]		Robison and Noshkin (1999)[b]		
Radionuclides	Mean (mCi/km^2)[†]	Range (mCi/km^2)	Mean (mCi/km^2)	Range (mCi/km^2)	Mean Up to 2-cm Depth (mCi/km^2)	Mean Up to 30-cm Depth (mCi/km^2)	Range (Bq/kg)
^{90}Sr	586	16–10,000			135	1,081	
$^{239+240}$Pu	463	15–14,000	267	5.8–4,650	243	1,811	
^{238}Pu			38				
^{241}Pu			493				
^{137}Cs	78	5–3,000			27	162	
^{60}Co	73	10–2,000			3	11	
^{102m}Rh	8.4	5–100					
^{241}Am	172	10–9,000	81	4.9–3,015	108[c]	730[c]	50–900
^{207}Bi	163	3–6,000			54	486	50–1,000
^{155}Eu	369	20–5,000			5	54	
^{152}Eu	2.5	1–50					
^{125}Sb	22	2–500					
^{101}Rh	1.2	1–10					

[a] 2.5 cm depth only

[b] Decay corrected to October 1998 from January 1973 data

[c] 1998 inventory for ^{241}Am was computed from decay and ingrowth from estimated levels of ^{241}Pu in Noshkin (in Hanson, 1980)

[†] 1 mCi/km^2 = 37 Bq/m^2; 1 mCi/km^2 is equivalent to 1.4 Bq/kg for 2 cm depth and 0.1 Bq/kg for 30 cm depth assuming 1.29 g/cm^3 sediment density

Figure 5 shows the $^{239+240}$Pu distribution in the top sediment layer from NVO-140 (AEC, 1973); this and similar maps for other radionuclides (^{241}Am and less detailed maps from NVO-140 for ^{90}Sr, ^{137}Cs, ^{207}Bi, ^{152}Eu) were digitized by PNNL for input to radionuclide mobilization and transport modeling (Figure 6). AEC (1973) indicated that ^{54}Mn and ^{57}Co significantly decayed and therefore were not detected in the marine environment. ^{106}Ru also decayed to an average of 0.6 pCi/g, while ^{154}Eu was found in seven samples (at or near Koa crater) with values of 0.5 ±0.6 pCi/g. AEC (1973) found ^{90}Sr as the most abundant radionuclide, followed by $^{239+240}$Pu, ^{155}Eu, ^{241}Am, ^{207}Bi, ^{137}Cs, ^{60}Co, ^{125}Sb, ^{102m}Rh, ^{152}Eu, ^{101}Rh, ^{154}Eu, and ^{106}Ru. Approximately 11–20% of the lagoon sediments contained activities of ^{90}Sr, $^{239+240}$Pu, ^{155}Eu, ^{241}Am, ^{125}Sb, ^{207}Bi, ^{60}Co, ^{102m}Rh, and ^{137}Cs above their respective average levels. For modeling present and future conditions, only ^{152}Eu, ^{207}Bi, ^{90}Sr, ^{137}Cs, ^{241}Am, and $^{239+240}$Pu have been retained.

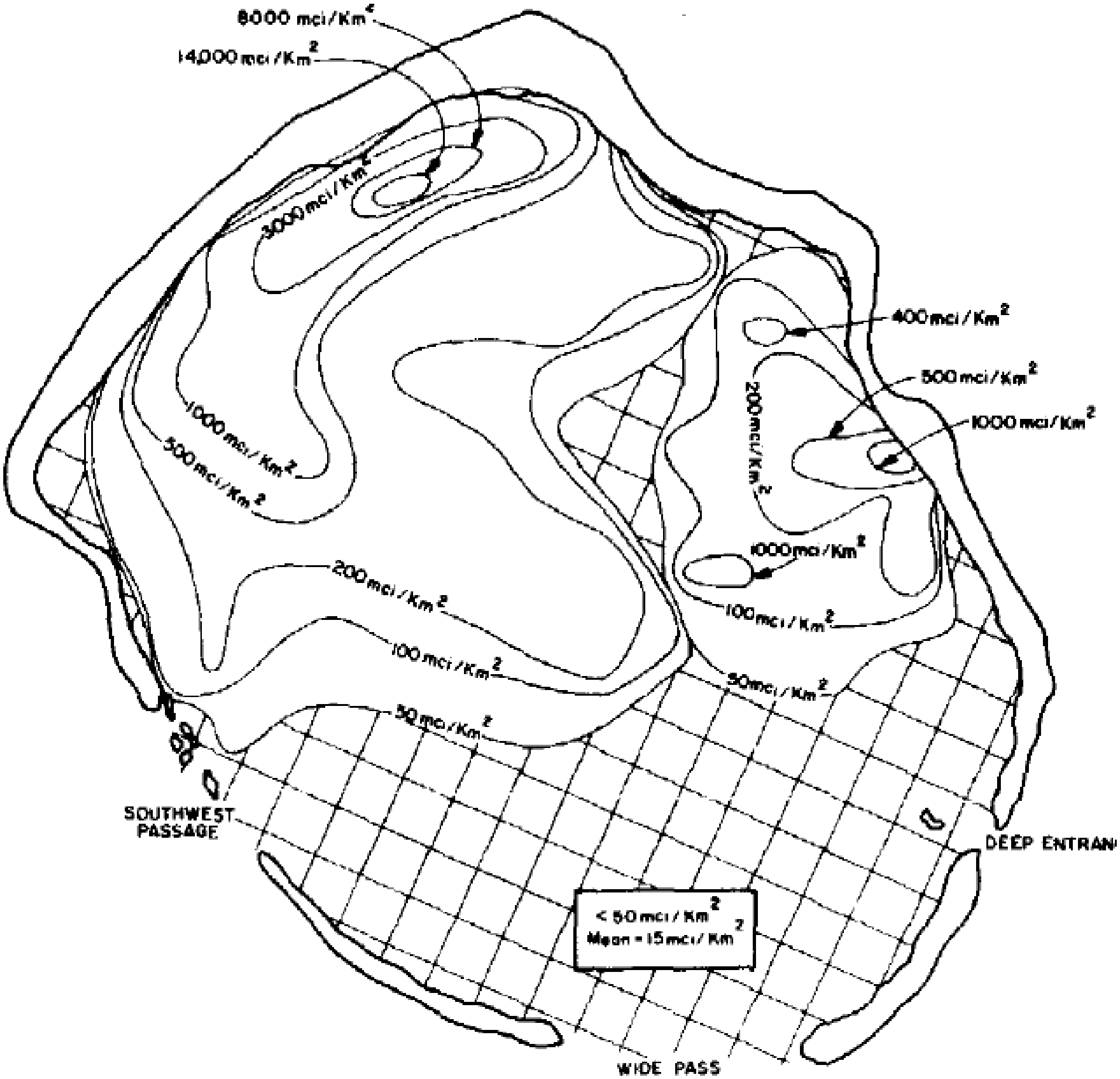

Activity levels of ^{239,240}Pu deposited in the sediments of Enev

Figure 5. Activities of $^{239+240}$Pu (mCi/km^2) in the sediment components in the top sediment layer of Enewetak Lagoon from NVO-140 (AEC, 1973). 1 mCi/km^2 = 37 Bq/m^2 and equivalent to 1.43 Bq/kg for 2 cm depth assuming 1.29 g/cm^3 sediment density

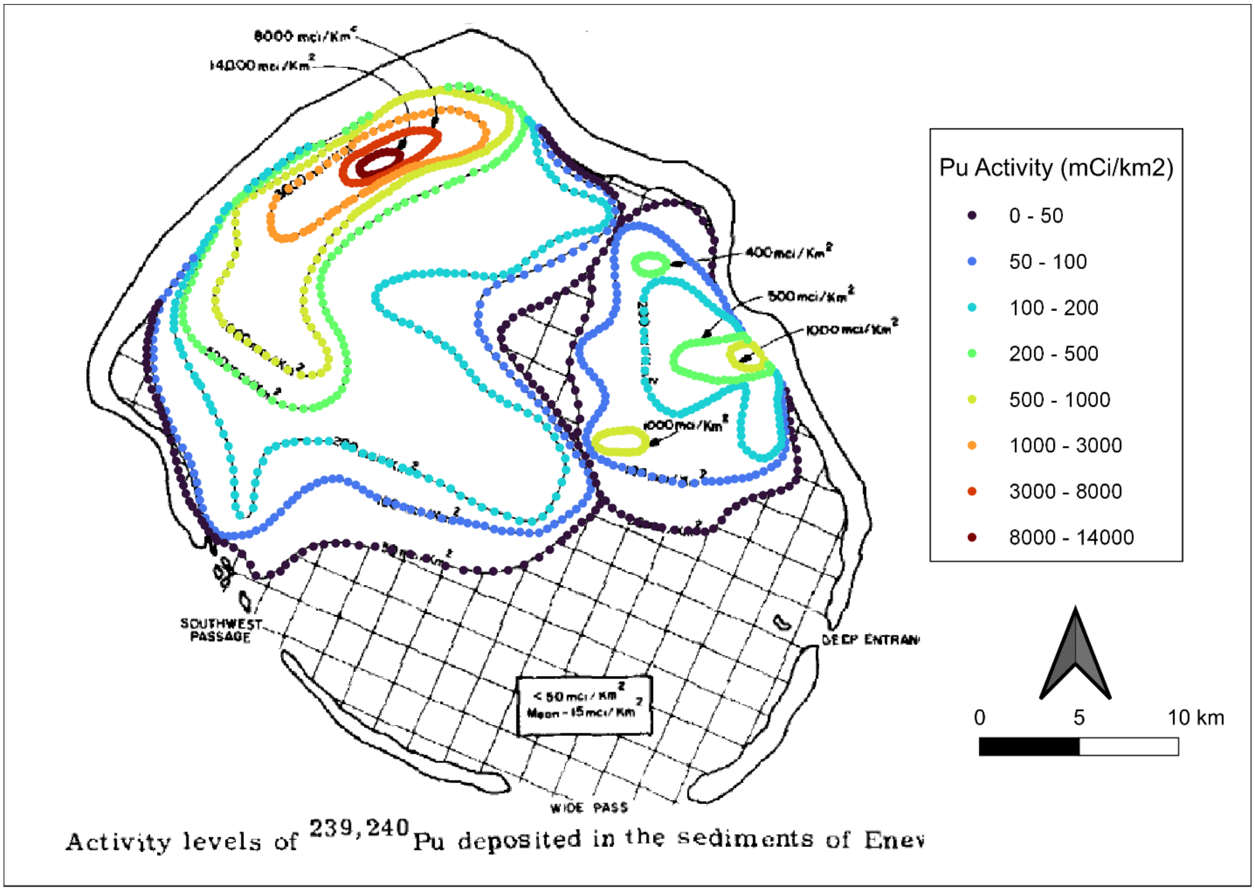

Figure 6. PNNL-digitized map of activities of $^{239+240}$Pu (mCi/km^2) in the sediment components in the top layer of Enewetak Lagoon. 1 mCi/km^2 = 37 Bq/m^2 and equivalent to 1.43 Bq/kg for 2 cm depth assuming 1.29 g/cm^3 sediment density

The highest radionuclide concentrations were observed within sediments from the northwest quadrant of the Enewetak lagoon, 2–3 km east of Bogallua (Alice) and Bokombako (Belle) islands and several kilometers southwest of MIKE and Koa craters (Noshkin [in Hansen 1980]). A second region of elevated concentrations is west of Runit (Yvonne); a portion of this region was affected by the failed Quince test that deposited unfissioned plutonium nearby as well as that from the failed Scaevola tests in the lagoon. AEC (1973) provided detailed sediment data for all radionuclides from both surface sediments and core sample sediments (see Tables 50 and 52, respectively, of the AEC report). Table 5 provides the raw data for two core samples from AEC (1973).

Table 5. Radionuclide concentrations (pCi/g) in the core samples from MIKE and Koa craters (AEC, 1973). 1 pCi/g = 37 Bq/kg

Sample No (lagoon floor depth)	Sediment Depth (cm)	^{60}Co	^{102m}Rh	^{101}Rh	^{125}Sb	^{137}Cs	^{155}Eu	^{207}Bi	^{241}Am	^{239}Pu	^{90}Sr
17E (92 ft)	0-5	10.8	2.4	0.59	2.4	13.1	42.9	3.17	20.1	51.4	56.3
	5-10	11.3	2.8	0.68	2.1	13.5	45.6	4.65	19.6	50.5	73.4
	10-15	27.1	4.3	0.98	8.1	16.4	63	11.4	22.4	60.8	91.4
	15-20	47.3	5.7	1.45	16.9	18.6	60.4	8.2	16.4	58.3	112.2
	20-25	53.7	5.4	1.41	16.4	17.2	54.3	2.5	14.1	51.4	117.1
	25-30	59.4	5.8	1.68	22.6	17.9	54.7	1.6	12.2	47.2	159
	30-35	55.5	5.1	1.48	25.8	15.9	46	0.7	10.4	40.9	104
	35-40	83.8	7	1.95	27.9	24	59.6	0.3	12.2	47.8	126
	40-45	83.5	7	1.9	29.1	23.9	61.2	0.3	13.6	45.5	132
	45-50	88.9	7.1	1.99	29.2	24.5	59.4	0.3	13.7	45.5	146
	50-56	71.3	6.3	1.77	19.5	20	47	0.5	12.6	91.4	113
16E (91 ft)	0-5	NA	3.4	0.77	3.9	14.3	40.4	4.45	15.3	34.6	49.6
	5-10	60.7	7.2	1.91	15.2	20.1	57.6	4.93	16.1	51.4	60.4
	10-15	52.1	6.3	1.72	19.7	19.4	49.5	0.5	12.7	46.4	88.7
	15-20	54.3	4.5	1.25	20.1	19.6	44.4	1.5	11.3	39.8	93.7
	20-25	68.3	6.2	1.54	22.9	21	49.4	0.5	10.7	42	81.9
	25-30	64.1	5.5	1.63	25.2	20.6	46.3	0.5	8.9	40.2	131
	30-38	64.2	5.7	1.61	22.4	20.8	45.1	0.4	7.9	44.3	106

Figure 7 shows a profile of ^{241}Am and ^{239}Pu concentrations based on the sediment core samples in Mike and Koa craters as reported by Noshkin (in Hanson, 1980) using the raw data in Table 5. The sediment concentrations were nonhomogenous along the sediment depth. ^{207}Bi was noted to decrease with depth at 17E station, while ^{60}Co, ^{102m}Rh, ^{101}Rh, ^{125}Sb, ^{137}Cs, and ^{90}Sr increased with depth. ^{155}Eu and ^{239}Pu were noted to be uniformly distributed along sediment depth, while ^{241}Am decreased with depth at station 17E. At 16E, all radionuclides are homogenously distributed, except for ^{207}Bi and ^{90}Sr.

In the sediments offshore of Runit (Yvonne) Island, radionuclide concentrations were slightly lower than in the northwest region, but significant concentrations were observed. Cleanup of major contaminated soils was performed, with Runit (Yvonne) Island being the sediment repository from 1977 through 1980.

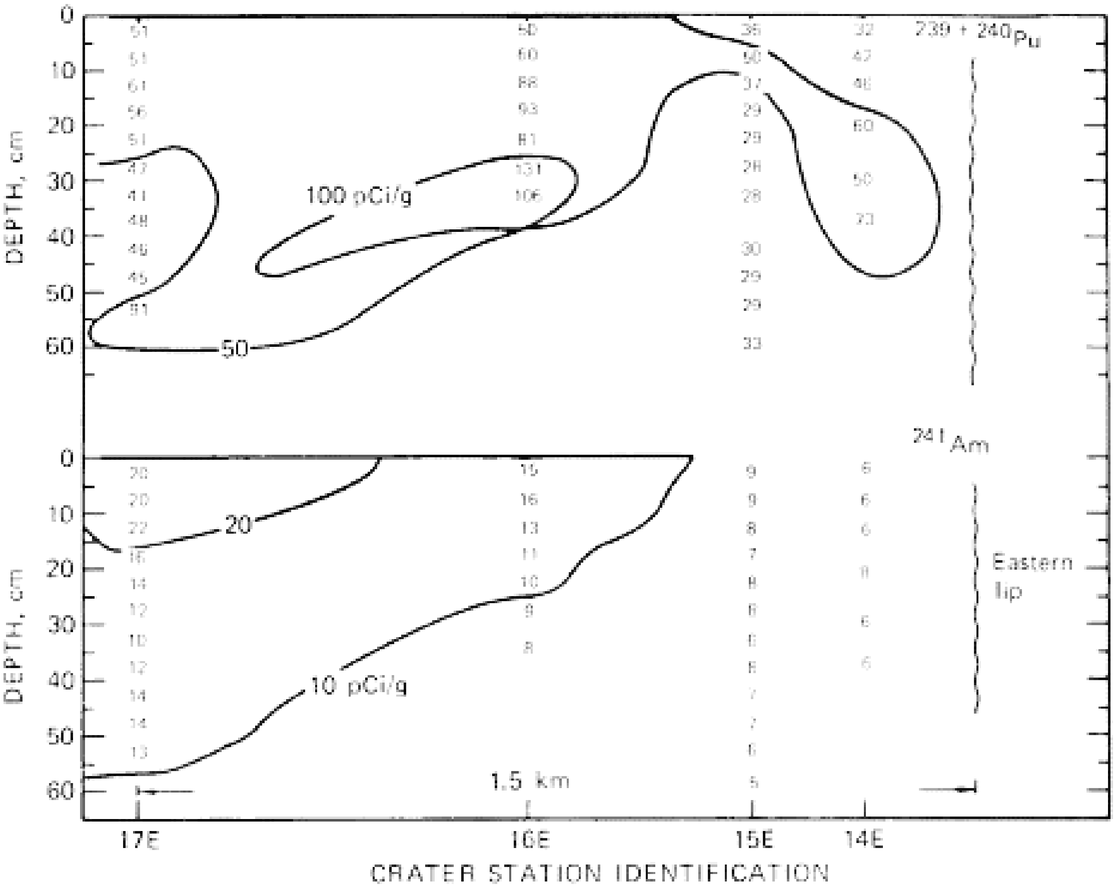

Figure 7. Vertical and areal concentration distribution pf $^{239+240}$Pu and ^{241}Am in sediments within Mike and Koa craters (Noshkin, 1980). 1pCi/g = 37 Bq/kg

Buesseler et al. (2018) collected sediment core samples at Mike Crater and near Runit Island. Table 6 provides the raw data from the study for sediment core samples. The highest sediment concentrations were found in Mike Crater with sampling to a depth of 62.5 cm. ^{137}Cs activity was in the 118–194 Bq/kg range of in Mike Crater sediment core sample. $^{239+240}$Pu concentrations were in the 1,294–1,644 Bq/kg range in Mike Crater sediment samples. ^{241}Am concentrations were found in the 677–926 Bq/kg range. Low ^{207}Bi concentrations were found in the 4.4–23.6 Bq/kg range.

Exact locations of the Runit Island shore samples were not provided, although they appear to be on the lagoon side near the Runit Dome. One sediment sample (Runit Shore 1) was taken up to 32.5 cm, while another (Runit Shore 2) was sampled up to 15 cm. ^{137}Cs activities were in the 0.3–3.1 Bq/kg range. $^{239+240}$Pu was in the 300–396 Bq/kg range. ^{241}Am was in the 54–83 Bq/kg range. At <2.5 Bq/kg, the activity of ^{207}Bi was very low. This study indicated that McMurtry et al. (1986) found activity as deep as 2 m below the seafloor near Runit Dome. Buesseler et al. (2018) concluded that the Pu inventory in the Runit Island sediment core is 1.6% of the inventory measured in the Mike Crater core. Previous studies (Noshkin and Robison, 1997) indicated that the waste disposal beneath the dome is <1% (225 GBq) of the total Pu inventory at Enewetak lagoon (44,000 GBq). Preexisting (i.e., prior to the dome placement) transuranic (TRU) waste with 67,000 GBq of activity has been found in marine sediments of Enewetak

Lagoon (Noshkin [in Hansen 1980]; Noshkin et al., 1987; Noshkin and Robison, 1997; Hamilton, 2021).

Table 6. Radionuclide concentrations (Bq/kg) in sediment core samples from 2015 (Buesseler, 2018).

Core area	Depth (cm)	^{137}Cs	^{241}Am	^{207}Bi	^{239}Pu	^{240}Pu
Runit Shore 1	0.5	BD	81	0.9	318	75
	1.5	0.3	80	1.3		
	2.5	3.1	78	1.3		
	3.5	0.6	76	BD		
	4.5	BD	83	0.9		
	12	BD	68	1.2		
	16	BD	60	1.9	244	56
	20.5	BD	75	0.7		
	26.5	BD	77	1.3		
	32.5	BD	81	2.5	319	77
Runit Shore 2	0.5	2.6	60	2.3		
	2.5	2.8	62	2		
	4.5	1.9	57	1.5		
	8	2.1	60	1.8		
	15	2.3	54	2.2		
Mike Crater	0.5	153	843	5.3	748	546
	2.5	122	717	8.7		
	4.5	162	733	11.8		
	8	138	787	BD		
	12	118	785	BD		
	16	154	831	5.8		
	20.5	161	926	BD	782	529
	26.5	137	882	BD		
	32.5	185	884	BD		
	38.5	194	768	13.1	1076	568
	44.5	172	762	BD		
	50.5	177	718	23.6		
	56.5	181	677	9.6		
	62.5	171	747	4.4	936	485

Based on the 1972 AEC survey, Noshkin and others estimated that a total inventory of 64 GBq of TRUs ($^{239+240}$Pu = 47.5 GBq, ^{238}Pu = 11.9 GBq, ^{241}Am = 4.8 GBq) were present in the lagoon sediment (up to 2.5 cm depth) within 0.7 km offshore of Runit Island (Noshkin [in Hansen 1980]; Noshkin and Robison, 1997).

Digitized contour plots (such as Figure 6) were used as input to radionuclide mobilization and transport modeling. The original source data (Noshkin [in Hansen 1980], NVO-140) were decay corrected to current and future times, with no other attenuation. The decay factors are provided in Table 7.

PNNL selected six parent radionuclides for consideration as listed in Table 7. Only a minor amount of ^{241}Pu was observed; therefore, it is neglected, including its ingrowth to ^{241}Am. Many radionuclides are short-lived compared to the time since the 1973 AEC survey, and it can be reasonably assumed that radionuclides such as ^{101}Rh, ^{102m}Rh, ^{60}Co, ^{155}Eu, and ^{155}Sb are no longer present in the environment. Also, PNNL assumed that washout from the lagoon is negligible compared to radioactive decay that reduces the radionuclide inventory.

Table 7. Decay factors for relevant radionuclides obtained from NuDat 2.3 (NNDC 2007).

Nuclide	Half-Life (yr)	1973	2015	2090
^{90}Sr (+ ^{90}Y)	28.9	1	0.365	0.060
^{137}Cs (+ ^{137m}Ba)	30.08	1	0.380	0.067
$^{239+240}$Pu	24,131	1	0.999	0.997
^{241}Am	432.6	1	0.935	0.829
^{207}Bi	32.98	1	0.414	0.086
^{152}Eu	13.54	1	0.116	0.003

Radionuclide concentrations in the lagoon sediment were derived from the AEC survey (1973). The contour maps in AEC (1973) were digitized and interpolated after radioactive decay to 2015. However, spatial data were missing in these contour maps in most of the southern part of the atoll. Therefore, a reasonable background for these southern regions with low sediment concentrations was estimated from the interpolated maps. Islands including Enewetak (Fred), Boken (Irwin), Ikuren (Glenn), Mut (Henry) and Kidrenen (Keith) are located near the low sediment concentration regions. Table 8 provides the minimum value for each radionuclide that was estimated as background 2015 conditions for these regions with no data. Table 8 also shows the concentrations per unit area which are comparable and lower than the minimum value reported in the contour maps within AEC (1973).

Table 8. Sediment concentrations for southern regions of Enewetak lagoon.

	Sediment Concentration		
Nuclide	Bq/m^3	Bq/kg	mCi/km^2
^{152}Eu	200	0.1	0.2
^{207}Bi	10,000	5	8.6
^{137}Cs (+ ^{137m}Ba)	3,000	1.5	2.6
^{241}Am	10,000	5	8.6

2.3 Lagoon Waters/Ocean

Measurements made at times ranging over several decades following the cessation of bomb testing at the atoll have shown a fairly stable level of radionuclide concentration in the lagoon waters. Measurements made in 1972 (AEC, 1973), 2015 (Buesseler, 2018), and 2018 (Hamilton, 2021) are in reasonable agreement, accounting for location within the lagoon, when corrected for radioactive decay. The primary sources list only ^{137}Cs and ^{239}Pu in common.

Lagoon water samples were collected during the 1972 AEC survey. The 55 L water samples were collected at various locations within the lagoon, with sampling depth ranging from 3–195 ft. Only ^{137}Cs and $^{239+240}$Pu were found ubiquitously in all lagoon water samples. The highest $^{239+240}$Pu concentration of 3,780 fCi/L was measured in a 190 ft deep sample at the northeast side near the Runit Island. The highest ^{137}Cs concentration of 8,910 fCi/L was measured in a 110 ft deep sample within the Koa Crater. About 1,510 fCi/L of $^{239+240}$Pu was also measured from the sample in Koa Crater. The following radionuclides were found to be below detectable limits: ^{102m}Rh, ^{125}Sb, ^{106}Ru,^{152}Eu, and ^{235}U. Radionuclides, including ^{60}Co, ^{155}Eu, ^{207} Bi, and ^{241}Am, were detected only in 15 samples from the northern part of the lagoon. The survey also noted that surface waters contained 30% higher concentration of $^{239+240}$Pu and ^{137}Cs than the bottom waters.

Buesseler et al. (2018) collected seawater (including lagoons) and groundwater samples. Table 9 provides the raw data collected at various locations in Enewetak Atoll.

Table 9. Lagoon seawater and groundwater sampling data from 2015 (Buesseler 2018).

B#	LatN	LonE	^{137}Cs (Bq/m^3)	^{226}Ra (Bq/m^3)	$^{239+240}$Pu (mBq/m^3)
Lagoon seawater					
B223	11.48602	165.3639	1.24	1.35	
B224	11.67945	163.6039	1.05	1.19	3
B225	11.30557	162.2933	1.04	0.84	0.5
B228	11.55083	162.3465	4.75	1.33	1,203
B229	11.55083	162.3465	3.11	1.29	
B230	11.55083	162.3465	2.31	1.26	1,552
B231	11.55083	162.3465	3.13	1.41	1,239
B205	11.39766	162.3653	1.3		
B206	11.36012	162.3457	1.28		
B207	11.34869	162.3326	1.87		
B226	11.34768	162.3189	1.54	0.96	
B227	11.47137	162.3141	1.39		
B232	11.55549	162.3371	1.37		
B233	11.53961	162.354	1.35		
B236	11.56047	162.2778	1.62	0.89	
B237	11.64987	162.219	2.66	0.98	
B244	11.66325	162.1888	2.37	0.92	
B245	11.66318	162.1889	34.6		606
B246	11.66318	162.1889	34.6		546
B247	11.66318	162.1889	34.6		911
B527	11.66365	162.2337	4.3	1.59	199
Groundwater					
B515	11.3402	162.3231	0.4	0.38	
B516	11.34135	162.3218		bd	
B517	11.34371	162.3313	2.4	1.11	13
B518	11.34191	162.3295	4.1	0.77	
B523	11.54954	162.3494	90.1	1.54	751
B525	11.55199	162.3468	109.3	2.45	780
B522	11.55124	162.3471	21.9	2.01	785
B524	11.55159	162.3466	8.2	1.55	
B528	11.66105	162.2376	110.3	1.45	
B526	11.66404	162.2336	10.2	1.98	

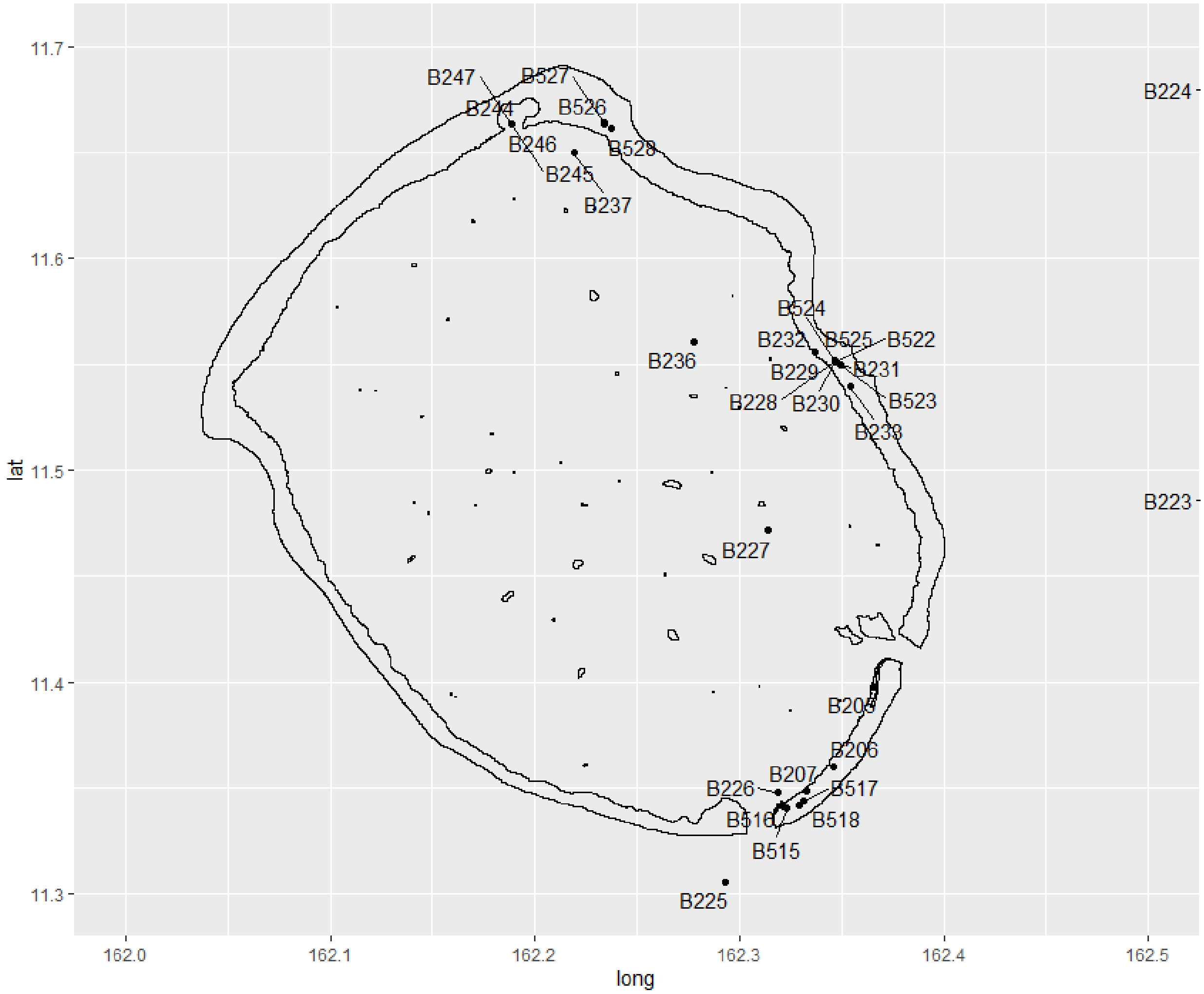

Figure 8. Sampling locations from Buesseler (2018).

The $^{240\text{Pu}/239}$Pu ratio was 0.065 ±0.003 in the lagoon waters, groundwater, and sediments at the vicinity of Runit Dome. This ratio was 0.225 ±0.013 in the groundwater within Mike Cater. The Pu isotopic data suggested conservative mixing between these two sources in the Enewetak Lagoon. Buesseler et al. (2018) estimated that 48% of the $^{239+240}$Pu in the lagoon waters was derived from a Runit Dome area source and 52% from waters originating from the Mike Crater area. This finding is surprising given that the Runit Dome and nearby lagoon sediments are associated with an estimate of <1% of the total Pu inventory in the entire atoll. The groundwater flux toward the lagoon was estimated as 2,100 Bq/day for $^{239+240}$Pu and 96,000 Bq/day for ^{137}Cs. The lagoon water flux to the north Pacific Ocean was estimated as 2.2 × 10^9 Bq/day for $^{239+240}$Pu and 1.5 × 10^9 Bq/day for ^{137}Cs. Groundwater flux is not a major source of Pu or Cs to lagoon seawater, particularly from the Runit Dome. Yet, isotopic ratio analyses showed that half of the Pu isotopes in lagoon water is associated with the Runit Dome source. Buesseler et al. (2018) therefore indicated that more comprehensive seafloor sampling with deeper cores in the Runit area may reveal higher inventories. With the available data, PNNL concluded that, while the fraction of total Pu associated with the Runit Dome area sediments is small, it contributes disproportionately to the total Pu flux to the lagoon waters. However, it should be noted that these inferences are based on samples in the immediate vicinity of the Mike Crater and Runit Dome. Although there may be high flux from Runit Dome groundwater to the nearby lagoon water, remobilization of Pu from lagoon sediments into the lagoon waters is likely to be the principal source of these isotopes during the post-testing period (Froehlich et al., 2017). The Fig, Quice, and Scaevola tests distributed large amounts of weapons-grade Pu (generally with a ^{240}Pu/^{239}Pu ratio of about 0.065) on and near Runit Island; therefore, the differences between fissioned and unfissioned fuel is not surprising.

Noshkin (in Hanson 1980) estimated that the lagoon water inventory of plutonium was only 0.68% of the content of the lagoon sediments to a depth of 2.5 cm and 0.14% of the sediment content to a depth of 16 cm.

AEC (1973) describes a small number of individual measurements of ^{207}Bi, and even fewer of ^{241}Am. Several of these are measurements of water near the bottom of MIKE and Koa craters; these have been eliminated from the following analyses. ^{207}Bi has a radiological half-life of 32.98 years; the ratio of ^{207}Bi to $^{239/240}$Pu in 1972 was about a factor of 7; decayed to 2015 this ratio is about 3. A simple ratio of 3 was used to estimate the 2015 background of ^{207}Bi for 2015 non-storm conditions. Similarly, the very limited measurements of ^{241}Am show a ratio of about 0.3 to $^{239/240}$Pu – which is in very close agreement to the much more numerous measurements of these radionuclides in terrestrial island soils. Therefore, a ratio of 0.3 to plutonium is used for americium.

Historical measurements of ^{90}Sr in lagoon waters are rare. AEC (1973) states that “Plutonium radionuclides were isolated from the hydroxide fraction and determined by alpha spectrometry, the residual fraction was concentrated and counted on a Ge(Li) diode for gamma emitters, and the ^{90}Sr fraction was sent to a participating laboratory for further analysis.” No further ^{90}Sr results are presented in the AEC report. However, Noshkin et al. (1974, UCRL-51612, Table 2 and Figure 7) reported both ^{137}Cs and ^{90}Sr for many samples that appear to coincide with those reported in AEC (1973). In this reasonably extensive compilation, the ratio of ^{90}Sr to ^{137}Cs is essentially unity, ranging from 0.5 to 1.8.

Likewise, historical measurements of ^{60}Co and ^{152}Eu in lagoon water are rare. Because the half-lives of ^{60}Co and ^{152}Eu are 5.27 years and 13.5 years, respectively, both should have decayed to essentially non-detectable levels in water by the years 2015 and 2090 used in this analysis and are omitted from the baseline.

The limited data available have been aggregated as was performed in AEC (1973) into the four quadrants of the lagoon. The results are shown in Table 10. To put in proper perspective the concentrations of the radionuclides measured in the lagoon water, a comparison with the natural concentration of ^{40}K is useful. ^{40}K in seawater is, on the average, 10,100 Bq/m^3 (Noshkin 1974), a concentration several orders of magnitude higher than that for any fission or activation product measured in any atoll water sample.

Table 10. Concentrations of radionuclides in surface water quadrants of Enewetak Lagoon.

Location	Concentration (Bq/m^3)				
Quadrant	^{137}Cs	$^{239+240}$Pu	^{207}Bi	^{241}Am	^{90}Sr
NW	7.96	1.24	3.71	0.37	8.00
NE	4.59	1.58	4.73	0.47	4.60
SW	4.56	0.80	2.40	0.24	4.50
SE	3.11	0.34	1.01	0.10	3.00

The islands located within each surface water quadrant are shown in Table 11.

Table 11. Islands located in each surface water quadrant of the Enewetak Lagoon.

Reference	Marshallese	US assigned	Reference	Marshallese	US assigned
NW			NE		
20	Boken - N	Irene	7	Runit	Yvonne
21	Bokinwotme	Edna	8	Alembel	Vera
22	Louj	Daisy	9	Billae	Wilma
23	Bokoluo	Alice	10	Aomon	Sally
24	Bokombako	Belle	11	Bijiri	Tilda
25	Kirunu	Clara	12	Lojwa	Ursula
			13	Aej	Olive
			14	Elle	Nancy
			15	Lujor	Pearl
			16	Bokenelab	Mary
			17	Kidrinnenen	Lucy
			18	Mijikadrek	Kate
			19	Enjebi	Janet
SW			SE		
26	Biken	Leroy	1	Enewetak	Fred
27	Boken - SSW	Irwin	2	Medren	Elmer
28	Ikuren	Glenn	3	Japtan	David
29	Kidrenen	Keith	4	Ananij	Bruce
30	Mut	Henry	5	Inedral	Uriah
31	Ribewon	James	6	Van	Van

2.4 Cactus Crater/Runit Dome/Wells

Cactus Crater was formed in May 1958 when the Cactus device was detonated on a manmade extension of Runit Island on the lagoon side of the reef. The test produced a crater roughly 112 m in diameter and 10 m in depth. The crater had an average volume of 3.3×10^4 m^3 but could hold up to 4.4×10^4 m^3 of water during high-tide periods. The total surface area was 6,900 m^2, of which 2,060 m^2 were covered with sedimentary deposits. Most of the crater rim is on land, but about a quarter of the eastern circumference was open and permitted exchange of water between the crater and the ocean during periods of high tide. Dye tracer studies showed that most of the water from the crater is lost by southwest overflow into the lagoon during high tides (Marsh et al., 1978). The dye studies also showed that only small amounts of crater waters enter the island’s groundwater. The mean residence time of the crater water was about 2.6 days with variability due to tidal flow (Marsh et al., 1978).

Cleanup of Enewetak Atoll extended from May 1977 to April 1980 and focused on reducing the concentration of transuranic elements in soils on some of the islands that might eventually be used for residence or for subsistence agriculture. Some of the contaminated soil was placed below the water level in the Cactus Crater, the rest of the contaminated material was mixed with concrete and placed above the ground over the crater in the shape of a dome. A concrete cap was constructed over the dome. The amount of soil and TRUs transferred to the crater obtained from cleanup records are shown in Table 12 (Noshkin and Robison, 1997). Approximately 50% of the total inventory under the concrete dome originated from five northern islands of the atoll. The remaining material was surface material translocated from one or more areas on the Runit Island. Only 24% of the total TRU was buried below ground level in the crater, while the remaining activity is associated with material placed above the water level under the dome. The average soil concentration of TRU in the undiluted crater fill was estimated as 2.4 Bq/g (Noshkin and Robison,1997). The bottom sediment from the crater was sampled in 1974 with TRU concentration of 4.7 Bq/g (Noshkin and Robison, 1997). Overall, the crater dome was estimated to contain 0.8% of the total TRU inventory contained in the top 16 cm of the lagoon sediment. A minimum of 30 GBq of residual activity was estimated to be already residing below the Cactus Crater from the test fallout (Davisson et al., 2012). This estimate was made from gamma measurements during drilling of Cactus Crater before the radioactive debris from other island soils was moved later into the crater.

Table 12. TRU activity and volume of soil placed in Cactus Crater (Noshkin and Robison, 1997). Data obtained from DNA, 1981.

Island	TRU Activity	Soil removed (m^3) to	
	(GBq)	Crater	Dome
Aomon (Sally)	48.1	8,100	0
Aomon Crypt (Sally)	33.3	342	7,130
Boken (Irene)	37.0	322	3,450
Enjebi (Janet)	96.2	32,890	7,633
Lujor (Pearl)	63.0	0	11,415
Runit (Yvonne)	267.4	0	8,210
Total	545.0	41,654	37,838

The National Academy of Sciences (NAS) performed a sampling study in 1980 (NAS, 1982). Table 13 and Table 14 show the mean radionuclide concentrations in soil core and water samples within the dome taken by NAS (1982). The NAS estimated that the wastes emplaced within the dome contained 462 GBq (12.5 Ci) of actinides and 1,850 GBq (50 Ci) of ^{90}Sr and ^{137}Cs, and approximately an additional 14,060 GBq (380 Ci) of activation and fission products in the crater fallback material.

Table 13. Mean activity of radionuclides in soil core samples from dome and crater by NAS in 1980 (Noshkin and Robison, 1997).

Radionuclide	Dome (Bq/g)	Crater (Bq/g)
$^{239+240}$Pu	1.13	0.35
^{241}Am	0.15	0.23
^{137}Cs	0.34	0.34
^{90}Sr	0.71	0.81

Table 14. Radionuclide concentrations measured in water within dome in drill hole CD-1. NAS sample collected March 28, 1980 (retrieved from Noshkin and Robison, 1997).

Sample Depth	Sample type	$^{239+240}$Pu (Bq/m^3)	^{241}Am (Bq/m^3)	^{137}Cs (Bq/m^3)	^{90}Sr (Bq/m^3)
Depth 7.6-8.2 m					
	Soluble (<4.5 µm)	2.1	0.26	10,000	11,000
	Particle (>4.5 µm)	1,600	1,600	2,900	3,000
Depth 8.2 - 9.7 m					
	Soluble (<4.5 µm)	1.5	<0.1	8,400	13,000
	Particle (>4.5 µm)	4,200	3,300	8,000	8,500

Based on the available information, PNNL estimated activities of several radionuclides contained in Runit Dome at the time of disposal and in the future. These estimates are presented in Table 15 and were used in the assessment of a future potential Runit Dome failure and subsequent release of its inventory. The TRU activity of 545 GBq was distributed between $^{239+240}$Pu and ^{241}Am, based on their isotopic ratios reported for respective islands in AEC (1973). Additionally, 30 GBq was added to total Pu inventory to account the residual activity with the Cactus Crater as indicated by Davisson and Hamilton (2012). Activities of ^{137}Cs, ^{90}Sr, ^{155}Eu, and ^{125}Sb were also estimated using activity ratios in the respective island soils reported in AEC (1973). Since the inventory with the dome was calculated during 1972, decay corrections were applied to calculate the inventory for future year 2090.

Table 15. Estimated activities of several radionuclides in Runit Dome contents (GBq) at selected times

Nuclide	1972	2090
$^{239+240}$Pu	469.5	467.9
^{241}Am	105.5	88.7
^{137}Cs	388.3	32.5
^{90}Sr	1030.1	77.9
^{155}Eu	516.2	0.0
^{125}Sb	37.6	0.0

2.5 Postulated Runit Dome Collapse

A hypothetical Runit Dome collapse scenario in the future year 2090 was considered in the ocean transport modeling and dose assessment. Because investigating the structural integrity was not within scope, PNNL did not determine the failure mechanism for the Runit Dome. The hypothetical failure scenario conservatively assumes the dome to collapse completely and all materials to be released. Under this condition, the entire radioactive inventory (see Table 15), was assumed to be distributed along a plume from the dome toward the lagoon waters up to a 2 m water depth (-2 m elevation) as shown in Figure 9. The radionuclide concentrations in island soils and lagoon sediments were estimated by distributing the entire radioactive inventory to the total number of model nodes within this postulated plume. The radionuclide concentration at each node (Bq/m^3) was calculated as the node activity (Bq) divided by the representative model mesh volume (m^3) of soil/sediment at each node (node area (m^2) × sediment depth (m)) within this plume. A sediment thickness of 50 cm was assumed for the plume. The radionuclide concentrations at each node were provided as inputs to FVCOM-ICM as initial conditions for simulations that considered the Runit Dome failure. Figure 9 shows the estimated ^{239}Pu concentrations at the nodes.

An average soil concentration for each radionuclide for the entire Runit Island was calculated from the hypothetical dome collapse as shown in Table 16. The soil concentrations for nodes located on land were averaged and then distributed throughout Runit Island using the ratio of the spill plume area over the land (0.03 km^2) to the entire island area (0.35 km^2). This is the same as assuming people spend equivalent times in all areas.

Table 16. Average soil concentrations (Bq/g) in Runit Island from dome collapse

^{241}Am	^{207}Bi	^{137}Cs	^{152}Eu	^{239}Pu	^{90}Sr
0.274	0	0.1003	0	1.443	0.2402

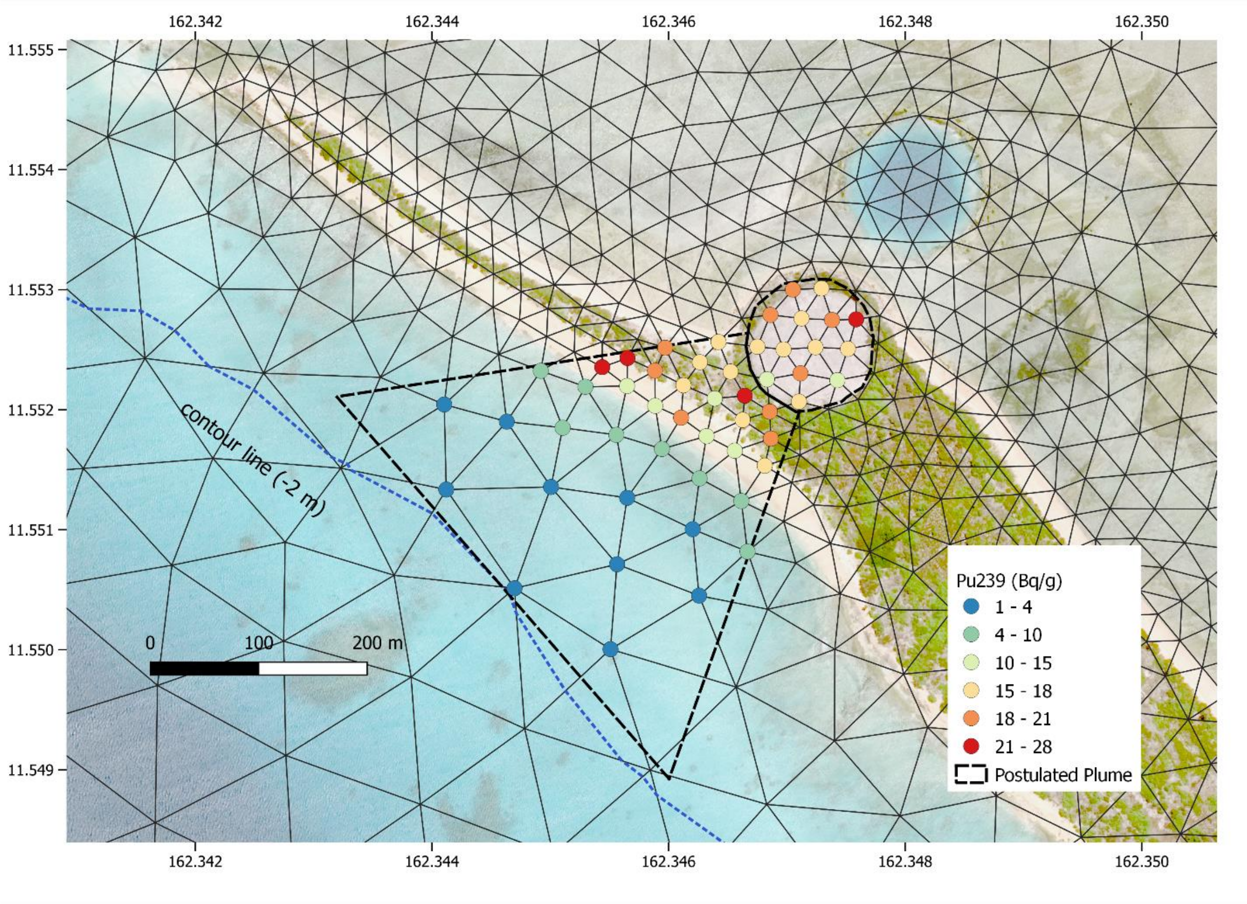

Figure 9. Postulated plume along with the ^{239}Pu concentrations (Bq/g) estimated from the hypothetical Runit Dome collapse.

3.0 Climate Scenarios

Specification of climate scenarios is an important part of this assessment. These scenarios provide the meteorological forcings during hypothetical but plausible severe storms. These forcings can generate severe hydrodynamic conditions within the lagoon and in the nearby ocean waters that can mobilize and transport radionuclides. The mobilized and transported sediment can result in radiation exposure to humans and biota.

This section briefly describes the climate of the Enewetak Atoll, selection of historically severe storms, likely sea level rise, and generation of climate scenarios. Technical details of the simulations of selected storms in the present and future climates are described in Appendix B.

3.1 Enewetak Atoll Climate

The RMI consists of 29 atolls and 5 isolated reef islands in the central Pacific Ocean. Enewetak Atoll (11º30ʹN, 162º15ʹE) is in the northwest corner of the RMI. It has a marine climate characterized by brisk, steady winds, moderate rainfall, and invariably high temperatures with typical partial cloudiness. The dry season occurs from December through March and the wet season from April through November. Temperature varies very little during the year, with the dry season being generally cooler than the wet season. During much of the year, the surface wind is from the northeast or east. A consistent shift in the wind associated with easterly waves is the most common type of disturbance during the wet season.

The average rainfall at is approximately 1,470 mm. Rainfall is not distributed uniformly throughout the year. Approximately 85% of the annual rainfall occurs during the wet season. Usually, there are many small rain showers even during the dry season. The wet season includes cumulus showers and a greater number of large, sustained rainfall events during disturbances and infrequent tropical storms or equatorial troughs.

While tropical cyclones (TCs) strike the RMI infrequently, disturbances in the weather are common and, on occasion, regular occurrences. TCs in the western north Pacific Ocean (WNP), known as typhoons, are extremely dangerous and destructive, particularly to exposed areas of low elevation such as Enewetak Atoll. Such storms develop from tropical disturbances. During the wet season, particularly July through September, westward-propagating, wave-like systems are common in the WNP. On average, these easterly waves have a horizontal scale of 3,500 to 4,000 km and travel to the west at an average speed of 7º longitude per day (i.e., a mean velocity of approximately 9 m s^{-1}). During the passage of such waves, there are systematic variations in the wind, cloud cover, and rainfall. Maximum cloudiness and precipitation occur just after the passage of the center of the tropical disturbances. The structure and detailed dynamic characteristics of such waves in the RMI area were studied by Reed and Recker (1971) using radiosonde and satellite data. The waves are most common in the wet season because the upper-level winds are more favorable for their growth. About one-third of such waves increase in intensity sufficiently to become TC (or hurricanes/typhoons), but this occurs most commonly well west of the RMI.

3.2 Historical Storms Selection

The International Best Track Archive for Climate Stewardship (IBTrACS) database provides global TC best track data in a centralized location. This database helps us understand TC distribution, frequency, and intensity worldwide (Knapp et al., 2010). This is the most complete global historical TC dataset available and includes data from 12 different agencies or historical databases. IBTrACS of TCs during 1960–2021 and occurring within a 700 mi radius with the Enewetak Atoll at the center were further analyzed (Figure 10). The choice of a 700 mi radius is mostly to identify the TCs influencing the RMI region. TCs span a large size range (100–1,000 mi) as measured by the radius of vanishing winds. Therefore, 700 mi was selected as the radius of influence.

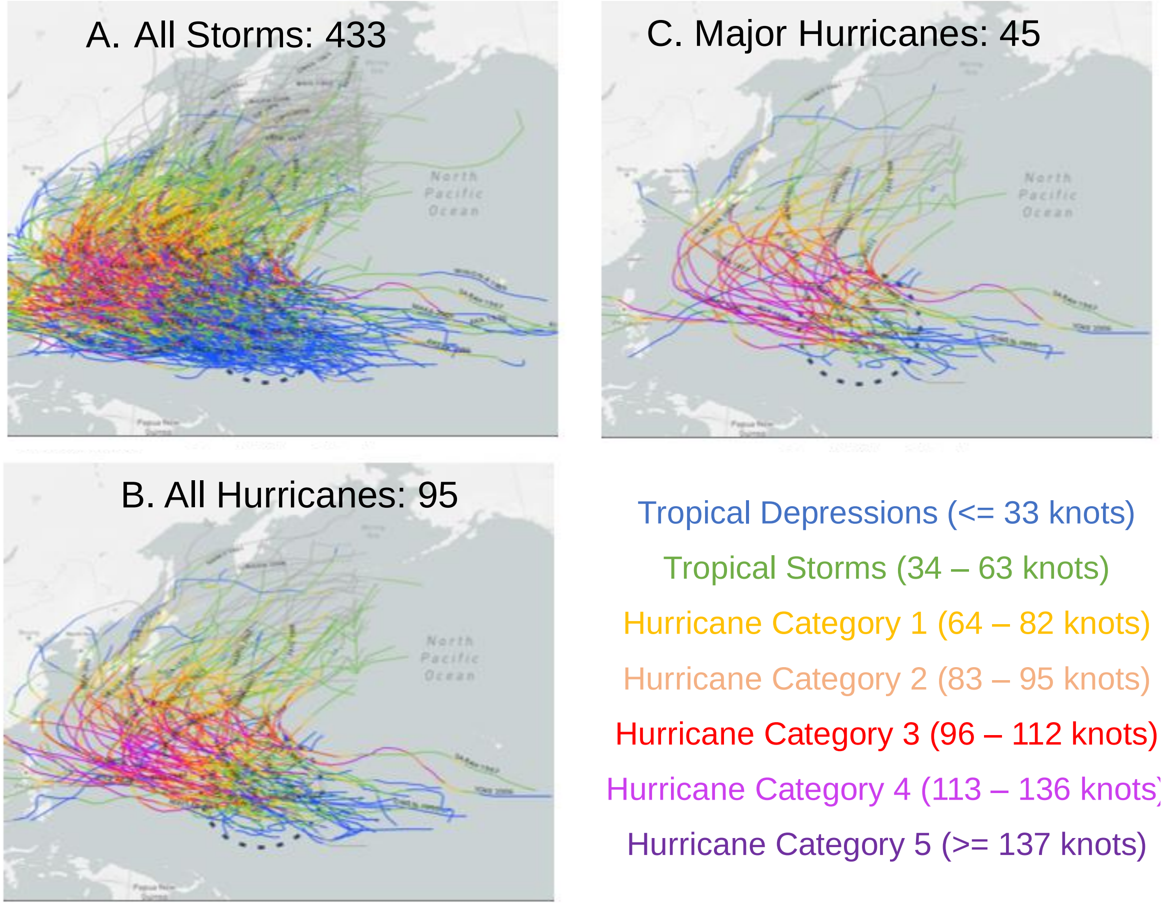
A. All Storms: 433

C. Major Hurricanes: 45

B. All Hurricanes: 95

Figure 10. Spatial distributions of hurricanes at Enewetak Atoll. A. all storms, B. all hurricanes, and C. major (Category 3–5) hurricanes near the RMI during 1960-2021. Storm counts are given in the headings of the panels. The color of the tracks indicates the strength category (Category 1-5). The black dashed circle in each panel shows a 700-mi radius circle with the atoll at the center.

PNNL identified 433 historical storms within 700 mi of the Enewetak Atoll. Stronger TCs occurred less frequently (i.e., of the 433 storms, 95 hurricanes, and 45 major hurricanes were found; see Figure 11). The storms (specifically stronger storms) are more frequent during the wetter months (July–November), but there are some stronger storms that also occur during December (Figure 11, Panel A). Significantly fewer storms occur January–June, possibly due to less active westward-propagating waves and unfavorable upper-level wind conditions.

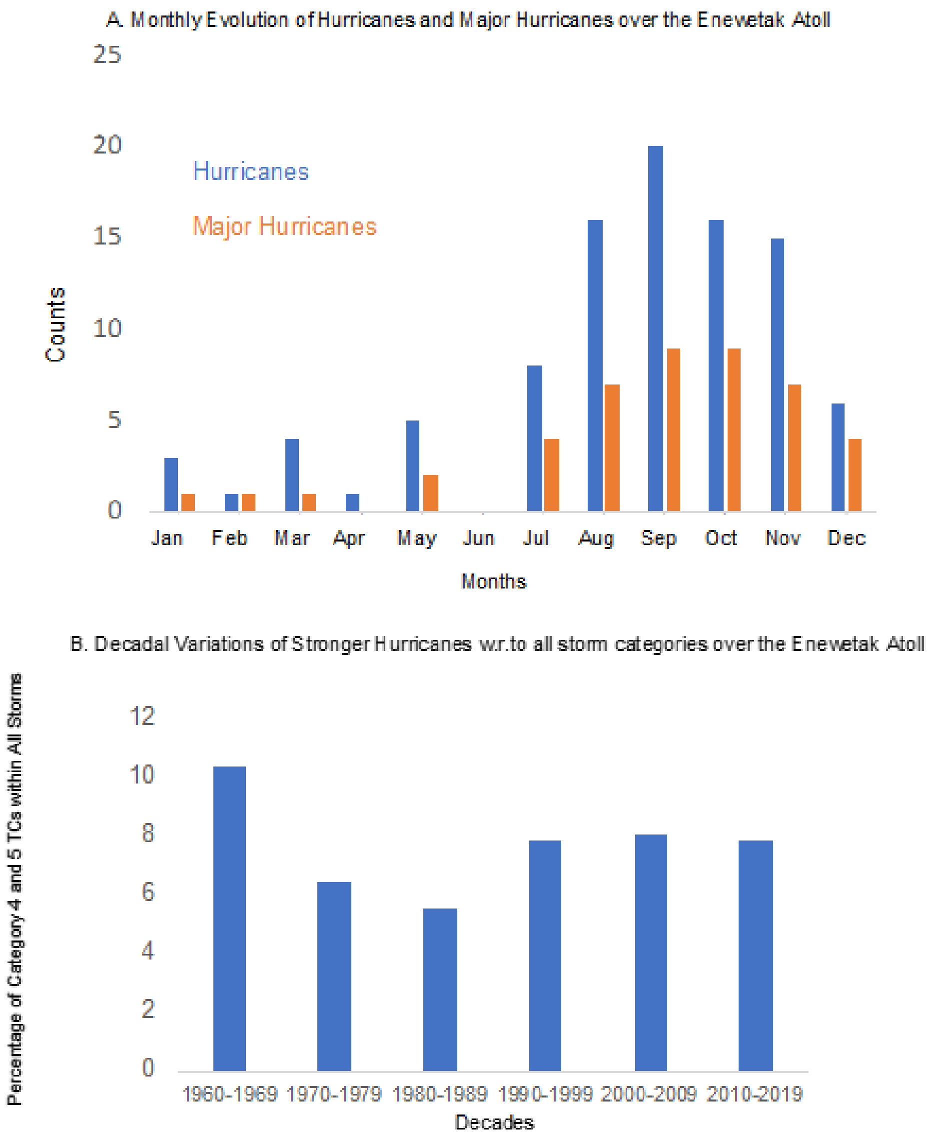

Figure 11. Panel A shows the monthly distribution of the number of hurricanes (blue) and major hurricanes (orange) within 700 mi of Enewetak Atoll during the period 1960–2021 in IBTrACS data. Panel B shows the decadal variations of category 4 and 5 hurricanes within all storms.

PNNL also found that within 700 mi of Enewetak Atoll, the fraction of stronger hurricanes (categories 4 and 5) with respect to all storms decreased from 1960 through the 1980s and then subsequently increased to remain relatively similar in the recent three decades (Figure 11, Panel B). This observation also is consistent with earlier studies in the WNP region (e.g., Knutson et al., 2019a; Lee et al., 2020).

Of the 45 major hurricanes, PNNL further shortlisted 14 based on their strength and proximity to the atoll. Two of these (i.e., Hurricane Gay in 1992 and Hurricane Melissa in 1994) were chosen for climate scenario assessment. Hurricane Gay was the strongest hurricane (i.e., remained a category 4 near Enewetak Atoll) that propagated closest to the atoll. Hurricane Melissa was relatively weak near the Enewetak Atoll, but it initially moved westward and subsequently curved northward, so Enewetak Atoll experienced high wind speeds twice during its passage.

PNNL also selected a more recent storm, Hurricane Nangka that occurred in 2015, for generating climate scenarios. The track and intensity of all three hurricanes are shown in Figure 12. These storms are referred to as Storm 1 (Hurricane Nangka), Storm 2 (Hurricane Melissa), and Storm 3 (Hurricane Gay) in this report.

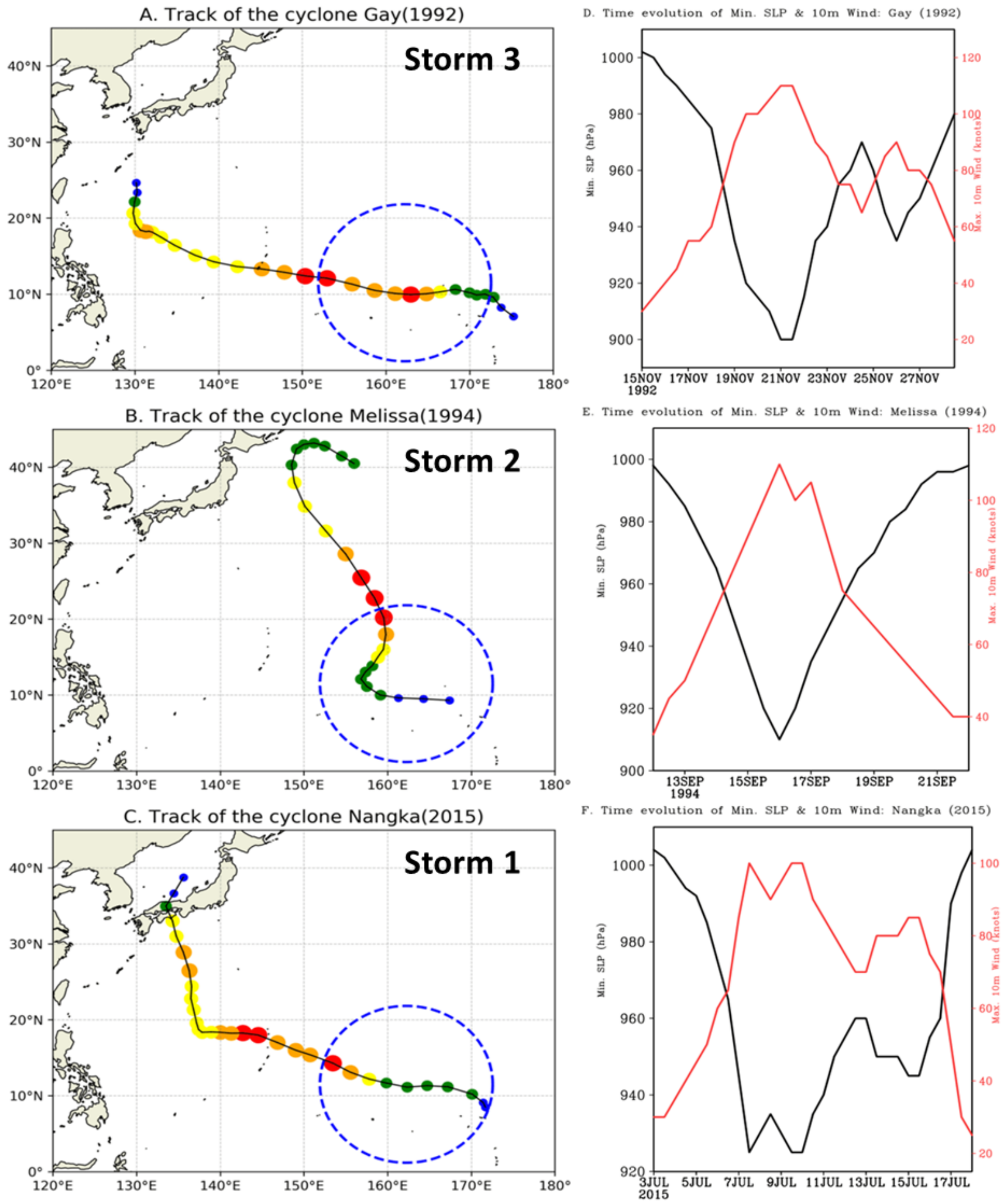

Figure 12. Panels A, B, and C show the historical tracks for Storm 3 (1992), Storm 2 (1994), and Storm 1 (2015). Panels D to F are similar to panels A to C but for the 10 m maximum sustained wind speed (knots; in red) and minimum sea-level pressure (in hPa). The blue dashed circles in panels A–C show a 700 mi radius circle with Enewetak Atoll at the center.

3.3 Sea-level Rise

Global mean sea level is rising and accelerating (Merrifield, 2011; Kopp et al., 2014). The sum of glacier and ice sheet contributions is now the dominant source of sea-level rise (Oppenheimer et al., 2019). Sea level in the western Pacific Ocean has been increasing at a rate two to three times the global average, resulting in almost 0.3 m of net rise since 1990. The high rates of sea-level rise in the western tropical Pacific Ocean have been tied to an intensification of the easterly trade winds that appear to be driven by variations in the latent heat content of the Earth's warming atmosphere, suggesting the possibility that these recent trends may continue under projected emission scenarios (e.g., Merrifield, 2011). Recent estimates (Kopp et al., 2014) that include a water-level rise due to thermal expansion and ice melting show possible sea levels in the tropics exceeding 2 m above the year 2000 levels by the end of the 21st century. Although several other processes drive variations in sea level (e.g., tides, mesoscale eddies, atmospheric circulation), there is no consensus on how these processes may be affected by global climate change (Collins et al., 2010; Knutson et al., 2010). Thus, while the rates of sea-level rise and the ultimate elevations of global sea levels by the year 2100 are debated, the existing data and predictive models all suggest that the eustatic sea level will be higher by the end of the century and that it will have a profound impact on low-lying coastal areas (Nicholls and Cazenave, 2010). Sea level is expected to continue to rise in the RMI region. A report from the Marshall Island National Weather service office and the Pacific Climate Change Science Program suggests, under a high emission scenario, sea level is projected to rise by 3–16 cm by 2030, 11–30 cm by 2055, and 22–62 cm by 2090 respectively (PCCSP, 2011). Sea-level rise combined with natural year-to-year changes will increase the impact of storm surges and coastal flooding. Based on the available information, PNNL used a 62-cm sea-level rise for 2090.

3.4 Climate Scenarios Generation

Realistically representing TC intensity is challenging for general circulation models (GCMs), partly because of their relatively coarser resolution of 100–200 km (Strachan et al., 2013). Studies have also shown that there can be substantial variations in the response of TCs to climate change over different oceanic basins (Oouchi et al., 2006; Walsh et al., 2016), but significant GCM model biases due to the low-horizontal resolution and uncertainty in representing physical processes limit the credibility of GCMs to projecting TC activities over different ocean basins. By embedding a high-resolution regional model in a GCM, dynamical downscaling provides a powerful way to reproduce the more realistic circulation structure, intensity, and frequency of TCs (Knutson et al., 2015; Gutowski et al. 2020).

In addition to direct downscaling of the historical and future climate simulated by GCMs, the impacts of a warmer climate on TCs also can be explored by using the pseudo-global-warming (PGW) method (Kimura and Kitoh, 2007; Hill and Lackmann, 2011; Ninomiya et al., 2017; Jisan et al., 2018; Chen et al., 2021). The PGW method is more effective and economical than traditional regional downscaling methods, and it supports the development of the storyline as a physically self-consistent unfolding of past events or of plausible future events or pathways (Shepherd et al., 2018). In the PGW method, differences in environmental conditions, such as sea surface temperature (SST), atmospheric temperature, humidity, and wind, are obtained as the mean monthly difference between the current and future climates simulated by the GCMs. These perturbations then are added to the initial and boundary conditions for selected historical events to determine how the events may unfold under future climate conditions. Before performing simulations with the PGW approach, the historical events are first simulated using initial and boundary conditions observed in the past for comparison with the events simulated under perturbed climate conditions.

PNNL selected the PGW approach for simulating future climate scenarios. The WRF-ARW model (Skamarock et al., 2019) was used to simulate the three selected storms both in the current climate and in the future climate. Details of model sensitivity tests and selected parameterization are provided in Appendix B.

All three chosen storms were simulated using WRF-ARW version 4.1.2 (Skamarock et al., 2019), with a single domain at horizontal grid spacing of ~9 km with 45 vertical levels between the surface and the model top at 10 hPa. The extent of the WRF-ARW model domain is shown in Figure 13. A high spatial resolution was used to better capture TC circulation, including the minimum sea level pressure and the structure of the eyewall (Gentry and Lackmann, 2010; Mukhopadhyay et al., 2011; Taraphdar et al., 2014).

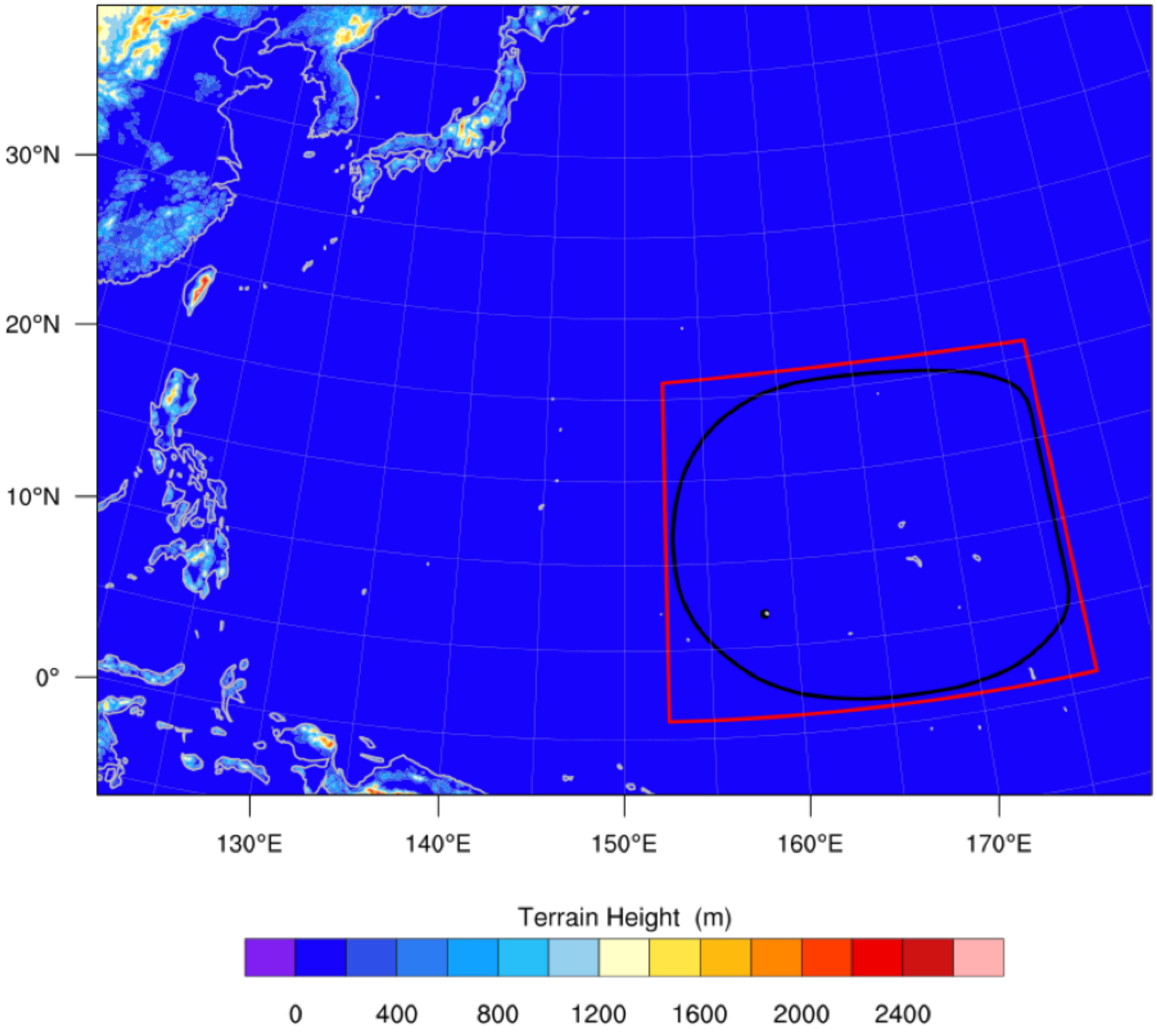

Figure 13. WRF-ARW model domain at 9 km horizontal resolution with color-shaded terrain elevation. The red box indicates the region of the central Pacific spanning152.5ºE – 176.5ºE longitude and 1ºN – 21ºN latitude. The area outlined in black indicates the ocean model domain.

PNNL performed a sensitivity analysis to evaluate WRF-ARW prediction sensitivity to planetary boundary layer and microphysics parameterizations (Appendix B). A comparison between observed and predicted storm tracks and intensities was used to determine the best performing model parameterization (Appendix B). Based on the sensitivity analysis, the final configuration of WRF-ARW was chosen for simulating the three storms.

Storms 1 and 3 were simulated reasonably well. Because of the unusual historical track of Storm 2, WRF-ARW was able to simulate the storm with reasonable accuracy only a few days after it started, at which time it was farther away from the Enewetak Atoll.

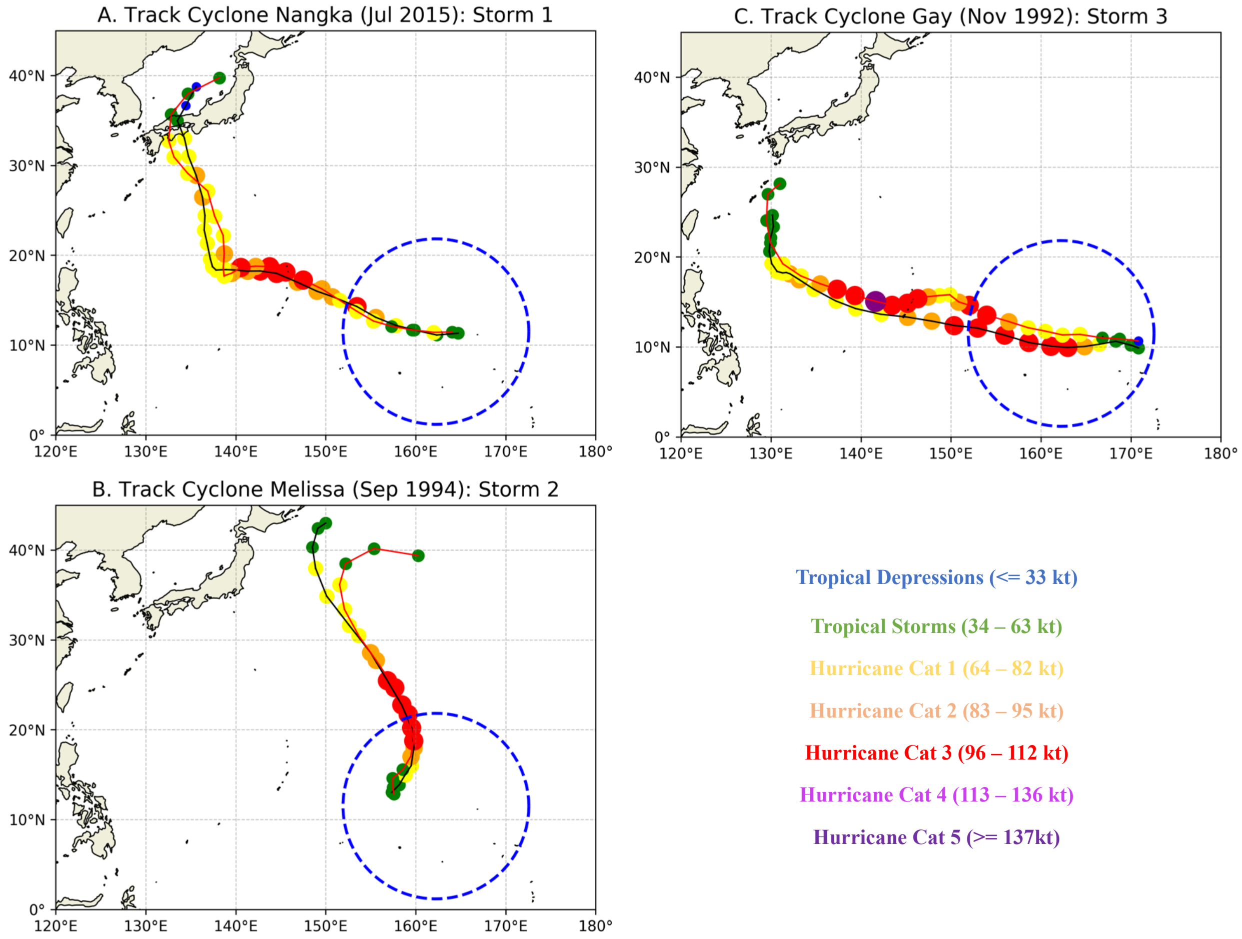

Figure 14. Observed and simulated tracks and intensities of the three selected storms. The observed storm tracks are shown by black lines and the predicted storm tracks are shown by the red lines. The colors of the dots along the tracks represent storm categories.

The selected storms were simulated under global warming scenarios by applying the PGW method. Climate perturbations were calculated as the difference of the monthly mean variable values (e.g., surface temperature, atmospheric temperature, and relative humidity) between present day (1990–2010) and future (2079–2099) conditions corresponding to the RCP8.5 scenario from the Coupled Model Intercomparison Project Phase 6 (CMIP6). The climate perturbations for each variable were then added to the hourly ERA5 initial and boundary conditions for each selected storm. The storms were simulated using the perturbed initial and boundary conditions of the same WRF-ARW settings as those used in simulating the storms in the present-day conditions. PNNL did not add changes in the wind field for the climate perturbations in the PGW simulations for the following reasons:

1. The wind field did not show significant changes over WNP in the warming future
2. Unlike SST, atmospheric temperature, and specific humidity for which all GCMs project increasing trends, different GCMs project different changes of circulation in WNP-ARW, so imposing the multimodel ensemble mean circulation changes may lead to an imbalanced atmospheric state that is inconsistent with the atmospheric temperature and specific humidity changes.

Figure 15 and Figure 16 show the predicted storm tracks and peak wind speeds of Storms 1 and 3, respectively, near the Enewetak Atoll. While the storm tracks were reasonably close, peak wind speeds in the future climate were significantly weaker for Storm 1 and somewhat weaker for Storm 3.

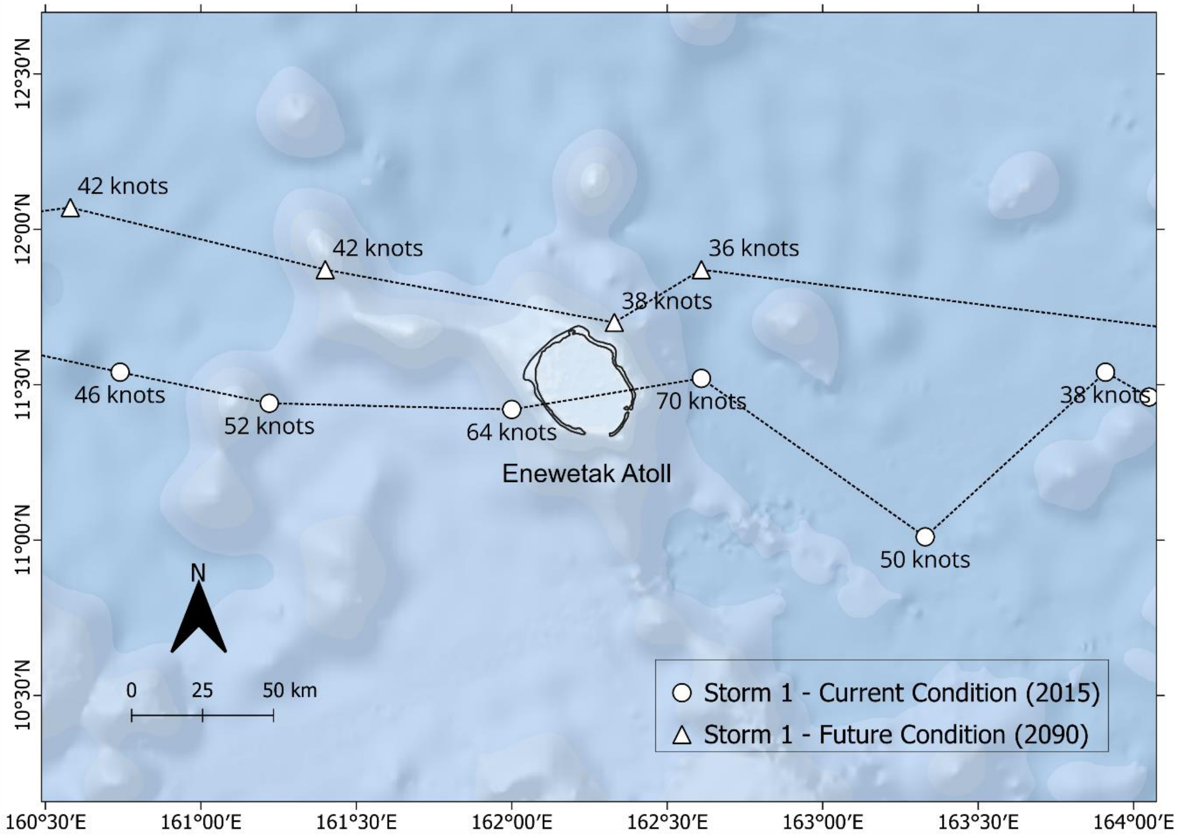

Figure 15. Comparison between predicted tracks and peak wind speeds of Storm 1 in current and future climates. Wind speeds values are shown in knots at 3-hour interval during the storm

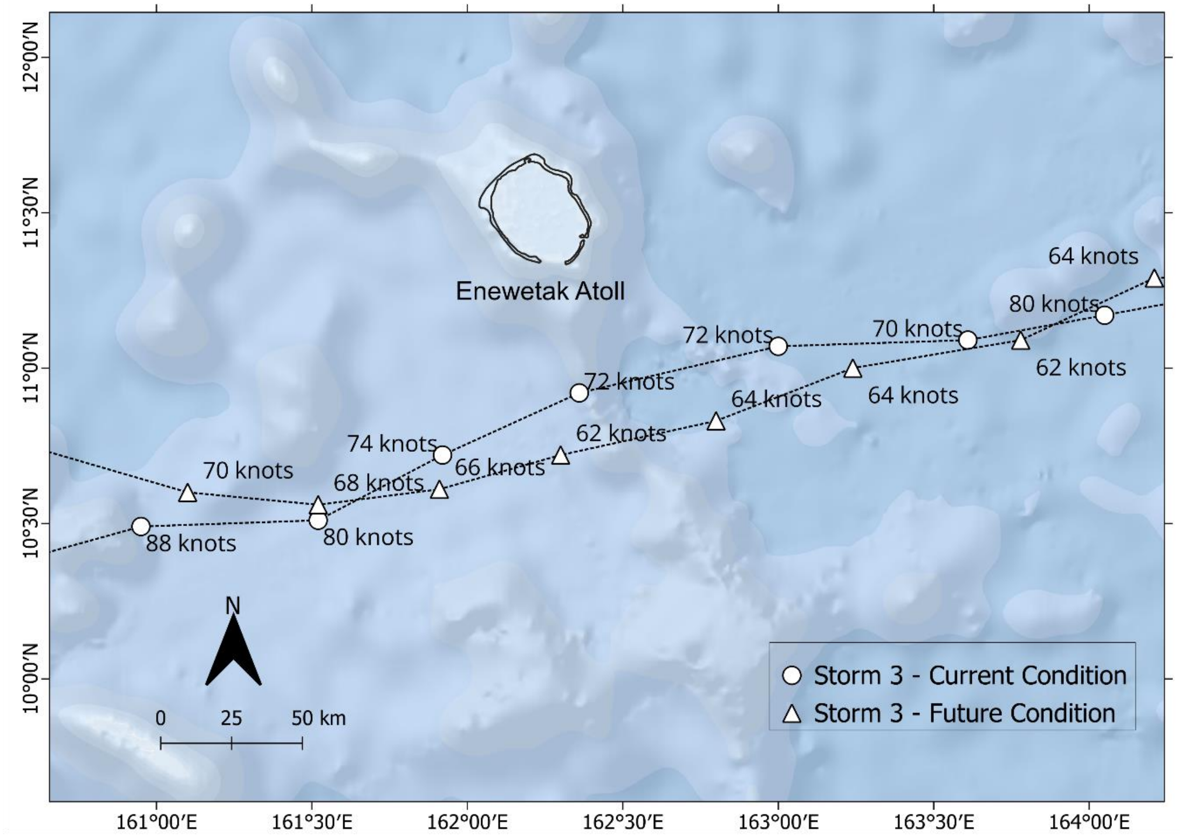

Figure 16. Comparison between predicted tracks and peak wind speeds of Storm 3 in current and future climates. Wind speeds values are shown in knots at 3-hour interval during the storm.

3.5 Uncertainties in Climate Scenarios

Characterizing future climate scenarios in the Pacific Ocean at a regional scale is somewhat limited because of several factors. Three major factors—limitations of observed tropical cyclone data, uncertainty associated with climate model physical processes, and uncertainty in the global model predictions—are discussed below.

The observed storm data have some limitations, including uncertainty in the storm track and intensity. The primary limitations are uncertainty in the estimated intensity for storms in the pre-satellite era (before 1979). Furthermore, changes in operational procedures and observing systems have led to significant heterogeneities in the TC best track record. Also, storms may have conflicting data from multiple sources although encouraging progress has been made in improving the consensus between different data sources in recent years. The IBTrACS includes data from 12 different agencies or databases and is one of today's most complete global data sources for historical TCs.

Numerical models inherently involve uncertainties (Box and Draper, 1987) that require significant efforts to quantify and reduce. Weather and climate models include representations of physical processes including radiation, cumulus convection, turbulence, and land surface that cannot be explicitly resolved at the grid scale. Parameterizations are needed to represent the effect of subgrid-scale processes in the atmosphere (Stensrud, 2007). The WRF-ARW model contains parametrizations of physical processes, including cloud microphysics, land-surface processes, longwave and shortwave radiation, planetary boundary layer (PBL), surface layer, and deep convection (i.e., cumulus convection). The physics options in WRF-ARW range from simple and numerically efficient schemes to sophisticated and more computationally costly parameterizations. The physics options also can range from well-tested schemes that are used in operational models to newly developed schemes (Carvalho et al., 2012).

Choosing the proper combination of physical schemes is extremely important because it strongly influences the simulation results (Weusthoff et al., 2011). However, the many possible combinations make a truly comprehensive test of all parameterization schemes infeasible (Stensrud, 2007). Therefore, PNNL selected parameterizations based on expert judgment and evaluation of a relatively small set of combinations in a sensitivity study (see Appendix B for details). The time limitations of this project did not allow the use of ensemble simulations that could have provided more insights into model sensitivities.

To address uncertainty in global models themselves, PNNL employed a multimodel ensemble approach. Eleven global models were investigated to determine the model that provided the best performing climate perturbations for the future compared to the current climate (see Appendix B for details).

PNNL selected a few historically severe storms for this assessment. While it is possible that other storms could result in similar or larger effects at the Enewetak Atoll, both in the present and in the future climate, selecting historically severe storms provides reasonable assurance that the climate scenarios presented in this report are among the most severe. For this reason, the climate scenarios should be considered a few representative scenarios among other plausible severe scenarios.

4.0 Ocean Modeling

To characterize the potential effects on human health and environmental impacts, PNNL employed ocean modeling to investigate the mobilization and transport of radionuclides present at Enewetak Atoll. The ocean models were forced with hypothetical storm scenarios, both in a present-day environment (approximately 2015), and in projected future environment (approximately 2090). The hydrodynamics of the lagoon and the ocean were modeled using a three-dimensional ocean circulation model over a relatively large domain encompassing the RMI. Subsequently, the mobilization and transport of radionuclides were simulated using a biogeochemical model forced by the simulated hydrodynamics. Radionuclides present in the lagoon waters, lagoon sediment, island soils, and Runit Dome were considered.

The ocean modeling and results are briefly summarized in this section. Technical details of the model development, simulations, and validation when possible are described in Appendix C.

4.1 Ocean and Lagoon Hydrodynamics Modeling

Ocean hydrodynamics modeling was an integral part of this assessment. PNNL used FVCOM (Chen et al., 2003, 2006) to produce a detailed, three-dimensional characterization of the ocean hydrodynamic conditions around the Enewetak Atoll. The model was set up for a full calendar year. The model was forced by the combination of global meteorological and oceanographic reanalysis model outputs. During the one-year simulation, the wind and atmospheric pressure forcing fields generated by the WRF-ARW model (see Section 2.0 and Appendix B) for three representative historical storms was embedded into the global meteorological forcing. FVCOM model outputs were provided for radionuclide mobilization and transport modeling.

4.1.1 Model Grid Generation

To sufficiently cover the area of potential impact from release and transport of radionuclides from the lagoon of the Enewetak Atoll and the Runit Dome, PNNL used a conservatively sized model domain. The model domain is centered on the Runit Dome with a 1,000 km radius and was further extended to the east to cover the entire RMI EEZ (Figure 17).

The model grid bathymetry was created using a combination of available public data sources, including the 15-arc minute, global topo-bathymetry dataset downloaded from General Bathymetric Chart of the Oceans (GEBCO), and the Advanced Spaceborne Thermal Emission and Reflection Radiometer Global Digital Terrain Model (ASTGTM) Version 3. The GEBCO bathymetry data were used for the entire model domain while the 1-arc second ASTGTM data were used to create a more accurate representation of the surface elevation of the islands of the Enewetak Atoll. After several iterations of grid refinement and model testing, PNNL finalized the model grid. The final model grid has a spatial resolution of <30 m (i.e., grid size in terms of the triangular side length) at the Runit Dome to a maximum of >10 km along the open boundaries (see Appendix C for details).

To resolve the vertical structure of large-scale ocean circulation in the model domain, PNNL used a vertical discretization composed of 30 terrain-following sigma layers. The sigma layer thickness distribution was specified to resolve the external boundary interactions with atmosphere and ocean bed in greater detail by using smaller layer thickness toward surface and bottom boundaries.

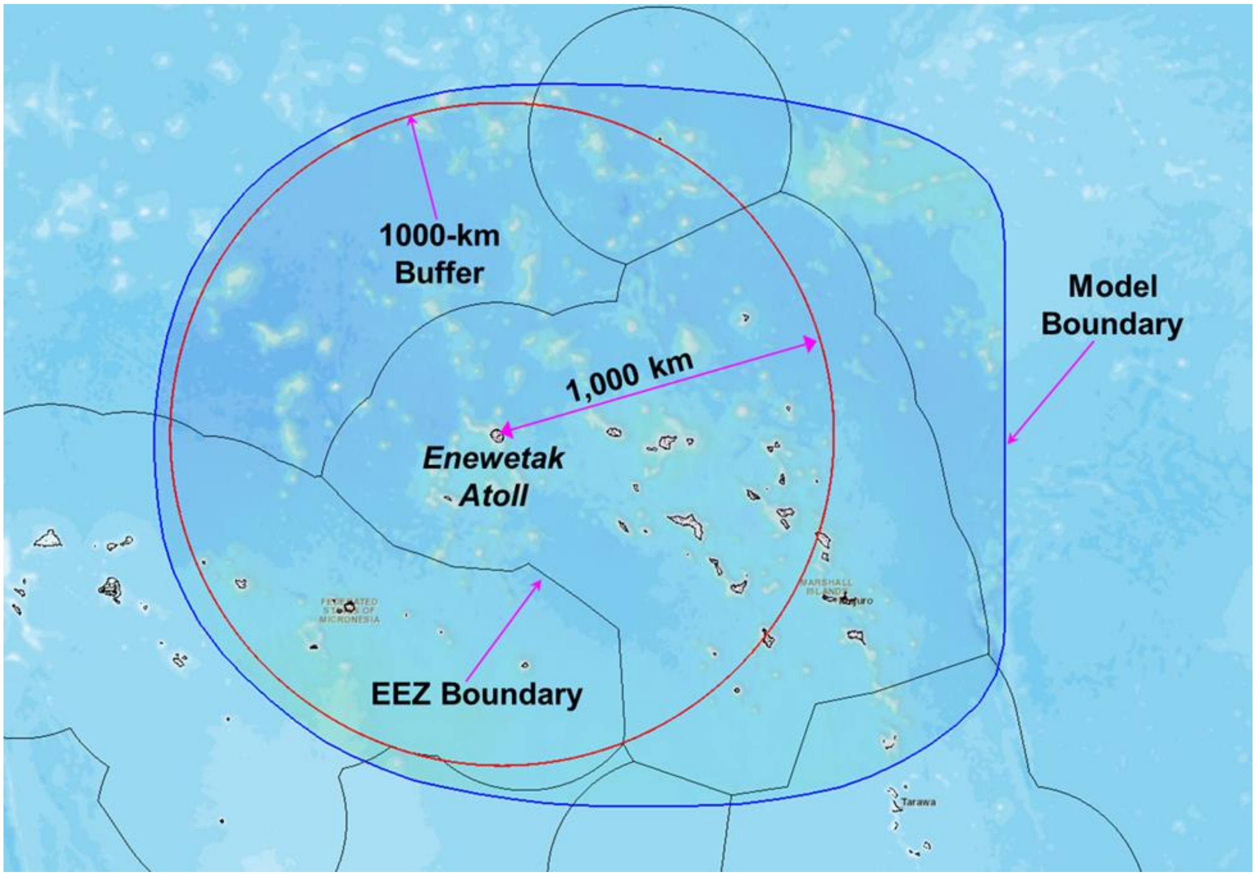

Figure 17. The ocean model domain (blue polygon) selected by PNNL. The RMI EEZ is also shown.

4.1.2 Model Setup for Current Conditions

To simulate ocean hydrodynamics, PNNL specified boundary conditions using water level, salinity, and temperature data from 3-hourly, 1/12-degree HYCOM global reanalysis (Metzger et al., 2017). The tidal forcing was obtained from Oregon State University's TPXO8-atlas tidal database (Egbert and Svetlana, 2002). The meteorological forcing was based on the global atmospheric reanalysis model product from the European Centre for Medium-Range Weather Forecasts ERA5.

To simulate selected hurricanes in the current climate, the ERA5 wind speeds and air pressures were replace by the high-resolution surface winds and air pressures predicted by the WRF-ARW current climate simulations. A full year of FVCOM simulation was performed by embedding the three selected storms, as modeled by WRF-ARW, at their respective times of occurrence.

4.1.3 Model Calibration and Validation

PNNL iteratively calibrated model parameters including bottom roughness and open boundary sponge layer configuration. The model predictions were compared to all available water level observations downloaded from Permanent Service for Mean Sea Level (PSMSL) website. Four of the six available PSMSL tidal stations were inside the FVCOM model domain and data at these stations were used for calibration. One of the stations, Kwajalein, did not have data for 2015. Therefore, PNNL configured the model for a separate period, September 2019, for comparing with available observed data. More details of the model calibration are provided in Appendix C. The model predictions matched tidal fluctuations at the four PSMSL stations well.

The calibrated model was used to simulate hydrodynamic conditions during Storm 1. Tidal elevation at the four PSMSL stations were reasonably well reproduced by the model (see Appendix C). The model was also able to reasonably well reproduce XTide predicted tidal fluctuations at Enewetak, after accounting for surge caused by Storm 1. PNNL also compared model-predicted vertical temperature profiles with available data at two National Data Buoy Center (NDBC) buoys. The temperature profiles were qualitatively compared and reproduced the general patterns of vertical temperature gradients (see Appendix C).

4.1.4 Current Climate Simulations

The WRF-ARW predicted meteorological conditions were embedded into the ERA5 meteorological forcings for the three selected storms during the times of their occurrence. FVCOM simulations were performed for December 2, 2014, to February 15, 2016. The month of December 2014 was used as a model spin-up period. The model was initialized with the HYCOM global dataset. Model predictions were archived at hourly timesteps. Appendix C provides some of the results.

4.1.5 Future Condition Simulations

For simulating future ocean conditions, the PNNL team configured FVCOM ocean model consistent with the CMIP6 future climate scenario by incorporating the perturbations in both meteorological and ocean conditions (e.g., sea level rise and warming temperature) into model forcing input files. The WRF-ARW predicted meteorological conditions for the three selected storms in the future climate were embedded into the ERA5 meteorological forcings. The FVCOM simulation was performed for a similar duration corresponding to the 2090 future period. Appendix C provides some of the results for the future simulations.

4.2 Radionuclide Mobilization and Transport

During a potential extreme weather event in the current or a future climate scenario, the marine waters in the lagoon may be disturbed by the hydrodynamic forces induced by elevated tides and currents. Under such conditions, the existing dynamic steady state of radionuclides in dissolved and particulate (sediment bound) phases may be disturbed. Under the influence of currents, radionuclides may be mobilized (e.g., by erosion and resuspension of lagoon sediment) and transported through currents. Such scenarios can be simulated with a pollutant mobilization and transport model with built-in sediment interactions and processes. PNNL developed a mobilization and transport model for legacy radionuclides. This model was developed using the externally coupled FVCOM-ICM. FVCOM-ICM is a FVCOM framework-based biogeochemical model with mature capabilities of simulating advection and diffusion of pollutant/contaminants (Khangaonkar et al., 2017, 2018, 2019). The radionuclide kinetics implemented in FVCOM-ICM include radioactive decay and partitioning onto suspended particulate matter (Figure 18). FVCOM-ICM also has the capability to simulate basic sediment-related processes (e.g., settling of suspended sediment, erosion of bottom sediment, and dynamic changes in sediment layer). PNNL improved the sediment-related processes to better simulate conditions expected in the Enewetak lagoon. More details of the FVCOM-ICM process parameterization are provided in Appendix D. The three-dimensional ocean current field, temperature, salinity, and eddy diffusivities from FVCOM hydrodynamic simulations were externally coupled with FVCOM-ICM to conduct the model runs for simulating mobilization and transport of radionuclides for each climate scenario.

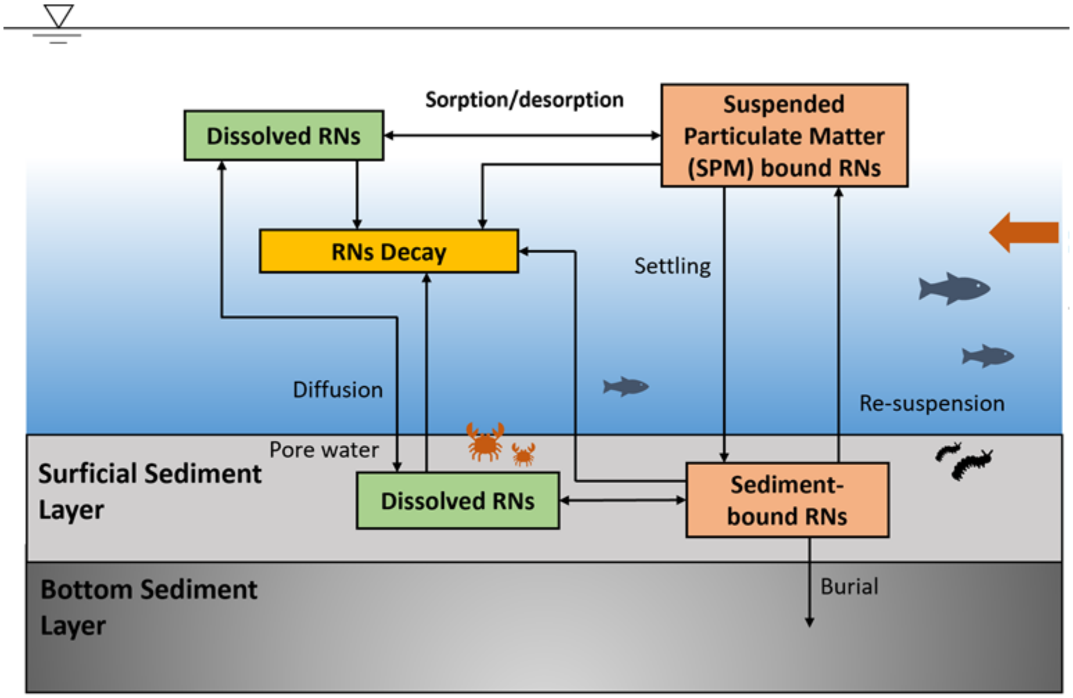

Figure 18. Primary radionuclide kinetics implemented in FVCOM-ICM.

FVCOM-ICM was set up to simulate nine storm scenarios—three storms in the current climate, three storms in the future climate, and three storms in the future climate combined with a postulated, hypothetical failure of the Runit Dome and subsequent release of radioactive material. The ocean hydrodynamics simulated by FVCOM were used as input. The lagoon sediment characteristics were estimated based on the sediment survey by United States Geological Survey (Wardlaw et al., 1991), sediment porosity following Emery (1954), critical bed shear stress by estimation approaches described by van Rijn (2020), and sediment settling velocity following analytical methods of Rubey (1933) and Richardson and Zaki (1954). The model scenario for Runit Dome failure was simulated by setting up the elevated initial radionuclide concentrations in the bottom sediments limited to the area of extent of the radionuclide material released during the assumed instantaneous collapse of the dome (Section 2.5). The loading of radionuclide flux from the pore-water diffusion of ground water into the lagoon waters was not considered in this study, because of unavailability of a robust concentration data and the parameter values required for a dedicated subsurface modeling effort.

For radionuclide kinetics, PNNL assumed that the suspended particulate matter included both organic and inorganic matter in the water. The partitioning of radionuclides from water onto the particulates was represented using the Langmuir isotherm-based partitioning model. Radioactive decay of radionuclides was modeled using a first-order exponential decay function based on the individual half-lives of the radionuclides. More details of the model setup are provided in Appendix D.

The nine storm simulations were performed individually for 30 days and included the WRF-ARW simulated storm. The model predictions (i.e., radionuclide concentrations at all model grid nodes) were output hourly. Figure 19 and Figure 20 are examples of FVCOM-ICM output; these plots show the distributions of maximum concentrations of ^{137}Cs and ^{239}Pu in the surface and bottom water layers, respectively. The plots also show the maximum concentrations that these radionuclides reached at any given location during Storm 1 simulation, irrespective of the time of

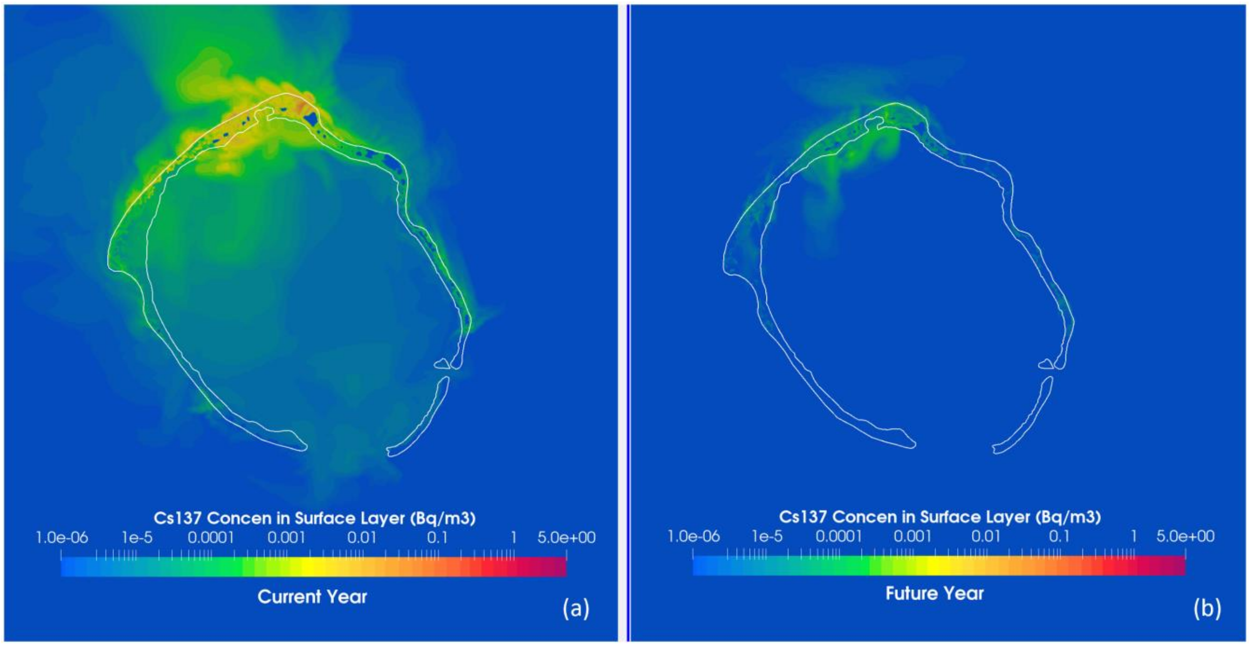

Figure 19. The maximum ^{137}Cs concentration distribution in the surface water layer for Storm 1 simulation in (a) the current climate and (b) the future climate (the color maps and contours are in log scale).

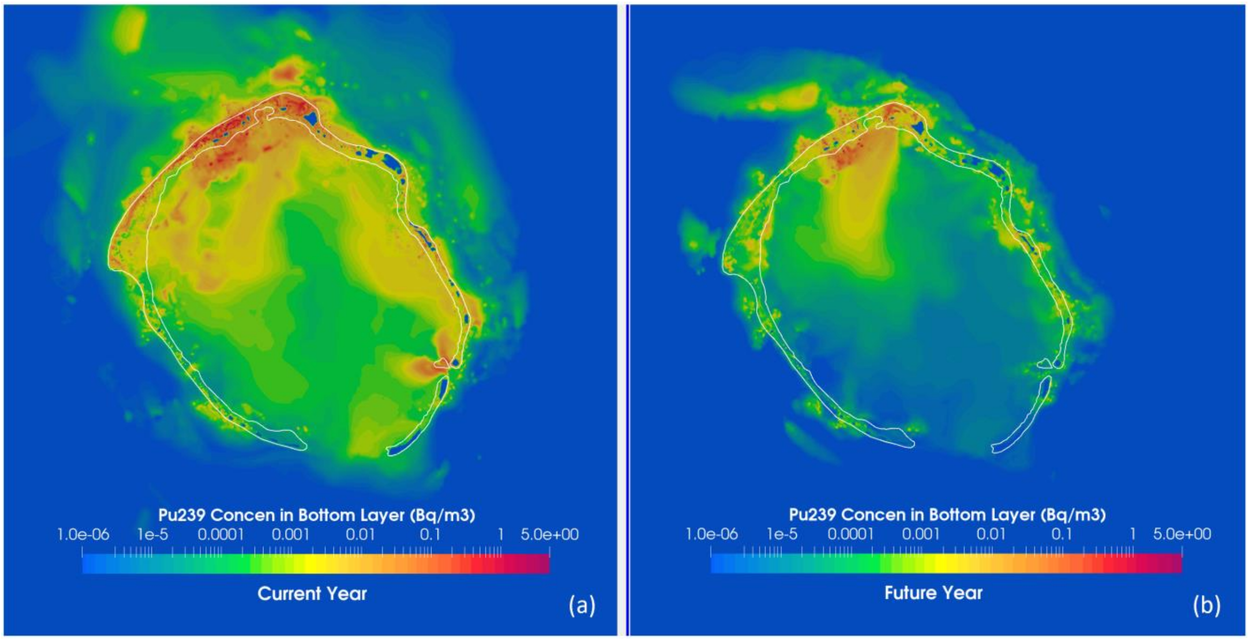

Figure 20. The maximum ^{239}Pu concentration distribution in the bottom water layer for Storm 1 simulation in (a) the current climate and (b) the future climate (the color maps and contours in log scale).

Occurrence. For estimating radiation dose, concentrations at specific times are used and integrated for the duration of the simulation. The lower maximum ^{137}Cs concentrations in the future occur partially because ^{137}Cs is relatively short-lived. Other differences are attributable to the changes in the hydrodynamics of Storm 1 in the current and future climates.

Figure 21 show the plots of maximum ^{239}Pu concentrations for future Storm 3 simulations with and without considering the postulated, hypothetical failure of the Runit Dome. With this hypothetical failure, more radioactive material would be available for mobilization and transport, resulting in greater concentrations both within and outside the lagoon.

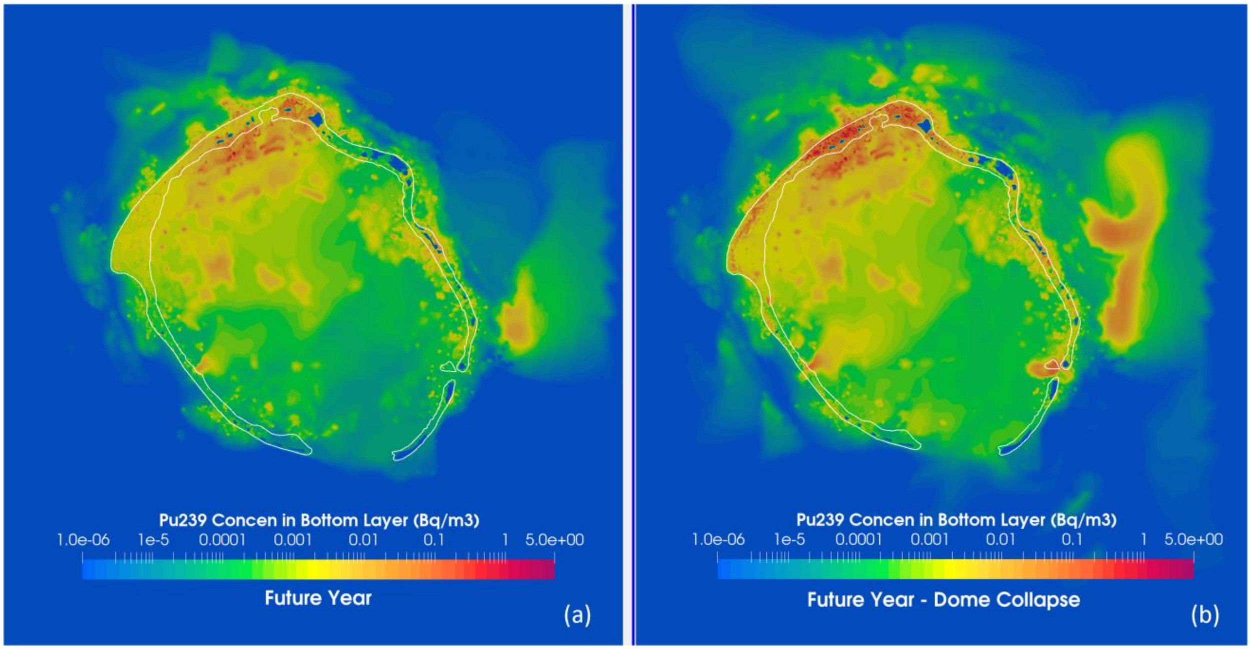

Figure 21. The maximum ^{239}Pu concentration distribution in the bottom water layer for Storm 3 simulation in (a) the future climate and (b) the future climate with dome collapse (the color maps and contours in log scale).

4.3 Ocean Model Data Processing for Dose Estimation

During storms, the eroded sediments-bound radionuclides were transported throughout the lagoon. Because of spatial variability in the circulation and transportation pattern, each island was affected differently. Island inhabitants and biota can face elevated exposure if radionuclide concentrations increase in waters adjacent to those islands. Shoreline residents, fishermen, and fish and other marine biota generally do not spend all their time in one place so they are exposed to varying levels of radionuclide concentrations during the year. Because of the transient nature and complex spatial distribution of radionuclide concentrations, a suitable temporal and spatial averaging method must be used to estimate appropriate radionuclide concentrations for each island. The islands are scattered around the lagoon (Figure 2) and each island's exposure concentration must be estimated using an appropriate nearby lagoon area.

For each of the 31 islands, a set of adjacent model mesh nodes were identified. These sets of receptor points were manually selected from the model mesh nodes on the lagoon side of the island starting from the shoreline to a depth of 2 m (Figure 22). FVCOM-ICM predicted hourly concentrations of the radionuclides for each model node. A volume-weighted spatial average was first computed at each hour using all nodes of a receptor points set using the representative water volumes at the nodes. Three spatially averaged radionuclide concentrations were computed—for the bottom water layer near the lagoon sediment bed, the surface water layer, and the entire water depth. Average radionuclide concentrations in sediment were computed using the radionuclide concentrations in the sediment bed and the bottom sediment thickness at each node. This process was repeated for all simulated storm scenarios. A sample of spatially averaged time series of ^{239}Pu is shown in Figure 23. For each storm scenario, the spatially averaged radionuclide concentrations for each island were then summed for the entire simulation period to provide time-integrated concentrations for dose estimation.

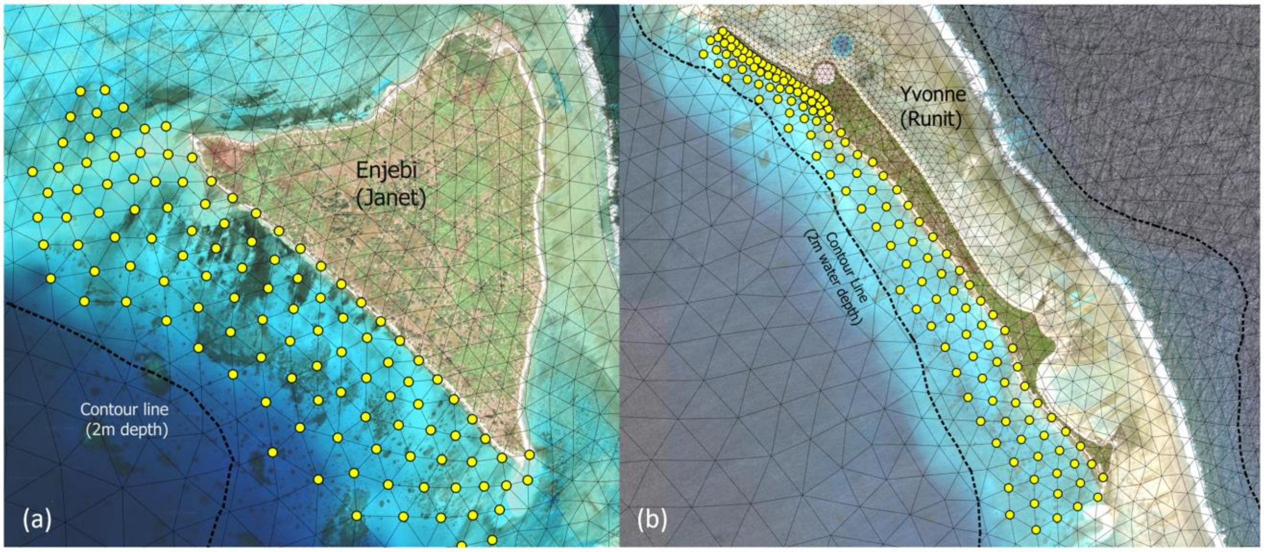

Figure 22. Examples of receptor point sets: (a) Enjebi (Janet) and (b) Runit (Yvonne).

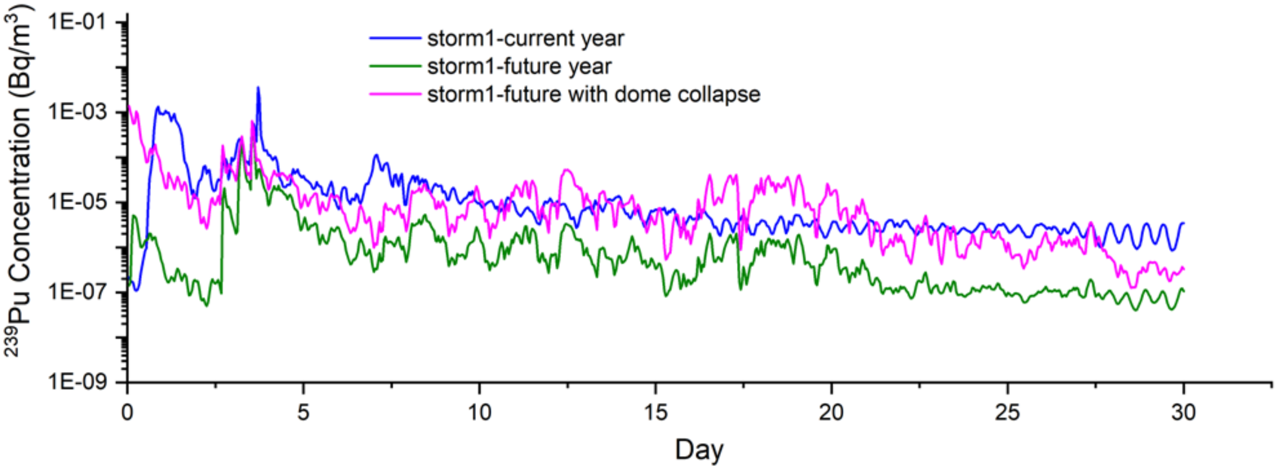

Figure 23. Time series of spatially averaged ^{239}Pu concentrations in the surface water layer near Runit Island for Storm 1.

5.0 Dose Estimation

A suite of potential exposure conditions was postulated to which the exposure scenario described in Appendix E was applied. The potential conditions correspond to “current conditions,” represented by radionuclide concentrations and weather conditions for the recent year 2015, and “future conditions” represented by radionuclide concentrations decayed to the year 2090 and weather conditions postulated in Section 3.0. For each time period, a baseline of normal weather (without storms) and three typhoon-type storms was evaluated. In addition, for the future 2090 case, the three storms were included a breach of the waste disposal site on Runit Island (the Runit Dome).

The individual time period baselines, storm perturbations, and, for the 2090 period, incremental perturbation of the dome collapse are described individually and then compared below.

5.1 Current Condition Baseline

For the current conditions, the Baseline scenario provided estimates of annual radiation dose to representative adults living on each island for a full year. The cumulative annual radiation effective dose estimated for each exposure pathway is shown in Table 17. Islands are listed approximately in order counterclockwise around the lagoon starting with Enewetak Island. Both the traditional Marshallese name and the names assigned by the U.S. military during nuclear weapons testing are presented. Doses are given in the S.I. units of millisievert/year (mSv/yr). For convenience, the total dose is also presented in the standard units used in the United States, millirem/year (mrem/yr).

For current conditions, the annual exposures to radiation were low, below current U.S. standards, for the currently inhabited southern islands including Enewetak (Fred) and Medren (Elmer). Doses were somewhat elevated starting at Runit Island northward and westward to Enjebi Island (Janet), although the dose for the small island Elle (Nancy) was higher than the others. The islands in the northwest quadrant, particularly Bokoluo (Alice) and Bokombako (Belle) remain relatively contaminated. The islands in the southwestern quadrant have low contamination.

Comparing doses estimated for current conditions, the southern islands were all well below the U.S. standards for permanent occupancy. Most of the northern islands were not hazardous for occasional visits but should not be used for full-time residence. The current condition dose calculated for Runit Island is not large. However, the model used did not account for the possibility for uptake of small particles of plutonium which are known to be present on Runit. These fine particles of plutonium represent an uncertain dose because they are rare and would be difficult to ingest or inhale, but the consequences of inhaling a single particle could be large. Thus, this island should remain off limits to atoll residents.

Table 17. Radiation Dose by Island for Selected Exposure Pathways for 2015 Current Conditions Baseline

		Terrestrial Pathways			Aquatic Pathways					Total Annual Dose	
Island name	US assigned name	External (mSv/yr)	Res.Inh. (mSv/yr)	Local Foods (mSv/yr)	Seafood (mSv/yr)	Swimming Boating (mSv/yr)	Boating (mSv/yr)	SeaSpray (mSv/yr)	Beach External (mSv/yr)	(mSv/yr)	(mrem/yr)
Enewetak	Fred	1.8E-03	8.6E-05	1.8E-02	4.1E-02	1.2E-09	1.2E-09	7.0E-10	5.1E-04	6.1E-02	6.1
Medren	Elmer	2.3E-03	1.3E-04	2.4E-02	1.3E-02	4.2E-10	4.2E-10	1.8E-10	4.1E-04	4.0E-02	4.0
Japtan	David	2.5E-03	6.1E-05	3.9E-02	1.3E-02	4.2E-10	4.2E-10	1.8E-10	4.1E-04	5.5E-02	5.5
Ananij	Bruce	2.4E-03	6.0E-05	3.6E-02	1.3E-02	4.2E-10	4.2E-10	1.8E-10	4.0E-04	5.2E-02	5.2
Inedral	Uriah	1.3E-03	7.3E-05	1.2E-02	1.3E-02	4.2E-10	4.2E-10	1.8E-10	5.3E-04	2.7E-02	2.7
Van	Van	1.6E-03	6.8E-05	2.2E-02	1.3E-02	4.2E-10	4.2E-10	1.8E-10	5.4E-04	3.7E-02	3.7
Runit	Yvonne	2.6E-02	5.8E-03	4.8E-01	6.1E-02	1.2E-09	1.2E-09	8.3E-10	1.3E-03	5.8E-01	57.6
Alembel	Vera	2.6E-02	1.3E-03	3.5E-01	6.1E-02	1.2E-09	1.2E-09	8.3E-10	5.0E-04	4.4E-01	44.1
Billae	Wilma	4.2E-02	2.0E-03	4.0E-01	6.1E-02	1.2E-09	1.2E-09	8.3E-10	4.8E-04	5.1E-01	50.6
Aomon	Sally	4.5E-02	2.3E-03	5.9E-01	6.1E-02	1.2E-09	1.2E-09	8.3E-10	5.7E-04	7.0E-01	70.2
Bijiri	Tilda	4.2E-02	1.8E-03	4.5E-01	6.1E-02	1.2E-09	1.2E-09	8.3E-10	5.4E-04	5.6E-01	55.5
Lojwa	Ursula	3.1E-02	7.7E-04	3.5E-01	6.1E-02	1.2E-09	1.2E-09	8.3E-10	4.5E-04	4.4E-01	44.2
Aej	Olive	6.9E-02	3.0E-03	8.3E-01	6.1E-02	1.2E-09	1.2E-09	8.3E-10	2.1E-03	9.6E-01	96.1
Elle	Nancy	5.9E-01	2.4E-02	5.1E+00	6.1E-02	1.2E-09	1.2E-09	8.3E-10	2.9E-03	5.8E+00	581.1
Lujor	Pearl	7.6E-02	1.1E-02	9.0E-01	6.1E-02	1.2E-09	1.2E-09	8.3E-10	1.2E-03	1.1E+00	105.2
Bokenelab	Mary	8.1E-02	3.6E-03	8.9E-01	6.1E-02	1.2E-09	1.2E-09	8.3E-10	3.8E-03	1.0E+00	104.4
Kidrinnenen	Lucy	8.9E-02	3.7E-03	1.0E+00	6.1E-02	1.2E-09	1.2E-09	8.3E-10	9.2E-03	1.2E+00	116.5
Mijikadrek	Kate	4.9E-02	1.6E-03	5.8E-01	6.1E-02	1.2E-09	1.2E-09	8.3E-10	1.3E-02	7.1E-01	70.9
Enjebi	Janet	1.9E-01	4.9E-03	2.2E+00	6.1E-02	1.2E-09	1.2E-09	8.3E-10	1.8E-02	2.5E+00	248.1
Boken–N	Irene	2.2E-01	1.1E-02	1.8E+00	4.9E-02	1.3E-09	1.3E-09	6.5E-10	2.1E-02	2.1E+00	205.5
Bokinwotme	Edna	1.5E-01	9.0E-03	1.2E+00	4.9E-02	1.3E-09	1.3E-09	6.5E-10	8.7E-03	1.4E+00	143.8
Louj	Daisy	2.4E-01	9.3E-03	2.0E+00	4.9E-02	1.3E-09	1.3E-09	6.5E-10	7.9E-03	2.3E+00	226.9
Bokoluo	Alice	9.5E-01	2.1E-02	1.1E+01	4.9E-02	1.3E-09	1.3E-09	6.5E-10	5.7E-03	1.2E+01	1167.6
Bokombako	Belle	1.4E+00	4.5E-02	1.2E+01	4.9E-02	1.3E-09	1.3E-09	6.5E-10	7.0E-03	1.4E+01	1385.5
Kirunu	Clara	1.1E-01	3.9E-03	1.9E+00	4.9E-02	1.3E-09	1.3E-09	6.5E-10	6.6E-03	2.0E+00	203.7
Biken	Leroy	9.2E-02	8.1E-04	7.5E-01	4.2E-02	1.3E-09	1.3E-09	6.1E-10	5.0E-04	8.9E-01	88.6
Boken–SSE	Irwin	2.0E-03	6.8E-05	1.5E-02	3.1E-02	8.0E-10	7.9E-10	4.2E-10	2.2E-04	4.9E-02	4.9
Ikuren	Glenn	4.4E-03	6.0E-05	5.2E-02	3.1E-02	8.0E-10	7.9E-10	4.2E-10	4.2E-04	8.8E-02	8.8
Kidrenen	Keith	8.4E-04	5.9E-05	1.6E-02	3.1E-02	8.0E-10	7.9E-10	4.2E-10	3.9E-04	4.9E-02	4.9
Mut	Henry	4.1E-03	7.2E-05	4.0E-02	3.1E-02	8.0E-10	7.9E-10	4.2E-10	2.2E-04	7.6E-02	7.6
Ribewon	James	1.8E-03	4.8E-05	1.4E-02	3.1E-02	8.0E-10	7.9E-10	4.2E-10	4.5E-04	4.8E-02	4.8

Five island groups are described to provide more detail on current conditions.

5.1.1 Enewetak Island

The baseline dose for an individual living on Enewetak and consuming a diet comprised totally of Enewetak Island grown foods is 0.06 mSv/year (6 mrem/year). The concentrations of residual soil radionuclides on Enewetak are small. The largest single pathway of exposure is consumption of seafoods, providing about two-thirds of the total dose. The seafoods of reef fish and octopus have the highest fraction of the ingestion dose; residual plutonium in the lagoon water has the greatest contribution to dose for both. Because of the nature of the local diet and the primary sources of food, coconuts and coconut products dominated the ingestion dose. The exposure scenario considered herein assumed that all local foods were grown on the individual islands. Most of the remaining dose is consumption of locally grown terrestrial foods; about half the dose is related to coconuts and coconut products. This dose is dominated by ^{137}Cs. The remaining 3% of the dose comes from external exposure to soils, where ^{90}Sr and ^{137}Cs control. Conditions on this island are similar to those on Medren and Japtan. Doses from lagoon-water-related pathways of swimming and boating were small compared to the terrestrial pathways, although sediments on the beaches may add up to one-tenth of the direct soil exposure dose. Inhalation of either island dusts or sea spray was generally a small fraction of the total dose from all other pathways.

5.1.2 Runit Island

The baseline dose for an individual living on Runit and consuming a diet comprised totally of Runit Island grown foods is 0.58 mSv/year (58 mrem/year). The concentrations of residual soil radionuclides on Runit are moderate, not counting the potential for contact with small particles of plutonium. The largest single pathway of exposure is consumption of terrestrial foods (0.48 mSv/a, 49 mrem/year) to which coconuts contribute 75%. The dominant radionuclide is ^{137}Cs via this pathway. Seafoods contribute about 10% of the dose; again plutonium isotopes and also ^{241}Am are the largest fractional contributors. External direct dose is about 5% of the total. These dose estimates do not include the possibility of inhalation of particulate plutonium which remains distributed in the soils and is a primary reason the island is currently off limits. Other pathways are similar to Enewetak and increase in proportion to the others.

5.1.3 Enjebi Island

The baseline dose for an individual living on Enjebi and consuming a diet comprised totally of Enjebi Island grown foods is 2.48 mSv/year (248 mrem/year). The concentrations of residual soil radionuclides on Enjebi are moderately high. Locally grown island foods would contribute nearly 90% of the total dose, of which coconuts and coconut products would be over half. The dominant radionuclide for this pathway is ^{137}Cs. Soil external could contribute about 7.5 % from ^{90}Sr and ^{137}Cs, and seafoods contribute about only 2.5% with contributions from ^{241}Am and plutonium isotopes. Other pathways are similar to Enewetak and increase in proportion to the others. The current dose levels are sufficiently high that residence has been discouraged on Enjebi.

5.1.4 Northwestern Islands

The islands in the northwest quadrant of the atoll, including Bokoluo and Bokombako, were subjected to the largest of the weapons tests, and as a result have some of the largest residual contaminations in both their surface soils and surrounding lagoon water and sediment. The baseline dose for an individual living on Bokombako and consuming a diet comprised totally of Bokombako Island grown foods is 14 mSv/year (1,400 mrem/year). The concentrations of residual soil radionuclides on Bokombako are high, as are those in the surrounding lagoon. Locally grown island foods would contribute nearly 90% of the total dose, of which coconuts and coconut products would be about one-third; ^{137}Cs and ^{90}Sr dominate. Seafoods are a small contributor in comparison, only about 0.3%. Soil external dose would be over 10%, primarily from ^{90}Sr and ^{137}Cs. Other pathways are similar to Enewetak and increase in proportion to the others. Residence is discouraged on these islands because of the high residual contamination.

5.1.5 Southwestern Islands

The southwestern islands have very low levels of contamination and are similar to Enewetak Island in magnitude and pathway structure.

5.2 Current Conditions, Storm Impacts

The main routes of radiation exposure to residents of the atoll's islands are related to the residual contamination of the island soils; the aquatic pathways such as swimming/diving, boating or fish consumption have generally small doses. To investigate the impacts of stirring up the contaminated bottom sediments during large storms, three plausible severe hurricanes were evaluated, as described in Sections 3.0 and 4.0.

To evaluate the potential doses resulting from storms, radiation doses were estimated as increments above the current levels for each island. Details of the results for the largest storm (the one with the greatest incremental changes), Storm 1 (the July storm), are presented for all pathways in Table 18. Because the storms did not change the contamination levels of the island soils above the waterline (except for a small amount of rainfall-related leaching into deeper layers), the doses from direct external radiation and uptake into local food products were unchanged – so the incremental change is zero. The storm mobilized and transported bottom sediments which temporarily result in increased concentrations of radionuclides in the lagoon waters. These increased concentrations resulted in small increases in the doses for swimming and boating and from locally caught seafood. The inhalation dose from sea spray was increased, but by a negligible amount. As is described in the section on biota doses, the dose to lagoon biota was also increased slightly.

The vigorous wave action and induced currents within the lagoon caused by the storm have an interesting result – the contaminated sediments near the islands were scoured by the storm and eventually settled either in the deeper portions of the lagoon or in the open ocean. As a result, the dose rates from the beach sands – direct external dose and inhalation of resuspended sediments – decreased from the baseline. The decrease is small, fractions of 1%, for all islands.

The results were similar for the other two storms investigated for current conditions. The results for all storms, and the baseline condition, are shown in Table 19. The scouring of the island sediments resulted in different deposition patterns within the lagoon, and a few of the southern islands showed the impact of very small increases in beach contamination. The impacts, increases and decreases, are very small – on the order of the dose accrued from one day of natural background or less. Generally, the effect of the storms on the radiological conditions was minor.

Table 18. Incremental change in radiation dose caused by the largest current conditions storm (Storm 1).

		Terrestrial Pathways			Aquatic Pathways					Incremental Annual Dose	
Island name	US assigned name	Soil External (mSv/yr)	Res.Inh. (mSv/yr)	Local Foods (mSv/yr)	Seafood (mSv/yr)	Swimming Boating (mSv/yr)	Boating (mSv/yr)	SeaSpray (mSv/yr)	Beach External (mSv/yr)	(mSv/a)	(mrem/yr)
Enewetak	Fred	0.00E+00	-1.11E-05	0.00E+00	2.89E-07	8.66E-16	8.54E-16	3.68E-15	-1.13E-04	-1.24E-04	-1.2E-02
Medren	Elmer	0.00E+00	-1.12E-06	0.00E+00	4.54E-07	2.01E-16	1.99E-16	3.63E-15	-7.05E-06	-7.72E-06	-7.7E-04
Japtan	David	0.00E+00	-1.07E-05	0.00E+00	9.90E-07	4.03E-16	3.97E-16	7.87E-15	-1.02E-04	-1.12E-04	-1.1E-02
Ananij	Bruce	0.00E+00	-1.32E-05	0.00E+00	2.56E-07	1.25E-16	1.23E-16	2.11E-15	-2.22E-04	-2.35E-04	-2.3E-02
Inedral	Uriah	0.00E+00	-1.79E-05	0.00E+00	6.73E-07	3.00E-16	2.96E-16	5.44E-15	-2.59E-04	-2.77E-04	-2.8E-02
Van	Van	0.00E+00	-1.79E-05	0.00E+00	3.35E-07	1.65E-16	1.63E-16	2.79E-15	-2.78E-04	-2.95E-04	-3.0E-02
Runit	Yvonne	0.00E+00	-6.39E-05	0.00E+00	5.87E-07	2.94E-16	2.90E-16	5.00E-15	-5.79E-04	-6.42E-04	-6.4E-02
Alembel	Vera	0.00E+00	-1.32E-05	0.00E+00	1.68E-07	1.27E-16	1.25E-16	1.51E-15	-3.02E-04	-3.15E-04	-3.2E-02
Billae	Wilma	0.00E+00	-1.79E-05	0.00E+00	3.53E-07	3.02E-16	2.98E-16	3.25E-15	-2.99E-04	-3.17E-04	-3.2E-02
Aomon	Sally	0.00E+00	-1.65E-05	0.00E+00	2.07E-07	2.14E-16	2.12E-16	1.95E-15	-3.29E-04	-3.45E-04	-3.4E-02
Bijiri	Tilda	0.00E+00	-1.20E-05	0.00E+00	1.97E-07	1.74E-16	1.72E-16	1.79E-15	-2.43E-04	-2.54E-04	-2.5E-02
Lojwa	Ursula	0.00E+00	-7.50E-06	0.00E+00	1.54E-07	1.41E-16	1.39E-16	1.43E-15	-1.65E-04	-1.72E-04	-1.7E-02
Aej	Olive	0.00E+00	-1.62E-05	0.00E+00	1.87E-07	2.15E-16	2.12E-16	1.72E-15	-9.25E-04	-9.41E-04	-9.4E-02
Elle	Nancy	0.00E+00	-1.20E-05	0.00E+00	1.41E-07	2.04E-16	2.01E-16	1.35E-15	-5.06E-04	-5.18E-04	-5.2E-02
Lujor	Pearl	0.00E+00	-1.94E-05	0.00E+00	2.53E-07	2.71E-16	2.67E-16	2.37E-15	-6.88E-04	-7.07E-04	-7.1E-02
Bokenelab	Mary	0.00E+00	-5.49E-05	0.00E+00	1.46E-07	2.61E-16	2.57E-16	1.44E-15	-3.13E-03	-3.19E-03	-3.2E-01
Kidrinnenen	Lucy	0.00E+00	-6.12E-05	0.00E+00	2.46E-07	5.20E-16	5.13E-16	2.55E-15	-5.52E-03	-5.58E-03	-5.6E-01
Mijikadrek	Kate	0.00E+00	-7.88E-05	0.00E+00	2.89E-07	5.66E-16	5.59E-16	3.08E-15	-6.10E-03	-6.17E-03	-6.2E-01
Enjebi	Janet	0.00E+00	-2.09E-04	0.00E+00	4.38E-07	8.70E-16	8.58E-16	4.64E-15	-1.14E-02	-1.16E-02	-1.2E+00
Boken–N	Irene	0.00E+00	-5.38E-04	0.00E+00	7.10E-07	1.11E-15	1.10E-15	7.22E-15	-1.62E-02	-1.67E-02	-1.7E+00
Bokinwotme	Edna	0.00E+00	-7.79E-04	0.00E+00	6.43E-07	3.84E-16	3.79E-16	6.93E-15	-7.98E-03	-8.76E-03	-8.8E-01
Louj	Daisy	0.00E+00	-3.41E-04	0.00E+00	7.63E-07	3.49E-16	3.45E-16	8.04E-15	-2.70E-03	-3.04E-03	-3.0E-01
Bokoluo	Alice	0.00E+00	-2.79E-04	0.00E+00	7.07E-07	3.30E-16	3.25E-16	9.17E-15	-2.08E-03	-2.36E-03	-2.4E-01
Bokombako	Belle	0.00E+00	-3.34E-04	0.00E+00	1.18E-06	4.97E-16	4.90E-16	1.40E-14	-2.49E-03	-2.82E-03	-2.8E-01
Kirunu	Clara	0.00E+00	-5.37E-04	0.00E+00	4.71E-07	1.96E-16	1.94E-16	5.27E-15	-3.24E-03	-3.78E-03	-3.8E-01
Biken	Leroy	0.00E+00	-2.81E-04	0.00E+00	1.91E-07	1.88E-16	1.86E-16	3.46E-15	-3.13E-03	-3.41E-03	-3.4E-01
Boken–SSE	Irwin	0.00E+00	1.55E-10	0.00E+00	3.00E-08	3.17E-17	3.13E-17	2.76E-16	3.22E-05	3.23E-05	3.2E-03
Ikuren	Glenn	0.00E+00	-8.25E-07	0.00E+00	3.27E-08	3.23E-17	3.18E-17	2.96E-16	-8.49E-05	-8.57E-05	-8.6E-03
Kidrenen	Keith	0.00E+00	-7.26E-07	0.00E+00	9.09E-09	1.65E-17	1.63E-17	1.10E-16	-7.56E-05	-7.63E-05	-7.6E-03
Mut	Henry	0.00E+00	-8.93E-08	0.00E+00	3.34E-08	3.21E-17	3.17E-17	3.06E-16	3.18E-05	3.17E-05	3.2E-03
Ribewon	James	0.00E+00	-5.47E-07	0.00E+00	1.68E-08	2.61E-17	2.57E-17	1.81E-16	-5.46E-05	-5.51E-05	-5.5E-03

Table 19. Comparison of baseline and storm incremental changes in radiation dose for 2015 conditions.

Island		2015 Current Conditions Dose (mSv/yr)				2015 Current Conditions Dose (mrem/yr)			
Island Name	U.S. Assigned Name	Baseline	Storm1	Storm2	Storm3	Baseline	Storm1	Storm2	Storm3
Enewetak	Fred	0.06	-1.2E-04	2.9E-06	-2.5E-04	6.1	-0.012	0.000	-0.025
Medren	Elmer	0.04	-7.7E-06	2.0E-05	-1.3E-04	4.0	-0.001	0.002	-0.013
Japtan	David	0.06	-1.1E-04	3.7E-05	-1.1E-04	5.5	-0.011	0.004	-0.011
Ananij	Bruce	0.05	-2.3E-04	-7.8E-05	-2.0E-04	5.2	-0.023	-0.008	-0.020
Inedral	Uriah	0.03	-2.8E-04	1.2E-05	-2.6E-04	2.7	-0.028	0.001	-0.026
Van	Van	0.04	-3.0E-04	-1.6E-04	-2.8E-04	3.7	-0.030	-0.016	-0.028
Runit	Yvonne	0.58	-6.4E-04	-8.7E-05	-4.8E-04	57.6	-0.064	-0.009	-0.048
Alembel	Vera	0.44	-3.2E-04	-5.4E-05	-2.0E-04	44.1	-0.032	-0.005	-0.020
Billae	Wilma	0.51	-3.2E-04	-5.4E-05	-1.8E-04	50.6	-0.032	-0.005	-0.018
Aomon	Sally	0.70	-3.4E-04	-1.7E-05	-3.4E-04	70.2	-0.034	-0.002	-0.034
Bijiri	Tilda	0.56	-2.5E-04	-6.3E-05	-2.9E-04	55.5	-0.025	-0.006	-0.029
Lojwa	Ursula	0.44	-1.7E-04	-1.3E-04	-2.0E-04	44.2	-0.017	-0.013	-0.020
Aej	Olive	0.96	-9.4E-04	-2.6E-04	-1.2E-03	96.1	-0.094	-0.026	-0.119
Elle	Nancy	5.81	-5.2E-04	-3.6E-04	-1.5E-03	581.1	-0.052	-0.036	-0.149
Lujor	Pearl	1.05	-7.1E-04	1.8E-05	-6.8E-04	105.2	-0.071	0.002	-0.068
Bokenelab	Mary	1.04	-3.2E-03	-1.1E-03	-2.9E-03	104.4	-0.319	-0.106	-0.293
Kidrinnenen	Lucy	1.17	-5.6E-03	-2.2E-03	-5.5E-03	116.5	-0.558	-0.223	-0.549
Mijikadrek	Kate	0.71	-6.2E-03	-1.6E-03	-5.1E-03	70.9	-0.617	-0.164	-0.506
Enjebi	Janet	2.48	-1.2E-02	-3.2E-03	-1.1E-02	248.1	-1.159	-0.324	-1.100
Boken–N	Irene	2.06	-1.7E-02	-7.2E-03	-1.2E-02	205.5	-1.672	-0.722	-1.181
Bokinwotme	Edna	1.44	-8.8E-03	-2.3E-03	-5.8E-03	143.8	-0.876	-0.232	-0.582
Louj	Daisy	2.27	-3.0E-03	3.5E-04	-4.1E-03	226.9	-0.304	0.035	-0.408
Bokoluo	Alice	11.68	-2.4E-03	-5.6E-04	-2.1E-03	1167.6	-0.236	-0.056	-0.208
Bokombako	Belle	13.86	-2.8E-03	-9.5E-04	-2.0E-03	1385.5	-0.282	-0.095	-0.195
Kirunu	Clara	2.04	-3.8E-03	-1.6E-03	-2.4E-03	203.7	-0.378	-0.159	-0.244
Biken	Leroy	0.89	-3.4E-03	-1.5E-03	-2.2E-03	88.6	-0.341	-0.145	-0.222
Boken–SSE	Irwin	0.05	3.2E-05	1.8E-07	-2.6E-06	4.9	0.003	0.000	0.000
Ikuren	Glenn	0.09	-8.6E-05	5.3E-06	-4.8E-05	8.8	-0.009	0.001	-0.005
Kidrenen	Keith	0.05	-7.6E-05	5.5E-06	-1.8E-04	4.9	-0.008	0.001	-0.018
Mut	Henry	0.08	3.2E-05	1.7E-09	-2.0E-06	7.6	0.003	0.000	0.000
Ribewon	James	0.05	-5.5E-05	-6.7E-06	-7.9E-05	4.8	-0.006	-0.001	-0.008

The same five island groups are described to provide more detail on the possible effects of storms on current conditions. The incremental dose increases and decreases of Table 18 caused by the evaluated storms are shown in graphical form in Figure 24.

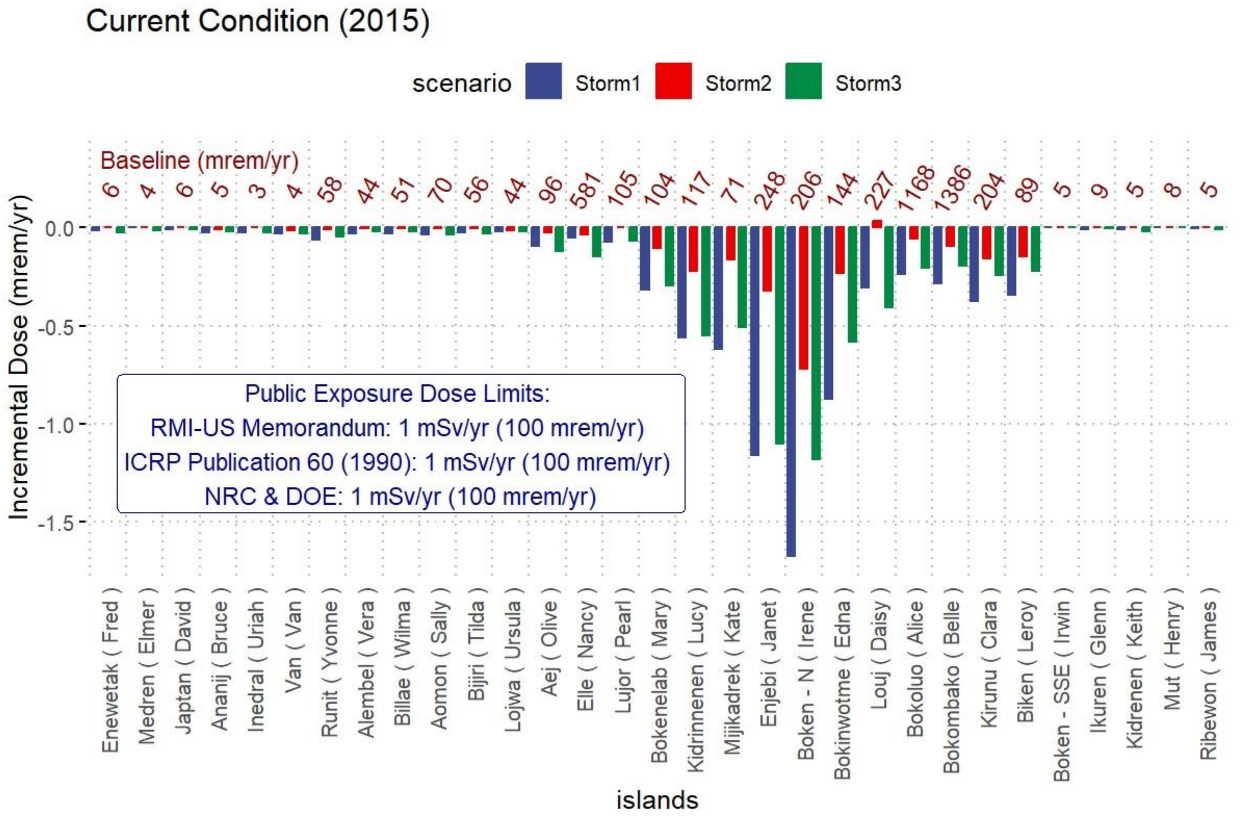

Figure 24. Incremental doses caused by the evaluated storms for each island under current conditions to existing baseline annual dose (values shown in red at top of the figure)

5.2.1 Enewetak Island

The southern islands centered on Enewetak Island are minimally impacted by the simulated storms. The redistribution of contaminated sediments and water by the storm generally cause decreases in dose rate because of scouring of the nearby sediments, but in some locations or conditions these sediments can deposit near an island and cause a small increase in dose. The turbulence within the lagoon caused by the storm briefly increases the concentrations of radionuclides in the water and thus increases concentrations in fish and other seafoods, which result in very small increases in dose via the water-related pathways. However, the scouring of the sediments frequently causes a decrease in contaminants on the beaches, which can result in a lower exposure rate near the shore from external and resuspension pathways. The dose from inhalation of sea spray during the event is negligible. The overall change in dose from any storm was less than 0.5%.

5.2.2 Runit Island

Results for Runit are similar to those for Enewetak. The wave-action scouring of sediments potentially reduces the dose from shoreline and long-term aquatic pathways. The dose from inhalation of sea spray during the event is negligible. The overall change in dose from any storm was less than 0.1%.

5.2.3 Enjebi Island

Results for Enjebi and islands in the immediate vicinity like Boken are similar to those for Enewetak and Runit. The magnitude of the changes caused by storms is largest in this region. The wave-action scouring of sediments potentially reduces the dose from shoreline and long-term aquatic pathways. The dose from inhalation of sea spray during the event is negligible. The overall reduction in dose from any storm was less than 0.8%.

5.2.4 Northwestern Islands

The northwestern island group is the most heavily contaminated. The primary change caused by storm-driven waves is a reduction in the near-shore sediment concentrations, transporting them away, resulting in a reduction in the direct external dose from the beaches. The overall reduction in dose is small because the dose is dominated by the terrestrial pathways that are not impacted by the storm.

5.2.5 Southwestern Islands

Because these islands have very low current contamination levels, the storms have a minimal impact on doses. There are some conditions that result in scouring of nearby sediments and others that result in local deposition. Radiological changes are in the range of 0.5% up or down on already low doses.

5.3 Future Conditions Baseline

To evaluate the potential for climate-related changes in the future, the existing radionuclide contamination levels in soils, sediments, and lagoon waters were reduced to account for radioactive decay. In the case of ^{137}Cs, the observed effective half-life in soils resulting from rainwater leaching of 8.5 years was applied; for all other radionuclides, only physical decay was considered. The year 2090 was selected to be representative of future conditions.

For the future conditions, just as for current conditions, the Baseline scenario provided estimates of annual radiation dose to representative adults living on each island for a full year. The cumulative annual radiation effective dose estimated for each exposure pathway is shown in Table 20. The future doses are expected to be smaller than exist under current conditions primarily because of the radioactive decay of the shorter-lived radioisotopes of ^{90}Sr and ^{137}Cs.

Radiation doses about 70 years in the future (year 2090) will be significantly lower than those currently possible throughout the atoll. All islands except Bokombako (Belle), and perhaps Bokoluo (Alice), in the far northwest of the atoll should be acceptable for residency. The two highest-dose islands are between the sites of the largest nuclear tests in the atoll and have the largest residual contamination levels. Even this far in the future, the dominant radionuclide is ^{90}Sr via the local food ingestion pathway for these two islands. For all islands, the possibility for consuming locally grown food would be the primary potential hazard.

The five island groups are described to provide more detail on anticipated future conditions.

5.3.1 Enewetak Island

The future baseline dose for an individual living on Enewetak and consuming a diet comprised totally of Enewetak grown foods is 0.04 mSv/year (4 mrem/year). The concentrations of residual soil radionuclides on Enewetak are small and will have decreased by radioactive decay. The largest single pathway of exposure is consumption of seafoods, providing nearly 95% of the total dose. The seafoods of reef fish and octopus have the highest fraction of the ingestion dose; residual Pu in the lagoon water has the greatest contribution to dose for both. Conditions on this island are similar to those on Medren and Japtan. Doses from lagoon-water-related pathways of swimming and boating were small compared to the terrestrial pathways.

5.3.2 Runit Island

The future baseline dose for an individual living on Runit and consuming a diet comprised totally of Runit grown foods is 0.08 mSv/year (8 mrem/year). The concentrations of residual soil radionuclides on Runit are moderate, not counting the potential for contact with small particles of Pu. Because of the decay of ^{90}Sr and ^{137}Cs, future seafoods would increase in fractional contribution to about 70% of the dose; again Pu isotopes and also ^{241}Am are the largest fractional contributors. External direct dose is about 3% of the total. These dose estimates do not include the possibility of inhalation of particulate Pu, which remains distributed in the soils and is a primary reason the island is currently off limits.

5.3.3 Enjebi Island

The future baseline dose for an individual living on Enjebi and consuming a diet comprised totally of Enjebi grown foods is 0.26 mSv/year (26 mrem/year). Locally grown island foods would contribute about two-thirds of the total dose, of which coconuts and coconut products would be over half. The dominant radionuclide for this pathway becomes ^{90}Sr. Soil external dose could contribute about 10% largely from ^{90}Sr, and seafoods contribute about 22% with contributions from ^{241}Am and Pu isotopes. The future projected dose levels would be such that residence could be allowed on Enjebi.

5.3.4 Northwestern Islands

The islands in the northwest quadrant of the atoll, including Bokoluo and Bokombako, will show some of the largest decreases in dose because of the decay and leaching of ^{90}Sr and ^{137}Cs. The baseline dose for an individual living on Bokombako and consuming a diet comprised totally of Bokombako grown foods is 0.19 mSv/year (19 mrem/year). Locally grown island foods would still contribute nearly two-thirds of the total dose. The fractional contribution from seafoods would grow to about 20% but also be a declining absolute value. Soil external dose would remain about 10%, primarily from ^{90}Sr. Residence would continue to be discouraged on these islands because of the high residual contamination.

5.3.5 Southwestern Islands

The southwestern islands have very low levels of contamination and are similar to Enewetak Island in magnitude and pathway structure.

5.4 Future Conditions Storm Impacts

As with the current conditions, the impact of storms on the future baseline were investigated. Because the storms do not change the contamination levels of the island soils above the waterline (except for a small amount of rainfall-related leaching into deeper layers), the doses from direct external radiation and uptake into local food products are unchanged so the incremental change is zero. Storms stir up bottom sediments which temporarily results in increased concentrations of radionuclides in the lagoon waters. The vigorous wave action and induced currents within the lagoon caused by storms have an interesting result, the contaminated sediments near the islands are scoured by the storm and eventually settle either in the deeper portions of the lagoon or in the open ocean. This may be seen in Table 21. The future storms appear to have different effects on currents within the lagoon, causing less scouring and more sediment deposition on beaches of some islands.

The five island groups are described to provide more detail on anticipated future storm-related conditions. The incremental dose increases and decreases of Table 21 caused by the evaluated storms are shown in graphical form in Figure 25.

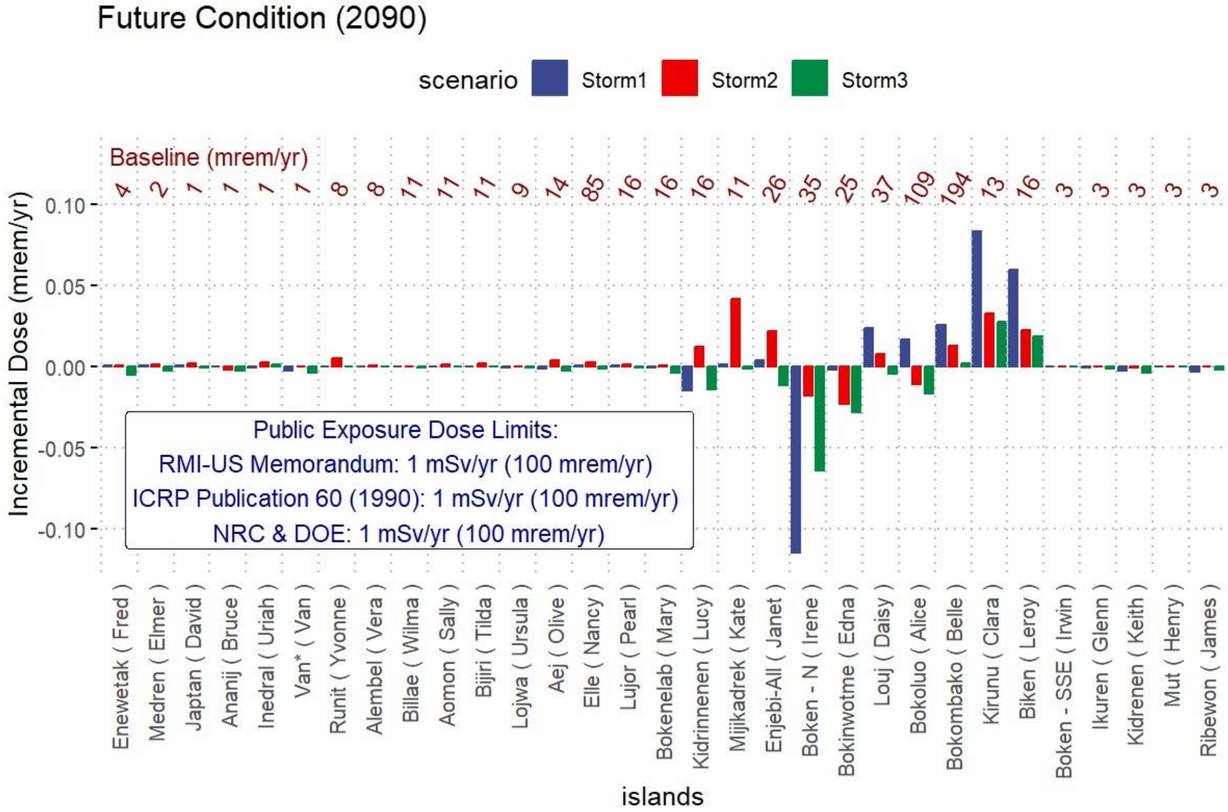

Figure 25. Incremental doses caused by the evaluated storms for each island under future conditions to baseline annual dose (values shown in red at top of the figure).

5.4.1 Enewetak Island

Future storms would have minimal impact on Enewetak or the nearby islands. Dose projections show storm-related increases or decreases in dose on the order of 0.1%.

5.4.2 Runit Island

Future storms would have minimal impact on Runit Island. Dose projections show storm-related increases or decreases in dose on the order of 0.1%.

5.4.3 Enjebi Island

Future storms would have minimal impact on Enjebi Island. Dose projections show storm-related increases or decreases in dose on the order of 0.1%.

5.4.4 Northwestern Islands

The islands in the northwest quadrant of the atoll, including Bokoluo and Bokombako, will show the largest impacts because they are the most contaminated, but the absolute magnitude of the impacts is small and less than 0.1% of the baseline.

5.4.5 Southwestern Islands

The southwestern islands have very low levels of contamination and are similar to Enewetak Island in magnitude and pathway structure of changes caused by storms.

5.5 Future Conditions Impacts of Storm with Runit Dome Failure

The feature with the largest visibility and greatest level of concern remaining from the U.S. nuclear testing series for the residents of Enewetak Atoll is the waste repository colloquially known as the Runit Dome. The main concern is failure of the dome with release of the stored wastes onto Runit Island and the adjacent lagoon. As discussed in Section 4.0, it was postulated that the dome would hypothetically collapse in a future storm and release its radionuclide inventory onto the island and into the nearby lagoon. As with the future storm effects described in Section 5.4, the results are evaluated in terms of incremental changes from the future baseline.

The incremental changes in dose resulting from collapse of the dome in future Storm 2 are shown in Table 22.

Table 20. Radiation dose by island for selected exposure pathways for 2090 Future Conditions Baseline.

		Terrestrial Pathways			Aquatic Pathways					Total Annual Dose	
Island Name	U.S. Assigned Name	External (mSv/yr)	Res.Inh. (mSv/yr)	Local Foods (mSv/yr)	Seafood (mSv/yr)	Swimming Boating (mSv/yr)	Boating (mSv/yr)	SeaSpray (mSv/yr)	Beach External (mSv/yr)	(mSv/yr)	(mrem/yr)
Enewetak	Fred	2.6E-04	7.8E-05	1.9E-03	0.039	2.5E-10	2.4E-10	6.9E-10	1.1E-04	0.041	4.1
Medren	Elmer	3.4E-04	1.2E-04	2.4E-03	0.012	8.1E-11	8.0E-11	1.7E-10	8.5E-05	0.015	1.5
Japtan	David	2.3E-04	5.1E-05	1.7E-03	0.012	8.1E-11	8.0E-11	1.7E-10	7.4E-05	0.014	1.4
Ananij	Bruce	2.5E-04	5.4E-05	1.9E-03	0.012	8.1E-11	8.0E-11	1.7E-10	6.4E-05	0.014	1.4
Inedral	Uriah	2.0E-04	6.4E-05	1.4E-03	0.012	8.1E-11	8.0E-11	1.7E-10	8.3E-05	0.014	1.4
Van	Van	1.8E-04	5.8E-05	1.3E-03	0.012	8.1E-11	8.0E-11	1.7E-10	8.5E-05	0.014	1.4
Runit	Yvonne	2.3E-03	5.7E-03	1.7E-02	0.057	2.5E-10	2.5E-10	8.1E-10	2.2E-04	0.082	8.2
Alembel	Vera	3.5E-03	1.2E-03	2.2E-02	0.057	2.5E-10	2.5E-10	8.1E-10	5.9E-05	0.084	8.4
Billae	Wilma	6.7E-03	2.0E-03	4.7E-02	0.057	2.5E-10	2.5E-10	8.1E-10	2.6E-05	0.112	11.2
Aomon	Sally	5.4E-03	2.2E-03	4.0E-02	0.057	2.5E-10	2.5E-10	8.1E-10	8.9E-05	0.105	10.5
Bijiri	Tilda	6.4E-03	1.7E-03	4.2E-02	0.057	2.5E-10	2.5E-10	8.1E-10	9.2E-05	0.107	10.7
Lojwa	Ursula	4.2E-03	7.5E-04	3.1E-02	0.057	2.5E-10	2.5E-10	8.1E-10	5.9E-05	0.093	9.3
Aej	Olive	9.4E-03	3.0E-03	6.6E-02	0.057	2.5E-10	2.5E-10	8.1E-10	3.2E-04	0.136	13.6
Elle	Nancy	9.9E-02	2.3E-02	6.7E-01	0.057	2.5E-10	2.5E-10	8.1E-10	3.4E-04	0.852	85.2
Lujor	Pearl	1.3E-02	1.1E-02	8.0E-02	0.057	2.5E-10	2.5E-10	8.1E-10	2.0E-04	0.161	16.1
Bokenelab	Mary	1.2E-02	3.5E-03	8.3E-02	0.057	2.5E-10	2.5E-10	8.1E-10	4.3E-04	0.155	15.5
Kidrinnenen	Lucy	1.3E-02	3.6E-03	9.0E-02	0.057	2.5E-10	2.5E-10	8.1E-10	1.2E-03	0.164	16.4
Mijikadrek	Kate	6.8E-03	1.5E-03	4.7E-02	0.057	2.5E-10	2.5E-10	8.1E-10	1.8E-03	0.114	11.4
Enjebi	Janet	2.5E-02	4.7E-03	1.8E-01	0.057	2.5E-10	2.5E-10	8.1E-10	2.9E-03	0.264	26.4
Boken – N	Irene	3.4E-02	1.1E-02	2.6E-01	0.045	2.5E-10	2.5E-10	6.4E-10	2.9E-03	0.349	34.9
Bokinwotme	Edna	2.5E-02	8.2E-03	1.8E-01	0.045	2.5E-10	2.5E-10	6.4E-10	4.8E-04	0.255	25.5
Louj	Daisy	4.0E-02	8.7E-03	2.8E-01	0.045	2.5E-10	2.5E-10	6.4E-10	1.2E-03	0.375	37.5
Bokoluo	Alice	1.3E-01	2.0E-02	8.9E-01	0.045	2.5E-10	2.5E-10	6.4E-10	9.0E-04	1.088	108.8
Bokombako	Belle	2.3E-01	4.3E-02	1.6E+00	0.045	2.5E-10	2.5E-10	6.4E-10	9.9E-04	1.939	193.9
Kirunu	Clara	9.8E-03	3.4E-03	7.4E-02	0.045	2.5E-10	2.5E-10	6.4E-10	8.8E-04	0.133	13.3
Biken	Leroy	1.4E-02	7.9E-04	1.0E-01	0.039	2.5E-10	2.5E-10	5.9E-10	9.0E-05	0.158	15.8
Boken–SSE	Irwin	3.0E-04	6.6E-05	2.1E-03	0.029	1.6E-10	1.5E-10	4.1E-10	4.4E-05	0.032	3.2
Ikuren	Glenn	5.7E-04	5.8E-05	4.2E-03	0.029	1.6E-10	1.5E-10	4.1E-10	8.2E-05	0.034	3.4
Kidrenen	Keith	6.3E-05	5.8E-05	4.3E-04	0.029	1.6E-10	1.5E-10	4.1E-10	7.5E-05	0.030	3.0
Mut	Henry	3.3E-04	7.0E-05	2.4E-03	0.029	1.6E-10	1.5E-10	4.1E-10	4.4E-05	0.032	3.2
Ribewon	James	2.9E-04	4.7E-05	2.1E-03	0.029	1.6E-10	1.5E-10	4.1E-10	8.8E-05	0.031	3.1

Table 21. Comparison of future baseline and storm incremental changes in radiation dose for 2090 conditions.

		2090 Future Conditions Dose (mSv/a)				2090 Future Conditions Dose (mrem/a)			
Island Name	U.S. Assigned Name	Baseline	Storm1	Storm2	Storm3	Baseline	Storm1	Storm2	Storm3
Enewetak	Fred	0.04	2.2E-06	5.1E-06	-5.0E-05	4.1	2.2E-04	5.1E-04	-0.005
Medren	Elmer	0.02	6.1E-06	1.4E-05	-3.0E-05	1.5	6.1E-04	0.0014	-0.003
Japtan	David	0.01	5.4E-06	1.9E-05	-6.2E-06	1.4	5.4E-04	0.0019	-6.2E-04
Ananij	Bruce	0.01	-1.7E-06	-2.2E-05	-2.7E-05	1.4	-1.7E-04	-0.0022	-0.003
Inedral	Uriah	0.01	-7.3E-06	2.2E-05	1.2E-05	1.4	-7.3E-04	0.0022	1.2E-03
Van	Van	0.01	-2.7E-05	-3.8E-07	-4.2E-05	1.4	-0.0027	-3.8E-05	-0.004
Runit	Yvonne	0.08	9.8E-07	5.2E-05	-3.7E-06	8.2	9.8E-05	0.0052	-3.7E-04
Alembel	Vera	0.08	4.2E-07	8.0E-06	-3.8E-06	8.4	4.2E-05	8.0E-04	-3.8E-04
Billae	Wilma	0.11	-4.1E-06	6.3E-07	-5.4E-06	11.2	-4.1E-04	6.3E-05	-5.4E-04
Aomon	Sally	0.11	-3.4E-06	1.3E-05	2.9E-07	10.5	-3.4E-04	0.0013	2.9E-05
Bijiri	Tilda	0.11	-2.0E-06	2.1E-05	-3.1E-06	10.7	-2.0E-04	0.0021	-3.1E-04
Lojwa	Ursula	0.09	-9.4E-06	1.3E-06	-1.1E-05	9.3	-9.4E-04	1.3E-04	-1.1E-03
Aej	Olive	0.14	-1.6E-05	3.5E-05	-3.0E-05	13.6	-0.0016	0.0035	-0.003
Elle	Nancy	0.85	4.4E-06	2.6E-05	-1.6E-05	85.2	4.4E-04	0.0026	-0.002
Lujor	Pearl	0.16	6.6E-06	1.3E-05	-8.6E-06	16.1	6.6E-04	0.0013	-8.6E-04
Bokenelab	Mary	0.16	-9.9E-06	5.2E-06	-3.7E-05	15.5	-9.9E-04	5.2E-04	-0.004
Kidrinnenen	Lucy	0.16	-1.5E-04	1.2E-04	-1.4E-04	16.4	-0.0146	0.012	-0.014
Mijikadrek	Kate	0.11	9.2E-06	4.2E-04	-1.3E-05	11.4	9.2E-04	0.042	-1.3E-03
Enjebi	Janet	0.26	3.5E-05	2.2E-04	-1.2E-04	26.4	0.0035	0.022	-0.012
Boken–N	Irene	0.35	-1.1E-03	-1.8E-04	-6.4E-04	34.9	-0.11	-0.018	-0.064
Bokinwotme	Edna	0.25	-2.2E-05	-2.3E-04	-2.8E-04	25.5	-0.002	-0.023	-0.028
Louj	Daisy	0.37	2.4E-04	7.3E-05	-4.4E-05	37.5	0.024	0.0073	-0.004
Bokoluo	Alice	1.09	1.6E-04	-1.1E-04	-1.7E-04	108.8	0.016	-0.0108	-0.017
Bokombako	Belle	1.94	2.6E-04	1.2E-04	1.8E-05	193.9	0.026	0.012	0.002
Kirunu	Clara	0.13	8.4E-04	3.3E-04	2.7E-04	13.3	0.084	0.033	0.027
Biken	Leroy	0.16	5.9E-04	2.2E-04	1.8E-04	15.8	0.059	0.022	0.018
Boken–SSE	Irwin	0.03	-2.0E-06	1.2E-07	-3.8E-06	3.2	-2.0E-04	1.2E-05	-3.8E-04
Ikuren	Glenn	0.03	-8.1E-06	-1.4E-06	-1.3E-05	3.4	-8.1E-04	-1.4E-04	-1.3E-03
Kidrenen	Keith	0.03	-2.4E-05	-4.5E-06	-3.9E-05	3.0	-0.0024	-4.5E-04	-0.004
Mut	Henry	0.03	-3.1E-07	2.8E-08	-1.7E-06	3.2	-3.1E-05	2.8E-06	-1.7E-04
Ribewon	James	0.03	-3.2E-05	-1.3E-06	-2.1E-05	3.1	-0.003	-1.3E-04	-0.002

Table 22. Radiation dose by island for selected exposure pathways for 2090 Storm 2, Runit Dome Collapse.

		Terrestrial Pathways			Aquatic Pathways					Incremental Annual Dose	
Island Name	U.S. Assigned Name	Soil External (mSv/yr)	Res.Inh. (mSv/yr)	Local Foods (mSv/yr)	Seafood (mSv/yr)	Swimming Boating (mSv/yr)	Boating (mSv/yr)	SeaSpray (mSv/yr)	Beach External (mSv/yr)	(mSv/yr)	(mrem/yr)
Enewetak	Fred	0	3.6E-06	0.00	1.1E-07	1.4E-16	1.4E-16	2.0E-15	1.0E-05	1.4E-05	1.4E-03
Medren	Elmer	0	4.0E-06	0.00	1.4E-07	1.7E-17	1.7E-17	1.2E-15	1.0E-05	1.4E-05	1.4E-03
Japtan	David	0	8.3E-06	0.00	3.6E-08	6.6E-18	6.5E-18	3.7E-16	1.9E-05	2.7E-05	0.003
Ananij	Bruce	0	-3.0E-06	0.00	2.1E-08	6.7E-18	6.6E-18	3.1E-16	-1.1E-05	-1.4E-05	-1.4E-03
Inedral	Uriah	0	8.4E-06	0.00	3.1E-08	9.8E-18	9.6E-18	4.9E-16	2.5E-05	3.3E-05	0.003
Van	Van	0	2.8E-06	0.00	4.4E-08	1.4E-17	1.4E-17	7.0E-16	8.6E-06	1.1E-05	1.1E-03
Runit	Yvonne	0.18	0.015	3.79	1.4E-08	4.9E-18	4.8E-18	2.1E-16	4.6E-04	4.0E+00	398.9
Alembel	Vera	0	5.9E-06	0.00	5.3E-08	1.7E-17	1.6E-17	7.2E-16	2.6E-05	3.2E-05	0.003
Billae	Wilma	0	2.0E-05	0.00	5.1E-08	1.8E-17	1.8E-17	7.2E-16	6.2E-05	8.2E-05	0.008
Aomon	Sally	0	6.5E-06	0.00	3.1E-08	6.6E-18	6.5E-18	4.0E-16	2.7E-05	3.4E-05	0.003
Bijiri	Tilda	0	4.1E-06	0.00	3.2E-08	6.9E-18	6.8E-18	4.2E-16	1.7E-05	2.1E-05	0.002
Lojwa	Ursula	0	5.0E-06	0.00	5.0E-08	1.3E-17	1.3E-17	6.9E-16	2.0E-05	2.5E-05	0.002
Aej	Olive	0	5.9E-06	0.00	4.9E-08	1.5E-17	1.4E-17	6.4E-16	6.8E-05	7.4E-05	0.007
Elle	Nancy	0	9.4E-06	0.00	6.0E-08	2.0E-17	2.0E-17	7.6E-16	1.1E-04	1.2E-04	0.012
Lujor	Pearl	0	4.7E-06	0.00	4.0E-08	1.1E-17	1.1E-17	5.2E-16	3.9E-05	4.4E-05	0.004
Bokenelab	Mary	0	9.5E-06	0.00	6.5E-08	2.0E-17	2.0E-17	8.1E-16	1.2E-04	1.3E-04	0.013
Kidrinnenen	Lucy	0	2.8E-05	0.00	1.2E-07	7.2E-17	7.1E-17	1.4E-15	5.7E-04	6.0E-04	0.060
Mijikadrek	Kate	0	3.8E-05	0.00	9.2E-08	2.7E-17	2.7E-17	1.1E-15	6.3E-04	6.6E-04	0.066
Enjebi	Janet	0	2.8E-05	0.00	2.4E-07	1.4E-16	1.4E-16	2.9E-15	3.6E-04	3.9E-04	0.039
Boken–N	Irene	0	1.3E-04	0.00	3.2E-07	9.7E-17	9.6E-17	3.7E-15	8.1E-04	9.3E-04	0.093
Bokinwotme	Edna	0	3.7E-04	0.00	5.8E-07	8.3E-17	8.2E-17	6.9E-15	9.0E-04	1.3E-03	0.13
Louj	Daisy	0	1.4E-04	0.00	5.3E-07	6.2E-17	6.1E-17	6.0E-15	2.6E-04	4.0E-04	0.040
Bokoluo	Alice	0	3.5E-05	0.00	3.4E-07	4.7E-17	4.6E-17	4.3E-15	6.7E-05	1.0E-04	0.010
Bokombako	Belle	0	1.5E-04	0.00	3.0E-07	4.4E-17	4.3E-17	3.6E-15	2.5E-04	4.0E-04	0.040
Kirunu	Clara	0	2.2E-04	0.00	2.9E-07	3.9E-17	3.8E-17	3.5E-15	3.2E-04	5.4E-04	0.054
Biken	Leroy	0	1.1E-04	0.00	1.4E-07	3.5E-17	3.4E-17	2.5E-15	2.7E-04	3.8E-04	0.038
Boken–SSE	Irwin	0	5.2E-08	0.00	1.5E-08	2.9E-18	2.8E-18	1.4E-16	6.7E-08	1.3E-07	1.3E-05
Ikuren	Glenn	0	7.7E-08	0.00	1.4E-08	3.2E-18	3.2E-18	1.4E-16	1.5E-07	2.4E-07	2.4E-05
Kidrenen	Keith	0	-1.4E-07	0.00	1.0E-08	3.7E-18	3.7E-18	1.3E-16	-3.5E-06	-3.6E-06	-3.6E-04
Mut	Henry	0	1.5E-07	0.00	1.6E-08	3.0E-18	3.0E-18	1.5E-16	2.1E-07	3.7E-07	3.7E-05
Ribewon	James	0	8.1E-07	0.00	8.6E-09	2.4E-18	2.4E-18	1.0E-16	-4.4E-07	3.8E-07	3.8E-05

The scouring of the sediments and spill from the Runit Dome by the storm wave action and induced currents would result in small increases in dose (or smaller decreases than without dome failure) at almost all other islands in the atoll. The contents of the waste stored in the dome would circulate with the currents in the lagoon in a generally counterclockwise manner. The increases (or reduced decreases) are greatest to the north and west of Runit. This may be seen in the incremental doses presented in Table 23.

Table 23. Comparison of future baseline and storm incremental changes in radiation dose for 2090 conditions with assumed collapse of Runit Dome.

		2090 Future Conditions Dose after Collapse (mSv/yr)				2090 Future Conditions Dose after Collapse (mrem/yr)			
Island Name	U.S. Assigned Name	Baseline	Storm1	Storm2	Storm3	Baseline	Storm1	Storm2	Storm3
Enewetak	Fred	0.04	7.7E-06	1.4E-05	-4.8E-05	4.1	7.7E-04	1.4E-03	-0.005
Medren	Elmer	0.02	6.5E-06	1.4E-05	-2.9E-05	1.5	6.5E-04	0.0014	-0.003
Japtan	David	0.01	6.4E-06	2.7E-05	-3.8E-06	1.4	6.4E-04	0.0027	-3.8E-04
Ananij	Bruce	0.01	2.8E-06	-1.4E-05	-2.2E-05	1.4	2.8E-04	-0.0014	-0.002
Inedral	Uriah	0.01	-6.1E-06	3.3E-05	2.2E-05	1.4	-6.1E-04	0.0033	2.2E-03
Van	Van	0.01	-2.1E-05	1.1E-05	-3.4E-05	1.4	-0.0021	1.1E-03	-0.003
Runit	Yvonne	0.08	3.988	3.989	3.988	8.2	398.8	398.9	398.8
Alembel	Vera	0.08	1.4E-05	3.2E-05	7.6E-06	8.4	1.4E-03	3.2E-03	7.6E-04
Billae	Wilma	0.11	3.1E-05	8.2E-05	6.5E-05	11.2	3.1E-03	8.2E-03	6.5E-03
Aomon	Sally	0.11	1.7E-05	3.4E-05	1.8E-05	10.5	1.7E-03	0.0034	1.8E-03
Bijiri	Tilda	0.11	-1.8E-06	2.1E-05	-2.9E-06	10.7	-1.8E-04	0.0021	-2.9E-04
Lojwa	Ursula	0.09	-1.5E-06	2.5E-05	1.6E-06	9.3	-1.5E-04	2.5E-03	1.6E-04
Aej	Olive	0.14	3.5E-06	7.4E-05	-4.3E-06	13.6	0.0004	0.0074	-4.3E-04
Elle	Nancy	0.85	3.6E-05	1.2E-04	8.9E-05	85.2	3.6E-03	0.0119	0.009
Lujor	Pearl	0.16	1.5E-05	4.4E-05	6.3E-06	16.1	1.5E-03	0.0044	6.3E-04
Bokenelab	Mary	0.16	4.0E-05	1.3E-04	1.3E-04	15.5	4.0E-03	1.3E-02	0.013
Kidrinnenen	Lucy	0.16	8.5E-05	6.0E-04	2.1E-04	16.4	0.0085	0.060	0.021
Mijikadrek	Kate	0.11	8.3E-05	6.6E-04	1.6E-04	11.4	8.3E-03	0.066	0.016
Enjebi	Janet	0.26	1.6E-04	3.9E-04	1.2E-04	26.4	0.0161	0.039	0.012
Boken–N	Irene	0.35	-9.0E-04	9.3E-04	-1.6E-04	34.9	-0.09	0.093	-0.016
Bokinwotme	Edna	0.25	5.8E-04	1.3E-03	1.1E-03	25.5	0.058	0.126	0.114
Louj	Daisy	0.37	2.8E-04	4.0E-04	1.4E-04	37.5	0.028	0.0397	0.014
Bokoluo	Alice	1.09	2.0E-04	1.0E-04	-2.9E-05	108.8	0.020	0.0103	-0.003
Bokombako	Belle	1.94	3.2E-04	4.0E-04	2.6E-04	193.9	0.032	0.040	0.026
Kirunu	Clara	0.13	9.5E-04	5.4E-04	5.1E-04	13.3	0.095	0.054	0.051
Biken	Leroy	0.16	6.8E-04	3.8E-04	3.6E-04	15.8	0.068	0.038	0.036
Boken–SSE	Irwin	0.03	-2.0E-06	1.3E-07	-3.6E-06	3.2	-2.0E-04	1.3E-05	-3.6E-04
Ikuren	Glenn	0.03	-7.7E-06	2.4E-07	-1.3E-05	3.4	-7.7E-04	2.4E-05	-1.3E-03
Kidrenen	Keith	0.03	-2.4E-05	-3.6E-06	-3.9E-05	3.0	-0.0024	-3.6E-04	-0.004
Mut	Henry	0.03	-2.7E-07	3.7E-07	-1.5E-06	3.2	-2.7E-05	3.7E-05	-1.5E-04
Ribewon	James	0.03	-3.2E-05	3.8E-07	-2.0E-05	3.1	-0.003	3.8E-05	-0.002

Away from Runit Island itself, none of the increases is greater than 1 mrem; most to the north are less than 0.2 mrem and those to the south are less than 0.01 mrem. These incremental doses, aside from at Runit Island, are of no consequence; they simply indicate the transport directions of currents within the lagoon.

The five island groups are described to provide more detail on anticipated future conditions following a postulated, hypothetical failure of the Runit Dome. The incremental dose increases and decreases of Table 23 caused by the evaluated storms are shown in graphical form in Figure 26.

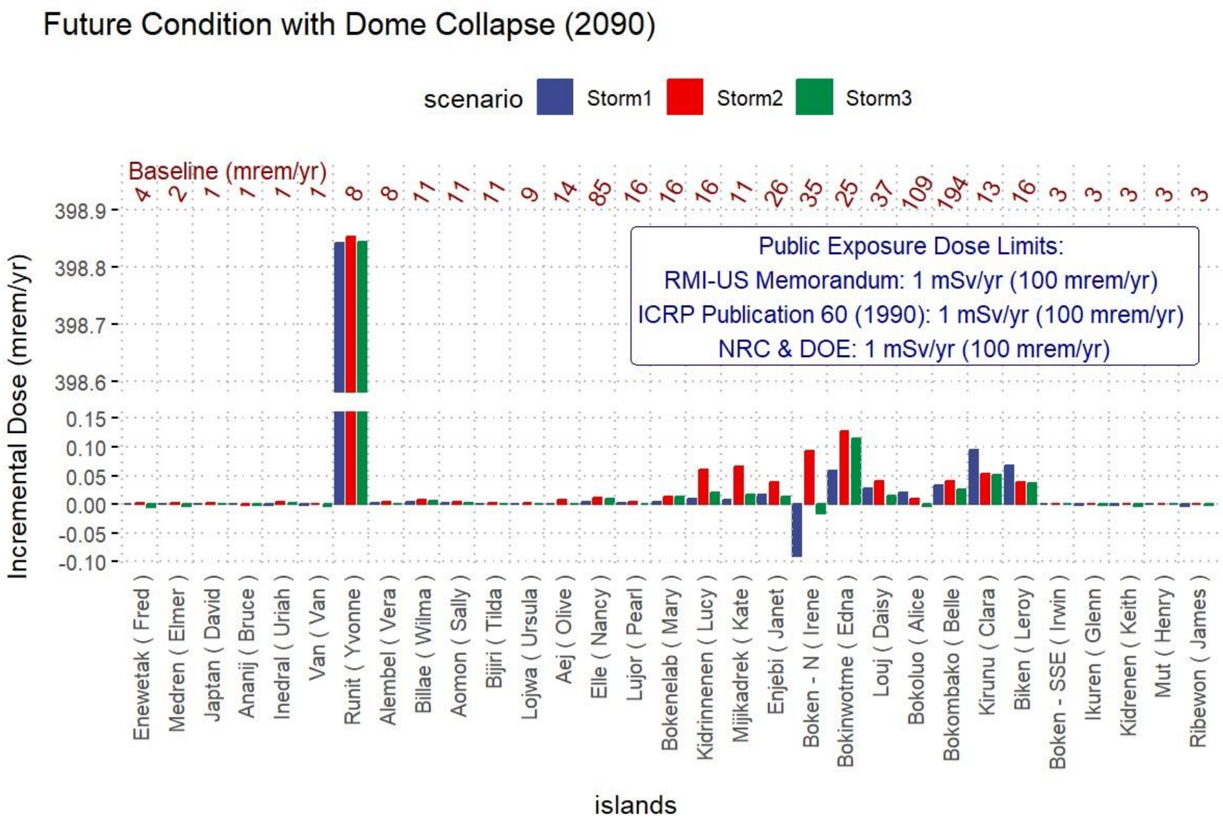

Figure 26. Incremental doses caused by the evaluated storms for each island under future conditions with the hypothetical Runit Dome failure.

5.5.1 Enewetak Island

Even with a failure of Runit Dome, future storms would have minimal impact on Enewetak or the nearby islands. Dose projections show storm-related increases or decreases in dose on the order of 0.1%.

5.5.2 Runit Island

The largest impact is, necessarily, on Runit Island itself. For this analysis, it has been assumed that the spill contaminates the northern end of the island but that a full-time resident spends an amount of time and consumes an amount of local crops proportional to the fraction of the island contaminated. As with the baseline analyses, the potential for encountering a Pu particle is neglected in this evaluation. Even so, the incremental increase in dose is quite large for a Runit Island resident. The dome contains a substantial inventory of fission products; the dominant radionuclides even in the future would be ^{137}Cs and ^{90}Sr. Because of the nature of the scenario, a large portion of the internal dose is assumed to come from consumption of coconuts and coconut products; this is unlikely in the immediate period after the dome failure because the local area would be devastated by the storm-driven spill. If the local foods pathway is neglected on Runit, the simple external dose contribution from the spread of contamination on the island soil and beach would still be on the order of 20 mrem (0.2 mSv). Without the terrestrial pathways, potential dose at Runit increases only slightly—direct exposure on the beach would dominate. On the other hand, should a resident live exclusively in the spill area, the doses could be about 12 times higher than that shown in Table 22.

5.5.3 Enjebi Island

Failure of the Runit Dome would result in transport of small amounts of contamination in a counterclockwise direction around the lagoon. Those islands nearest to the northwest of Runit would see the largest deposition of additional contaminated sediments near the shore and on the beaches; however, as shown by the example of Enjebi Island, the increases in dose would be small. The increases projected for Enjebi from this type of event are on the order of 0.1% over the projected future baseline. The main pathways with increases would be related to deposition on the beaches of Enjebi or similar islands. The radionuclides that would result in the increase are primarily the ^{90}Sr and ^{137}Cs within the dome waste materials.

5.5.4 Northwestern Islands

The islands in the northwest quadrant of the atoll, including Bokoluo and Bokombako, will show impacts of the same order of magnitude as Enjebi from sediments deposited from the Runit Dome on their beaches. However, because the future baseline for these more-contaminated islands is already higher than the others, the fractional increase in dose is small, on the order of less than 0.1%.

5.5.5 Southwestern Islands

The southwestern islands would have very low levels of deposition from a release from Runit Dome and are similar to Enewetak Island in magnitude and pathway structure of changes caused by storms.

5.6 Comparison of Postulated Doses to Natural Background Radiation

The baseline doses presented above for the southern islands under current conditions, and nearly all islands under future conditions assuming the Runit Dome is intact, are very small. All are significantly less than dose resulting from naturally occurring radionuclides in the atoll environment. Natural radionuclides include ^{40}K, ^{210}Pb, and ^{210}Po, in addition to radiation doses from cosmic and cosmogenic sources.

The average annual effective dose from natural background sources in most areas of the world is 2.4 mSv (UNSCEAR, 1988). The major contribution (> 60%) to this natural exposure is from Rn. Exposure to Rn is insignificant in the Marshall Islands because of the maritime conditions, low concentrations in soil of the parent Ra radionuclide, and because of the open, outdoor lifestyle of the Marshallese people (Robison et al., 1987). The external dose from terrestrial radiation and cosmogenic radionuclides is very low (0.02 mSv/year) so that most of the natural background dose is due to the external cosmic radiation and food ingestion pathways. The dose from cosmic radiation is ~0.22 mSv/year (Gudiksen et al., 1976) and naturally occurring ^{40}K contributes 0.18 mSv/year to the internal dose (Robison, et al. 1987). Naturally occurring ^{210}Po and ^{210}Pb in the “imports unavailable diet” used in this report would lead to an annual effective dose of ~7.3 mSv (730 mrem) (Noshkin et al., 1994). These radionuclides are present in seafood worldwide; they contribute such a large dose to the Marshallese because of the assumed large quantity of seafood consumption.

5.7 Biota Dose Estimation

Estimated doses to biota resulting from radionuclides in the lagoon waters and sediments are listed in Table 24 through Table 29 for benthic fish, crustaceans, macroalgae (seaweeds), mollusks/bivalves, pelagic fish, and corals, respectively. The seaweeds, corals, and pelagic fish are primarily exposed to lagoon water and the others are exposed to water and lagoon sediments.

Under existing conditions, the primary exposure to bottom-dwelling biota is via contaminated sediments. The primary radionuclide resulting in external exposure to the benthic organisms is ^{207}Bi, which in many instances provides over 90% of the external dose. ^{90}Sr, ^{137}Cs, and ^{241}Am each provide less than one-tenth the dose rate as the ^{207}Bi. ^{207}Bi is an interesting radionuclide in this situation; it is not a fission product and is rarely seen in the environment. The ^{207}Bi appears to be a result of the extreme nuclear conditions associated with the largest fusion bomb tests. ^{207}Bi has a half-life of about 33 years, roughly the same as ^{137}Cs or ^{90}Sr, and so will continue to decay in parallel to those other key radionuclides. The primary contribution to internal dose from sediments is associated with ^{239}Pu, with a lesser contribution of ^{241}Am. The lagoon water contributes only about 1% to the dose to the benthic organisms.

For the pelagic (nonbottom-dwelling) organisms, the doses result from lagoon water exposure only. As a result, the dose to pelagic fish and macroalgae (seaweeds) is only about 1% that of the benthic organisms. The primary radionuclide contributing dose is ^{239}Pu, with somewhat lower contributions from ^{241}Am and ^{90}Sr.

For the undisturbed future conditions, radiation doses are projected to be lower by factors of 2 to 5 depending on the location. Those islands that currently have minimal contamination in the surrounding shallow lagoon water have a larger component of dose from the actinides (Pu/Am) and a smaller fraction from the Bi, Sr, and Cs nuclides. As a result, the decrease in dose rate is smaller than for those islands in the northern atoll with higher fallout depositions.

The postulated storm events have an impact on the biota doses in ways similar to the impacts on humans. The wave action and induced currents tend to scour sediments away from many islands, and to deposit small amounts at others. The storms uniformly increase the content of suspended sediment and thus radionuclides in the lagoon water for a brief period, and so result in minor increases in dose to pelagic fish, macroalgae, and corals. The doses to benthic organisms are more complicated because they are dominated by sediment exposures, so in locations where the scouring of sediments is high, the biota doses decrease somewhat, which is indicated in the tables by a negative dose increment. Where sediments deposit, doses may increase. In either case, for the overall change from the baseline (either current 2015 conditions or future 2090 conditions) the changes in dose rate are generally on the order of 1%. However, for the islands in the northeastern quadrant, around Enjebi Island, the scouring in some storms under current conditions can result in substantial decreases of dose. For the same islands in future conditions, there may be smaller increases in dose.

In the event that the Runit Dome fails during a storm, the soils, sediments, and other radioactive materials in the dome could be distributed throughout the atoll. The circulation for the three storms evaluated tends to be counterclockwise within the lagoon, so biota dose can increase particularly for Runit itself and the islands to the north and west. The lagoon biota doses at Runit in the case of a dome collapse could increase by 30% over the difference without the dome failure. The islands seeing the largest impact from dome failure are Runit (about 30%), Bokinwotme (about 30% to 88%), and Kidrennenen, Biken, and Boken–N (up to 10%). The overall changes in dose rate are still small, at most about 0.2 mGy/d to totals of less than 0.5 microGray/day.

There are few legal standards for limitation of radiation dose to biota. The nuclear industry in general has adopted the position that measures implemented to protect individual humans from harmful effects of ionizing radiation are also protective of populations of fish, wildlife, and terrestrial plants. This approach has been adopted by the International Atomic Energy Agency (IAEA, 2014) and the United Nations Scientific Committee on the Effects of Atomic Radiation (UNSCEAR, 2011). DOE took the risk thresholds determined by IAEA and by others and refined them into the following biota dose rate limits as appropriate values for the protection of populations from effects of ionizing radiation (DOE 2019):

- The absorbed dose to aquatic animals should not exceed 10 mGy/d (400 µGy/hr, 1 rad/d)
- The absorbed dose to terrestrial plants should not exceed 10 mGy/d (400 µGy/hr, 1 rad/d)
- The absorbed dose to terrestrial animals should not exceed 1 mGy/d (40 µGy/hr, 0.1 rad/d).

The DOE standard methods are general screening values that are applied in a graded approach. They are derived from very conservative assumptions regarding the exposure to sources of ionizing radiation. They are used here as a conservative estimate of action levels.

It may be seen from the estimates of biota dose that the highest values associated with current conditions are nearly a factor of 500 lower than the action levels recommended by the United States and international agencies, with most islands being factors of 1,000 less. No radiation-related impacts to biota in the Enewetak lagoon are anticipated for current nor postulated future conditions.

Table 24. Estimated doses (uGy/day) to benthic fish resulting from radionuclides in the lagoon waters and sediments.

Island		2015				2090				2090 Runit Dome Collapse		
Island Name	U.S. Assigned Name	Baseline	Storm1	Storm 2	Storm 3	Baseline	Storm1	Storm 2	Storm 3	Storm1	Storm 2	Storm 3
Enewetak	Fred	0.45	-0.035	0.001	-0.070	0.33	0.001	0.001	-0.014	0.002	0.004	-0.013
Medren	Elmer	0.19	-0.002	0.005	-0.035	0.09	0.002	0.004	-0.008	0.002	0.004	-0.008
Japtan	David	0.19	-0.031	0.010	-0.031	0.09	0.001	0.004	-0.001	0.001	0.007	-0.001
Ananij	Bruce	0.18	-0.063	-0.021	-0.054	0.08	0.000	-0.005	-0.006	0.001	-0.003	-0.005
Inedral	Uriah	0.21	-0.074	0.003	-0.069	0.09	-0.002	0.005	0.002	-0.001	0.007	0.005
Van	Van	0.22	-0.079	-0.043	-0.075	0.09	-0.006	-0.0001	-0.009	-0.005	0.002	-0.008
Runit	Yvonne	0.66	-0.164	-0.023	-0.123	0.36	0.000	0.010	-0.001	0.112	0.134	0.118
Alembel	Vera	0.44	-0.086	-0.015	-0.055	0.31	0.000	0.002	-0.001	0.003	0.008	0.002
Billae	Wilma	0.44	-0.086	-0.015	-0.049	0.30	-0.001	0.0002	-0.001	0.008	0.019	0.015
Aomon	Sally	0.46	-0.094	-0.005	-0.094	0.32	-0.001	0.003	0.000	0.004	0.008	0.004
Bijiri	Tilda	0.45	-0.069	-0.017	-0.078	0.32	-0.0005	0.005	-0.001	-0.0005	0.005	-0.001
Lojwa	Ursula	0.43	-0.047	-0.036	-0.055	0.31	-0.002	0.000	-0.003	-0.0004	0.006	0.000
Aej	Olive	0.91	-0.262	-0.071	-0.333	0.39	-0.004	0.009	-0.008	0.001	0.020	-0.001
Elle	Nancy	1.12	-0.145	-0.100	-0.417	0.39	0.001	0.007	-0.004	0.009	0.032	0.023
Lujor	Pearl	0.63	-0.195	0.005	-0.188	0.35	0.002	0.003	-0.002	0.004	0.011	0.002
Bokenelab	Mary	1.37	-0.891	-0.297	-0.819	0.42	-0.003	0.001	-0.010	0.011	0.035	0.035
Kidrinnenen	Lucy	2.91	-1.567	-0.625	-1.543	0.63	-0.040	0.033	-0.039	0.023	0.165	0.057
Mijikadrek	Kate	3.89	-1.730	-0.461	-1.418	0.82	0.003	0.113	-0.004	0.023	0.180	0.043
Enjebi	Janet	5.51	-3.236	-0.904	-3.072	1.15	0.010	0.059	-0.031	0.043	0.104	0.033
Boken–N	Irene	6.14	-4.637	-2.003	-3.279	1.10	-0.296	-0.046	-0.167	-0.232	0.242	-0.041
Bokinwotme	Edna	2.79	-2.343	-0.621	-1.558	0.39	-0.005	-0.054	-0.064	0.131	0.289	0.261
Louj	Daisy	2.61	-0.803	0.092	-1.080	0.66	0.055	0.018	-0.008	0.063	0.089	0.032
Bokoluo	Alice	1.94	-0.615	-0.145	-0.543	0.53	0.033	-0.021	-0.033	0.040	0.021	-0.006
Bokombako	Belle	2.33	-0.744	-0.250	-0.514	0.57	0.057	0.028	0.005	0.070	0.085	0.054
Kirunu	Clara	2.23	-0.980	-0.412	-0.635	0.55	0.182	0.073	0.062	0.205	0.117	0.111
Biken	Leroy	0.38	-0.887	-0.377	-0.579	0.26	0.121	0.046	0.039	0.137	0.077	0.073
Boken–SSE	Irwin	0.22	0.009	0.00005	-0.001	0.16	-0.001	0.00003	-0.001	-0.001	0.00003	-0.001
Ikuren	Glenn	0.27	-0.024	0.001	-0.014	0.17	-0.002	-0.0004	-0.004	-0.002	0.00006	-0.004
Kidrenen	Keith	0.26	-0.022	0.002	-0.052	0.17	-0.007	-0.001	-0.011	-0.007	-0.001	-0.011
Mut	Henry	0.22	0.009	-0.000005	-0.001	0.16	-0.00009	0.00001	-0.0005	-0.00008	0.00010	-0.00044
Ribewon	James	0.28	-0.016	-0.002	-0.022	0.18	-0.009	-0.00036	-0.006	-0.009	-0.00013	-0.006

Table 25. Estimated doses (uGy/day) to crustaceans resulting from radionuclides in the lagoon waters and sediments.

Island		2015				2090				2090 Runit Dome Collapse		
Island Name	U.S. Assigned Name	Baseline	Storm1	Storm 2	Storm 3	Baseline	Storm1	Storm 2	Storm 3	Storm1	Storm 2	Storm 3
Enewetak	Fred	0.19	-0.033	0.001	-0.067	0.06	0.001	0.001	-0.013	0.002	0.004	-0.013
Medren	Elmer	0.13	-0.002	0.000	-0.033	0.04	0.002	0.004	-0.008	0.002	0.004	-0.008
Japtan	David	0.13	-0.029	0.009	-0.029	0.03	0.001	0.004	-0.001	0.001	0.006	-0.001
Ananij	Bruce	0.12	-0.059	-0.020	-0.051	0.03	0.000	-0.005	-0.006	0.001	-0.003	-0.005
Inedral	Uriah	0.16	-0.069	0.003	-0.065	0.03	-0.001	0.005	0.002	-0.001	0.007	0.004
Van	Van	0.16	-0.074	-0.040	-0.071	0.03	-0.006	-0.0001	-0.009	-0.004	0.002	-0.007
Runit	Yvonne	0.40	-0.156	-0.022	-0.117	0.10	0.000	0.009	-0.001	0.093	0.113	0.098
Alembel	Vera	0.19	-0.081	-0.014	-0.052	0.05	0.000	0.002	-0.001	0.003	0.007	0.002
Billae	Wilma	0.18	-0.077	-0.015	-0.047	0.04	-0.001	0.0002	-0.001	0.007	0.017	0.013
Aomon	Sally	0.21	-0.087	-0.004	-0.087	0.06	-0.001	0.003	0.000	0.004	0.007	0.004
Bijiri	Tilda	0.20	-0.065	-0.016	-0.073	0.06	-0.0005	0.005	-0.001	-0.0004	0.005	-0.001
Lojwa	Ursula	0.18	-0.044	-0.033	-0.051	0.05	-0.002	0.000	-0.002	-0.0004	0.005	0.000
Aej	Olive	0.63	-0.249	-0.068	-0.316	0.12	-0.004	0.009	-0.008	0.001	0.019	-0.001
Elle	Nancy	0.83	-0.134	-0.094	-0.393	0.13	0.001	0.007	-0.004	0.009	0.030	0.022
Lujor	Pearl	0.37	-0.184	0.005	-0.177	0.09	0.002	0.003	-0.002	0.004	0.011	0.001
Bokenelab	Mary	1.07	-0.843	-0.281	-0.775	0.15	-0.003	0.001	-0.010	0.010	0.033	0.033
Kidrinnenen	Lucy	2.54	-1.488	-0.593	-1.466	0.35	-0.038	0.031	-0.037	0.022	0.157	0.054
Mijikadrek	Kate	3.46	-1.640	-0.437	-1.344	0.53	0.002	0.108	-0.004	0.021	0.171	0.041
Enjebi	Janet	4.99	-3.074	-0.859	-2.918	0.84	0.009	0.056	-0.030	0.041	0.099	0.031
Boken–N	Irene	5.64	-4.386	-1.896	-3.108	0.85	-0.280	-0.043	-0.158	-0.220	0.230	-0.039
Bokinwotme	Edna	2.40	-2.155	-0.571	-1.436	0.17	-0.004	-0.050	-0.060	0.123	0.270	0.244
Louj	Daisy	2.20	-0.727	0.084	-0.986	0.43	0.051	0.018	-0.007	0.059	0.082	0.029
Bokoluo	Alice	1.52	-0.536	-0.124	-0.473	0.29	0.030	-0.019	-0.030	0.036	0.019	-0.005
Bokombako	Belle	1.87	-0.642	-0.214	-0.443	0.33	0.051	0.025	0.004	0.063	0.076	0.049
Kirunu	Clara	1.86	-0.892	-0.372	-0.573	0.32	0.169	0.068	0.057	0.189	0.108	0.103
Biken	Leroy	0.18	-0.805	-0.339	-0.520	0.05	0.110	0.043	0.035	0.125	0.071	0.067
Boken–SSE	Irwin	0.09	0.009	0.00003	0.000	0.03	0.000	0.00002	-0.001	0.000	0.00002	-0.001
Ikuren	Glenn	0.14	-0.023	0.001	-0.013	0.04	-0.002	-0.0004	-0.004	-0.002	0.00005	-0.003
Kidrenen	Keith	0.14	-0.020	0.001	-0.049	0.04	-0.006	-0.001	-0.010	-0.006	-0.001	-0.010
Mut	Henry	0.09	0.009	-0.000002	0.000	0.03	-0.00006	0.00001	-0.0003	-0.00006	0.00007	-0.00032
Ribewon	James	0.15	-0.015	-0.002	-0.021	0.04	-0.009	-0.00034	-0.005	-0.008	-0.00012	-0.005

Table 26. Estimated doses (uGy/day) to macroalgae (seaweed) resulting from radionuclides in the lagoon waters and sediments.

Island		2015				2090				2090 Runit Dome Collapse		
Island Name	U.S. Assigned Name	Baseline	Storm1	Storm 2	Storm 3	Baseline	Storm1	Storm 2	Storm 3	Storm1	Storm 2	Storm 3
Enewetak	Fred	0.47	2.0E-06	1.3E-06	6.8E-06	0.47	2.8E-07	9.5E-07	1.3E-06	3.3E-06	1.4E-06	2.3E-06
Medren	Elmer	0.10	1.0E-06	9.8E-08	8.8E-07	0.10	2.5E-08	1.4E-08	3.4E-07	9.1E-07	3.4E-07	9.4E-07
Japtan	David	0.10	2.1E-06	7.9E-08	4.7E-07	0.10	3.7E-08	1.3E-08	1.9E-07	1.6E-06	1.6E-07	1.3E-06
Ananij	Bruce	0.10	6.3E-07	2.7E-07	8.5E-07	0.10	5.4E-08	5.2E-08	4.5E-07	4.3E-07	1.9E-07	8.8E-07
Inedral	Uriah	0.10	1.5E-06	1.1E-07	1.1E-06	0.10	1.1E-07	1.7E-08	5.2E-07	7.2E-07	3.1E-07	9.0E-07
Van	Van	0.10	8.5E-07	3.2E-07	9.8E-07	0.10	1.1E-07	2.2E-07	4.6E-07	6.5E-07	4.5E-07	8.5E-07
Runit	Yvonne	0.49	1.6E-06	2.4E-07	1.4E-06	0.48	2.1E-07	3.0E-08	7.8E-07	9.7E-07	1.3E-07	1.1E-06
Alembel	Vera	0.49	5.4E-07	1.9E-07	1.2E-06	0.48	1.1E-07	1.8E-07	5.1E-07	1.7E-06	4.2E-07	1.2E-06
Billae	Wilma	0.49	1.2E-06	2.3E-07	2.0E-06	0.48	7.2E-08	1.0E-07	5.9E-07	2.4E-06	4.3E-07	1.1E-06
Aomon	Sally	0.49	7.6E-07	3.2E-07	1.5E-06	0.48	1.0E-07	1.9E-07	4.4E-07	1.4E-06	2.2E-07	7.5E-07
Bijiri	Tilda	0.49	6.6E-07	3.2E-07	1.7E-06	0.48	1.3E-07	1.8E-07	4.5E-07	1.4E-06	2.3E-07	7.4E-07
Lojwa	Ursula	0.49	5.4E-07	2.6E-07	1.3E-06	0.48	1.1E-07	2.1E-07	3.7E-07	1.2E-06	4.0E-07	6.7E-07
Aej	Olive	0.49	6.5E-07	6.4E-07	1.5E-06	0.48	1.1E-07	2.9E-07	4.8E-07	2.2E-06	3.6E-07	8.8E-07
Elle	Nancy	0.49	5.4E-07	6.5E-07	1.2E-06	0.48	8.2E-08	2.9E-07	4.2E-07	2.6E-06	4.1E-07	1.1E-06
Lujor	Pearl	0.49	9.1E-07	5.0E-07	1.9E-06	0.48	6.7E-08	2.3E-07	4.0E-07	1.5E-06	2.9E-07	8.0E-07
Bokenelab	Mary	0.49	6.1E-07	6.1E-07	1.7E-06	0.48	6.2E-08	3.3E-07	3.8E-07	2.2E-06	4.3E-07	8.9E-07
Kidrinnenen	Lucy	0.49	1.1E-06	6.8E-07	2.8E-06	0.48	1.1E-07	4.0E-07	4.3E-07	3.9E-06	7.3E-07	1.3E-06
Mijikadrek	Kate	0.49	1.4E-06	7.1E-07	4.9E-06	0.48	2.0E-07	4.5E-07	6.0E-07	3.4E-06	6.1E-07	1.2E-06
Enjebi	Janet	0.49	2.1E-06	1.4E-06	7.4E-06	0.48	3.0E-07	1.0E-06	1.3E-06	3.4E-06	1.4E-06	2.3E-06
Boken–N	Irene	0.38	3.1E-06	2.7E-06	5.2E-06	0.38	1.8E-06	6.5E-07	3.2E-06	6.1E-06	1.8E-06	5.6E-06
Bokinwotme	Edna	0.38	3.2E-06	4.0E-06	3.4E-06	0.38	5.8E-07	1.0E-06	9.0E-07	7.0E-05	3.5E-06	3.7E-06
Louj	Daisy	0.38	3.6E-06	1.5E-06	3.9E-06	0.38	5.8E-07	1.4E-06	2.6E-06	2.8E-05	2.9E-06	4.2E-06
Bokoluo	Alice	0.38	5.1E-06	1.1E-06	9.5E-06	0.38	1.2E-06	1.5E-06	3.9E-06	1.5E-05	2.4E-06	8.9E-06
Bokombako	Belle	0.38	7.1E-06	1.5E-06	8.1E-06	0.38	4.7E-07	9.8E-07	2.8E-06	2.7E-05	1.9E-06	5.9E-06
Kirunu	Clara	0.38	2.5E-06	1.5E-06	6.5E-06	0.38	2.6E-07	7.2E-07	4.5E-06	3.1E-05	1.8E-06	8.1E-06
Biken	Leroy	0.38	2.4E-06	1.3E-06	6.0E-06	0.37	2.5E-07	6.7E-07	4.2E-06	2.9E-05	1.7E-06	7.5E-06
Boken–SSE	Irwin	0.25	1.0E-07	1.1E-07	4.8E-07	0.24	1.0E-08	1.2E-08	6.0E-08	8.2E-08	5.6E-08	4.3E-07
Ikuren	Glenn	0.25	1.1E-07	1.1E-07	4.1E-07	0.24	7.5E-09	1.3E-08	3.5E-08	8.6E-08	5.7E-08	2.0E-07
Kidrenen	Keith	0.25	5.7E-08	4.8E-08	2.7E-07	0.24	2.2E-08	2.3E-08	5.8E-08	6.1E-08	7.3E-08	3.1E-07
Mut	Henry	0.25	1.1E-07	1.4E-07	6.1E-07	0.24	9.1E-09	1.3E-08	4.6E-08	1.0E-07	6.0E-08	2.6E-07
Ribewon	James	0.25	8.4E-08	5.5E-08	4.9E-07	0.24	2.3E-08	1.3E-08	7.7E-08	6.6E-08	5.0E-08	3.0E-07

Table 27. Estimated doses (uGy/day) to mollusks resulting from radionuclides in the lagoon waters and sediments.

Island		2015				2090				2090 Runit Dome Collapse		
Island Name	U.S. Assigned Name	Baseline	Storm1	Storm 2	Storm 3	Baseline	Storm1	Storm 2	Storm 3	Storm1	Storm 2	Storm 3
Enewetak	Fred	0.34	-0.037	0.001	-0.075	0.19	0.001	0.002	-0.015	0.002	0.004	-0.014
Medren	Elmer	0.23	-0.003	0.006	-0.039	0.12	0.002	0.004	-0.009	0.002	0.004	-0.009
Japtan	David	0.23	-0.033	0.011	-0.034	0.11	0.001	0.005	-0.002	0.002	0.007	-0.001
Ananij	Bruce	0.22	-0.069	-0.023	-0.059	0.11	0.000	-0.005	-0.007	0.001	-0.003	-0.005
Inedral	Uriah	0.26	-0.080	0.003	-0.075	0.11	-0.002	0.005	0.003	-0.001	0.008	0.005
Van	Van	0.27	-0.086	-0.047	-0.082	0.11	-0.007	-0.0001	-0.010	-0.005	0.003	-0.008
Runit	Yvonne	0.84	-0.177	-0.024	-0.132	0.47	0.000	0.011	-0.001	0.135	0.160	0.142
Alembel	Vera	0.61	-0.093	-0.016	-0.059	0.42	0.000	0.002	-0.001	0.003	0.008	0.002
Billae	Wilma	0.61	-0.097	-0.015	-0.052	0.41	-0.001	0.0002	-0.001	0.008	0.021	0.017
Aomon	Sally	0.63	-0.103	-0.005	-0.102	0.43	-0.001	0.003	0.000	0.004	0.009	0.005
Bijiri	Tilda	0.62	-0.076	-0.019	-0.086	0.43	-0.0005	0.005	-0.001	-0.0005	0.005	-0.001
Lojwa	Ursula	0.59	-0.051	-0.039	-0.059	0.42	-0.002	0.000	-0.003	-0.0005	0.006	0.000
Aej	Olive	1.11	-0.281	-0.077	-0.358	0.50	-0.005	0.010	-0.009	0.001	0.021	-0.001
Elle	Nancy	1.33	-0.159	-0.108	-0.450	0.51	0.001	0.007	-0.005	0.010	0.034	0.025
Lujor	Pearl	0.81	-0.211	0.005	-0.203	0.46	0.002	0.003	-0.003	0.004	0.012	0.002
Bokenelab	Mary	1.60	-0.959	-0.320	-0.882	0.54	-0.003	0.001	-0.011	0.012	0.037	0.038
Kidrinnenen	Lucy	3.25	-1.681	-0.671	-1.655	0.76	-0.043	0.035	-0.042	0.025	0.177	0.061
Mijikadrek	Kate	4.32	-1.859	-0.495	-1.523	0.96	0.003	0.122	-0.004	0.024	0.194	0.046
Enjebi	Janet	6.06	-3.472	-0.971	-3.297	1.31	0.010	0.064	-0.034	0.047	0.111	0.035
Boken - N	Irene	6.73	-5.000	-2.159	-3.529	1.26	-0.322	-0.050	-0.181	-0.252	0.263	-0.045
Bokinwotme	Edna	3.19	-2.597	-0.690	-1.724	0.49	-0.005	-0.060	-0.072	0.145	0.321	0.290
Louj	Daisy	3.02	-0.904	0.103	-1.208	0.80	0.062	0.020	-0.010	0.071	0.101	0.037
Bokoluo	Alice	2.34	-0.711	-0.170	-0.629	0.66	0.038	-0.025	-0.039	0.046	0.024	-0.007
Bokombako	Belle	2.79	-0.869	-0.293	-0.601	0.71	0.066	0.032	0.005	0.081	0.098	0.062
Kirunu	Clara	2.61	-1.101	-0.466	-0.718	0.68	0.207	0.082	0.070	0.233	0.133	0.127
Biken	Leroy	0.41	-0.991	-0.424	-0.651	0.25	0.134	0.051	0.043	0.152	0.086	0.082
Boken - SSE	Irwin	0.30	0.010	0.00007	-0.001	0.22	-0.001	0.00004	-0.001	-0.001	0.00004	-0.001
Ikuren	Glenn	0.36	-0.026	0.002	-0.015	0.23	-0.002	-0.0004	-0.004	-0.002	0.00008	-0.004
Kidrenen	Keith	0.35	-0.024	0.002	-0.056	0.23	-0.007	-0.001	-0.012	-0.007	-0.001	-0.012
Mut	Henry	0.30	0.009	-0.000007	-0.001	0.22	-0.00012	0.00001	-0.0006	-0.00011	0.00014	-0.00058
Ribewon	James	0.37	-0.017	-0.002	-0.024	0.23	-0.010	-0.00039	-0.006	-0.010	-0.00014	-0.006

Table 28. Estimated doses (uGy/day) to pelagic fish resulting from radionuclides in the lagoon waters and sediments.

Island		2015				2090				2090 Runit Dome Collapse		
Island Name	U.S. Assigned Name	Baseline	Storm1	Storm 2	Storm 3	Baseline	Storm1	Storm 2	Storm 3	Storm1	Storm 2	Storm 3
Enewetak	Fred	0.029	1.6E-07	6.5E-08	3.7E-07	0.025	1.5E-08	4.5E-08	8.0E-08	1.7E-07	6.9E-08	1.7E-07
Medren	Elmer	0.010	2.2E-07	8.4E-09	8.8E-08	0.007	3.3E-09	1.9E-09	3.5E-08	1.6E-07	6.8E-08	1.5E-07
Japtan	David	0.010	4.7E-07	6.9E-09	5.0E-08	0.007	3.8E-09	1.3E-09	1.6E-08	3.0E-07	1.8E-08	2.2E-07
Ananij	Bruce	0.010	1.2E-07	1.7E-08	7.5E-08	0.007	3.4E-09	3.2E-09	3.3E-08	4.1E-08	1.2E-08	9.6E-08
Inedral	Uriah	0.010	3.2E-07	7.5E-09	1.0E-07	0.007	6.4E-09	1.3E-09	4.0E-08	7.0E-08	1.8E-08	9.0E-08
Van	Van	0.010	1.6E-07	1.9E-08	8.5E-08	0.007	6.4E-09	1.2E-08	3.4E-08	5.6E-08	2.6E-08	7.9E-08
Runit	Yvonne	0.038	2.9E-07	1.4E-08	9.9E-08	0.033	1.1E-08	2.1E-09	5.0E-08	6.6E-08	8.2E-09	8.2E-08
Alembel	Vera	0.038	8.4E-08	1.4E-08	1.1E-07	0.033	6.9E-09	1.3E-08	3.6E-08	1.1E-07	3.0E-08	8.7E-08
Billae	Wilma	0.038	1.8E-07	1.5E-08	2.0E-07	0.033	4.6E-09	7.7E-09	4.2E-08	1.6E-07	2.9E-08	8.8E-08
Aomon	Sally	0.038	1.1E-07	2.4E-08	1.5E-07	0.033	6.6E-09	1.4E-08	3.1E-08	9.6E-08	1.7E-08	6.3E-08
Bijiri	Tilda	0.038	9.9E-08	2.4E-08	1.7E-07	0.033	8.0E-09	1.4E-08	3.2E-08	9.8E-08	1.8E-08	6.1E-08
Lojwa	Ursula	0.038	7.8E-08	1.9E-08	1.2E-07	0.033	6.4E-09	1.5E-08	2.6E-08	8.1E-08	2.8E-08	5.1E-08
Aej	Olive	0.038	9.5E-08	4.9E-08	1.4E-07	0.033	7.5E-09	2.2E-08	3.4E-08	1.5E-07	2.7E-08	7.2E-08
Elle	Nancy	0.038	7.3E-08	5.0E-08	1.2E-07	0.033	6.6E-09	2.3E-08	3.1E-08	1.8E-07	3.3E-08	9.2E-08
Lujor	Pearl	0.038	1.3E-07	3.7E-08	1.7E-07	0.033	4.2E-09	1.7E-08	2.8E-08	1.0E-07	2.2E-08	6.6E-08
Bokenelab	Mary	0.038	7.6E-08	4.8E-08	1.9E-07	0.033	5.4E-09	2.7E-08	2.9E-08	1.5E-07	3.5E-08	8.1E-08
Kidrinnenen	Lucy	0.038	1.3E-07	5.9E-08	3.0E-07	0.033	1.0E-08	3.3E-08	3.6E-08	3.1E-07	6.5E-08	1.2E-07
Mijikadrek	Kate	0.038	1.5E-07	6.0E-08	5.4E-07	0.033	1.9E-08	3.7E-08	4.8E-08	2.5E-07	5.0E-08	1.1E-07
Enjebi	Janet	0.038	2.3E-07	1.3E-07	8.2E-07	0.033	2.9E-08	9.1E-08	1.2E-07	2.7E-07	1.3E-07	2.2E-07
Boken–N	Irene	0.034	3.7E-07	3.2E-07	6.6E-07	0.026	2.2E-07	5.2E-08	3.5E-07	6.0E-07	1.7E-07	6.2E-07
Bokinwotme	Edna	0.034	3.4E-07	4.4E-07	3.6E-07	0.026	6.0E-08	9.3E-08	7.9E-08	6.8E-06	3.1E-07	3.6E-07
Louj	Daisy	0.034	4.0E-07	1.6E-07	4.2E-07	0.026	5.9E-08	1.4E-07	2.4E-07	2.8E-06	2.8E-07	4.0E-07
Bokoluo	Alice	0.034	4.0E-07	9.3E-08	7.5E-07	0.026	8.7E-08	1.2E-07	3.1E-07	1.2E-06	1.8E-07	7.2E-07
Bokombako	Belle	0.034	6.4E-07	1.3E-07	7.6E-07	0.026	4.3E-08	8.8E-08	2.5E-07	2.4E-06	1.6E-07	5.5E-07
Kirunu	Clara	0.034	2.5E-07	1.6E-07	7.0E-07	0.026	2.4E-08	6.9E-08	4.1E-07	3.0E-06	1.5E-07	7.7E-07
Biken	Leroy	0.031	1.2E-07	7.3E-08	3.1E-07	0.024	1.2E-08	3.4E-08	2.1E-07	1.4E-06	8.5E-08	3.8E-07
Boken–SSE	Irwin	0.021	1.6E-08	7.3E-09	4.4E-08	0.017	1.6E-09	1.0E-09	5.5E-09	9.1E-09	7.5E-09	8.1E-08
Ikuren	Glenn	0.021	1.7E-08	7.5E-09	4.0E-08	0.017	9.9E-10	1.2E-09	3.6E-09	9.4E-09	7.0E-09	4.2E-08
Kidrenen	Keith	0.021	5.1E-09	3.4E-09	2.5E-08	0.017	1.6E-09	1.6E-09	4.9E-09	5.1E-09	5.5E-09	5.0E-08
Mut	Henry	0.021	1.8E-08	9.9E-09	5.6E-08	0.017	9.6E-10	1.1E-09	5.0E-09	1.1E-08	7.9E-09	5.1E-08
Ribewon	James	0.021	9.3E-09	3.9E-09	4.3E-08	0.017	1.7E-09	9.5E-10	6.5E-09	5.6E-09	4.6E-09	4.9E-08

Table 29. Estimated doses (uGy/day) to corals resulting from radionuclides in the lagoon waters and sediments.

Island		2015				2090				2090 Runit Dome Collapse		
Island Name	U.S. Assigned Name	Baseline	Storm1	Storm 2	Storm 3	Baseline	Storm1	Storm 2	Storm 3	Storm1	Storm 2	Storm 3
Enewetak	Fred	0.066	2.5E-07	1.6E-07	8.4E-07	0.058	3.4E-08	1.1E-07	1.5E-07	4.0E-07	1.6E-07	2.7E-07
Medren	Elmer	0.018	1.2E-07	1.3E-08	1.1E-07	0.013	3.0E-09	1.7E-09	4.0E-08	1.1E-07	3.9E-08	1.1E-07
Japtan	David	0.018	2.5E-07	1.0E-08	5.7E-08	0.013	4.4E-09	1.6E-09	2.3E-08	1.9E-07	1.9E-08	1.5E-07
Ananij	Bruce	0.018	7.5E-08	3.4E-08	1.0E-07	0.013	6.6E-09	6.3E-09	5.4E-08	5.1E-08	2.3E-08	1.0E-07
Inedral	Uriah	0.018	1.8E-07	1.5E-08	1.4E-07	0.013	1.3E-08	2.1E-09	6.2E-08	8.5E-08	3.7E-08	1.1E-07
Van	Van	0.018	1.0E-07	4.0E-08	1.2E-07	0.013	1.3E-08	2.7E-08	5.5E-08	7.8E-08	5.4E-08	1.0E-07
Runit	Yvonne	0.067	1.9E-07	3.0E-08	1.7E-07	0.059	2.5E-08	3.7E-09	9.3E-08	1.2E-07	1.5E-08	1.3E-07
Alembel	Vera	0.067	6.7E-08	2.4E-08	1.5E-07	0.059	1.4E-08	2.2E-08	6.1E-08	2.0E-07	5.0E-08	1.4E-07
Billae	Wilma	0.067	1.5E-07	2.9E-08	2.4E-07	0.059	8.8E-09	1.2E-08	7.1E-08	2.9E-07	5.1E-08	1.3E-07
Aomon	Sally	0.067	9.4E-08	4.1E-08	1.9E-07	0.059	1.3E-08	2.2E-08	5.3E-08	1.6E-07	2.7E-08	9.0E-08
Bijiri	Tilda	0.067	8.1E-08	4.0E-08	2.1E-07	0.059	1.6E-08	2.2E-08	5.4E-08	1.7E-07	2.8E-08	8.9E-08
Lojwa	Ursula	0.067	6.7E-08	3.2E-08	1.6E-07	0.059	1.3E-08	2.5E-08	4.5E-08	1.4E-07	4.8E-08	8.1E-08
Aej	Olive	0.067	8.0E-08	8.1E-08	1.8E-07	0.059	1.3E-08	3.4E-08	5.8E-08	2.6E-07	4.3E-08	1.1E-07
Elle	Nancy	0.067	6.8E-08	8.1E-08	1.5E-07	0.059	1.0E-08	3.5E-08	5.0E-08	3.1E-07	5.0E-08	1.3E-07
Lujor	Pearl	0.067	1.1E-07	6.2E-08	2.4E-07	0.059	8.2E-09	2.7E-08	4.8E-08	1.8E-07	3.5E-08	9.6E-08
Bokenelab	Mary	0.067	7.6E-08	7.6E-08	2.1E-07	0.059	7.5E-09	4.0E-08	4.5E-08	2.7E-07	5.2E-08	1.1E-07
Kidrinnenen	Lucy	0.067	1.4E-07	8.5E-08	3.4E-07	0.059	1.3E-08	4.8E-08	5.1E-08	4.7E-07	8.7E-08	1.5E-07
Mijikadrek	Kate	0.067	1.7E-07	8.9E-08	6.0E-07	0.059	2.4E-08	5.4E-08	7.2E-08	4.1E-07	7.4E-08	1.4E-07
Enjebi	Janet	0.067	2.6E-07	1.7E-07	9.1E-07	0.059	3.6E-08	1.2E-07	1.6E-07	4.1E-07	1.7E-07	2.8E-07
Boken–N	Irene	0.061	3.8E-07	3.3E-07	6.3E-07	0.048	2.1E-07	7.8E-08	3.8E-07	7.3E-07	2.2E-07	6.6E-07
Bokinwotme	Edna	0.061	3.9E-07	4.8E-07	4.1E-07	0.048	6.9E-08	1.2E-07	1.1E-07	8.3E-06	4.2E-07	4.4E-07
Louj	Daisy	0.061	4.4E-07	1.8E-07	4.7E-07	0.048	6.9E-08	1.6E-07	3.1E-07	3.4E-06	3.5E-07	5.0E-07
Bokoluo	Alice	0.061	6.2E-07	1.4E-07	1.2E-06	0.048	1.5E-07	1.7E-07	4.6E-07	1.8E-06	2.9E-07	1.1E-06
Bokombako	Belle	0.061	8.7E-07	1.8E-07	9.8E-07	0.048	5.6E-08	1.2E-07	3.3E-07	3.2E-06	2.3E-07	7.0E-07
Kirunu	Clara	0.061	3.1E-07	1.8E-07	7.9E-07	0.048	3.2E-08	8.6E-08	5.4E-07	3.7E-06	2.2E-07	9.6E-07
Biken	Leroy	0.061	2.9E-07	1.7E-07	7.3E-07	0.047	3.0E-08	8.1E-08	5.1E-07	3.5E-06	2.1E-07	9.1E-07
Boken–SSE	Irwin	0.038	1.5E-08	1.4E-08	6.1E-08	0.031	1.3E-09	1.4E-09	7.2E-09	1.0E-08	6.7E-09	5.0E-08
Ikuren	Glenn	0.038	1.5E-08	1.4E-08	5.2E-08	0.031	9.4E-10	1.6E-09	4.2E-09	1.0E-08	6.8E-09	2.3E-08
Kidrenen	Keith	0.038	7.3E-09	6.3E-09	3.6E-08	0.031	2.7E-09	2.7E-09	7.0E-09	7.4E-09	8.8E-09	3.6E-08
Mut	Henry	0.038	1.6E-08	1.8E-08	7.7E-08	0.031	1.1E-09	1.6E-09	5.5E-09	1.2E-08	7.1E-09	3.0E-08
Ribewon	James	0.038	1.1E-08	7.3E-09	6.3E-08	0.031	2.7E-09	1.5E-09	9.2E-09	8.0E-09	6.0E-09	3.5E-08

6.0 Conclusions

Nuclear testing at Enewetak Atoll has left a legacy of residual radioactive contamination. In Phase 1, PNNL conducted an extensive review of the existing literature concerning radioactive contamination of the atoll and the waste disposal site on Runit Island (the Runit Dome). Despite the lack of detailed monitoring in recent years, sufficient information exists to estimate radionuclide inventories and concentrations in island soils, lagoon sediments, and the Runit Dome. In Phase 2, PNNL proceeded with assessing human and biota impacts.

As described in Section 2.0, PNNL estimated the concentrations of radionuclides in island soils, lagoon sediments, lagoon waters, and the Runit Dome from available data. PNNL postulated that severe storms could mobilize and transport the existing radionuclides in the lagoon sediments and those potentially released from the Runit Dome. The transported radionuclides could affect humans and biota.

PNNL performed the radiation dose assessment, supported by climate scenarios specifications, ocean hydrodynamics simulations, and lagoon sediment mobilization and transport. Future conditions are difficult to forecast, but current observational science indicates that the western Pacific Ocean will warm, with resulting sea-level rise and intensified storms. Because climate change impacts studies near the RMI are limited, PNNL performed regional climate simulations using the PGW approach to specify plausible, severe storm scenarios in the future climate. The climate scenarios created for this assessment showed that future warming of the western Pacific is indicated. However, as described in Section 3.0 and Appendix B, significant changes in climate parameters that strengthen storms are predicted for the western Pacific and less so for the central Pacific where Enewetak Atoll is located. Consequently, simulated future storms near the Enewetak Atoll were weaker than those in the current climate.

PNNL created hypothetical yet plausible severe storm scenarios using three historically severe storms that passed near the Enewetak Atoll. These storms were simulated in the current and the future climate using a high-resolution regional climate model and represent a range of plausible intensities and tracks (Section 4.0 and Appendix C and Appendix D). The predicted meteorological forcings in the current and future climates were used to drive the PNNL ocean model. The ocean model generated hydrodynamics of the ocean and the lagoon. The range of simulated hydrodynamic conditions similarly represent plausible conditions for radionuclide mobilization and transport.

The simulated hydrodynamics were used to drive a toxic contaminant fate and transport model. A postulated, hypothetical failure of the Runit Dome was also considered under future storm scenarios. The hypothetical dome failure resulted in additional radioactive material being deposited on the land and in the lagoon adjacent to Runit Island. Altogether, the nine radionuclide mobilization and transport scenarios are considered representative of potential redistribution of radionuclides and associated human and biota impacts. The estimated baseline (no-storm, natural weather) doses for the southern islands under current conditions, and nearly all islands under future conditions assuming the Runit Dome remains intact, are very small. All are significantly less than dose resulting from naturally occurring radionuclides in the atoll environment. The effects of storms on dose depended on storm intensity and track that can result in scouring, transport, and deposition that varied among islands. The incremental doses from storm condition varied from small increases to small decreases. Under the investigated severe storm scenarios, the incremental effects on dose were small because of generally small radionuclide concentrations and limited duration of the storms.

The effect of the postulated, hypothetical Runit Dome failure and subsequent release of radioactive material resulted in additional contributions to dose—again, small increases and decreases among islands other than Runit. For Runit Island, when a hypothetical failure of the Runit Dome was considered, the incremental increase in dose was quite large. Following Runit Dome failure, if the local food pathway was neglected, the incremental human dose was estimated to be about 20 mrem/year (0.2 mSv/year). Considering local food consumption would increase this dose approximately 20 times (about 400 mrem/year [4 mSv/year]). These doses for the Runit Island resulting from the hypothetical dome failure scenario were compared with other expected doses described by DOE (2017) and the National Research Council (1994):

- U.S. Environmental Protection Agency dose limit for public drinking water systems is 4 mrem/year (0.04 mSv/year)
- U.S. Nuclear Regulatory Commission (NRC) criteria for decommissioning for unrestricted use is 25 mrem/year (0.25 mSv/year)
- DOE and NRC dose limit for the public is 100 mrem/year (1 mSv/year)
- RMI-U.S. memorandum dose limit for the public is 100 mrem/year (1 mSv/year)
- for the U.S. population, the average natural background dose is approximately 310 mrem/year (0.31 mSv/year) and including man-made radiation results in a dose of 620 mrem/year (0.62 mSv/year)
- U.S. Department of Homeland Security emergency guideline for public relocation is 2,000 mrem/year (20 mSv/year).

The baseline, storm-related, and postulated, hypothetical Runit Dome failure radiation doses to lagoon biota are all very small fractions of the levels recommended to maintain environmental health and diversity. The impacts of radionuclides now and in the future on the natural environment are small.

The draft report was released publicly to solicit comments from interested stakeholders. Several notices for availability of the draft report and the opportunity for commenting on the draft report were published in U.S. and RMI periodicals. PNNL compiled all comments received on the report. The authors carefully considered each comment and prepared responses to them. Several comments provided useful insights and their recommendations were accepted by the authors. The draft report was updated to incorporate these recommendations.

7.0 References

AEC (United States Atomic Energy Commission). 1973. *Enewetak Radiological Survey*. NVO-140, Volume I. United States Atomic Energy Commission Nevada Operations Office, Las Vegas, Nevada.

Atkinson, M., Smith, S.V. and Stroup, E.D. 1981. Circulation in Enewetak Atoll lagoon1. Limnology and Oceanography 26(6), 1074-1083.

Bateman, H. 1910. The solution of a system of differential equations occurring in the theory of radioactive transformations. Proceedings of Cambridge Philosophical Society, 15, 423-427.

Beck, H. L., Bouville, A., Moroz, B. E., Simon, S. L. 2010. Fallout deposition in the Marshall Islands from Bikini and Enewetak nuclear weapons tests. Health physics, 99(2), 124.

Bindoff, N.L., P.A. Stott, K.M. AchutaRao, M.R. Allen, N. Gillett, D. Gutzler, K. Hansingo, G. Hegerl, Y. Hu, S. Jain, I.I. Mokhov, J. Overland, J. Perlwitz, R. Sebbari and X. Zhang, 2013: Detection and Attribution of Climate Change: from Global to Regional. In: *Climate Change 2013: The Physical Science Basis*. Contribution of Working Group I to the Fifth Assessment Report of the Intergovernmental Panel on Climate Change [Stocker, T.F., D. Qin, G.-K. Plattner, M. Tignor, S.K. Allen, J. Boschung, A. Nauels, Y. Xia, V. Bex and P.M. Midgley (eds.)]. Cambridge University Press, Cambridge, United Kingdom and New York, New York.

Bretherton, C.S. and S. Park. 2009. A new moist turbulence parameterization in the Community Atmosphere Model. J. Climate, 22, 3422–3448.

Buesseler, Ken O., Matthew A. Charette, Steven M. Pike, Paul B. Henderson, Lauren E. Kipp. 2018. “Lingering radioactivity at the Bikini and Enewetak Atolls.” *Science of The Total Environment* 621(2018): 1185-1198. https://doi.org/10.1016/j.scitotenv.2017.10.109.

Carvalho, D., A. Rocha, M. Gomez-Gesteira, and C. Santos. 2012. A sensitivity study of the WRF model in wind simulation for an area of high wind energy. Environ. Model Softw., 33, 7, 23 – 34.

Chan, J.C.L. and K.S. Liu. 2004. Global warming and western North Pacific typhoon activity from an observational perspective. *Journal of Climate*, 17, 4590–4602.

Chen, J., Z. Wang, C.-Y. Tam, N.-C. Lau, D.-S.D. Lau, and H.-Y. Mok. 2020. Impacts of climate change on tropical cyclones and induced storm surges in the Pearl River Delta region using pseudo-global-warming method. Scientific Report, 10:1965, https://doi.org/10.1038/s41598-020-58824-8.

Chand, S.S., K.J.E. Walsh, S.J. Camargo, J. Kossin, K.J. Tory, M.F. Wehner, J.C.L. Chan, P.J. Klotzbach, A.J. Dowdy, S.S. Bell, H.A. Ramsay, and H. Murakami. 2022. Declining tropical cyclone frequency under global warming. Nature Climate Change, 12, 655 – 661. https:doi.org/10.1038/s41558-022-01388-4.

Chapra, S.C. 1996. Surface Water Quality Modeling. First Edition. McGraw–Hill, New York. 784pp.

Chen, Changsheng S., Hedong D. Liu, and Robert C. Beardsley. 2003. “An unstructured grid, finite-volume, three-dimensional, primitive equations ocean model: Application to coastal ocean and estuaries.” *Journal of Atmospheric and Oceanic Technology* 20(1): 159-186. https://doi.org/10.1175/1520-0426(2003)020<0159:AUGFVT>2.0.CO;2.

Chen, C., C. Robert, and G. Cowles. An unstructured grid, finite-volume coastal ocean model (FVCOM) system. Oceanography 2006, 19, 78–89.

Chen, Changsheng, Robert C. Beardsley, Geoffrey Cowles, Jianhua Qi, Zhiqang Lai, Guoping Gao, David Stuebe, Hedong Liu, Qichun Xu, Pengfei Xue, Jianzhong Ge, Song Hu, Rubao Ji, Rucheng Tian, Haosheng Huang, Lunyu Wu, Huichan Lin, Yunfang Sun, and Liuzhi Zhao. 2013. *An Unstructured Grid, Finite Volume Community Ocean Model–FVCOM. FVCOM User Manual, Version 3.1.6, Fourth Edition*. Department of Fisheries Oceanography, School for Marine Science and Technology, University of Massachusetts-Dartmouth, New Bedford, Massachusetts and Department of Physical Oceanography, Woods Hole Oceanographic Institution, Woods Hole, Massachusetts. 416 p.

Chen, X., O.M. Pauluis, L.R. Leung, and F. Zhang. 2018c. Multiscale atmospheric overturning of the Indian summer monsoon as seen through isentropic analysis. Journal of the Atmospheric Sciences, 75(9), 3011–3030. https://doi.org/10.1175/JAS-D-18-0068.1.

Chen, X., O.M. Pauluis, and F. Zhang. 2018a. Regional simulation of Indian summer monsoon intraseasonal oscillations at gray-zone resolution. Atmospheric Chemistry and Physics, 18(2), 1003–1022. https://doi.org/10.5194/acp-18-1003-2018.

Chen, X., O.M. Pauluis, and F. Zhang. 2018b. Atmospheric overturning across multiple scales of an MJO event during the CINDY/DYNAMO campaign. Journal of the Atmospheric Sciences, 75, 381–399. https://doi.org/10.1175/JAS-D-17-0060.1

Chen, Y., Z. Duan, J. Yang, Y. Deng, T. Wu, and J. Ou. 2021. Typhoons of western North Pacific basin under warming climate and implications for future wind hazard of East Asia. Journal of Wind Engineering & Industrial Aerodynamics, 208, 104415.

Chung, E.-S., A. Timmermann, B.J. Soden, K.-J. Ha, L. Shi, and V.O. John. 2019. Reconciling opposing Walker circulation trends in observations and model projections. Nature Climate Change, 9, 405 – 412.

Collins, M., S.-I. An, W. Cai, A. Ganachaud, E. Guilyardi, F.-F. Jin, M. Jochum, M. Lengaigne, S. Power, A. Timmermann, G. Vecchi, and A. Wittenberg. 2010. The impact of global warming on the tropical Pacific Ocean and El Nino. Nature Geoscience, v. 3, p. 391–397.

Davisson, M.L., T.F. Hamilton, and A.F.B. Tompson. 2012. Radioactive waste buried beneath Runit Dome on Enewetak Atoll, Marshall Islands. Int. J. Environment and Pollution, Vol. 49, Nos. 3/4, pp.161–178.

DNA (Defense Nuclear Agency). 1975. *Environmental Impact Statement. Cleanup, Rehabilitation, Resettlement of Enewetak Atoll–Marshall Islands*. Defense Nuclear Agency, Washington D.C.

DOE (U.S. Department of Energy). 1982. *Enewetak Radiological Support Project; Final Report*. NVO-213. United States Department of Energy, Nevada Operations Office, Las Vegas, Nevada.

DOE (U.S. Department of Energy). 1987a. The Natural History of Enewetak Atoll. Volume I–The Ecosystem: Environments, Biotas, and Processes. United States Department of Energy Office of Energy Research, Office Health and Environmental Research, Ecological Research Division. DOE/EV/00703-T1-Vol. 1 (DE87006110).

DOE (United States Department of Energy). 1987b. The Natural History of Enewetak Atoll. Volume II–The Ecosystem: Biogeography and Systematics. United States Department of Energy Office of Energy Research, Office Health and Environmental Research, Ecological Research Division. DOE/EV/00703-T1-Vol. 2 (DE87006111).

DOE (United States Department of Energy). 2011. Radiation Protection of the Public and the Environment, DOE Order 458.1, Washington, DC.

DOE (United States Department of Energy). 2015. United States Nuclear Tests – July 1945 through September 1992, DOE/NV—209-REV 16, Washington, D.C.

DOE (United States Department of Energy). 2017. The DOE Ionizing Radiation Dose Ranges Chart. Office of Environment, Health, Safety and Security. AU-22 001-2018. Available at https://www.energy.gov/sites/prod/files/2018/01/f46/doe-ionizing-radiation-dose-ranges-jan-2018.pdf.

DOE (United States Department of Energy). 2019. A Graded Approach For Evaluating Radiation Doses To Aquatic And Terrestrial Biota, DOE-STD-1153-2019, Washington, DC.

Dunkerton, T., M. Montgomery, and Z. Wang. 2009. Tropical cyclogenesis in a tropical wave critical layer: easterly waves. *Atmospheric Chemistry and Physics*, 9, 5587–5646.

EG&G 1981-Tipton, W. J., Meibaum, R. A. 1981, *An Aerial Radiological and Photographic Survey of the Eleven Atolls and Two Islands Within the Northern Marshall Islands*, EG&G Measurements Group. EG&G-1183-1758, UC41.

Egbert, G.D.E.; Svetlana, Y. Efficient Inverse Modeling of Barotropic Ocean Tides. J. Atmos. Ocean. Technol. 2002, 19, 183–204.

Emanuel, K. 1987. The dependence of hurricane intensity on climate. *Nature*, 326, 483–485.

Emanuel, K. 2001. Contributions of tropical cyclones to meridional heat transport by the Oceans. *Journal of Geophysical Research*, 106, 14771–14782.

Emanuel, K. 2005. Increasing destructiveness of tropical cyclones over the past 30 years. *Nature*, 436, 686–688.

Emery, K.O. 1954. Geology of Bikini and nearby atolls. U.S. Geol. Surv. Prof. Pap. 260:1-265

England, M., S. McGregor, P. Spence, G.A. Meehl, A. Timmermann, W. Cai, A.S. Gupta, M.J. McPhaden, A, Purich, and A. Santoso. 2014. Recent intensification of wind-driven circulation in the Pacific and the ongoing warming hiatus. Nature Climate Change, 4, 222 – 227.

EPA. 1997. Establishment of Cleanup Levels for CERCLA Sites with Radioactive Contamination. EPA Memorandum OSWER No. 9200.4-18. United States Environmental Protection Agency, Washington, DC.

EPA. 1999. Cancer Risk Coefficients for Environmental Exposure to Radionuclides. Federal Guidance Report No. 13, EPA 402-R-99-001. United States Environmental Protection Agency, Washington, DC.

Froehlich, M. B., Tims, S. G., Fallon, S. J., Wallner, A., & Fifield, L. K. 2017. Nuclear weapons produced 236U, 239Pu and 240Pu archived in a Porites Lutea coral from Enewetak Atoll. Journal of environmental radioactivity, 178, 349-353.

Gentry, M. and G.M. Lackmann. 2010. Sensitivity of simulated tropical cyclone structure and intensity to horizontal resolution. Monthly Weather Review, 138, 688 – 704.

Gudiksen, P.H., T.R. Crites, and W L. Robison. 1976. External dose estimated for future Bikini Atoll inhabitants, UCRL- 51879 Rev. 1. Lawrence Livermore National Laboratory, Livermore CA.

Gutowski, W.J., P.A. Ullrich, A. Hall, L.R. Leung, T. O'Brien, C. Patricola, R.W. Arritt, M.S. Bukovsky, K.V. Calvin, Z. Feng, A.D. Jones, G.J. Kooperman, E. Monier, M.S. Pritchard, S.C. Pryor, Y. Qian, A.M. Rhoades, A.F. Roberts, K. Sakaguchi, N. Urban, and C. Zarzycki. 2020. The Ongoing Need for High-Resolution Regional Climate Models: Process Understanding and

Stakeholder Information. Bulletin of American Meteorological Society, 101(5), E664-E683, doi:10.1175/BAMS-D-19-0113.1.

Hamilton, T., Jernströem, J., Martinelli, R., Kehl, S., Eriksson, M., Williams, R., Betti, M. 2009. Frequency distribution, isotopic composition and physical characterization of plutonium-bearing particles from the Fig-Quince zone on Runit Island, Enewetak Atoll. Journal of radioanalytical and nuclear chemistry, 282(3), 1019-1026.

Hamilton, T.F. 2013. *A Visual Description of the Concrete Exterior of the Cactus Crater Containment Structure*. Center for Accelerator Mass Spectrometry, Lawrence Livermore National Laboratory, Livermore, California. LLNL-TR-648143, October 2013.

Hamilton, T.F. 2021. Marshall Islands Dose Assessment and Radioecology Program: Report on the (i) 2018 Visual Study of Exterior Concrete of the Cactus Crater Containment Structure (ii) Periodic Monitoring of Groundwater on Runit Island And (iii) Initial Health Risk Assessment from Contaminants in the Cactus Crater Containment Structure. Lawrence Livermore National Laboratory, Livermore, California. LLNL-TR-827628, December 2021.

Hanson, W.C. 1980. *Transuranic elements in the environment: a summary of environmental research on transuranium radionuclides funded by the US Department of Energy through calendar year 1979*. Prepared for U.S. Department of Energy. DOE/TIC-22800

Held, I. and M. Zhao. 2011. The response of tropical cyclone statistics to an increase in CO2 with fixed sea surface temperature. Journal of Climate, 24, 5353 – 5364.

Hersbach, H., Bell, B., Berrisford, P., Hirahara, S., Horányi, A., Muñoz-Sabater, J., Nicolas, J., Peubey, C., Radu, R., Schepers, D., Simmons, A., Soci, C., Abdalla, S., Abellan, X., Balsamo, G., Bechtold, P., Biavati, G., Bidlot, J., Bonavita, M., Chiara, G., Dahlgren, P., Dee, D., Diamantakis, M., Dragani, R., Flemming, J., Forbes, R., Fuentes, M., Geer, A., Haimberger, L., Healy, S., Hogan, R.J., Hólm, E., Janisková, M., Keeley, S., Laloyaux, P., Lopez, P., Lupu, C., Radnoti, G., Rosnay, P., Rozum, I., Vamborg, F., Villaume, S. and Thépaut, J.N. 2020. The ERA5 global reanalysis. *Quarterly Journal of the Royal Meteorological Society* 146(730), 1999-2049.

Higashi, H., Morino, Y., Furuichi, N., and Ohara, T. 2015. *Ocean dynamic processes causing spatially heterogeneous distribution of sedimentary caesium-137 massively released from the Fukushima Daiichi Nuclear Power Plant*. *Biogeosciences*, 12, 7107–7128.Holland, G.J. 1997. The maximum potential intensity of tropical cyclones. *Journal of Atmospheric Sciences*, 54, 2519–2541.

Hong, S.-Y. and J.-O.J. Lim. 2006. The WRF Single-Moment 6-Class Microphysics Scheme (WSM6), *J. Korean Meteorol. Soc.*, 42(2), 129– 151.

Hong, S.-Y., Y. Noh, and J. Dudhia. 2006. A new vertical diffusion package with an explicit treatment of entrainment processes. *Mon. Wea. Rev.*, 134, 2318–2341.

Hill, K.A. and G.M. Lackmann. 2011. The impact of future climate change on TC intensity and structure: A downscaling approach. Journal of Climate, 24, 4644 – 4661.

Hu, Y., H. Huang, and C. Zhou. 2018. Widening and weakening of the Hadley circulations under global warming. Sci. Bull., 63, 640 – 644.

Iacono, M.J., J.S. Delamere, E.J. Mlawer, M.W. Shephard, S.A. Clough, and W.D. Collins. 2008. Radiative forcing by long-lived greenhouse gases: Calculations with the AER radiative transfer models. *Journal of Geophysical Research*, 113 (D13103). https://doi.org/10.1029/2008JD009944.

IAEA 2010. Handbook of Parameter Values for the Prediction of Radionuclide Transfer in Terrestrial and Freshwater Environments. TRS-472. International Atomic Energy Agency, Vienna, Austria.

IAEA 2014. Handbook of Parameter Values for the Prediction of Radionuclide Transfer to Wildlife. TRS-479. International Atomic Energy Agency, Vienna, Austria.

IAEA. 2014. Radiation Protection and Safety of Radiation Sources: International Basic Safety Standards General Safety Requirements. General Safety Requirements Part 3, No. GSR Part 3. Vienna, Austria, 2014.

IAEA 2021. Soil-Plant Transfer of Radionuclides in Non-temperate Environments. TECDOC-1979. International Atomic Energy Agency, Vienna, Austria.

Jisan, M.A., S. Bao, L.J. Pietrafesa, D. Shen, P.T. Gayes, and J. Hallstrom. 2018. Hurricane Mathew (2016) and its impact under global warming scenarios. Modeling of Earth Systems Environment, 4, 97 -109.

Khangaonkar, T., Long, W., Xu, W., 2017. Assessment of circulation and inter-basin transport in the Salish Sea including Johnstone Strait and Discovery Islands pathways. Ocean Modelling, 109, pp.11-32.

Khangaonkar, Tarang, Adi Nugraha, Wenwei Xu, Wen Long, Laura Bianucci, Anise Ahmed, Teizeen Mohamedali, Greg Pelletier. 2018. “Analysis of hypoxia and sensitivity to nutrient pollution in Salish Sea.” *Journal of Geophysical Research: Oceans* 123: 4735– 4761. https://doi.org/10.1029/2017JC013650.

Khangaonkar, T., Nugraha, A., Xu, W., Balaguru, K., 2019. Salish Sea response to global climate change, sea level rise, and future nutrient loads. Journal of Geophysical Research: Oceans, 124(6), pp.3876-3904

Kim, T., Khangaonkar, T. 2012. An Offline Unstructured Biogeochemical Model (UBM) for Complex Estuarine and Coastal Environments. Environmental Modelling & Software, 31: 47-63. doi: 10.1016/j.envsoft.2011.11.010

Kimura, F. and A. Kitoh. 2007. A downscaling by pseudo global warming method. The Final Report ICCAP 4346, Research Institute for Humanity and Nature (RIHN), Kyoto, Japan.

Kopp, R.E., R.M. Horton, C.M. Little, J.X. Mitrovica, M. Oppenheimer, D.J. Rasmussen, B.H. Strauss, and C. Tebaldi. 2014. Probabilistic 21st and 22nd century sea-level projections at a global network of tide-gauge sites. Earth’s Future, v. 2, p.1–24.

Knapp, K.R., M.C. Kruk, D.H. Levinson, H.J. Diamond, and C.J. Neumann. 2010. The International Best Track Archive for Climate Stewardship (IBTrACS), *Bulletin of the American Meteorological Society*, 91, 363–376.

Knutson, T.R., J.J. Sirutis, M. Zhao, R.E. Tuleya, M. Bender, G.A. Vecchi, G. Villarini, and D. Chavas. 2015. Global projections of intense tropical cyclone activity for the late twenty-first century from dynamical downscaling of CMIP5/RCP4.5 scenarios. Journal of Climate, 28, 7203 – 7224.

Knutson, T.R., J.L. McBride, J. Chan, K. Emanuel, G. Holland, C. Landsea, I. Held, J.P. Kossin, and S.M. Srivastava. 2010. Tropical cyclones and climate change. Nature Geoscience, v. 3, p. 157–163.

Knutson, T.R., S.J. Camargo, J.C.L. Chan, K. Emanuel, C.-H. Ho, J. Kossin, M. Mohapatra, M. Satoh, M. Sugi, K. Walsh, and L. Wu. 2019a. Tropical Cyclones and Climate Change

Assessment: Part I. Detection and attribution. *Bulletin of the American Meteorological Society*, https://doi.org//10.1175/BAMS-D-18-0189.1.

Knutson, T.R., S.J. Camargo, J.C.L. Chan, K. Emanuel, C.-H. Ho, J. Kossin, M. Mohapatra, M. Satoh, M. Sugi, K. Walsh, and L. Wu. 2019b. Tropical Cyclones and Climate Change Assessment: Part II. Projected response to anthropogenic warming. *Bulletin of the American Meteorological Society*, https://doi.org/10.1175/BAMS-D-18-0194.1.

Knutson, T.R. and R.E. Tuleya. 2004. Impact of CO_2-induced warming on simulated hurricane intensity and precipitation: Sensitivity to the choice of climate model and convective parameterization. *Journal of Climate*, 17. 3477–3495.

Lanzanate, J.R. 2019. Uncertainties in tropical-cyclone translation speed. Nature, 570, E6-E15, https://doi.org/10.1038/s41586-019-1223-2.

Lee, T.-C., T.R. Knutson, T. Nakaegawa, M. Ying, and E.J. Cha. 2020. Third assessment on impacts of climate change on tropical cyclones in the Typhoon Committee Region–Part I: Observed changes, detection and attribution. *Tropical Cyclone Research and Review*, 9, 1–22.

Li, C.Y., W. Zhou, and T.C. Lee. 2015. Climatological characteristic and observed trend of tropical cyclone-induced rainfall and their influences on long term rainfall variations in Hong Kong*. Monthly Weather Review*, 143, 2192–2206.

Lim, K.-S.S. and S.-Y. Hong. 2010. Development of an effective double-moment cloud microphysics scheme with prognostic cloud condensation nuclei (CCN) for weather and climate models. *Monthly Weather Review*, 138(29), 1587– 1612. https://doi.org/10.1175/2009mwr2968.1

Maragos, J.E. 2011. Enewetak Atoll, Marshall Islands. In *Encyclopedia of Modern Coral Reefs: Structure, Form and Process*, edited by David Hopley, Springer

Marsh, K.V., K. Wong, G. Holladay, V.E. Noshkin, and R. Buddemeier. 1978. Radiological and chemical studies of the ground water at Enewetak Atoll. 1. Sampling, field measurements, and analytical methods. Lawrence Livermore National Laboratory, Report UCRL-51913.

McMurtry, G.M., R.C. Schneider, P.L. Colin, R.W. Buddemeier, and T.H. Suchanek. 1986. Vertical distribution of fallout radionuclides in Enewetak lagoon sediments: Effects of burial and bioturbation on the radionuclide inventory. Bulletin of Marine Science, 38(1), 35-55.

Metzger E.J., R.W. Helber, P.J. Hogan, P.G.Posey, P.G. Thoppil, T.L. Townsend, A.J. Wallcraft, O.M. Smedstad, and D.S. Franklin, 2017. Global Ocean Forecast System 3.1 Validation Testing. NRL Report NRL/MR/7320--17-9722

Merrifield, M.A. 2011. A shift in western tropical Pacific sea level trends during the 1990s. Journal of Climate, v. 24, p. 4126–4138.

Moon, I.-J., S.-H. Kim, J.C.L. Chan. 2019. Climate change and tropical cyclone trend. *Nature*, 570, E3–E5, https://doi.org/10.1038/s41586-019-1222-3.

Mori, M., M. Kimoto, M. Ishii, S. Yokoi, T. Mochizuki, Y. Chikamoto, M. Watanabe, T. Nozawa, H. Tatebe, T.-T. Sakamoto, Y. Komuro, Y. Imada, and H. Koyama. 2013 Hindcast prediction and near future projection of tropical cyclone activity over the western North Pacific using CMIP5 near-term experiments with MIROC. *Journal of the Meteorological Society of Japan*, 91, 431–452.

Mukhopadhyay, P., S. Taraphdar, and B.N. Goswami. 2011. Influence of moist processes on track and intensity forecast of cyclones over the north Indian Ocean. Journal of Geophysical Research Atmosphere, 116(D05116). https://doi.org/10.1029/2010JD014700.

Murakami, H., T.L. Delworth, W.F. Cooke, M. Zhao, and P.-C. Hsu. 2020. Detected climatic change in global distribution of tropical cyclones. *Proceedings of the National Academy of Science*, USA, 117, 10706–10714.

Nakanishi, M. and H. Niino. 2004. An improved Mellor-Yamada level-3 model with condensation physics: Its design and verification. *Boundary-Layer Meteorology*, 112, 1-31. https://doi.org/10.1023/b:boun.0000020164.04146.98

NAS (National Academy of Sciences). 1982. Evaluation of Enewetak radioactivity containment. National Research Council, PB83-204263.

National Nuclear Decay Data Center (NNDC). 2007. NuDat 2.3 database. Brookhaven National Laboratory, NY. https://www.nndc.bnl.gov/nudat/

National Research Council. 1994. Radiological Assessments for the Resettlement of Rongelap in the Republic of the Marshall Islands. Washington, DC: The National Academies Press. https://doi.org/10.17226/2352.

Neale, R.B. and Coauthors. 2012. Description of the NCAR Community Atmosphere Model (CAM 5.0). NCAR Tech. Note TN-486, 274 pp. Available at https://www2.cesm.ucar.edu/models/cesm1.0/cam/docs/description/cam5_desc.pdf.

Nicholls, R.J. and A. Cazenave. 2010. Sea-level rise and its impact on coastal zones. Science, v. 328, p. 1517–1520.

Ninomiya, J., N. Mori, T. Takemi, and O. Arakawa. 2017. SST ensemble experiment-based impact assessment of climate change on storm surge caused by pseudo-global warming: Case study of typhoon Vera in 1959. Coastal Engineering Journal, 59, 1740002.

Niu, G., Z.L. Yang, K. Mitchell, F. Chen, M. Ek, M. Barlage, and Y. Xia. 2011. The community Noah land surface model with multi-parametrization options (Noah-MP): 1. Model description and evaluation with local-scale measurements. *Journal of Geophysical Research*, 116. https://doi.org/10.1029/2010jd015139.

Nolan, D.S. 2007. What is trigger for tropical cyclogenesis? Aust. Meteorol. Mag., 56, 241 – 266.

Noshkin, V. E. 1980. “Transuranium radionuclides in components of the benthic environment of Enewetak Atoll." In *Transuranic Elements in the Environment*, Edited by Hanson, W.C. Prepared for U.S. Department of Energy. DOE/TIC-228001980.

Noshkin VE, Robison WL, Wong KM. 1994. Concentration of 210Po and 210Pb in the diet at the Marshall Islands. Sci. Total Environ. 155 pp87-104

Noshkin, V. E. and W.L. Robison. 1997. Assessment of a radioactive waste disposal site at Enewetak Atoll. *Health Physics*, 73(1), 234-247.

NRC.1991. 10 CFR Part 20, Subpart D—Radiation Dose Limits for Individual Members of the Public. 56 FR 23398, May 21, 1991.

NRC. 2016. 10 CFR 20 Part 61.41 Protection of the general population from releases of radioactivity, 81 FR 86909, December 2, 2016.

Oouchi, K., J. Yoshimura, H. Yoshimura, R. Mizuta, S. Kusunoki, and A. Noda. 2006. Tropical cyclone climatology in a global-warming climate as simulated in a 20-km mesh global atmospheric model: Frequency and wind intensity analyses. Journal of the Meteorological Society of Japan, 84, 259 – 276.

Oppenheimer, M., B.C. Glavovic, J. Hinkel, R. van de Wal, A.K. Magnan, A. Abd-Elgawad, R. Cai, M. Cifuentes-Jara, R.M. DeConto, T. Ghosh, J. Hay, F. Isla, B. Marzeion, B. Meyssignac, and Z. Sebesvari. 2019: Sea Level Rise and Implications for Low-Lying Islands, Coasts and Communities. In: IPCC Special Report on the Ocean and Cryosphere in a Changing Climate [H.-O. Pörtner, D.C. Roberts, V. Masson-Delmotte, P. Zhai, M. Tignor, E. Poloczanska, K. Mintenbeck, A. Alegría, M. Nicolai, A. Okem, J. Petzold, B. Rama, N.M. Weyer (eds.)]. Cambridge University Press, Cambridge, UK and New York, NY, USA, pp. 321–445. https://doi.org/10.1017/9781009157964.006.

Pauluis, O., D.M.W. Frierson, S.T. Garner, I.M. Held, and G.K. Vallis. 2006. The hypohydrostatic rescaling and its impacts on mode- ling of atmospheric convection. Theoretical and Computational Fluid Dynamics, 20(5–6), 485–499. https://doi.org/10.1007/ s00162-006-0026-x.

Pauluis, O. and S. Garner. 2006. Sensitivity of radiative-convective equilibrium simulations to horizontal resolution. Journal of Atmospheric Sciences, 63(7), 1910–1923. https://doi.org/10.1175/JAS3705.1.

PCCSP (Pacific Climate Change Science Program). 2011. Current and future climate of the Marshall Islands. Marshall Islands National Weather Service Office, Australian Bureau of Meteorology, and Commonwealth Scientific and Industrial Research Organisation. Available at https://www.pacificclimatechangescience.org/wp-content/uploads/2013/06/8_PCCSP_Marshall_Islands_8pp.pdf.

Perera, C., Smith, J., Wu, W., Perkey, D., Priestas, A. 2020. Erosion rate of sand and mud mixtures. International Journal of Sediment Research, 35, 563-575

Pita, G.I., J.P Pinelli, K.R. Gurley, and S. Hamid. 2013. Hurricane vulnerability modeling: Developments and future trends. Journal of Wind Engineering & Industrial Aerodynamics, 114, 96 – 105.

Pleim, J.E. 2007. A combined local and nonlocal closure model for the atmospheric boundary layer. Part I: Model description and testing. *Journal of Applied Meteorology and Climatology*, 46, 1383 – 1395. https://doi.org/10.1175/jam2539.1

Ramsay, H. and A. Sobel. 2011. Effect of relative and absolute sea surface temperature on tropical cyclone potential intensity using a single-column model. Journal of Climate, 24, 183 – 193.

Ramsay, H. 2017. The global climatology of tropical cyclones. *Oxford Research Encyclopedia of Natural Hazard Science*, Oxford University Press.

Reed, R.J. and E.E. Recker. 1971. Structure and properties of synoptic-scale wave disturbances in the Equatorial Western Pacific. *Journal of Atmospheric Science*, 28, 1117–1133.

Richardson, J.F. and Zaki, W.N. 1954. Sedimentation and fluidisation, Part I. Transaction of the Institute of Chemical Engineers., 32(1), 3553.

Robison, W.L. 1979. *Preliminary Reassessment of the Potential Radiological Doses for Residents Resettling Enewetak Atoll*. UCID-18219, Lawrence Livermore National Laboratory, Livermore, California.

Robison, W. L. 1973. Dose estimate for the marine food chain. In: Enewetak Survey Report. U.S. Atomic Energy Commission, Nevada Operations Office, Report NVO- 140, Volume 1

Robison, W.L., Noshkin, V. E. 1981. Analysis of core “soil” and “water” samples from the Cactus Crater disposal site at Enewetak Atoll. Lawrence Livermore National Laboratory, Report UCID-18935

Robison, W.L., C.L Conrado, and W.A. Phillips. 1987. Enjebi dose assessment, UCRL-53805. Lawrence Livermore National Laboratory, Livermore CA.

Robison, W.L., Philips, W.A. 1989. Estimates of the Radiological Dose from Ingestion of 137Cs and 90Sr to Infants, Children, and Adults in the Marshall Islands. Lawrence Livermore National Laboratory, UCRL-53917.

Robison, W.L., Conrado, C.L., and Bogen, K.T. 1994. An Updated Dose Assessment for Rongelap Island, Lawrence Livermore National Laboratory, UCRL-LR-107036.

Robison, W. L., Noshkin, V.E. 1999. Radionuclide characterization and associated dose from long-lived radionuclides in close-in fallout delivered to the marine environment at Bikini and Enewetak Atolls. *Science of the Total Environment* 237: 311-327.

Rubey, W.W. 1933. Settling velocities of gravel, sand, and silt particles, American Journal of Science, 5th Series, 25(148), 325338

Shen, C.W., Q.Y. Duan, W. Gong, Y. Gan, Z. Di, C. Wang, and S. Miao. 2020. An objective approach to generating multi-physics ensemble precipitation forecasts based on the WRF model. J. Meteor. Res., 34, 3, 601 – 620.

Shen, J., B. Hong, L. Schugam, Y. Zhao, and J. White. 2012. Modeling of polychlorinated biphenyls (PCBs) in the Baltimore Harbor. Ecological Modelling. Vol 242. 54-68.

Shin, H.H. and S.-Y. Hong, 2015: Representation of the subgrid-scale turbulent transport in convective boundary layers at gray-zone resolutions. *Mon. Wea. Rev.*, 143, 250–271.

Skamarock, W. C., Klemp, J. B., Dudhia, J., Gill, D. O., Liu, Z., Berner, J., … Huang, X. -yu. (2019). A Description of the Advanced Research WRF Model Version 4 (No. NCAR/TN-556+STR). doi:10.5065/1dfh-6p97.

Shepherd, T.G., Boyd, E., Calel, R.A. *et al.* Storylines: an alternative approach to representing uncertainty in physical aspects of climate change. *Climatic Change* **151**, 555–571 (2018). https://doi.org/10.1007/s10584-018-2317-9.

Shinn, J. H., D.N. Homan, and W.L. Robison. 1997. Resuspension studies in the Marshall Islands. Health Physics, 73(1), 248-257.

Simon. S.L. and J.C. Graham. 1995. *Republic of Marshall Islands Findings of the Nationwide Radiological Survey; Data Tables and Sampling Maps Volume 1*. RMI Nationwide Radiological Study, Majuro, Marshall Islands. Copyright 1995 by S. L. Simon and J.C. Graham and Republic of Marshall Islands.

Skamarock, W.C., J.B. Klemp, J. Dudhia, D.O. Gill, Z. Liu, Z., J. Berner, W. Wang, J.G. Powers, M.G. Duda, D. Barker, and X.-yu Huang. 2019. A Description of the Advanced Research WRF Model Version 4 (No. NCAR/TN-556+STR). doi:10.5065/1dfh-6p97

Sukoriansky, S., B. Galperin, and V. Perov. 2005. Application of a new spectral theory of stably stratified turbulence to the atmospheric boundary layer over sea ice. *Boundary-Layer Meteorology*, 117(2), 231 – 257. https://doi.org/10.1007/s10546-004-6848-4.

Strachan, J., P.L. Vidale, K. Hodges, M. Roberts, and M.-E. Demory. 2013. Investigating global tropical cyclone activity with a hierarchy of AGCMs: The role of model resolution. Journal of Climate, 26, 133 – 152.

Stensrud, D.J. 2007. Parameterization Schemes. Key to understanding Numerical Weather Prediction Models. Cambridge University Press, Cambridge, United Kingdom.

Stowasser, M., Y. Wang, and K. Hamilton. 2007. Tropical cyclone changes in the western North Pacific in a global warming scenario. *Journal of Climate*, 20, 2378–2396.

Sugi, M., A. Noda, and N. Sato. 2002. Influence of the global warming on tropical cyclone climatology: An experiment with the JMA global model. *Journal of Meteorological Society of Japan*, 80, 249–272.

Sugi, M., H. Murakami, and J. Yoshimura. 2012. On the mechanism of tropical cyclone frequency changes due to global warming. Journal of Meteorological Society of Japan, 90A, 397–408.

Taraphdar, S. and O.M. Pauluis. 2021. Impact of planetary boundary layer and cloud microphysics on the sensitivity of monsoon precipitation using a gray-zone regional model. Earth and Space Science, 8, e2020EA001535. https://doi.org/10.1029/2020EA001535.

Taraphdar, S., O.M. Pauluis, L. Xue, C. Liu, R. Rasmussen, R.S. Ajayamohan, et al. 2021. WRF gray-zone simulations of precipitation over the Middle-East and the UAE: Impacts of physical parameterizations and resolution. *Journal of Geophysical Research: Atmospheres*, 126(10), e2021JD034648. https://doi.org/10.1029/2021JD034648

Taraphdar, S., P. Mukhopadhyay, L.R. Leung, F. Zhang, S. Abhilash, and B.N. Goswami. 2014. The role of moist processes in the intrinsic predictability of Indian Ocean cyclones. Journal of Geophysical Research: Atmospheres, 119(13), 8032–8048. https://doi.org/10.1002/2013JD021265.

Taraphdar, S., L.R. Leung, and S. Hagos. 2015. Linkage of remote sea surface temperatures and Atlantic tropical cyclone activity mediated by the African monsoon. Geophysical Research Letters, 42, 572 – 578, doi:10.1002/2014GL062600.

Taylor, K.E. 2001. Summarizing multiple aspects of model performance in a single diagram. *Journal of Geophysical Research*, 106, 7183 – 7192. https://doi.org/10.1029/2000JD900719.

Taylor, R.C. 1973. An Atlas of Pacific Islands Rainfall. Hawaii Institute of Geophysics, University of Hawaii, Honolulu, HIG-73-9.

Thompson, G. and T. Eidhammer. 2014. A study of aerosol impacts on clouds and precipitation development in a large winter cyclone. *Journal of the Atmospheric Sciences*, 71, 3636 – 3658. https://doi.org/10.1175/jas-d-13-0305.1

Ting, M., J. Kossin, S. Camargo, and C. Li. 2019. Past and future hurricane intensity change along the US East Coast. Scientific Report, 9, 7795.

UNDP (United National Development Programme). 2022. Republic of The Marshall Islands Climate Security Risk Assessment Profile. Available at https://www.undp.org/sites/g/files/zskgke326/files/2022-11/climate-security-risk-assessment-rmi-profile.pdf.

UNSCEAR (United Nations Scientific Committee on the Effects of Atomic Radiation). 1988. Sources and effects of ionizing radiation. Report to the General Assembly with Annexes, United Nations, New York.

UNSCEAR (United Nations Scientific Committee on the Effects of Atomic Radiation). 2011. UNSCEAR 2008 Report to the General Assembly, with scientific annexes, Volume II: Report to the General Assembly, Scientific Annexes C, D, and E, 2011.

van Rijn, L.C. 2020. Literature Review of Critical Bed-shear Stresses for Mud-Sand Mixtures. https://www.leovanrijn-sediment.com/papers/Threshsandmud2020.pdf

Vecchi, G., B.J. Soden, A.T. Wittenberg, I.M. Held, A. Leetma, and M.J. Harrison. 2006. Weakening of tropical Pacific atmospheric circulation due to anthropogenic forcing. Nature, 571, 550 – 554.

Wang, S., A.H. Sobel, F. Zhang, Y.Q. Sun, Y. Yue, and L. Zhou. 2015. Regional simulation of the October and November MJO events observed during the CINDY/DYNAMO field campaign at Gray zone resolution. Journal of Climate, 28, 2097–2119. https://doi.org/10.1175/ jcli-d-14-00294.1.

Walsh, K.J.E., J.L. McBride, P.J. Klotzbach, S. Balachandran, S.J. Camargo, G. Holland, T.R. Knutson, J.P. Kossin, T.-c. Lee, A. Sobel, and M. Sugi. 2016. Tropical cyclones and climate change. WIREs Clim Change, 7: 65-89. https://doi.org/10.1002/wcc.371.

Wardlaw, B. R., Henry, T. W., Martin, W. E. 1991. Sediment facies of Enewetak Atoll lagoon, Prepared in Cooperation with the Defense Nuclear Agency. U.S. Geological Survey Professional Paper 1513-B.

Webster, P.J., G.J. Holland, J.A. Curry, and H.-R. Chang. 2005. Changes in tropical cyclone number, duration, and intensity in a warming environment. *Science*, 309, 1844–1846.

Weusthoff, T., D. Leuenberger, C. Keil, and G.C. Craig. 2011. Best member selection for convective-scale ensembles. Meteorol. Z., 20, 153 – 164, doi: 10.1127/0941-2948/2011/0211.

Yoshida, K., M. Sugi, R. Mizuta, H. Murakami, and M. Ishii. 2017. Future changes in tropical cyclone activity in high resolution large ensemble simulations. Geophysical Research Letter, 44, 9910 – 9917.

Zhang, F., S. Taraphdar, and S. Wang. 2017. The role of global circumnavigating mode in the MJO initiation and propagation. *Journal of Geophysical Research: Atmospheres*, 122, 5837–5856. https://doi.org/10.1002/2016JD025665.

Zhang, C. and Y. Wang. 2017. Projected future changes of tropical cyclone activity over the western North and South Pacific in a 20-km mesh regional climate model. *Journal of Climate*, 30, 5923–5941.

Zhang, F., S. Taraphdar, and S. Wang. 2017. The role of global circumnavigating mode in the MJO initiation and propagation. Journal of Geophysical Research: Atmospheres, 122, 5837–5856. https://doi.org/10.1002/2016JD025665.

Appendix A
Enewetak Soil Concentration Data from NWRS

The primary source of information for radionuclides in the soils of the Enewetak Atoll is the *RMI Nationwide Radiological Study* (NWRS) (Simon and Graham, 1995). Volume 1of the NWRS includes information on the RMI atolls of Ailinginae, Ailinglaplap, Ailuk, Arno, Aur, Bikar, Bikini, Ebon, Enewetak, Erikub, and Jabat. For Enewetak Atoll, the information was collected for 31 islands and organized in 14 different maps, from southeast to north and back to southwest.

The NWRS collected several sample types and measurements including soil profiles, surface soil samples and in situ gamma spectrometry measurements, all of which may be useful for the current project. Data from these various measurements and samples are presented in Table A.1. Radionuclides included ^{137}Cs, ^{241}Am, $^{239+240}$Pu, and ^{60}Co. These measurements were assumed to be made during 1992 for purposes of radioactive to future dates.

Short explanations of the types of samples and the data reported in the NWRS follow. Not all sample types were acquired from every island of the atoll; in particular, only a few samples might exist for the smallest islands.

Soil profiles: A soil sample taken from the ground surface to 30 cm depth was separated into six 5 cm thick increments. Each profile increment was prepared and analyzed separately in the laboratory. Gamma-emitting radionuclides (e.g., ^{137}Cs, ^{241}Am) were measured in each profile increment, and the total radioactivity from the surface to 30 cm depth was determined. This value was reported as Bq/m^2 (i.e., the amount of radioactivity [Bq] for a particular radionuclide per square meter of soil [m^2] for the 30 cm depth). ^{137}Cs and ^{241}Am are both reported in the data tables. If data on ^{241}Am are not reported, it can be assumed the radionuclide was not detected.

Trans (transuranics): A surface soil sample taken from the ground surface to a depth of 5 cm intended for radiochemical analysis of transuranic radionuclides. Transuranic radionuclides include $^{239+240}$Pu and ^{241}Am . 'Trans' samples were taken at the site of the in situ gamma spectrometry measurement. Each 'trans' sample was a composite of three smaller samples of size 15 cm x 15 cm x 5 cm (deep). The three samples were located randomly within 15 m of the gamma spectrometer. The 'trans' samples are intended to estimate the average transuranic soil concentration within the vicinity of the gamma spectrometer.

Gamma: An in situ gamma spectrometry measurement using a high-purity germanium detector and multichannel analyzer. The gamma spectral measurement is used to determine the local average soil inventory (Bq/m^2) of gamma-emitting radionuclides (e.g., ^{137}Cs, ^{241}Am). The gamma spectrum registers the gamma-ray emissions from each radionuclide separately, thus distinguishing fallout radioactivity from natural radioactivity. Numerous calibrations and calculations are required to determine the radionuclide inventory in the soil from the gamma spectrum. Thus, the term 'estimate' specifies that the value reported is calculated from other types of data.

Error: Each 'estimate' of soil inventory or sample radioactivity is accompanied by a determination of the uncertainty of the estimate and appears in the column labeled 'error.' The determinations of potential error give a range that the true value is expected to lie within. The range can be determined by adding and subtracting the 'error' value from the 'estimate.' For example, if the inventory estimate of ^{137}Cs is 9,000 Bq/m^2 and the potential error is 770 Bq/m^2, the probability range is 9,770–8,230 Bq/m^2. Errors are reported for all sample types in the next adjacent column to the measurement.

External Exposure Rate: Data from the in situ gamma spectrum, soil profiles, and surface soil samples also were used to estimate the external dose rate from ^{137}Cs. Because of the familiarity of many readers with older units of externally received radiation dose (mrem), external dose rate is reported in units of mrem per year (mrem/y) for 1995.

A total of 176 samples and measurements were made for the 31 islands included in the NWRS for Enewetak Atoll. Not all radionuclides were included for analysis in every sample, especially for islands in the southern part of the atoll that had much lower exposure to fallout radionuclides.

Table A.1. Sampling and measured data for Enewetak Atoll from the NWRS

	NWRSMap #	Island	Sample Number	^{137}Cs In situ est. (Bq/m^2)	±1 σ	External Dose Rate (mrem/yr)	^{241}Am 0-5 cm (Bq/kg)	±1 σ	$^{239+240}$Pu 0-5 cm (Bq/kg)	±1 σ	^{60}Co 0-5 cm (Bq/kg)	±1 σ
1	1	Enewetak	1									
2	1	Enewetak	2	480	72	0.18						
3	2b	Medren	Me1	220	32	0.082						
4	2b	Medren	Me2	1,200	150	0.45						
5	2a	Japtan	Ja1	1,400	110	0.52						
6	2a	Japtan	Ja2	2,700	170	1.0						
7	3	Ananij	An1	2,700	240	1.0						
8	3	Ananij	An2	1,400	170	0.54						
9	3	Ananij	An3	1,300	150	0.48						
10	4	Inedral	In1	49	88	0.018	no detect				no detect	
11	4	Inedral	In2	490	190	0.18	no detect				0.27	0.072
12	4	Van	Va1	760	94	0.28	no detect				no detect	
13	4	Van	Va2	1,500	180	0.56	no detect				no detect	
14	4	Van	Va3	790	93	0.29	no detect				no detect	
15	5	Runit	Ru6	40,000	2,400	15	95	9.2	780	57	8.8	1.5
16	5	Runit	Ru7	160,000	8,200	61						
17	5	Runit	Ru8				27	2.2			10	0.79
18	5	Runit	Ru8	130,000	7,400	52	140	10	1,200	150	27	1.7
19	5	Runit	Ru9				43	3.9	350	32	6.4	0.65
20	5	Runit	Ru10	660	130	0.24	3	0.34			0.30	0.057
21	5	Runit	Ru11	3,200	470	1.2	62	5.9	160	11	0.98	0.62
22	5	Runit	Ru12	2,700	370	1	100	72			1.1	0.22
23	5	Runit	Ru13				47	4.6	260	20	7	6.2
24	5	Runit	Ru14				190	16	890	99	16	2.8
25	5	Runit	Ru15				43	5.4			14	1
26	5	Runit	Ru16	3,000	200	1.1	44	5	360	33	8.2	0.94
27	5	Runit	Ru17	140,000	8,500	54						
28	5	Runit	Ru18	130,000	7,000	51						
29	5	Runit	Ru1	1,400	280	0.53	36	2.9			2.8	0.41
30	5	Runit	Ru2	810	22	0.3	15	1.7			5.2	0.40
31	5	Runit	RU3	13,000	970	4.9	210	16			no detect	
32	5	Runit	Ru4	8,000	940	3	410	28			8.4	1.2
33	5	Runit	Ru5	10,000	760	3.8	17	1.9			3.5	0.49

	NWRSMap #	Island	Sample Number	^{137}Cs In situ est. (Bq/m^2)	±1 σ	External Dose Rate (mrem/yr)	^{241}Am 0-5 cm (Bq/kg)	±1 σ	$^{239+240}$Pu 0-5 cm (Bq/kg)	±1 σ	^{60}Co 0-5 cm (Bq/kg)	±1 σ
34	5	Runit	Ru19	22,000	1,400	8.3	120	10			no detect	
35	5	Runit	Ru20	3,700	420	1.4	40	3.8			1.8	0.37
36	5	Runit	Ru21	24,000	1,700	9.1	160	11			11	1.7
37	5	Runit	Ru22	7,500	640	2.8	180	15			no detect	
38	5	Runit	Ru23	4,700	510	1.8	31	3.1			1.8	0.30
39	5	Runit	Ru24	2,200	300	0.8	51	3.4			2.8	0.26
40	5	Runit	Ru25	29	28	0.01	4.7	0.42			0.36	0.068
41	5	Runit	Ru26	120	140	0.042	no detect				no detect	
42	5	Runit	Ru27	780	160	0.29	no detect				no detect	
43	6a	Alembel	AL1	14,000	950	5.2	53	4.5	83	14	1.1	0.49
44	6a	Alembel	AL2	12,000	890	4.6	no detect				no detect	
45	6a	Alembel	AL3	25,000	1,600	9.6						
46	6a	Alembel	AL4	15,000	1,000	5.8	65	6.1	110	8.2	1.3	0.18
47	6a	Billae	BL1	4,200	370	1.6	no detect				no detect	
48	6a	Billae	BL2	15,000	1,000	5.8	60	4.8	180	11	1.8	0.30
49	6b	Aomon	AO1	18,000	1,100	6.7	5.9	1.1	83	14	no detect	
50	6b	Aomon	AO10	4,500	420	1.7	33	2.5	170	23	no detect	
51	6b	Aomon	AO11	12,000	620	4.4						
52	6b	Aomon	AO12									
53	6b	Aomon	AO13	56,000	3,000	22	11	1.5	39	3.8	0.35	0.14
54	6b	Aomon	AO2				180	14	1,100	180	no detect	
55	6b	Aomon	AO3	7,300	550	2.7	5.7	0.72			0.56	0.2
56	6b	Aomon	AO4	24,000	1,400	9	67	5.7	99	15	0.98	0.3
57	6b	Aomon	AO5	35,000	1,900	13	3.9	0.53			1.1	0.17
58	6b	Aomon	AO6	11,000	770	4.3	7.4	0.87			0.3	0.17
59	6b	Aomon	AO7				17	1.7	71	11	1	0.21
60	6b	Aomon	AO8	67,000	3,600	26	4.3	0.48			0.4	0.15
61	6b	Aomon	AO9	30,000	1,700	11	20	2	51	5.3	0.68	0.32
62	6b	Bijiri	BI1	10,000	690	3.8	190	17			no detect	
63	6b	Bijiri	BI2	33,000	2,200	13	64	5.8	270	19	2	0.62
64	6b	Bijiri	BI3	14,000	1,000	5.5	27	2.9			2.9	0.44
65	6b	Bijiri	BI4	12,000	780	4.4	37	3.6	55	5.3	1.4	0.3
66	6b	Bijiri	BI5	5,700	450	2.1	20	2.1	45	4.2	no detect	
67	6b	Bijiri	BI6	15,000	1,100	5.8	120	9.6	180			
68	6b	Lojwa	LO1	12,000	780	4.5	21	1.9	63	4.7	1.1	0.39
69	6b	Lojwa	LO2	8,800	620	3.3	16	1.6	64	4.5	no detect	

	NWRSMap #	Island	Sample Number	^{137}Cs In situ est. (Bq/m^2)	±1 σ	External Dose Rate (mrem/yr)	^{241}Am 0-5 cm (Bq/kg)	±1 σ	$^{239+240}$Pu 0-5 cm (Bq/kg)	±1 σ	^{60}Co 0-5 cm (Bq/kg)	±1 σ
70	6b	Lojwa	LO3	3,300	320	1.2	3.4	0.49			0.3	0.1
71	6b	Lojwa	LO4	13,000	900	5.1	26	2.5	81	9.5	no detect	
72	6b	Lojwa	LO5	23,000	1,400	8.8	32	3.5	99	5.9	1.8	0.36
73	6b	Lojwa	LO6	13,000	860	4.9	17	1.7	41	5	0.59	0.17
74	7	Aej	Ae1	57,000	3,100	22	no detect				no detect	
75	7	Aej	Ae2	8,900	630	3.4	no detect				no detect	
76	7	Aej	Ae3	22,000	1,300	3.4	no detect				no detect	
77	7	Aej	Ae4	42,000	2,400	16	no detect				no detect	
78	7	Elle	El1	87,000	4,800	34	800	60	1,800	380	18	2.9
79	7	Elle	El2	91,000	5,000	35	1,100	110	2,200	160	23	3.4
80	7	Lujor	Lu1	17,000	1,300	6.5	no detect				no detect	
81	7	Lujor	Lu2	32,000	2,300	12	no detect				no detect	
82	7	Lujor	Lu3	12,000	790	4.4	no detect				no detect	
83	7	Lujor	Lu4	59,000	3,400	23	no detect				no detect	
84	7	Lujor	Lu5	62,000	3,600	24	no detect				no detect	
85	8	Bokenelab	BO1	12,000	800	4.4	no detect				no detect	
86	8	Bokenelab	BO2	47,000	2,600	18	no detect				no detect	
87	8	Bokenelab	BO3	32,000	1,800	12	no detect				no detect	
88	8	Kidrinnenen	KI1	8,800	780	3.3	no detect				no detect	
89	8	Kidrinnenen	KI2	25,000	1,700	9.4	no detect				no detect	
90	8	Kidrinnenen	KI3	6,700	640	2.5	no detect				no detect	
91	8	Kidrinnenen	KI4	100,000	6,500	40	no detect				no detect	
92	8	Mijikadrek	MI1	25,000	1,600	9.4	61	6.8	110	5.4	no detect	
93	8	Mijikadrek	MI2	20,000	1,400	7.7	77	6.2	120	11	no detect	
94	8	Mijikadrek	MI3				25	2.4			no detect	
95	9	Enjebi	13	220,000	11,000	84	430	36	2,300	460	38	4.5
96	9	Enjebi	14	140,000	7,400	56	250	27	150	31	14	1.8
97	9	Enjebi	4	180,000	9,300	71	36	3.2	77	9.1	1.8	0.30
98	9	Enjebi	17	120,000	6,700	48	120	11	400	35	6.4	1.1
99	9	Enjebi	18	130,000	7,000	50	480	39	330	46	5.6	1.8
100	9	Enjebi	19	430,000	22,000	170	600	58	1,000	150	16	2.8
101	9	Enjebi	2	160,000	8,000	60	320	23	700	140	8.1	1.3
102	9	Enjebi	25	220,000	12,000	86	480	33	870	190	9.0	1.2
103	9	Enjebi	1	64,000	3,400	25	52	4.6	150	20	2.2	0.63
104	9	Enjebi	10	74,000	3,900	29	170	14	530	66	7.2	1.8
105	9	Enjebi	11	79,000	7,200	31	57	5.4	200	23	1.9	0.42

	NWRSMap #	Island	Sample Number	^{137}Cs In situ est. (Bq/m^2)	±1 σ	External Dose Rate (mrem/yr)	^{241}Am 0-5 cm (Bq/kg)	±1 σ	$^{239+240}$Pu 0-5 cm (Bq/kg)	±1 σ	^{60}Co 0-5 cm (Bq/kg)	±1 σ
106	9	Enjebi	12	39,000	2,200	15	58	5.3	310	28	4.4	0.99
107	9	Enjebi	15	70,000	3,700	27	120	9.2	430	44	4.6	1.0
108	9	Enjebi	16	15,000	1,200	5.6	63	5.9	690	52	3.5	0.55
109	9	Enjebi	20	62,000	3,600	24	42	3.5	200	21	6.7	0.72
110	9	Enjebi	21	24,000	1,600	9.1	100	7.5	260	18	4.4	0.59
111	9	Enjebi	22	9,200	680	3.5	31	3.2	100	13	1.5	0.31
112	9	Enjebi	23	49,000	2,900	19	42	4.6	84	10	2.2	0.36
113	9	Enjebi	24	44,000	2,600	17	70	6.7	260	27	2.3	0.46
114	9	Enjebi	26	31,000	2,000	12	34	3.1	89	8.8	1.2	0.25
115	9	Enjebi	27	92,000	5,000	36	240	23	330	50	4.4	1.2
116	9	Enjebi	28	51,000	2,900	20	65	7.7	150	14	4.0	0.57
117	9	Enjebi	29	54,000	2,900	21	110	8.7	380	52	no detect	
118	9	Enjebi	3	76,000	4,000	29	140	15	280	26	5.0	0.81
119	9	Enjebi	30	49,000	2,700	19	28	2.9	57	6.7	no detect	
120	9	Enjebi	31	34,000	2,300	13						
121	9	Enjebi	32	55,000	3,000	21	120	9.3	360	35	3.4	0.81
122	9	Enjebi	33				23	2.9	84	10	1.9	0.31
123	9	Enjebi	34	35,000	2,300	13	32	3.1	72	9.5	no detect	
124	9	Enjebi	35	41,000	2,300	16	35	2.9	140	6.8	1.3	0.30
125	9	Enjebi	5	75,000	4,000	29	58	8.1	160	11	4.4	0.86
126	9	Enjebi	6	19,000	2,000	7.3						
127	9	Enjebi	7	72,000	3,800	28	23	1.8	66	6.3	1	0.23
128	9	Enjebi	8	84,000	4,400	32	320	23	1,600	340	11	2.0
129	9	Enjebi	9	1,200	100	0.46	40	4.1			no detect	
130	10	Boken	Bok1				47	3.6	210	17	1.5	0.38
131	10	Boken	Bok10	4,200	490	1.6	120	10			2.7	0.65
132	10	Boken	Bok11	9,500	1,200	3.6	150	14	850	60	25	2.2
133	10	Boken	Bok2	2,800	350	1	86	6.3	230	29	1.6	0.36
134	10	Boken	Bok3	2,900	380	1.1	74	6.7			1.6	0.41
135	10	Boken	Bok4	29,000	1,700	11	190	18			5.3	1.1
136	10	Boken	Bok5	2,900	350	1.1	65	6.2			1.2	0.34
137	10	Boken	Bok6	8,800	900	3.3	no detect				no detect	
138	10	Boken	Bok7	670	120	0.25	no detect				no detect	
139	10	Boken	Bok8	110,000	5,700	42	330	32	3100	590	50	4.3
140	10	Boken	Bok9	35,000	2,400	13	64	5.1			33	1.9
141	11	Bokinwotme	Bknw1	13,000	870	4.8	160	15	800	90	no detect	

	NWRSMap #	Island	Sample Number	^{137}Cs In situ est. (Bq/m^2)	±1 σ	External Dose Rate (mrem/yr)	^{241}Am 0-5 cm (Bq/kg)	±1 σ	$^{239+240}$Pu 0-5 cm (Bq/kg)	±1 σ	^{60}Co 0-5 cm (Bq/kg)	±1 σ
142	11	Bokinwotme	Bknw2	15,000	990	5.9	no detect				no detect	
143	11	Bokinwotme	Bknw3	19,000	1,200	7.2	no detect				no detect	
144	11	Louj	Lj1	22,000	1,400	8.2	270	18	720	110	10	1
145	11	Louj	Lj2	550	470	2.1	no detect				no detect	
146	11	Louj	Lj3	14,000	930	5.2	no detect				no detect	
147	11	Louj	Lj4	57,000	3,100	22	no detect				no detect	
148	12	Bokoluo	Bkk1	380,000	19,000	150	890	97	1,100	240	36	7
149	12	Bokoluo	Bkk2	520,000	27,000	200	no detect				no detect	
150	12	Bokoluo	Bkk3	350,000	18,000	140	no detect				no detect	
151	12	Bokoluo	Bkk4	250,000	13,000	100	no detect				no detect	
152	12	Bokoluo	Bkk5	440,000	22,000	170	770	50	2,100	410	79	4.6
153	12	Bokombako	bkm1	25,000	1,500	9.4	no detect				no detect	
154	12	Bokombako	Bkm2	270,000	14,000	110	no detect				no detect	
155	12	Bokombako	Bkm3	12,000	810	4.5	no detect				no detect	
156	12	Bokombako	Bkm4	330,000	17,000	130	no detect				no detect	
157	12	Bokombako	Bkm5	240,000	12,000	96	no detect				no detect	
158	12	Bokombako	Bkm6	330,000	17,000	130	1,100	80	4,100	580	100	7.7
159	12	Kirunu	Ki1	22,000	1,400	8.2	no detect				no detect	
160	12	Kirunu	Ki2	220,000	11,000	86	no detect				no detect	
161	12	Kirunu	Ki3	100,000	5,400	40	no detect				no detect	
162	12	Kirunu	Ki4	74,000	4,000	28	48	4.6	280	56	5.5	0.7
163	13	Biken	Bk1	8,600	640	3.2	no detect				no detect	
164	13	Biken	Bk2	8,800	700	3.3	19	2.2	74	7	5.9	0.45
165	14	Boken	Bk1	52	52	0.019	no detect				0.79	0.17
166	14	Boken	Bk2	280	77	0.1	no detect				no detect	
167	14	Ikuren	Ik1	2,600	210	0.96	no detect				no detect	
168	14	Ikuren	Ik2	2,300	220	0.86	no detect				no detect	
169	14	Ikuren	Ik3	870	100	0.32	no detect				no detect	
170	14	Kidrenen	Kd1	690	150	0.26	no detect				no detect	
171	14	Kidrenen	Kd2	260	58	0.094	no detect				no detect	
172	14	Kidrenen	Kd3	2,100	270	0.79	no detect				no detect	
173	14	Mut	Mu1	3,000	290	1.1	no detect				no detect	
174	14	Mut	Mu2	800	110	0.3	no detect				3.9	0.23
175	14	Ribewon	Ri1	240	67	0.087	no detect				no detect	
176	14	Ribewon	Ri2	15	46	0.0055	no detect				no detect	

Appendix B
Climate Scenarios

Evaluating the effects of climate change on the potential of legacy radionuclides existing in the environment of the Enewetak Atoll was a central motivation for this assessment. However, studies investigating the effects of climate change over the central Pacific Ocean near the RMI are limited. PNNL did not identify existing suitable assessments of climate change that could be easily adapted to assessing the future potential of legacy radionuclides on human and biota health. Because most of the radionuclides at the Enewetak Atoll are stored in the lagoon sediment, a plausible mechanism that could make them available for mobilization and transport such that humans and biota could be exposed to radiation doses is from the scouring and ocean water circulation caused under the effects of severe storms and hurricanes.

Therefore, PNNL performed an independent assessment of a few selected, historically severe storms that have affected the Enewetak Atoll in the past. To accomplish this task, PNNL identified historically severe storms, identified likely changes in future climate that may affect storm behavior, and performed simulations of the selected storms in a present-day climate (about 2015) and in a future climate (about 2090) to create plausible, severe storm scenarios. These scenarios were then used to drive ocean models to estimate mobilization and transport of legacy radionuclides.

B.1 Climate Model

PNNL employed the WRF-ARW modeling system to create plausible, severe storm scenarios for the RMI region. WRF-ARW has been developed for the past two decades. It is a flexible, state-of-the-art atmospheric simulation system and readily adaptable and efficient on available parallel computing platforms. The system is suitable for use in a broad range of applications across scales ranging from meters to thousands of kilometers. Its applications include idealized simulations (e.g., large eddies, convection, baroclinic waves), parameterization research, data assimilation research, real-time numerical weather prediction, hurricane research, regional climate research, fire research, and coupled model applications.

Figure B.1 shows a flowchart of the WRF-ARW modeling system. The modeling system has the following components:

- WRF preprocessing system
- WRF data assimilation
- WRF-ARW solver
- Post-processing and visualization tools.

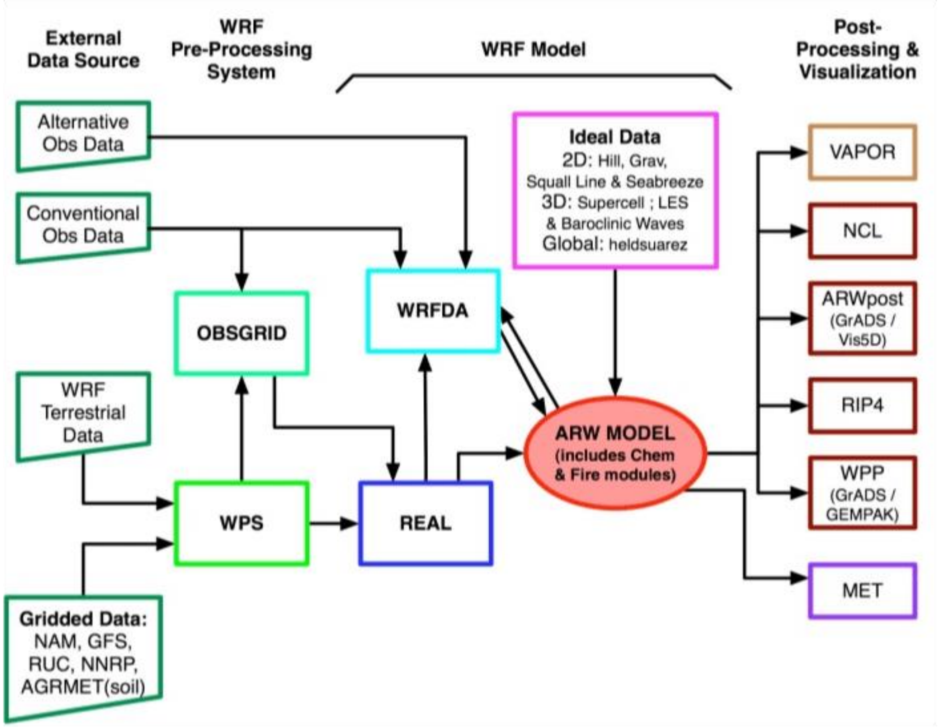

Figure B.1. Components of the WRF-ARW Model

B.1.1 WRF Preprocessing System

This component (shown as WPS) is primarily used for real-case simulations. Its functions include defining simulation domains, interpolating terrestrial data (e.g., terrain, land use, and soil types) to the simulation domain, and incorporating meteorological data from another model to this simulation domain.

B.1.2 WRF Data Assimilation

This component is optional but can be used to ingest observations into the interpolated analyses created by the WRF preprocessing system. It can also be used to update the WRF model's initial conditions when it is run in cycling mode.

B.1.3 WRF-ARW Solver

This is the primary component of the modeling system, composed of several initialization programs for idealized or real-data simulations and the numerical integration program. WRF is a fully compressible, nonhydrostatic (with hydrostatic options) model suitable for regional and global applications. The WRF model has both one-way and two-way nesting with multiple nesting options and the availability of the moving nest (prescribed move and vortex tracking). It uses the mass-based hybrid sigma-pressure vertical coordinate where vertical grid spacing can vary with heights. WRF has full physics options for land-surface, PBL, atmospheric and surface radiation, cloud microphysics, and cumulus convection.

B.1.4 Post-processing and Visualization Tools

The modeling system supports many software packages including RIP4 (based on National Center for Atmospheric Research [NCAR] Graphics), NCAR Command Language, and conversion programs for other readily available graphics and computational packages like Python and GrADS.

B.2 WRF-ARW Model Setup

PNNL used the nonhydrostatic WRF-ARW model version 4.1.2 (Skamarock et al., 2019). The model domain consisted of 801 × 601 grid points and covered the majority of the central to west Pacific region from 5°S–43°N and 115°E–180°E (Figure B.2). The model grid had a 9 km horizontal grid spacing and 45 stretched vertical levels with the model top at 10 hPa. The black box shows the region of primary interest for this study.

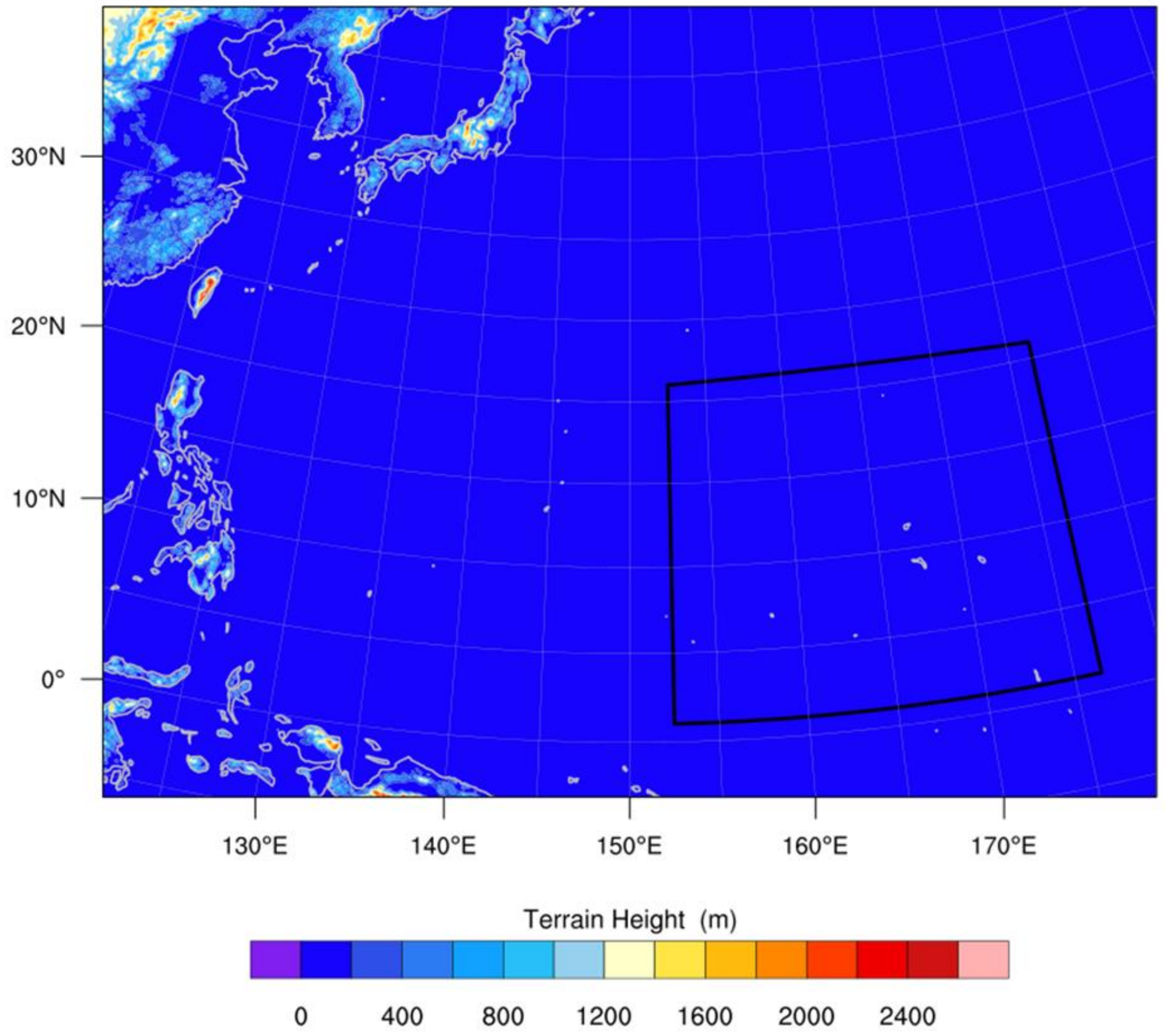

Figure B.2. WRF-ARW model domain with terrain elevations shown by shaded colors. The black box includes the central Pacific region spanning 152.5°E – 176.5°E longitude and 1°N – 21°N latitude.

B.2.1 Selecting WRF-ARF Physical Process Parameterization Schemes

PNNL evaluated four distinct bulk microphysical schemes: the WRF double-moment 6-class microphysics (WDM6) scheme (Lim and Hong, 2010); the aerosol-aware Thompson–Eidhammer (THOMP) scheme (Thompson and Eidhammer, 2014); the CAM V5.1 double-moment 5-class scheme (Neale et al., 2012; NCAR Tech Note), and the WRF single moment 6-class microphysics (WSM6) scheme (Hong and Lim, 2006). The first two schemes (WDM6 and THOMP) are the most sophisticated, with six hydrometeor classes and a double-moment representation for warm rain. Though the third scheme uses the double moment, it has 5 class hydrometeors instead of six. The WSM6 scheme is very similar to WDM6 but uses a single moment. Additionally, the THOMP scheme has prognostic variables for ice-friendly and water-friendly nuclei that are initialized from a global monthly climatology based on aerosol properties.

Land-surface processes and land-atmosphere interactions are represented by the Noah land-surface model with multiparameterization options (Niu et al., 2011). Atmospheric radiative heating is calculated by the Rapid Radiative Transfer Model (Iacono et al., 2008) for longwave and shortwave radiation schemes. The PNNL model configuration did not use any parameterization for deep convection; instead, the model relied on the resolved dynamics to capture the impact of convective activity.

PNNL also compared six different PBL schemes: the Mellor-Yamada-Nakanishi-Nino (MYNN) levels 2.5 (Nakanishi and Niino, 2004); the Asymmetrical Convective Model version 2 (ACM2) scheme (Pleim, 2007); the Quasi Normal Scale Elimination (QNSE) scheme (Sukoriansky et al., 2005); the Yonsei University (YSU) boundary layer (Hong et al., 2006); the University of Washington (UW) scheme (Bretherton and Park, 2009); and the Shin-Hong (SH) scheme (Shin and Hong, 2015). The ACM2 is a first-order nonlocal closure scheme that uses nonlocal upward and local downward mixing. This scheme uses local closure at stable or neutral conditions and nonlocal closure for unstable conditions, also known as a hybrid scheme. In the free troposphere, the eddy diffusivity coefficient is a function of local wind shear and local Richardson number. In convective conditions, ACM2 can simulate rapid upward transport in buoyant plumes and local shear-induced turbulent diffusion. YSU is also a nonlocal K scheme with an explicit entrainment layer and parabolic K profile in an unstable mixed layer. The SH scheme includes scale dependency for vertical transport in convective PBL. Vertical mixing in the stable PBL and free atmosphere follows the YSU scheme. In contrast, MYNN and QNSE are local closure schemes that include turbulent kinetic energy as a prognostic variable. Eddy diffusivity coefficients for momentum and heat are parameterized through a mixing length theory but are explicitly dependent on the boundary layer depth. The UW is also a turbulent kinetic energy-based scheme, adopted in WRF from the Community Earth System Model. All PBL parameterizations are tied to their respective surface layer schemes. PNNL performed sensitivity tests to identify the best performing PBL and microphysics scheme. The aerosol-aware THOMP microphysics scheme was the default cloud microphysics parameterization during the sensitivity tests. Sensitivity tests for cloud microphysics parameterizations were performed using the best performing PBL scheme.

PNNL identified three major hurricanes (Hurricanes Gay in November 1992, Melissa in September 1994, and Nangka in July 2015) based on their severity and proximity to the Enewetak Atoll. Hurricanes Gay and Nangka propagated in an east-west direction, whereas Melissa initially moved westward and subsequently curved northward. Therefore, Enewetak Atoll experienced high wind speeds twice during Hurricane Melissa’s passage. Hurricane Gay was the strongest of the three and passed closet to the atoll. In all three hurricane simulations initial and boundary condition were provided by the ERA5 reanalysis (Hersbach et al., 2020) because of its superior performance for seasonal simulations compared to other reanalyses (Taraphdar et al., 2021). The lateral boundary and SST were updated every 3 hours using the ERA5 reanalysis. All Hurricane Gay simulations were initialized at 0000 UTC on November 17, 1992, and integrated for 14 days to capture the lifecycle of the hurricane. Similarly, Hurricanes Nangka and Mellissa simulations were initialized at 0000 UTC on July 5, 2015, and 0000 UTC on September 13, 1994, respectively, to capture their time evolution. A spectral nudging was used for the first three days to relax the horizontal wind with a meridional wavenumber 0–2 and zonal wavenumber 0–4 to constrain the large-scale flow and convergence in the domain and to allow for the mesoscale to saturate in the spectral space (Wang et al., 2015; Zhang et al., 2017). Simulated hurricane tracks, minimum sea-level pressure, and surface winds predicted by the WRF-ARW model were compared with the IBTrACS data.

The sensitivity of WRF-ARW predictions to PBL and cloud physics process parameterizations was tested using Hurricane Gay as the representative storm. The relative performance of six commonly used PBL parameterizations was evaluated first by comparing the predicted hurricane track and intensity to the observed best track data from IBTrACS.

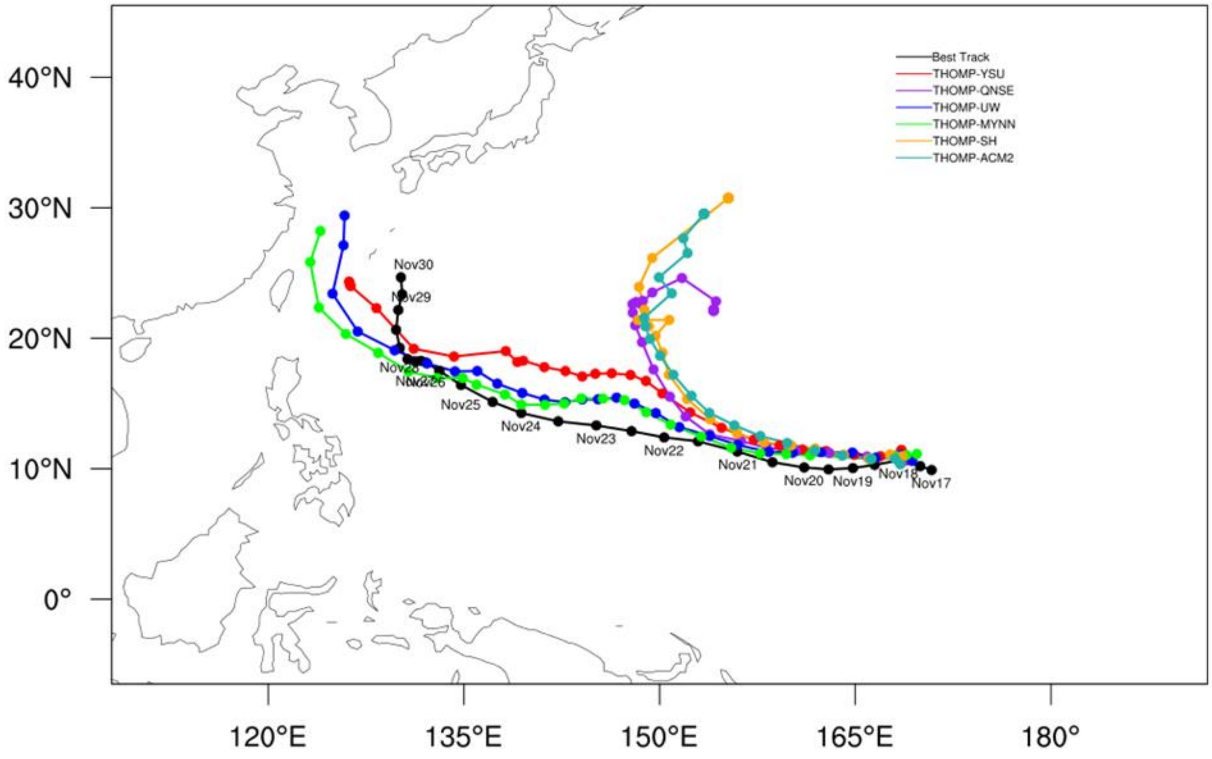

Figure B.3. Comparison of tracks of Hurricane Gay simulated by THOMP-YSU (red), THOMP-QNSE (purple), THOMP-UW (blue), THOMP-MYNN (green), THOMP-SH (orange), and THOMP-ACM2 (cyan) PBL schemes with the best track data (black).

PNNL conducted the sensitivity tests for PBL schemes at a 9 km resolution; the cloud microphysics parameterization for these tests was the same—THOMP. Figure B.3 shows the comparison between tracks predicted by the selected PBL schemes and the best track. The observed track showed an initial westward movement (until November 21) followed by west–northwestward movement (Figure B.3; black line). All PBL schemes simulate the track in reasonable agreement with the observations for the first few days. Subsequently, the predicted tracks started to deviate and made two distinct patterns. One group (i.e., THOMP-YSU, THOMP-UW, and THOMP-MYNN) predicted a track similar to the observation (i.e., northwestward movement), but the other group of schemes (i.e., THOMP-QNSE, THOMP-SH, and THOMP-ACM2) predicted tracks that deviated significantly northward compared to the observation. Among the first group, THOMP-MYNN and THOMP-UW schemes showed predicted tracks closer to the observed track than the THOMP-YSU scheme.

Next, PNNL compared the predicted storm intensity for the THOMP-YSU, THOMP-UW, and THOMP-MYNN schemes with the observed storm intensity (Figure B.4). Observations showed that Hurricane Gay was an intense hurricane with two peaks around November 21 and 26, 1992. The first peak was the stronger with surface winds reaching 110 knots and minimum sea-level pressure slightly above 900 hPa.

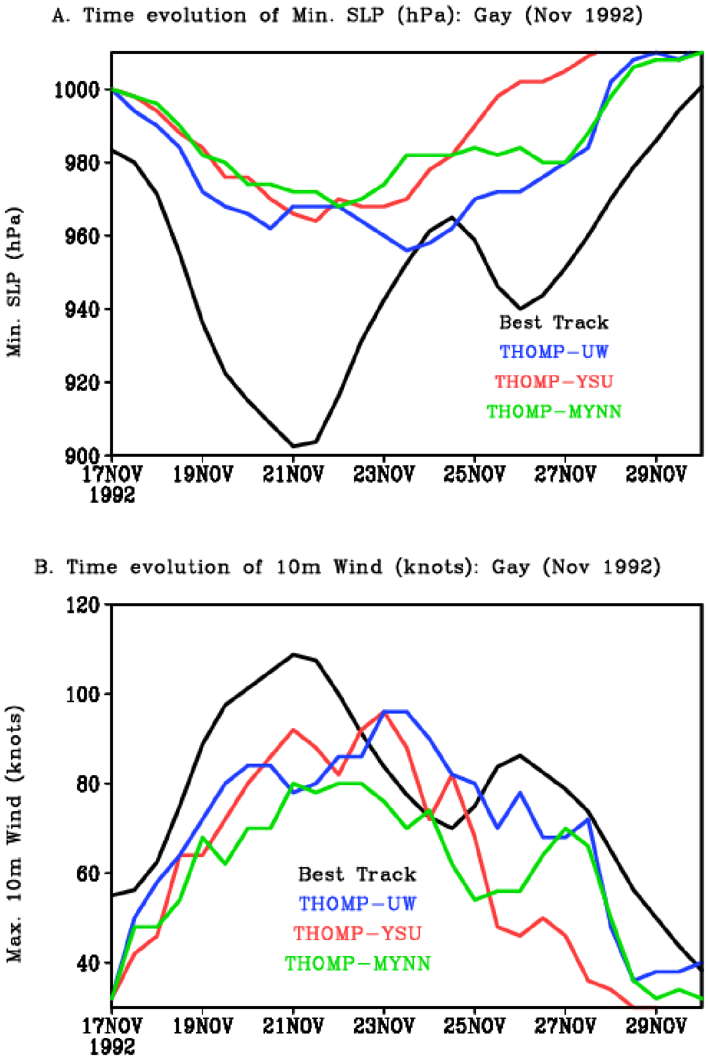

Figure B.4. Time evolution of minimum sea-level pressure (panel A) and maximum sustained 10 m wind speed (panel B) for Hurricane Gay from the best track data (black), THOMP-YSU (red), THOMP-UW (blue), and THOMP-MYNN (green).

The WRF-ARW simulations predicted a weaker storm in all PBL configurations. The THOMP-MYNN scheme simulated the weakest storm compared to THOMP-UW and THOMP-YSU schemes, although the THOMP-MYNN predicted track was closer to the observed storm track. A qualitative track and intensity evolution comparison showed that the THOMP-UW scheme performed better among the three schemes. To quantitatively compare the performance of the different PBL schemes, PNNL computed the normalized pattern statistics for the minimum sea-level pressure and maximum 10 m wind (Figure B.5).

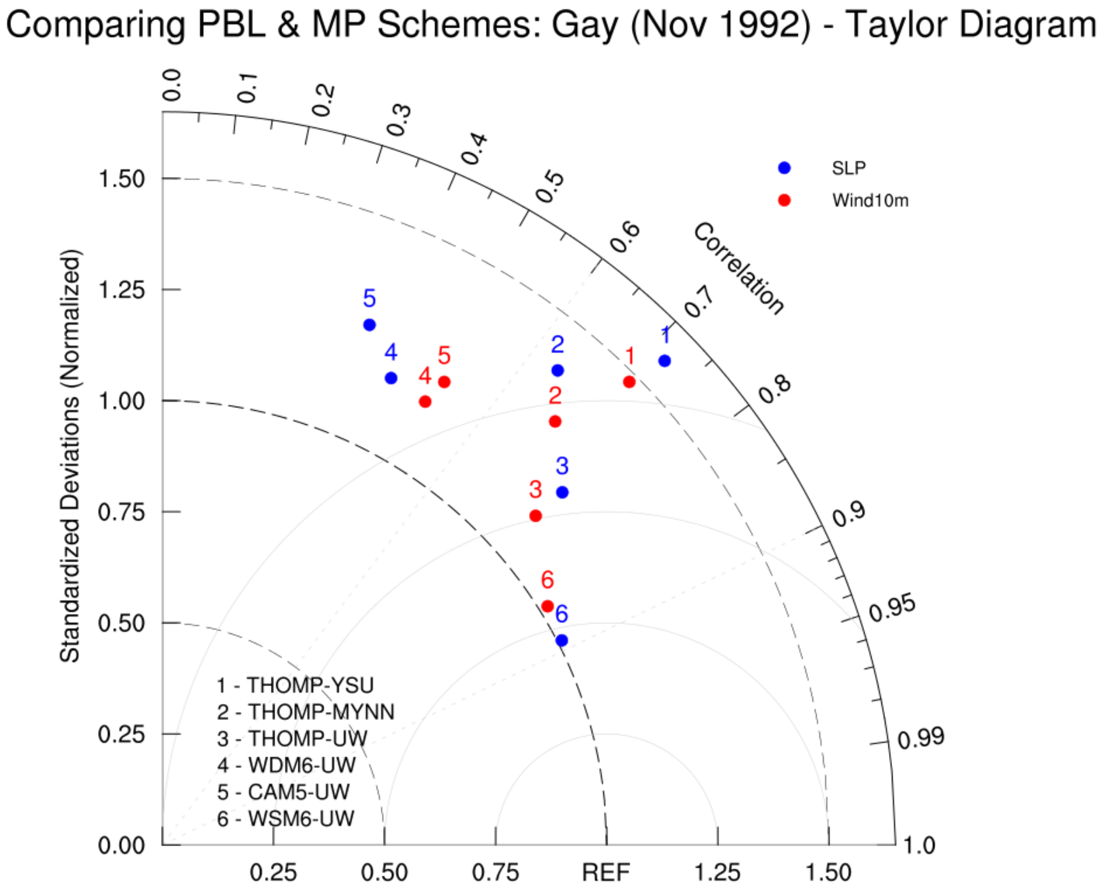

Figure B.5. The normalized pattern statistics (Taylor diagram) comparing different PBL (THOMP-YSU, THOMP-MYNN, and THOMP-UW) and cloud microphysics parameterization (THOMP-UW, WDM6-UW, CAM5-UW, and WSM6-UW) predictions with observations for the minimum sea-level pressure (SLP; blue) and 10 m wind (Wind10m; red). The Best Track data are used here as a reference point (REF). The numbers between 1 to 6 refer to different PBL and MP parameterization combinations listed in the figure.

The results are presented as a Taylor diagram (Taylor, 2001), in which the distance from the origin indicates the normalized standard deviation, and the cosine of the angle of the position vector indicates the pattern correlation between the observed and the simulated variable. The distance from the reference point (marked as “REF”) to the plotted points denotes the root-mean-square error (RMSE). With respect to PBL parameterizations (1, 2, and 3), the results in Figure B.5 clearly show that the THOMP-UW (blue) simulations have the minimum RMSE and maximum correlation, and the variability is also very similar to observation. The composited daily track errors (figure not shown) also supported the better performance of THOMP-UW, as seen by the minimum track errors in PBL sensitivity runs. Therefore, PNNL’s quantitative analysis suggested that the THOMP-UW simulations outperform the other PBL scheme simulations with respect to storm track and intensity (Figure B.3–Figure B.5).

After identifying the best performing PBL scheme for the selected hurricanes, PNNL evaluated the sensitivity of cloud microphysics parameterizations, while keeping the best performing PBL scheme the same among these sensitivity tests. PNNL performed four sensitivity tests by changing the cloud microphysics schemes (i.e., THOMP, WDM6, CAM5, and WSM6) between tests. Figure B.6 shows the comparison between the storm tracks predicted by the selected cloud microphysics parameterizations and the best track data. The deviation between the tracks predicted by the microphysics schemes from the observed track was generally marginal, although the CAM5-UW predicted track was moved away from the observed tracks, especially near the end of the simulation. The other three schemes performed relatively well.

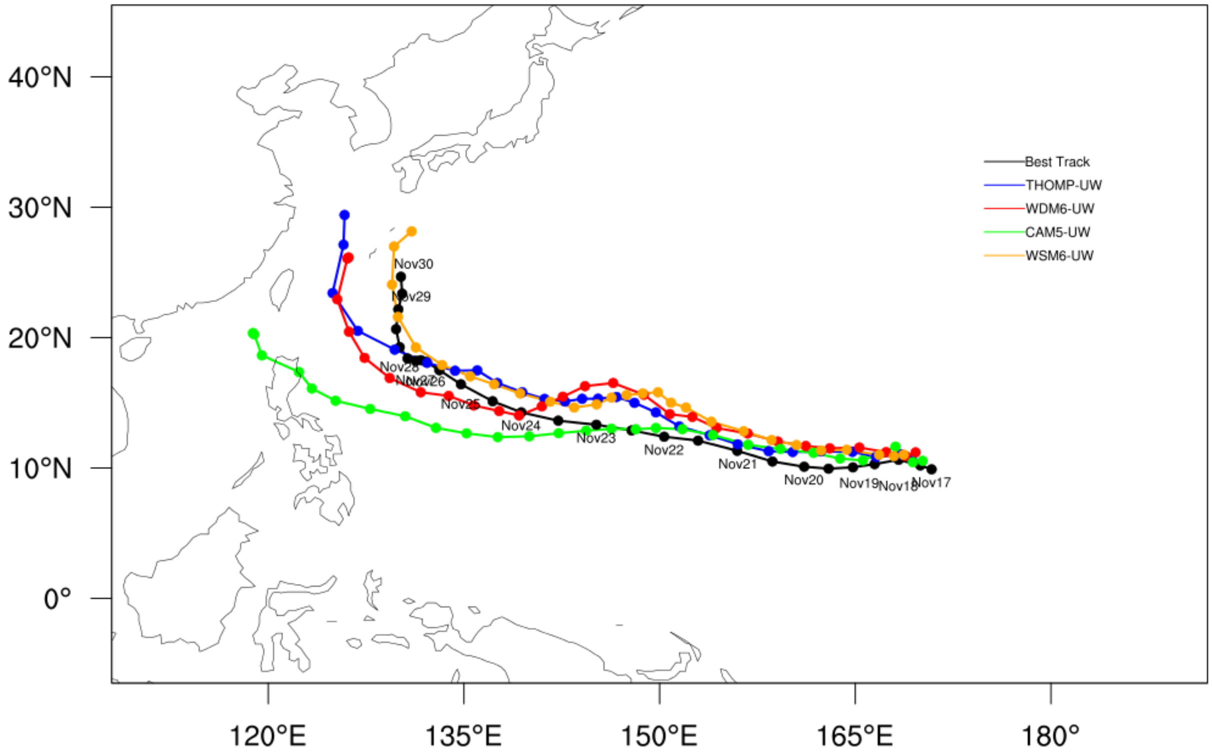

Figure B.6. Comparison of Hurricane Gay tracks simulated by THOMP-UW (blue), WDM6-UW (red), CAM5-UW (green), and WSM6-UW (orange) with the best track data (black).

Next, PNNL evaluated the storm intensity predicted by the different cloud microphysics schemes (Figure B.7). The storm intensity estimations are improved in the cloud microphysics sensitivity experiments (Figure B.7) compared to the PBL sensitivity (Figure B.4). This result suggested that cloud microphysics plays an important role in the intensity estimation for hurricanes, whereas PBL plays a more significant role in storm track estimation. However, these two processes are not independent—there is an interaction between the two that influence both storm track and intensity. Investigating this interaction was beyond the scope of this assessment. Qualitatively, WSM6-UW performed better compared to the observed storm track and intensity evolution. Also, the WSM6-UW simulations outperform the other cloud microphysics schemes as indicated on the Taylor diagram (Figure B.5). Therefore, PNNL selected WSM6 as the preferred cloud microphysics scheme and UW as the preferred PBL scheme.

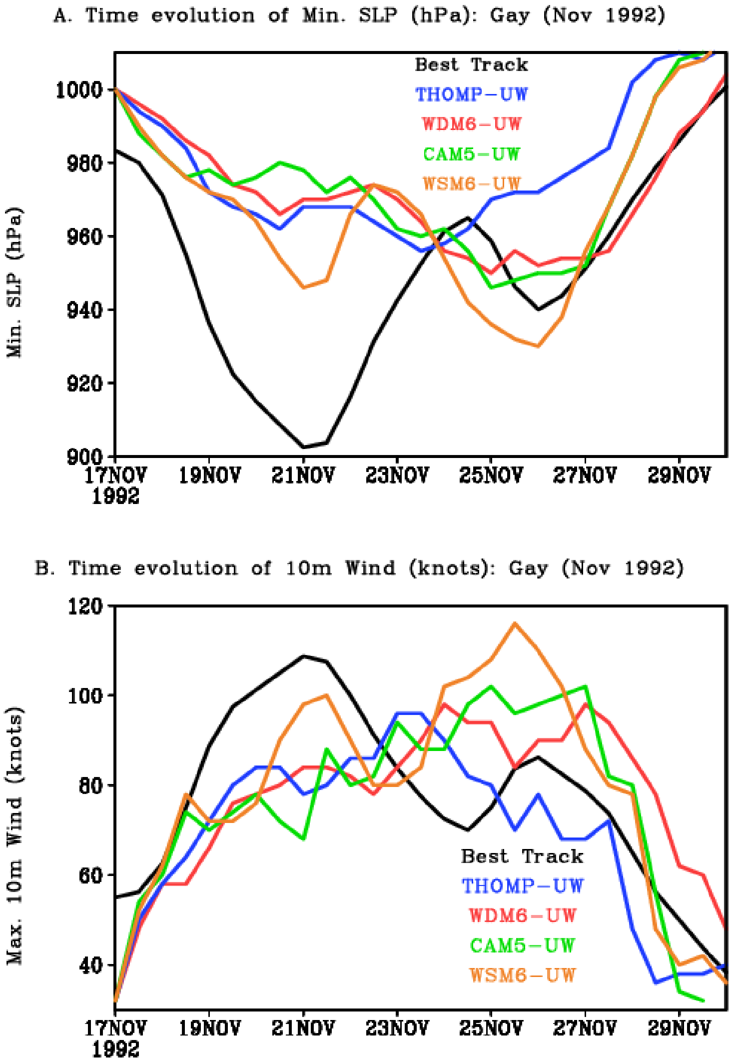

Figure B.7. Time evolution of minimum sea-level pressure (panel A) and maximum sustained 10 m wind speed (panel B) for Hurricane Gay from the best track data (black), THOMP-UW (blue), WDM6-UW (red), CAM5-UW (green), and WSM6-UW (orange).

B.2.2 Storm Simulations in the Current Climate

PNNL used the WRF-ARW model to simulate the three chosen hurricanes under current climate conditions. These simulations were forced by the ERA5 reanalysis data to provide initial and boundary conditions. The UW PBL and WSM6 cloud microphysics schemes were used in the WRF-ARW configuration. Hourly model outputs were stored. Figure B.8 shows the WRF-ARW simulated storm tracks for the selected storms at 12-hour increments.

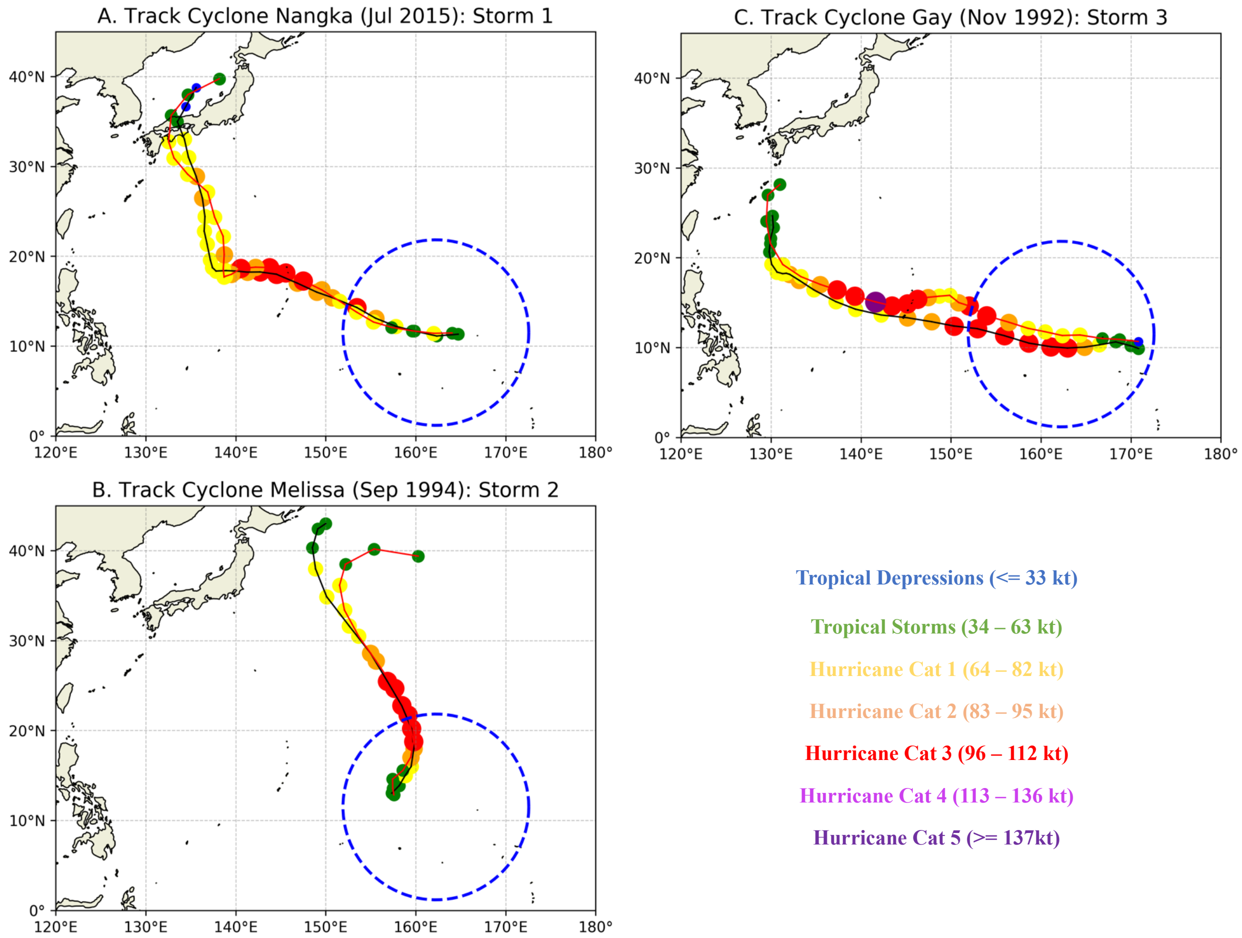

A. Track Cyclone Nangka (Jul 2015): Storm 1

C. Track Cyclone Gay (Nov 1992): Storm 3

B. Track Cyclone Melissa (Sep 1994): Storm 2

Figure B.8. Observed and simulated tracks and intensities of the three selected storms. The observed storm tracks are shown by black lines and the predicted storm tracks in current climate (about 2015) are shown by red lines. The colors of the dots along the tracks represent storm categories.

B.2.3 Storm Simulations in the Future Climate

To simulate the three selected hurricanes in the future climate, PNNL first calculated the climate perturbations for the PGW method. The perturbations were calculated as the difference of the monthly mean variable values (e.g., SST, surface pressure, surface temperature, atmospheric temperature, relative humidity, and geopotential height) between present day (1990–2010) and future (2079–2099) conditions under the RCP8.5 scenario based on the CMIP6 11 individual models (MIRROC6, FGOALS, MPI-ESM, GFDL-AM4, CESM, ACCESS-CM2, E3SM, NorESM2, EC-Earth3, CanESM5, and CMCC-CM2) and their multimodel ensemble mean. The climate perturbations for each variable were then added to the hourly ERA5 initial and boundary conditions for each selected hurricane to provide the perturbed initial and boundary conditions for future simulations.

The selected hurricanes were simulated using the perturbed initial and boundary conditions using the same WRF-ARF configuration as that used for the current climate simulations. Therefore, each selected hurricane was simulated 11 times to create a multimodel ensemble. PNNL did not add changes in the wind field for the climate perturbations in the PGW simulations because the wind field did not show significant changes over WNP in the warming future. Additionally, unlike SST, atmospheric temperature, and specific humidity for which all GCMs project increasing trends, different GCMs project different changes of circulation in WNP. Therefore, imposing the multimodal ensemble mean circulation changes may lead to an imbalanced atmospheric state inconsistent with the atmospheric temperature and specific humidity changes.

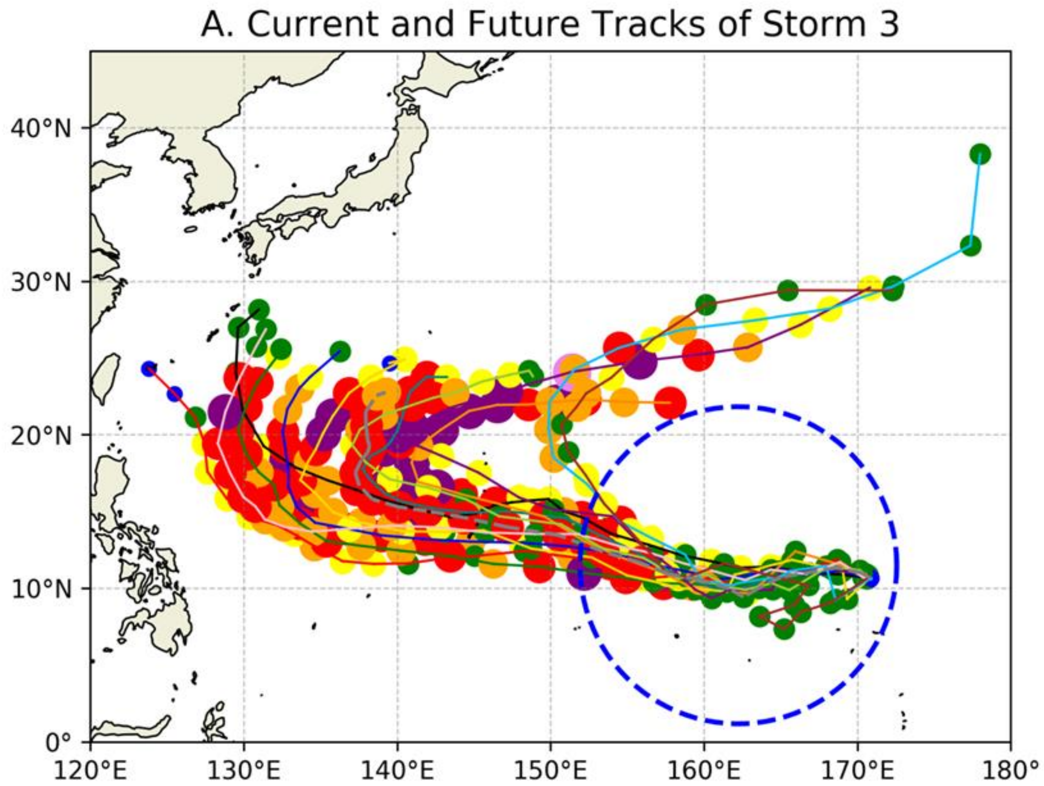

Figure B.9. WRF-ARW simulated storm tracks of Storm 3 in the current climate (black) and 11 future climate simulations corresponding to MIRROC6, FGOALS, MPI-ESM, GFDL, ACCESS, CESM, CMCC, NorESM2, EC-Earth3, E3SM, and CanESM5 CMIP6 models using the PGW method. The gray dashed line represents the ensemble mean storm track. The dots along the storm tracks are plotted every 12 hours and are colored by categories.

Figure B.9 shows the tracks of Storm 3 simulated under warming climate conditions perturbed by 11 individual CMIP6 models predictions (colored lines) along with their ensemble mean (dashed gray line) and the current climate WRF-ARW simulation (black line). As shown, for the first few days all simulated future storm tracks are reasonably close. Subsequently, the individual simulations start to diverge, especially in the western Pacific.

To quantify the performance difference among the CMIP6 models, PNNL computed the normalized pattern statistics for the minimum sea-level pressure (blue) and maximum 10 m wind (red; Figure B.10). In the Taylor diagram, distance from the origin indicates the normalized standard deviation and the cosine of the angle of the position vector indicates the pattern correlation between the observed and simulated variable. The distance from the reference point (marked as “REF”) to the plotted points denotes the RMSE. In Figure B.10, REF indicates the current climate simulation using WRF-ARW, which reasonably captured the observed hurricane's evolution and structure. The results in Figure B.10 clearly show that the MIRROC6 (number 1) model had the minimum RMSE and maximum correlation, and the variability was very similar to the current climate for sea-level pressure and 10 m wind. Therefore, PNNL concluded that the MIRROC6 perturbation for future climate experiment performs better than the others with respect to storm track and intensity.

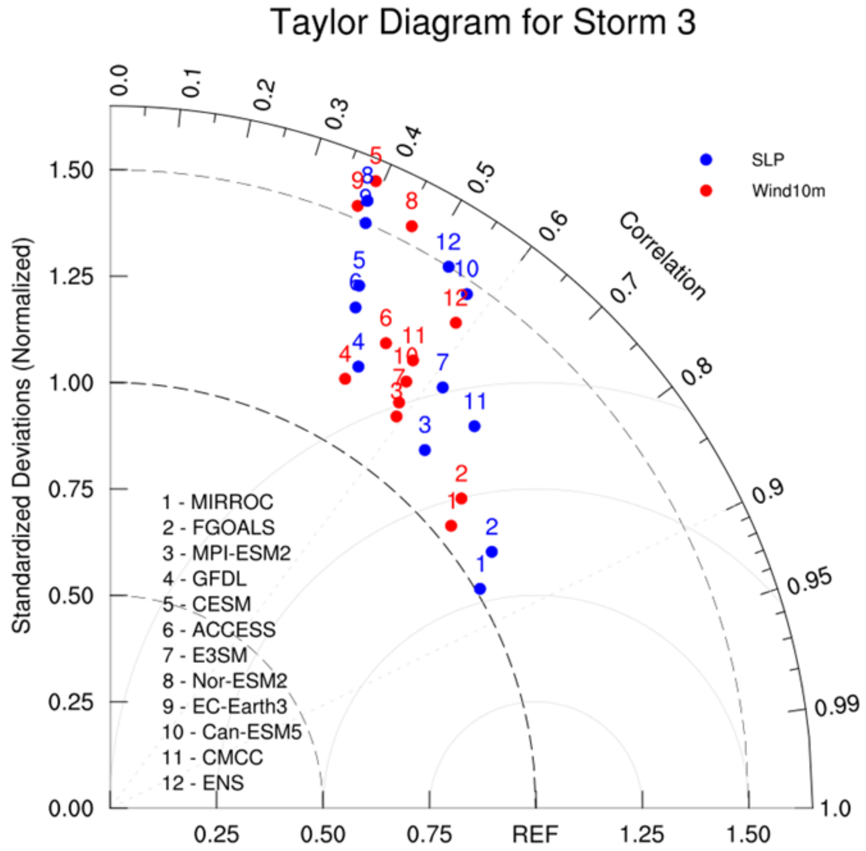

Figure B.10. The normalized pattern statistics difference (Taylor diagram) comparing different future WRF-PGW simulations for the minimum sea-level pressure (blue) and 10 m wind (red). The current climate simulation is the reference point (REF). The numbers “1” to “11” indicate the 11 climate models, and the number “12” is their ensemble mean, respectively.

PNNL selected MIRROC6 predictions to estimate the future perturbations. Figure B.11 shows the sea-surface temperature perturbation used in the WRF-ARW future simulation compared to the current climate conditions. Perturbations from the MIRROC6 model prediction were also used for other climate variables.

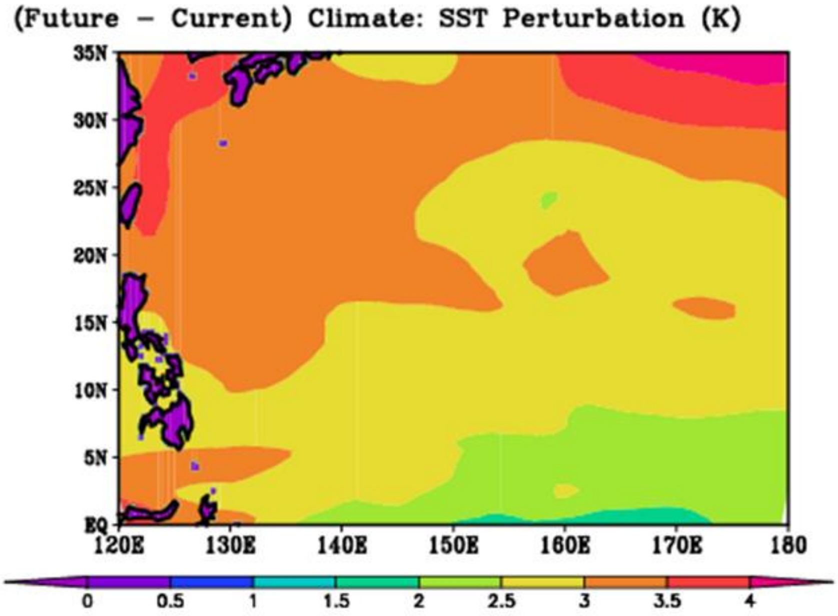

Figure B.11. Perturbations in sea-surface temperature for the future climate using the MIRROC6 model.

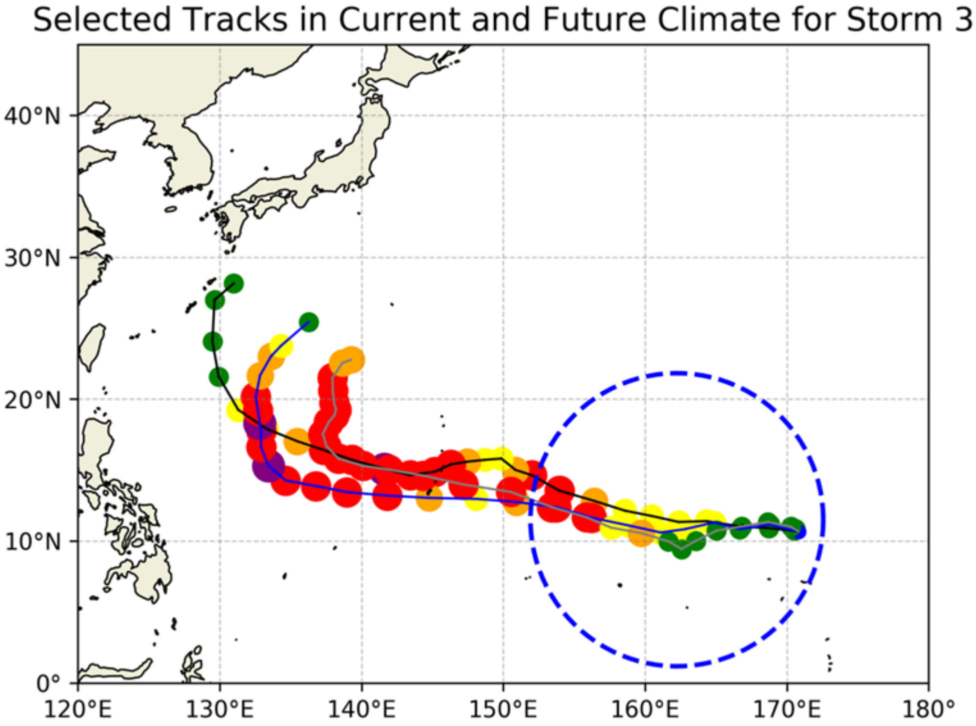

Figure B.12. WRF-ARW simulated storm tracks of Storm 3 in the current climate (black) and in the future climate using MIRROC6 perturbations (blue). The 11-member ensemble mean storm track is also shown (gray). The dots along the storm tracks are plotted every 12 hours and are colored by categories.

Figure B.12 shows three tracks for Storm 3—from the current climate simulation (black), the MIRROC6 future climate simulation using PGW, and the ensemble mean track of all 11 models in the future climate. The future climate simulation predicted a stronger hurricane over the west Pacific (west of 150°E longitude). The hurricane tracks over the central Pacific remained very similar in the current and future climate conditions. Figure B.13 shows the time evolution of Storm 3 intensity in terms of minimum sea-level pressure (Figure B.13, top panel) and maximum sustained 10 m wind speed (Figure B.13, bottom panel) in the current climate (black) and the future climate (blue); the ensemble mean is also shown (gray).

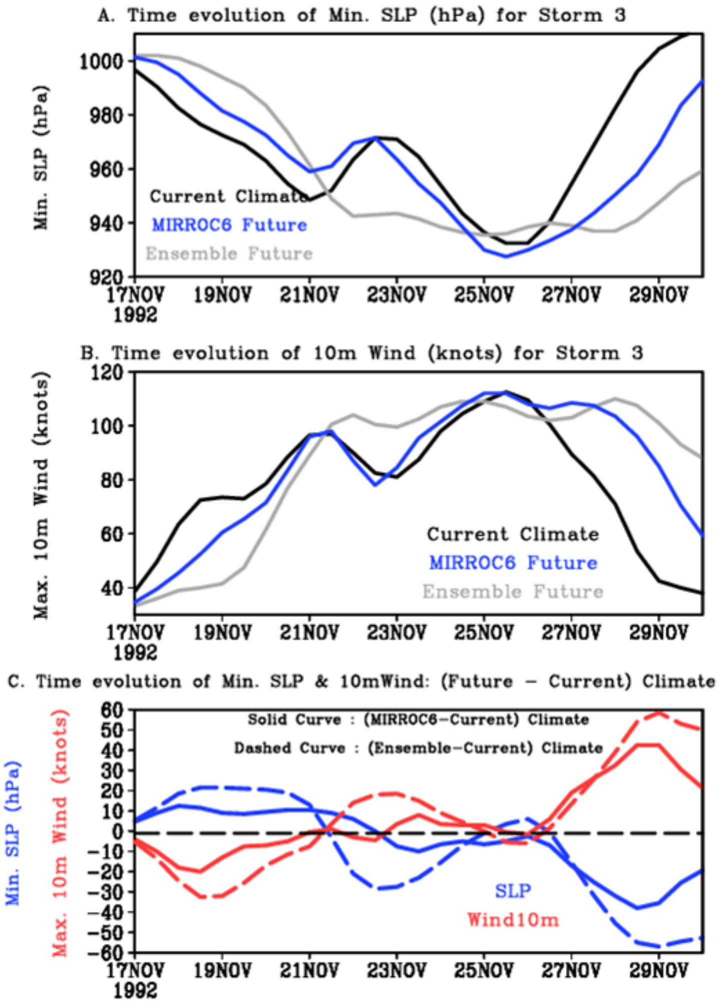

Figure B.13. Time evolutions of minimum sea-level pressure (panel A) and maximum sustained 10 m wind (panel B) for Storm 3, respectively, for the current climate (black), the future climate (blue), and the 11-member ensemble mean (gray) simulations. Panel C shows the difference in future to current climate simulation for minimum sea-level pressure (blue) and maximum sustained 10 m wind (red).

Future climate simulations were weaker than the current climate early in the storm (before November 22) but are stronger later (past November 27). Similar results were obtained for the other ensemble simulations. The storm also tended to last longer in the future climate (Figure B.13, panels A and B); this is likely a result of warmer sea-surface temperatures over the northwest Pacific (Figure B.11).

Figure B.14 shows the difference in wind speeds in the future climate compared to the current climate. The spatial distribution of surface wind speed differences showed a decrease in the future climate compared to the current climate early in the storm (Figure B.14). Later in the storm, the northwest Pacific showed an increase in surface wind speeds while the central Pacific showed a decrease. These results are also consistent with the sea-surface temperature trends (Figure B.11).

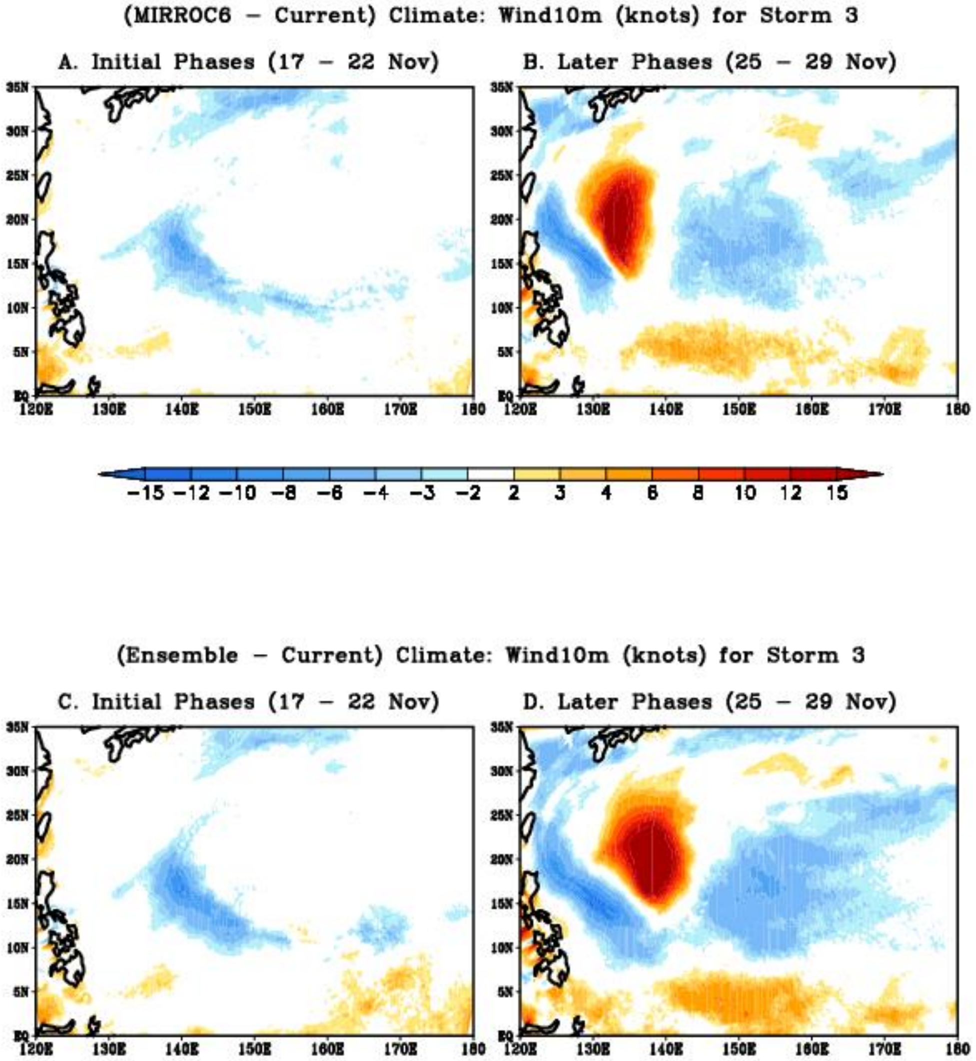

Figure B.14. Spatial distribution of differences between future and current climate maximum sustained 10 m winds. The top panel shows differences in the future using MIRROC6 perturbations and the bottom panel shows difference in the future from the ensemble mean.

The behavior of the surface wind speeds is also consistent with the surface latent heat flux over the northwest Pacific (Figure B.15). The increase in the latent heat flux results in positive feedback to hurricanes due to ocean-atmosphere interactions and helps to intensify the storms. This result agrees with previous studies demonstrating warm sea-surface temperature's important role in TC intensification. On the other hand, atmospheric warming significantly negatively impacts TC intensity by increasing atmospheric stability. Overall, the effect of atmospheric warming is smaller than the effect of sea-surface temperature increase. However, the weakening of surface wind speeds early in the storm cannot be explained by the increased latent heat flux. This result might indicate the importance of atmospheric warming during the early phases of a hurricane. The warmer atmosphere might increase atmospheric stability and negatively impact hurricane intensity. This hypothesis needs to be explored in detail with more sophisticated numerical experiments.

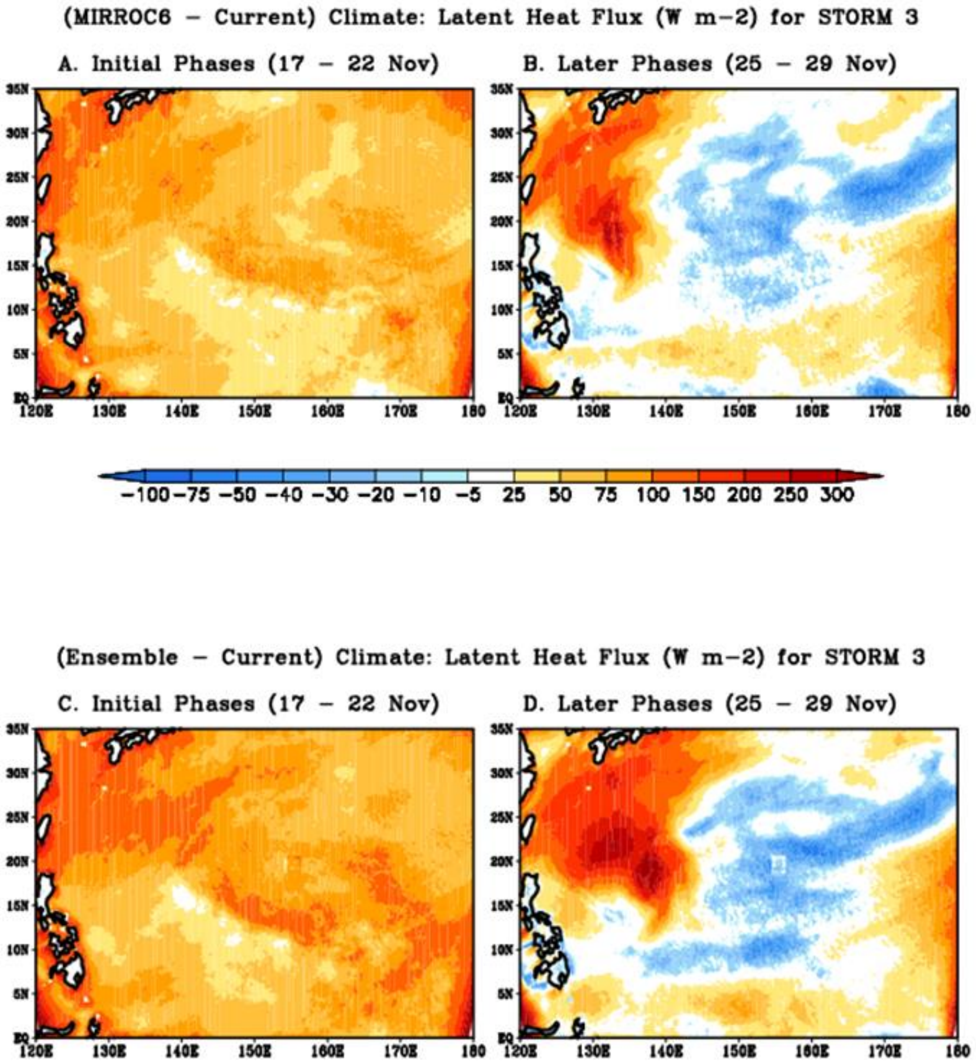

Figure B.15. Spatial distribution of surface latent heat flux difference (W m^{-2}) between future climate and current climate simulations using MIRROC6 perturbations (top panel). The difference from the 11-member ensemble mean and current climate simulation is also shown (bottom panel).

Hourly WRF-ARW outputs for the surface and three-dimensional atmospheric variables were provided to the ocean model as input for the current and future climate simulations.

B.2.4 Discussion

During current climate simulations, the predicted hurricane track was sensitive to the choice of PBL parameterization, whereas the cloud microphysics processes impacted the predicted intensity of hurricanes. With the proper choices of PBL and cloud microphysics parametrizations, simulations of the three selected hurricanes (Gay, November 1992; Melissa, September 1994; and Nangka July 2015) in the current climate were represented realistically with respect to observed best track data.

A range of predicted tracks and intensities were found in future climate simulations using the WRF-PGW approach. Intermodel spreads for tracks and intensities were more prominent over the west Pacific than the central Pacific. Among the 11 models, MIRROC6 performed the best. MIRROC6 future track was similar to the current climate early in the storm and then deviated northward compared to the northwestward movement of the storm in the current climate. The storm intensity (based on sea-level pressure and 10 m winds) was weaker early in the MIRROC6 future simulation, but stronger later in the storm compared to the current climate simulation. The longer lifetime for future hurricanes can be attributed to the warmer sea-surface temperatures over the northwest Pacific. The increase in the wind speed in the latter half of the future storm was consistent with the warmer sea-surface temperatures and the increase in the surface latent heat fluxes over the northwest Pacific. The warmer atmosphere might dominate during the hurricane's early phase, increasing the atmospheric stability and providing negative feedback to the hurricane's intensity.

There are significant uncertainties in the climate simulations presented here. These uncertainties arise from (1) limitations of observed hurricane data, (2) uncertainties associated with WRF-ARW physical processes, and (3) uncertainty in the forcings data for future hurricane simulation propagated from the global models. Uncertainty from the first source may be reduced by improving the data collected from buoys, satellites, and other remote sensing techniques and by improving track and intensity estimation algorithms. The storm may have conflicting data from multiple sources. Encouraging progress has been made in improving the consensus between different data sources in recent years.

Uncertainty from the second source may be reduced by performing sensitivity experiments on dominant physical processes, improving parameterizations of these processes, and choosing the appropriate parameterizations that perform better over a range of storm conditions. An ensemble approach using Monte Carlo techniques could be employed, although they require significant time and effort. Uncertainty from the third source can be reduced by accounting for variations in future predictions of multiple models not only for a specific future year but a range of years, possibly as part of an ensemble of simulations. However, this approach also required significantly increased computational time.

PNNL chose appropriate process parameterizations using sensitivity analyses. The team also employed a multimodel ensemble approach for estimating perturbations for the future climate compared to the current climate. These steps provide assurance that the climate simulations for this study are reasonable for the RMI region of the Pacific.

Appendix C
Ocean Modeling

Simulating ocean hydrodynamics and circulation around the Enewetak Atoll was an integral element of the overall approach for simulating the mobilization and transport of radionuclides present at the atoll. PNNL used FVCOM (Chen et al., 2003, 2006) to produce a detailed, three-dimensional characterization of the ocean hydrodynamic conditions around the Enewetak Atoll. The characterization, which includes ocean currents, temperature, salinity, water surface elevation, and turbulent eddy diffusivity, was accomplished by setting up and running FVCOM for a full calendar year forced by the combination of global meteorological and oceanographic reanalysis model outputs. During the one-year simulation, the wind and atmospheric pressure forcing field generated by the WRF-ARW simulations in Section 3.0 for three representative historical storms were embedded into the global meteorological forcing to provide an improved representation of the storms.

FVCOM itself is based on an unstructured grid framework, which has the flexibility to resolve detailed shoreline and topographic features with localized, high-resolution meshes within a larger model domain. In the vertical direction, FVCOM uses a terrain-following sigma-coordinate system to capture the rapid bathymetry changes from emerged atolls to deep ocean trenches. The ocean modeling process with FVCOM involved the following major steps: 1) generating the model grid for the domain of interest; 2) setting up the model with forcing data and conducting diagnostic runs to improve the model grid as needed; 3) calibrating the model against available observational data through parameter tuning; 4) conducting model simulations for the baseline year of 2015 that has three downscaled storms embedded in the meteorological forcing; 5) archiving hourly, three-dimensional model output to drive ICM-radionuclide simulations; 6) processing the model outputs to analyze model results for further validation; and 7) repeating steps 4 and 5 for the future climate condition. These steps are described in the following sections.

C.1 Model Grid Generation

To accurately digitize the coastlines during mesh generation, several coastline references, including the coastline vector shapefile covering global EEZ boundaries,[1] NOAA nautical charts, and georeferenced satellite images such as Google Maps and World Imagery were used. Considering that mean circulation is largely driven by the wind with the prevailing winds consistently easterly and northeasterly around the Enewetak Atoll, it is anticipated that the released radionuclide plume could generally travel toward the west and southwest directions (i.e., leaving the RMI territory and impacting areas to the west/southwest). Therefore, to sufficiently cover a broader potentially impacted area in addition to RMI, the model domain was designed to center around Runit Dome with a 1,000 km radius, and further extend toward the east to cover the entire EEZ of RMI. Figure C.1 shows the ocean model domain boundary.

The model grid bathymetry was created using a combination of available public data sources, including the 15-arc minute, global topo-bathymetry dataset downloaded from GEBCO,[2] and the ASTGTM v003 1-arc second global Digital Elevation Model (DEM) for the Marshall Islands.[3] Specifically, the GEBCO global bathymetry dataset was used for the entire model domain while

---

[1] https://www.marineregions.org/downloads.php

[2] https://download.gebco.net/

[3] https://rmi-data.sprep.org/resource/1-arc-second-digital-elevation-model-and-hillshade

the 1-arc second DEM was used for a more accurate representation of the surface elevation of the islands of the Enewetak Atoll.

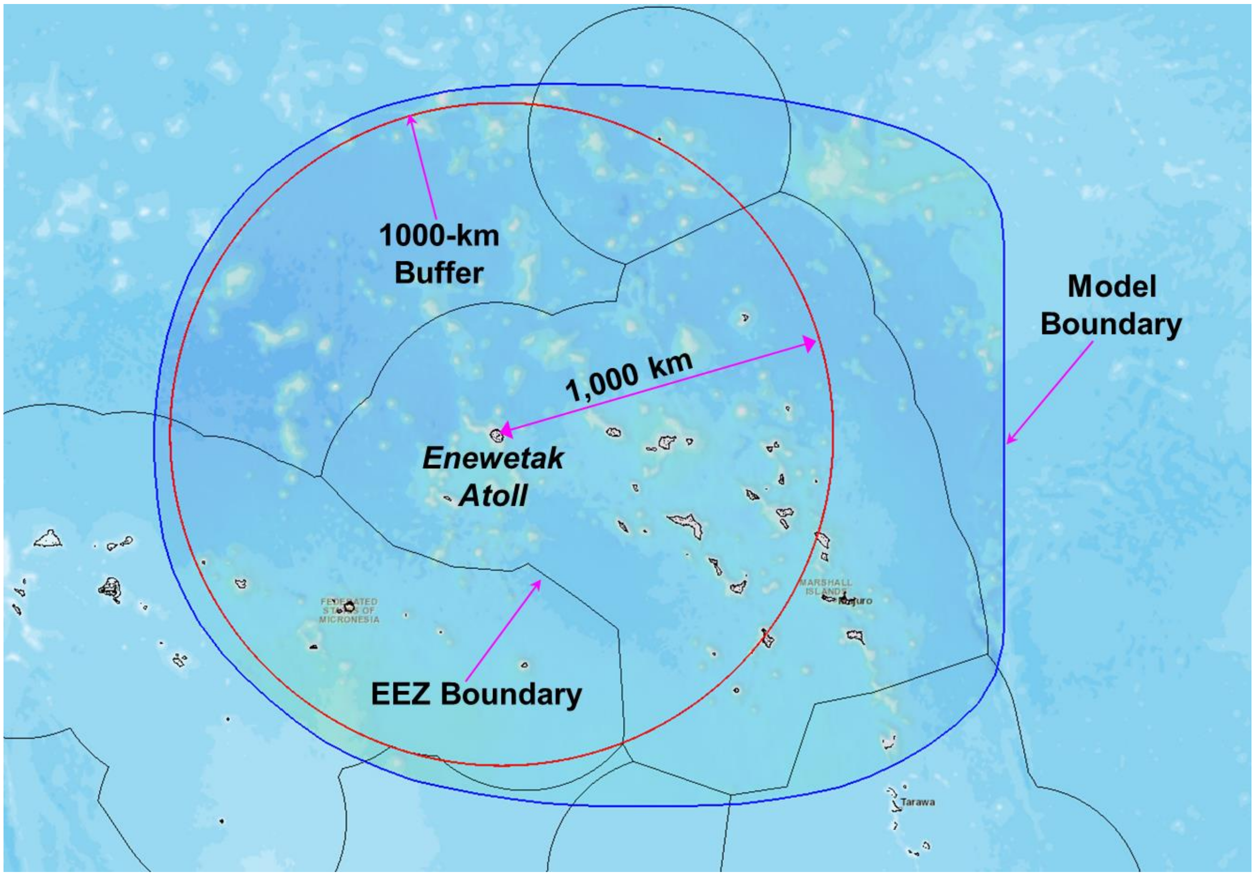

Figure C.1. Ocean model domain coverage (blue polygon) with reference to the EEZ boundaries (black polygons).

The horizontal grid resolution varies throughout the model domain, depending on the bathymetry gradients and areas of interest. After several iterations of grid refinement and model testing, the final model grid was determined. The final model grid has a spatial resolution of <30 m (i.e., grid size in terms of the triangular side length) at the Runit Dome to a maximum of >10 km along the open boundaries (Figure C.2). By using relatively high grid resolutions for the Enewetak Atoll, the model can reasonably resolve fine-scale shoreline features and manmade structures such as the Runit Dome (Figure C.3), which affects near-shore hydrodynamics and transport of radionuclides. In addition, to accurately simulate radionuclide release and transport around the Enewetak Atoll especially during storm events, wetting and drying of the intertidal zones was simulated in the model by explicitly covering all land and water areas with computational grid (Figure C.3). The final model grid has a total number of 201,470 nodes and 401,859 elements.

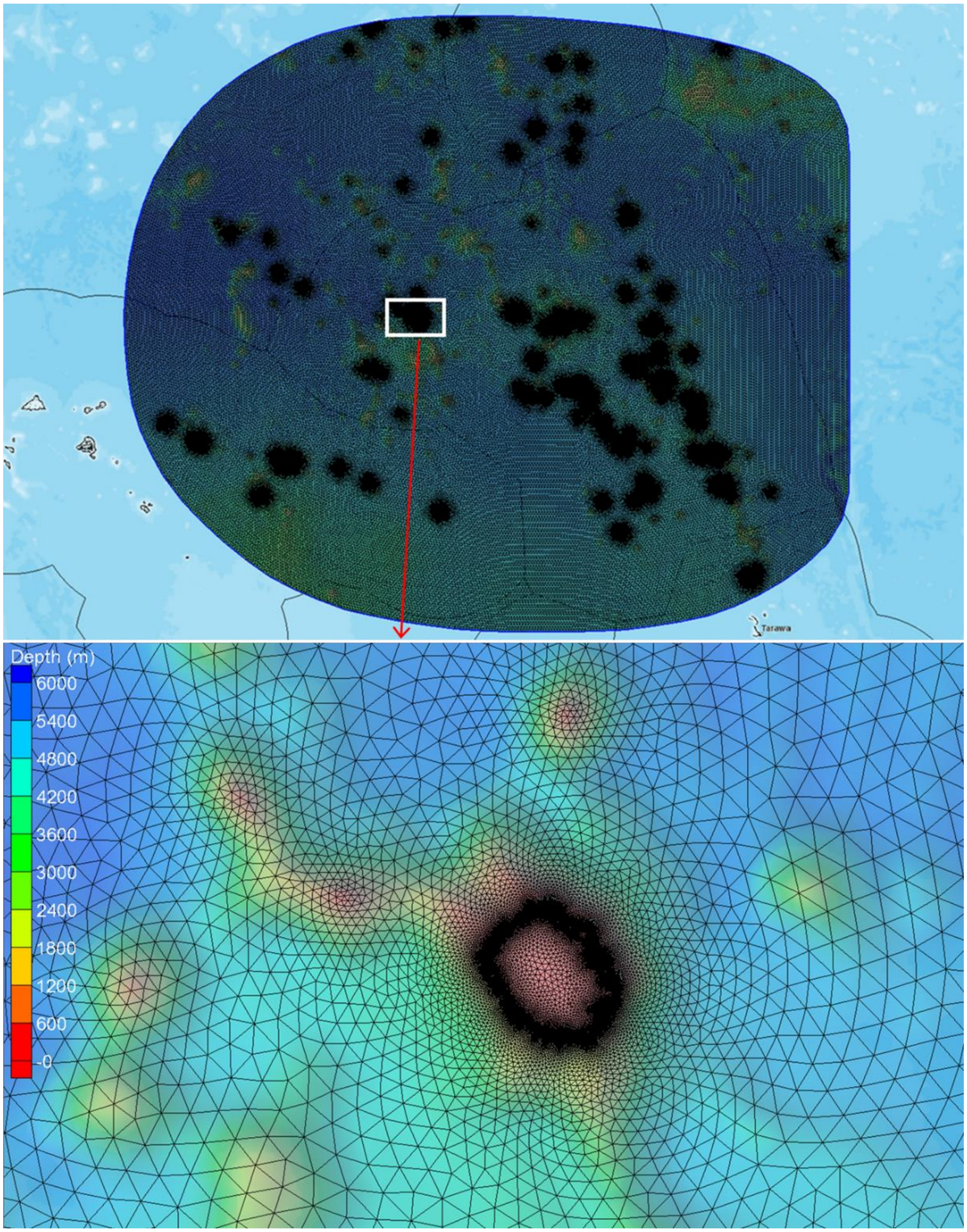

Figure C.2. Model grid for the whole domain (upper panel) and zoom-in view of the Enewetak Atoll and surrounding regions.

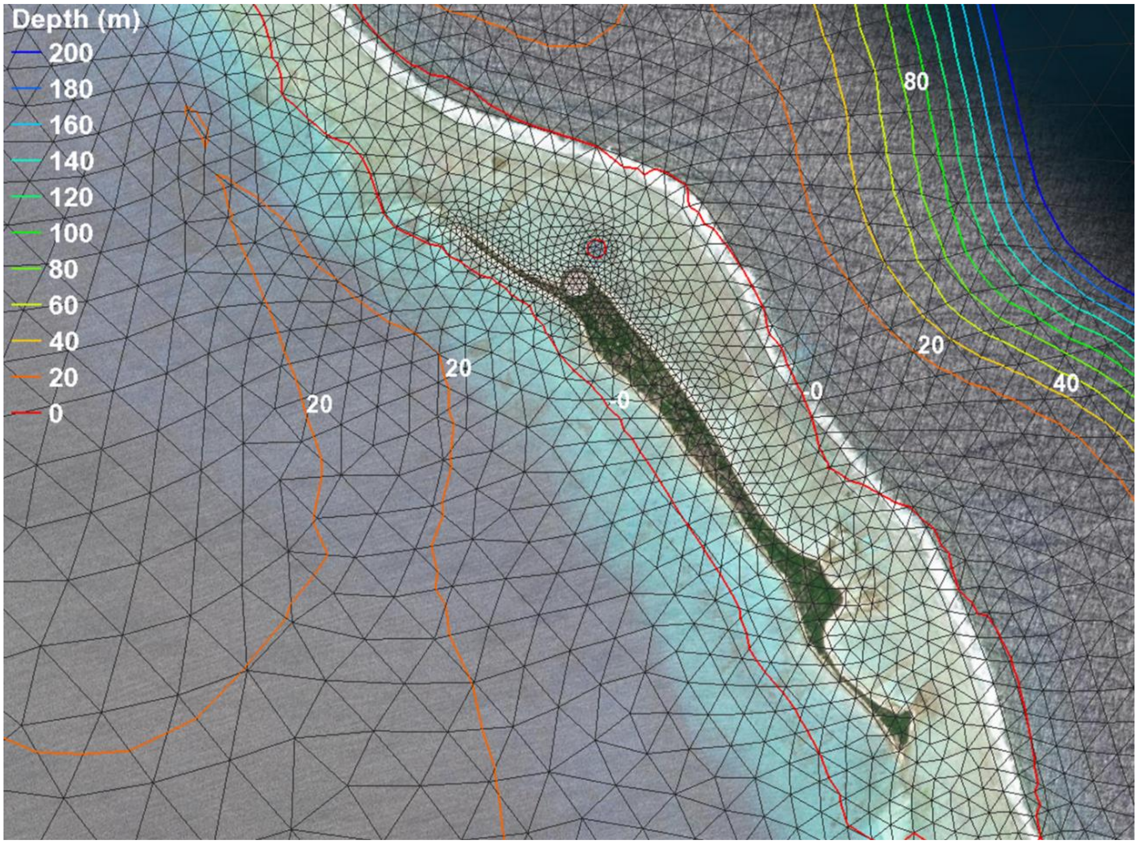

Figure C.3. Zoom-in view of the model grid for the Runit Dome and Runit Island showing the high-resolution mesh used to resolve the Runit Dome structure.

To resolve the vertical structure of large-scale ocean circulation in the model domain, the vertical discretization used 30 terrain-following sigma layers in the FVCOM model. The sigma layer thickness distribution was specified to resolve the external boundary interactions with atmosphere and ocean bed in greater detail by using smaller layer thickness toward surface and bottom boundaries with an appropriate power function.

C.2 FVCOM Setup for Historical Conditions

After the grid was developed, the FVCOM hydrodynamic model was driven by various forcing data, including meteorological data (e.g., winds, atmospheric pressure, relative humidity, air temperature, solar radiation) covering the entire model domain and hydrodynamic conditions (e.g., tides, temperature, salinity) at the open ocean boundary. For open boundary conditions, both tides and subtidal oceanographic conditions including water level, salinity and temperature were obtained from three hourly, 1/12-degree HYCOM global reanalysis[4] (Metzger et al., 2017). The tidal forcing was obtained from Oregon State University's TPXO8-atlas tidal database (Egbert and Svetlana, 2002), which includes a total of 13 major tidal constituents. The meteorological forcing was based on the global atmospheric reanalysis model product, i.e., the European Centre for Medium-Range Weather Forecasts ERA5, which has a spatial resolution of 0.25 degree and temporal resolution of 1 hour (Hersbach et al., 2023). Both HYCOM and ERA5

---

[4] https://www.hycom.org/dataserver/gofs-3pt1/reanalysis

products have been widely used by the oceanographic community. Example plots of the HYCOM and ERA5 forcing parameters over the hydrodynamic model domain are shown in Figure C.4 through Figure C.8. Strong spatial gradients can be seen in both forcing products. For example, temperatures are generally warmer toward south/southwest (i.e., the equator) in the model domain for both ocean (Figure C.4) and atmosphere (Figure C.7), while the ocean surface salinity shows an opposite trend (Figure C.5).

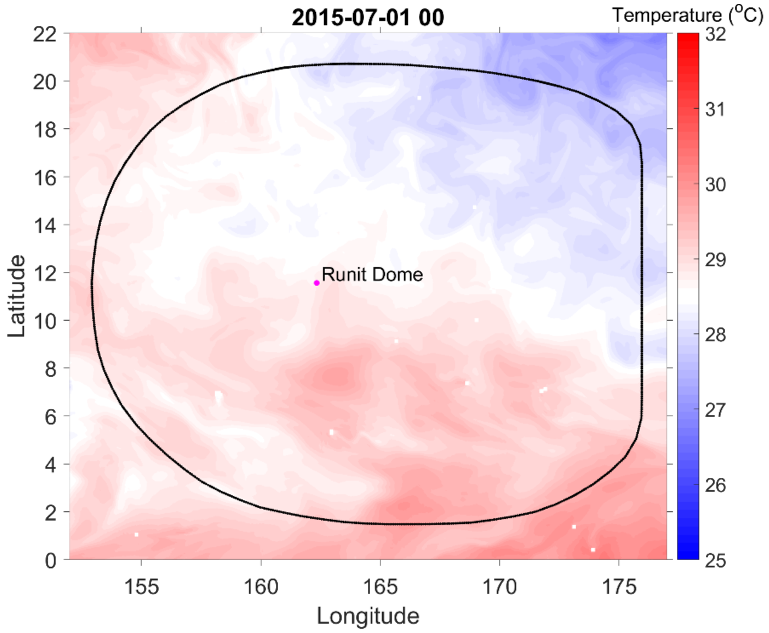

Figure C.4. Example plot of the HYCOM surface temperature field over the FVCOM domain on July 1, 2015.

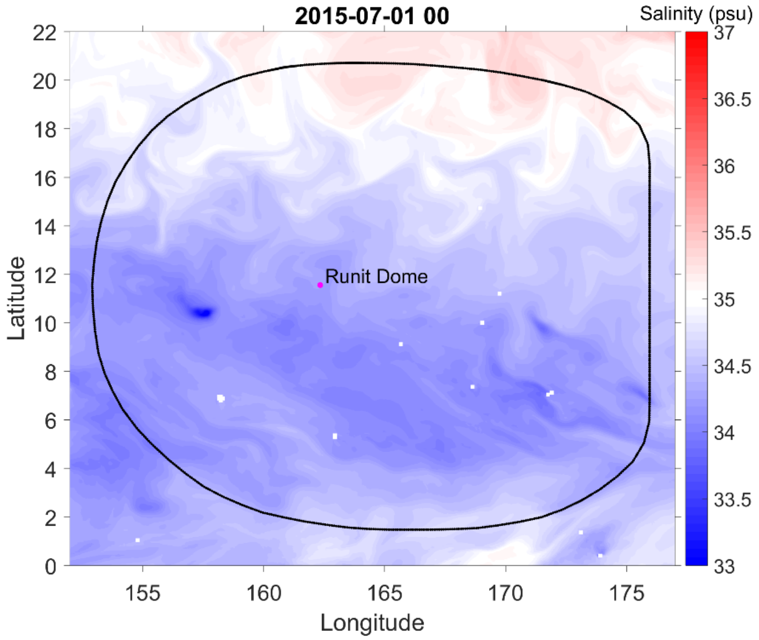

Figure C.5. Example plot of the HYCOM surface salinity field over the FVCOM domain on July 1, 2015.

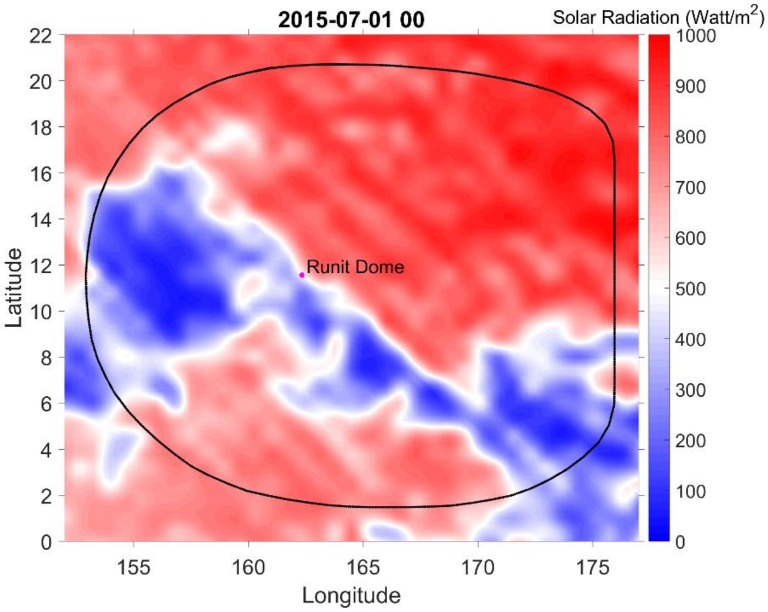

Figure C.6. Example plot of the ERA5 downward shortwave solar radiation field over the FVCOM domain on July 1, 2015.

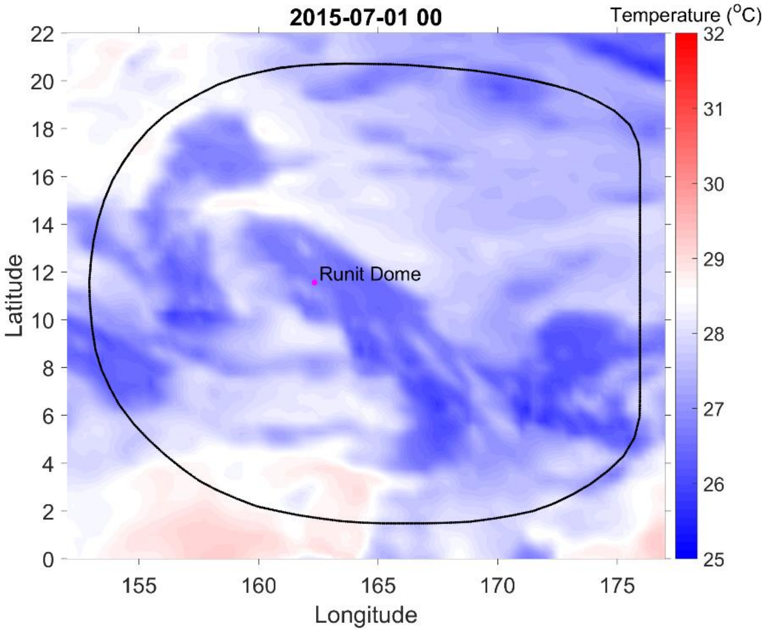

Figure C.7. Example plot of the ERA5 surface air temperature field over the FVCOM domain on July 1, 2015.

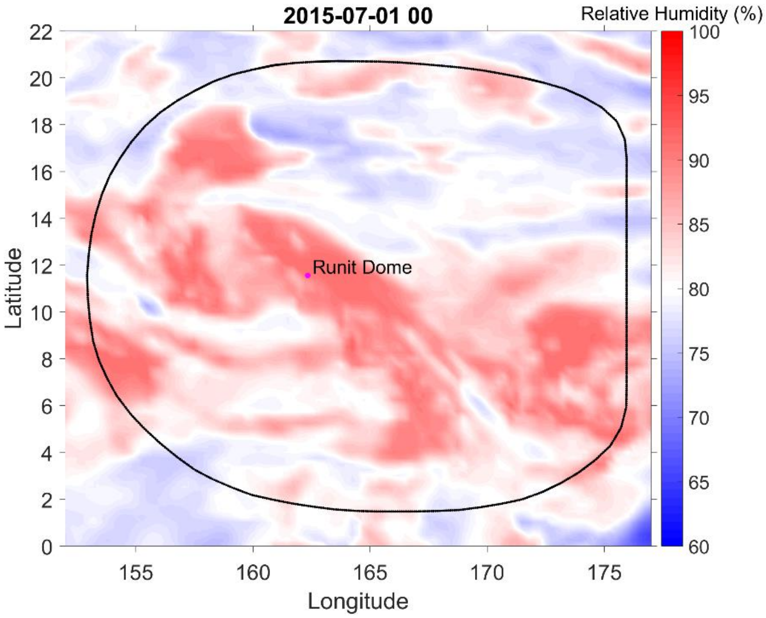

Figure C.8. Example plot of the ERA5 surface air relative humidity field over the FVCOM domain on July 1, 2015.

To better characterize the hydrodynamic impacts of episodic storm events on radionuclide release and transport from Enewetak Atoll, it is critical to drive the hydrodynamic model with meteorological forcing that has sufficient resolutions in both time and space. PNNL used the high-resolution surface wind and air pressure forcings produced by the WRF-ARW simulations. Specifically, during the storm period, the two most important forcing variables in the ERA5 product (i.e., air pressure and wind) controlling storm surge simulations, were replaced with corresponding output from the high-resolution WRF-ARW model predictions. To facilitate FVCOM model simulations for the full year of 2015, we embedded three historical storm events into the year 2015 forcing input based on their times of occurrence during the year. Figure C.9 shows the embedded high-resolution surface wind and air pressure fields during storm landfall near Enewetak Atoll for Storm 1 (the July 2015 storm). Typical typhoon structures such as lower air pressure in the eye of storm and stronger wind toward the eye wall was very well captured by the WRF-ARW model.

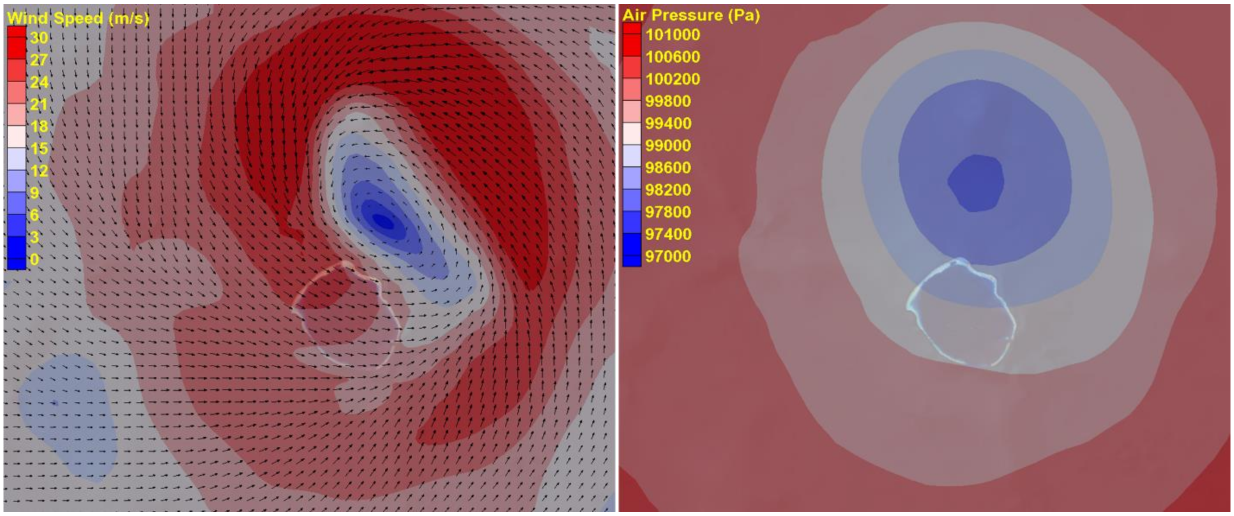

Figure C.9. Example plot of wind (left panel) and air pressure (right panel) field around the Enewetak Atoll during Storm 1 (July 2015 Storm) landfall at 7/5/2015 15:00:00 GMT. The forcing field was predicted by PNNL's high-resolution WRF-ARW model.

To produce a full year of FVCOM simulation for year 2015 with three embedded historical storms, the model simulation period was set to start on December 2, 2014, with the last month of year 2014 used as the model spin-up period. The model was initialized with oceanographic condition interpolated from the HYCOM global dataset. The model output was archived at hourly timestep and included all hydrodynamic variables that are necessary to drive FVCOM-ICM simulations.

C.3 Model Calibration

Before conducting the full-year simulation, model parameters, such as bottom roughness and open boundary sponge layer configuration, were iteratively calibrated. The iterative calibration compared model predictions to all available water level observations downloaded from PSMSL[5] website. Figure C.10 shows all available tidal gauges inside the FVCOM domain. Because Station Kwajalein does not have data in 2015, PNNL configured the model for a separate period (September 2019) to perform water-level calibration. Figure C.11 shows the model-predicted water surface elevations compared with the observed water levels at all water-level stations inside the model domain. The results show excellent matching between model predictions and field data, suggesting the model has been well calibrated for tidal predictions.

---

[5] https://psmsl.org/

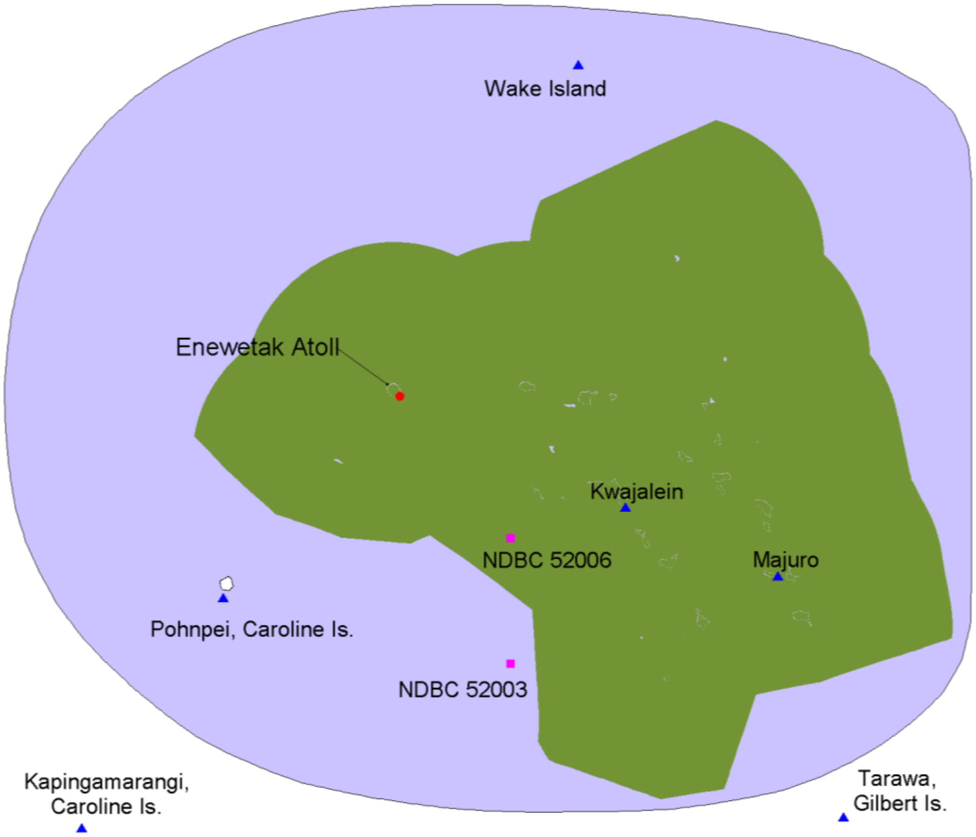

Figure C.10. Locations of the PSMSL tidal stations near the FVCOM domain. The four stations within the domain were used for model prediction comparison. NDBC locations are National Data Buoy Center buoys.

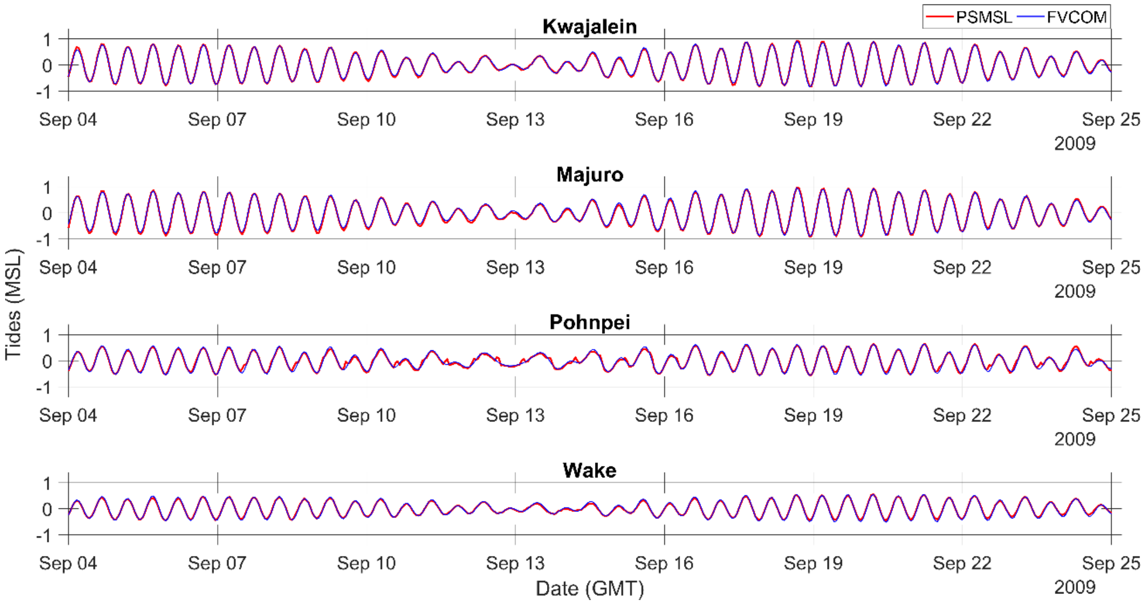

Figure C.11. Tidal elevation comparisons between FVCOM predictions and PSMSL measurements at four tidal gauges within the RMI model domain.

C.4 Model Validation

After the model was calibrated for tides, more realistic hydrodynamic simulations were performed by driving the model with additional forcing inputs, such as meteorological forcing and ocean boundary conditions as described previously. Because of the constraints of time and data availability, qualitative model validation was primarily used to verify that FVCOM can reasonably reproduce the hydrodynamic conditions within the domain of interest. Figure C.12 shows water-level comparisons during the Storm 1 simulation period. An overall good match between model predictions and field measurements was obtained.

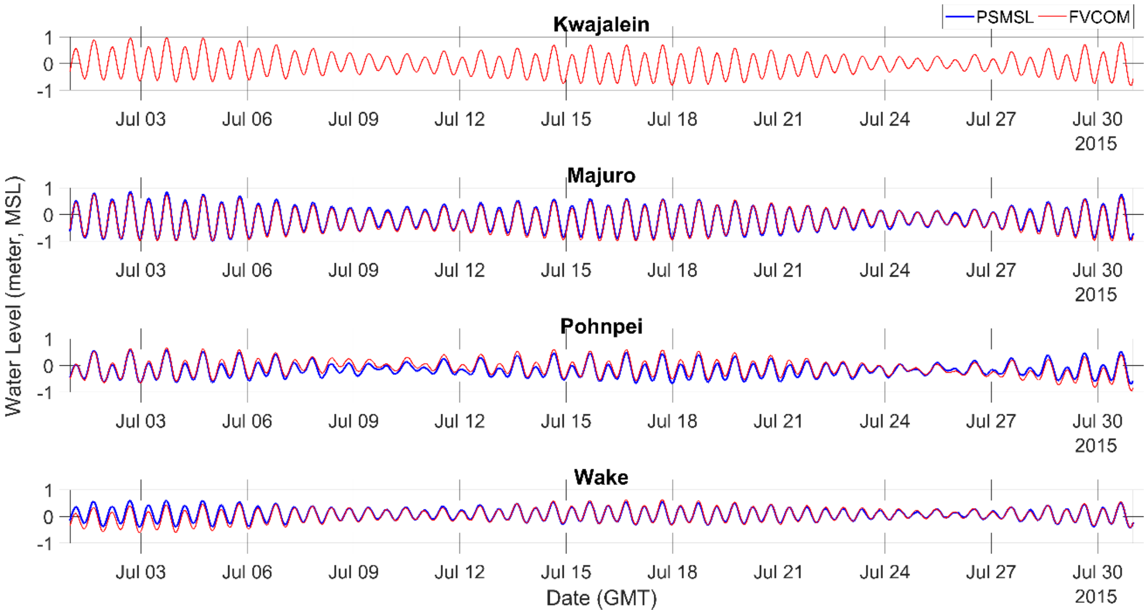

Figure C.12. Tidal elevation comparisons between FVCOM predictions and PSMSL measurements at four tidal gauges within the RMI model domain during Storm 1 (July 2015) simulation period (note field data for the simulation period were unavailable at Kwajalein).

Figure C.13 shows additional comparisons between the water level simulated by FVCOM and tidal level predictions downloaded from XTide website[6] at the Enewetak tidal gage (the location of this gage is shown in Figure C.10) during the Storm 1 simulation period. Overall, the FVCOM simulations compared with XTide predictions very well. Increased water levels predicted by the FVCOM model during the storm landfall time around 7/5/205 were caused by storm surge induced by Storm 1. In summary, the overall good performance of FVCOM in simulating tidal water level across the entire model domain suggests the model is reproducing tidal-driven circulation very well, which plays an important role, especially in exchanging water and radionuclides between the Enewetak lagoon and the ambient ocean.

---

[6] http://tbone.biol.sc.edu/tide/

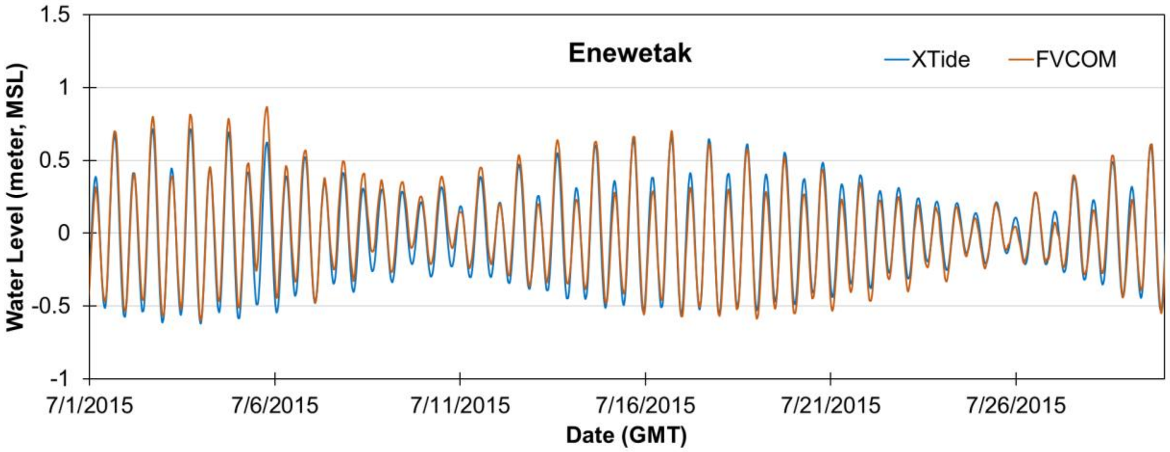

Figure C.13. Tidal elevation comparisons between FVCOM predictions and XTide tidal gage during Storm 1 (July 2015) simulation period.

In addition to tides, wind, and air pressure, density gradients play an important role in modulating water circulation, especially in the open ocean. For the area of interest in this study, vertical thermal gradient is important as it controls vertical straitification and mixing. Therefore, it is vital to examine the model's performance in simulating the vertical temperature profile. Figure C.14 and Figure C.15 compare the annual vertical temperature profiles between FVCOM predictions and field measurements at two NDBC buoys 52003 and 52006, respectively (see Figure C.10). Qualitatively, the model-predicted temperature profiles compared reasonably well with field data by successfully reproducing the general patterns of vertical temperature gradients.

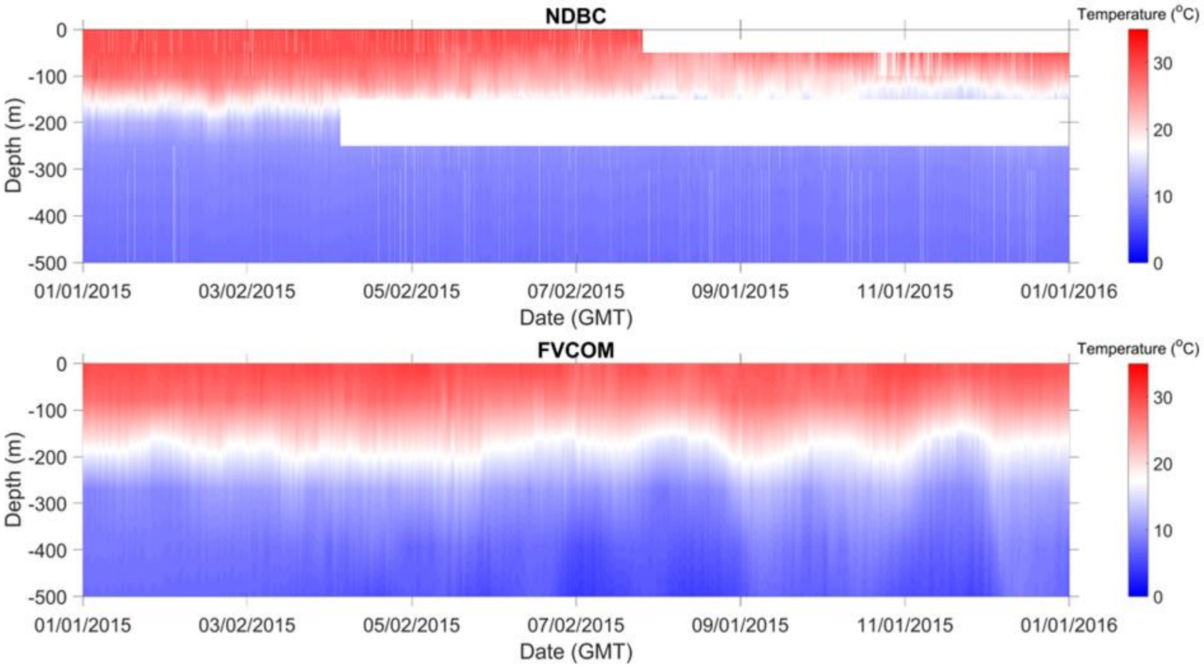

Figure C.14. Vertical temperature profile comparisons between field measurements (upper panel) and FVCOM predictions (lower panel) at NDBC 52003 for the full year of 2015. Note data gaps are present in the NDBC dataset.

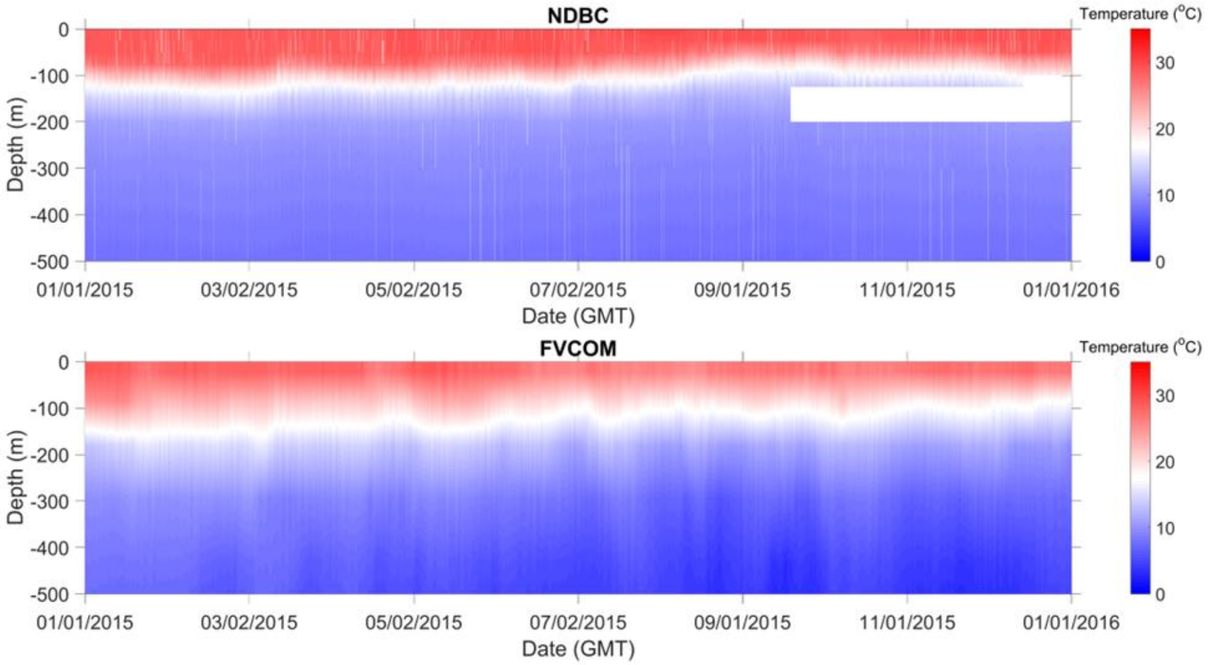

Figure C.15. Vertical temperature profile comparisons between field measurements (upper panel) and FVCOM predictions (lower panel) at NDBC 52006 for the full year of 2015. Note data gaps are present in the NDBC dataset.

C.5 Model Predictions in Current Climate

Figure C.16 shows the instantaneous surface current field around Enewetak Atoll during the Storm 1 landfall period in July 2015. Driven by the strong typhoon wind field, intensified surface currents exceeding 2 m/s were predicted in many shallower areas along the edges of the atoll. Correspondingly, the bottom shear stress also showed similar responses during the storm event (Figure C.17). Relatively high shear stresses greater than 3 Pa were predicted on the west side of the atoll.

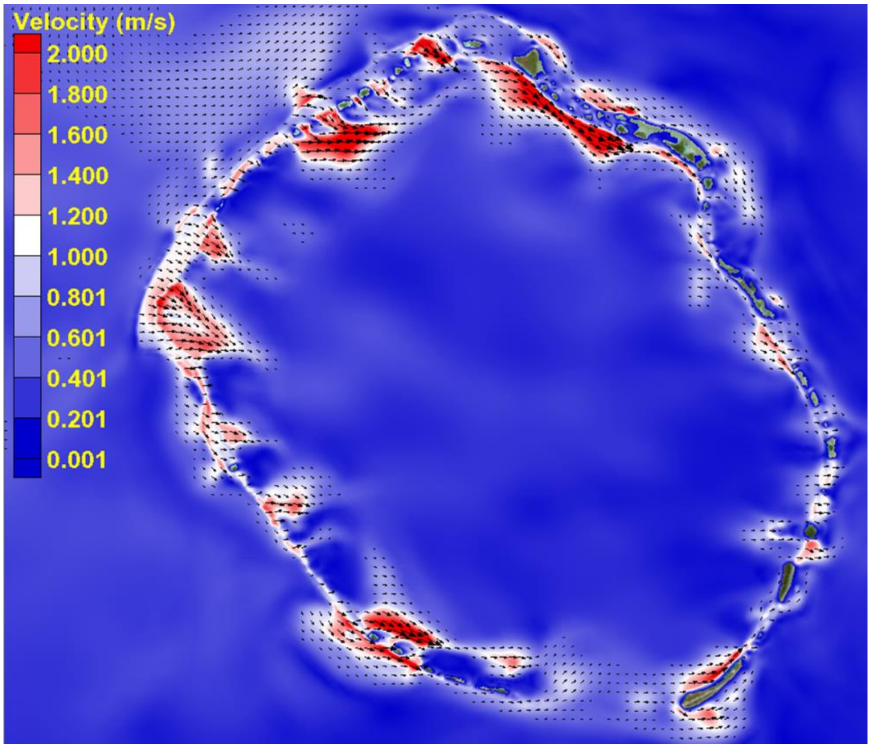

Figure C.16. Instantaneous surface current field around Enewetak Atoll during Storm 1 (July 2015) landfall at 7/5/2015 15:00:00 GMT.

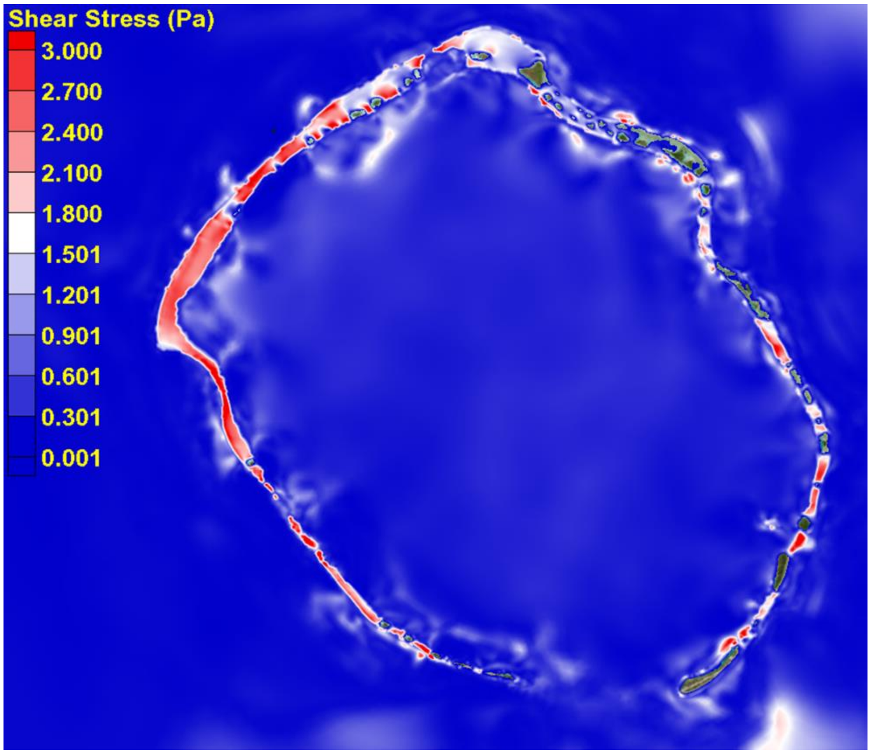

Figure C.17. Instantaneous bottom shear stress (Pa) distribution around Enewetak Atoll during Storm 1 (July 2015) landfall at 7/5/2015 15:00:00 GMT.

C.6 Future Conditions Simulations

For future condition simulations, FVCOM was configured in a similar way; however, the model was forced with a perturbated version of the forcing files used for current condition simulation. As mentioned previously, the two most important forcing variables affecting hydrodynamic circulation during the typhoon events are surface wind and air pressure, which were simulated by the WRF-ARW model after incorporating the future climate perturbations from CMIP6 projections (see Section 3.0 and Appendix B). Compared to the baseline condition in year 2015, the projected sea-level rise for the future period is another important factor. A warmer climate is also expected in the future, which is directly reflected as increased air and ocean temperature conditions compared to those in the current condition. Therefore, these two changes were implemented in the FVCOM forcings by superposing additional temperature perturbations obtained from CMIP6 projections. The predicted sea-level rise of 0.62 m for 2090 in the central and western Pacific was added to the 2015 baseline water levels open boundary conditions. For surface air temperature and ocean temperature perturbations, the spatially varying increments between future (Year 2090) and current (Year 2015) climate conditions (Figure C.18) were superimposed onto the current forcing inputs.

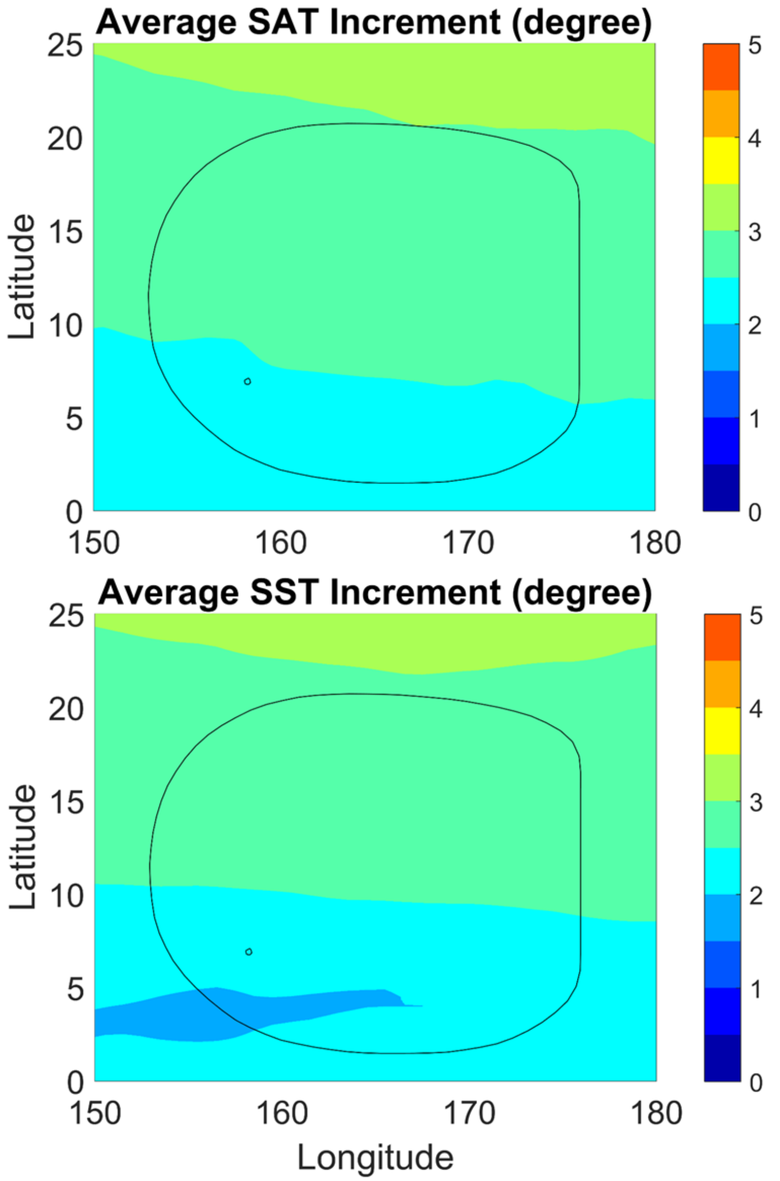

Figure C.18. Spatially varying temperature increment between baseline (Year 2015) and future (Year 2090) for surface air temperature (upper panel) and SST (lower panel) obtained from CMIP6 projections.

Figure C.19 shows the water level time series during Storm 1 event for both current and future climate conditions at the center of Enewetak Lagoon. Figure C.20 shows the vertical temperature profile comparisons between the current and future climate conditions. In both conditions, the water temperature inside the lagoon shows very small vertical gradients at this location, suggesting the water column is generally well mixed in the vertical direction. On average, the water temperature in the future condition is about ~2 degrees warmer than the current climate, which is consistent with CMIP6 projections. Similar results were also obtained for Storms 2 and 3, which are not shown here. The FVCOM-predicted hydrodynamic conditions for the three selected storms, both for the current and future climates, were provided for input to FVCOM-ICM.

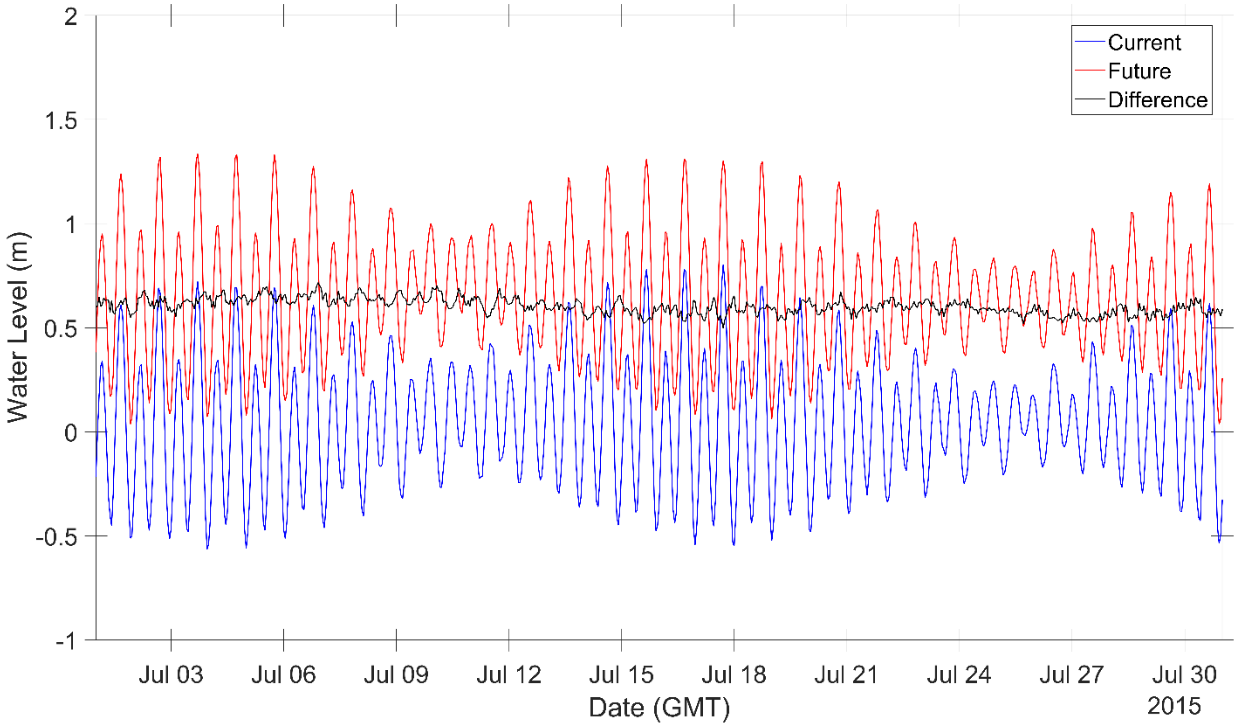

Figure C.19. Model-predicted water level for current condition, future condition, and the difference during Storm 1 (July 2015) period at the center of Enewetak Lagoon.

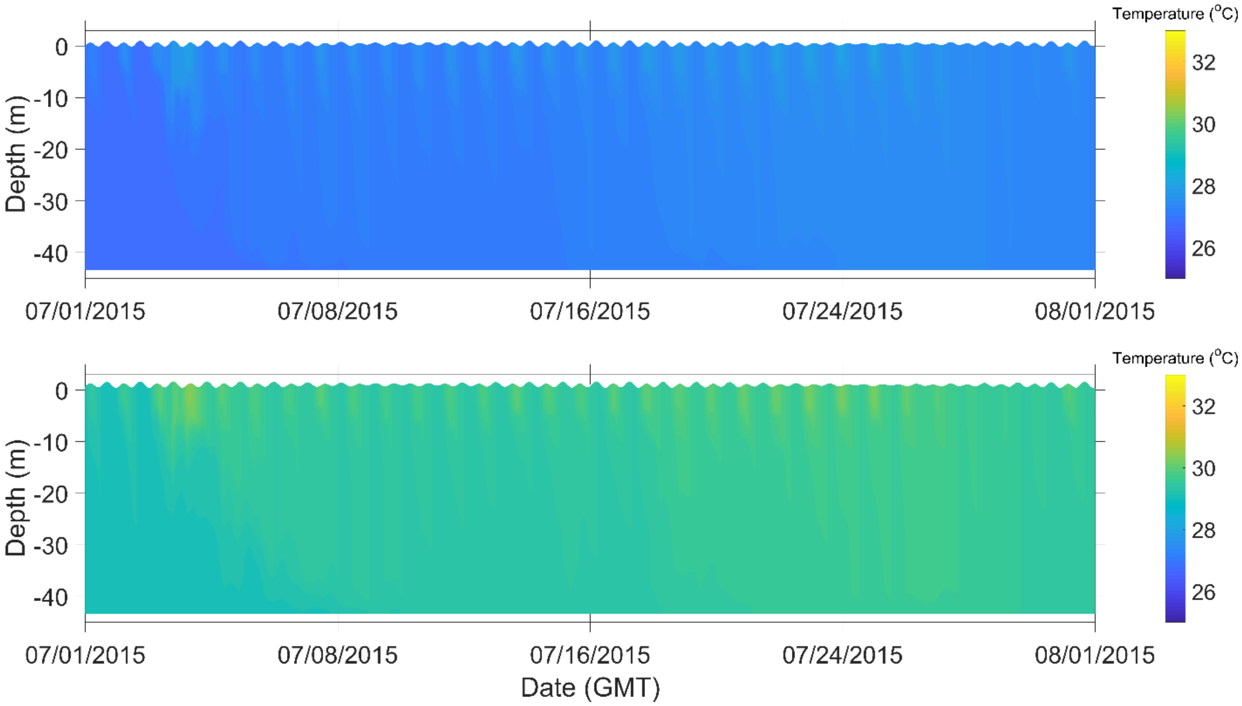

Figure C.20. Model-predicted water temperature profiles for current (top panel) and future (bottom panel) climate conditions during Storm 1 (July 2015) period at the center of Enewetak Lagoon.

Appendix D
Mobilization and Transport of Radionuclides

The hydrodynamic stresses, such as elevated tides and currents induced by the potentially extreme weather events in the current or a future climate scenario, may cause redistributions of radionuclides through the resuspended or eroded sediments in the lagoon. Such a scenario can be simulated with a pollutant fate transport model with built-in sediment interactions and processes. In this project, the transport of radionuclides with associated kinetics is simulated using the externally coupled FVCOM-ICM. FVCOM-ICM is a FVCOM framework-based biogeochemical model with mature capabilities of simulating the advection and diffusion of pollutants/contaminants (Khangaonkar et al., 2017, 2018, 2019). The radionuclide kinetics implemented in FVCOM-ICM include radioactive decay and partitioning onto suspended particulate matter (Figure D.1). The three-dimensional ocean current field, temperature, salinity, and eddy diffusivities from FVCOM hydrodynamic simulations were externally coupled with FVCOM-ICM to conduct the model runs for simulating the mobilization and transport of radionuclides for each climate scenario.

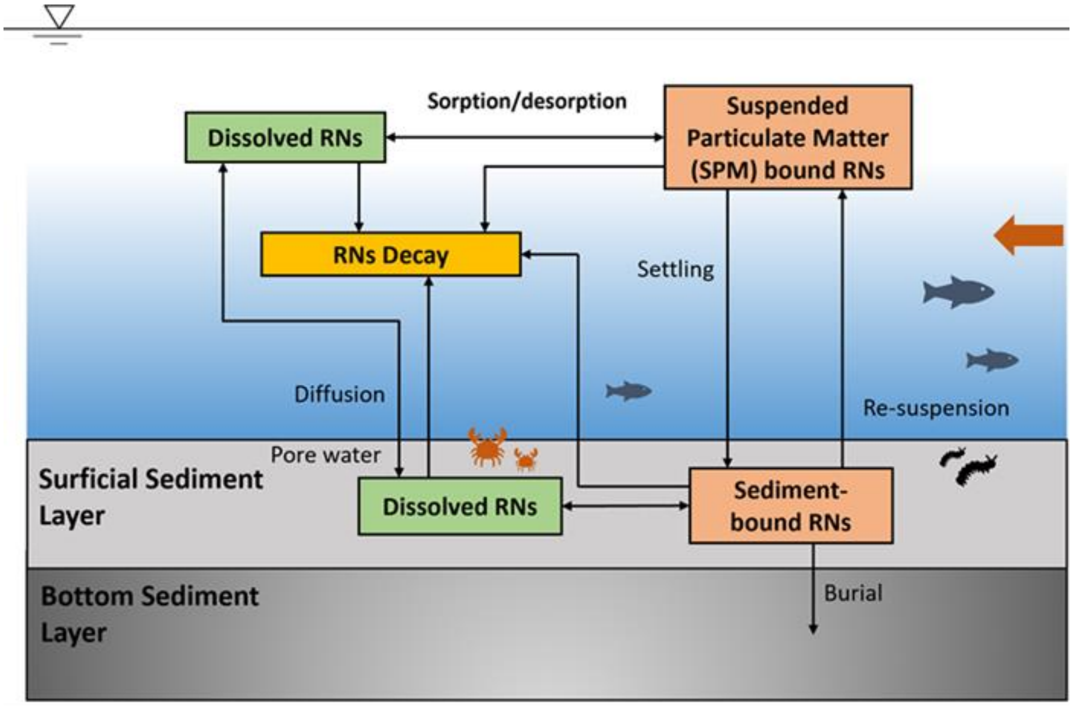

Figure D.1. Schematic representation of the radionuclide fate and transport processes implemented in FVCOM-ICM.

D.1 Sediment Processes and Radionuclide Kinetics

The most critical aspect of simulating the transport and mobilization is capturing the complex interactions of radionuclides with the sediments and associated sedimentation processes. The current version of FVCOM-ICM can simulate the basic sediment processes such as settling, erosion and dynamically changing surficial sediment layers. The primitive mechanistic understanding-based sediment processes implemented in the radionuclide kinetic module are adopted from the approach used to study the radionuclide (^{137}Cs) fate and transport in coastal ocean waters by Higashi et al. (2015). However, the sedimentation-related parameterization in Higashi et al.'s approach was improved here to better emulate the conditions that may arise in the lagoon.

D.1.1 Sediment Bed Erosion and Resuspension

The primitive model implemented to simulate erosion is primarily based on the critical bed shear stress τ_{cr} (N/m^2) and the erosion coefficient E (kg m^{-2}s^{-1}), which is analogous to the erosion rate in other sediment erosion models proposed in the literature (Eq.1).

$$M_{sus} = Max\left[0.0, E\left\{\left(\frac{\tau_b}{\tau_{cr}}\right) - 1.0\right\}\right] \tag{1}$$

Here, τ_b (N/m^2) is the bed shear stress estimated in hydrodynamic computations performed with FVCOM. M_{sus} (kg m^{-2}s^{-1}) is the suspended sediment flux that arise from the sediment bed due to erosion. Both τ_{cr} and E are determined based on the characteristics of the sediment bed (Section D.2.2).

D.1.2 Settling of Sediment Particles

The level of intrusion of radionuclides from the sediment bed into the water column is primarily dictated by the interplay between the erosion and settling processes; hence, the correct determination of the settling velocity of sediment particles is important. However, in the absence of site-specific field or laboratory experiment data to estimate the settling velocity, this study relies on the available analytical or semi-empirical methods to estimate the particle settling velocity. The model considers only one representative grain size for the settling process, and the free settling velocity for a typical spherical-shaped particle is determined using the analytical method proposed by Rubey (1933) (Eqs. 2 and 3).

$$w_{sdf} = F_1\sqrt{Rgd} \tag{2}$$

where

$$F_1 = \sqrt{\frac{2}{3} + \frac{36\nu^2}{Rgd^3}} - \sqrt{\frac{36\nu^2}{Rgd^3}} \tag{3}$$

Here, ν (m^2/s) is the kinematic viscosity of sea water; $R = \left(\frac{\rho_s}{\rho_w} - 1\right)$ is the submerged specific gravity, where ρ_s (kg/m^3) and ρ_w (kg/m^3) are the densities of sediment particles and water, respectively; d (m) is the diameter of the representative sediment particle; g (m^2/s) is the gravitational acceleration; w_{sdf} (m/s) is the free settling velocity for a single particle.

The equation is only valid for a single particle under free settling conditions. However, under higher suspended sediment concentrations that exhibit high erosion during significantly high bed shear stresses, the free settling principles are no longer valid as the particle collisions obstruct the settling, and therefore, the settling can be substantially diminished. To simulate this type of settling under the compounded effect from erosion, the model uses the hindered settling principles as proposed by Richardson and Zaki (1954) (Eq. 4).

$$w_{sdm} = w_{sdf}(1 - C)^n \tag{4}$$

In Eq. 4, w_{sdm} (m/s) is the effective settling velocity; C (m^3/m^3) is the volumetric suspended sediment concentration; n is a non-dimensional empirical coefficient that depends on the Reynolds number. Richardson and Zaki (1954) determined the maximum value for $n \approx 5.5$ experimentally. This study uses n = 5.5 as a conservative approach due to the absence of data to empirically determine n.

D.1.3 Radionuclide Kinetics

The dominant kinetic processes related to radionuclides implemented in the model include radionuclide partitioning onto the suspended matter and radioactive decay together with the sediment processes. For the kinetics computations, the suspended particulate matter (SPM) is assumed to be a representation of both bulk organic and inorganic matter in the water column, although the sediment parametrization is based on solid inorganic sediments, excluding the marine biota. The partitioning of radionuclides into SPM assumes equilibrium conditions and uses the Langmuir isotherm-based partitioning model.

$$f_{pi} = \frac{K_{di}M_s}{\varphi + K_{di}M_s} \tag{5}$$

$$f_{di} = \frac{\varphi}{\varphi + K_{di}M_s} \tag{6}$$

$$C_{pi} = f_{pi}C_{ti} \tag{7}$$

Eq. 5, 6, and 7 briefly describe the partitioning model implemented in FVCOM-ICM. f_{pi} and f_{di} are the fractions of i^{th} radionuclide in particulate and dissolved phases, respectively. K_{di} is the equilibrium partitioning coefficient of i^{th} radionuclide, and M_s is the concentration of the particulate matter. φ is the porosity (i.e., ratio of the volume of water to the total volume of water and solids). C_{pi} and C_{ti} are the concentrations of i^{th} radionuclide in the particulate phase and the total concentration of ith radionuclide in the water column or sediment layer. In addition to partitioning, radionuclides associated with all phases (dissolved or particulate) undergo radioactive decay. The radioactive decay process was modeled using a simple first-order exponential decay function based on the half-life of the radionuclides (Equation). The effect of progeny creation or other transformation processes during the decay was assumed to be negligible and was not considered in model kinetics.

$$A_i(t) = A_{oi}e^{-\lambda_i t} \tag{8}$$

In Eq. 8, A_{oi} is the initial activity of ith radionuclide; $A_i(t)$ is the i^{th} radionuclide activity after time t; λ_i is the decay constant, which is based on the half-life of the i^{th} radionuclide ($\lambda_i = Ln(2)/T_{i1/2}$; with $T_{i1/2}$ being the half-life of the ith radionuclide).

D.2 FVCOM-ICM Setup and Simulations

The primary objective of FVCOM-ICM simulations was to investigate the mobilization and transport of radionuclide-adsorbed suspended sediments throughout the atoll domain and surrounding outer ocean under the hydrodynamic stresses caused by the three selected extreme storms under current (2015) and future (2090) climates. Therefore, the FVCOM-ICM simulations were conducted as separate scenarios, which included three storms in both the current and future climates. In addition, PNNL also performed simulations of three future scenarios in which a hypothetical failure of the Runit Dome was postulated to release radioactive material on land and in the lagoon adjacent to the dome. It should be noted that these scenarios are hypothetical and do not consider the likelihood or mechanics of the structural collapse of the Runit Dome. Under the hypothetical dome failure scenario, the model only simulated the fate and transport of released radionuclide-adsorbed sediments.

Because FVCOM-ICM operates on the same unstructured mesh that FVCOM used, the FVCOM NetCDF solutions files, which include hydrodynamic conditions and the grid information, were input directly into FVCOM-ICM. The following sections describe the model setup for different scenarios in detail.

D.2.1 Parameter Selection for Sediment Processes

A realistic representation of sediment processes (i.e., erosion and sedimentation) in the model depends on accurate estimation of sediments-specific parameters used in the mechanistic model. Very limited site-specific quantitative data for sediment-related parameters such as types of sediments, densities, porosity were available. Therefore, the sediment-related parameters were estimated using the qualitative and very limited quantitative information provided by the comprehensive survey on sediment geology (Wardlaw et al., 1991). Figure D.2 shows the delineation of sediment types in the uppermost sediment and soil layers of the atoll, including the lagoon and the islands.

The lagoon sediment and the islands' upper soil layer were characterized with six sediment types/classes (Figure D.2). The sediment type/class of coral knolls was excluded from the characterization assuming that they are tightly attached to the bed and less likely to be resuspended with the hydrodynamic stresses. Table D.1 shows some quantitative sediment characteristics as reported by Wardlaw et al. (1991). The sediment-related properties are determined using the fractions of sand and mud content and average grain sizes based on Van Rijn (2020). Because of lack of site-specific measurements, PNNL assumed a constant sediment porosity of 0.54 (Emery, 1954). FVCOM-ICM uses only one size class of suspended sediments for transport calculations. An average grain size of 0.062 mm was used to determine the theoretical maximum free settling velocity of the eroded sediment.

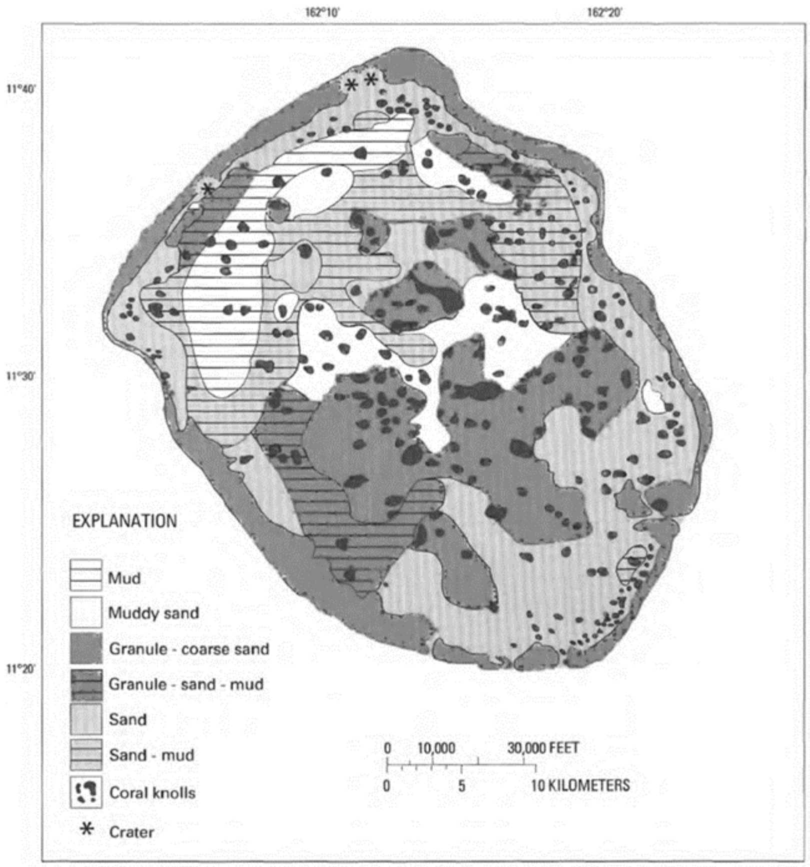

Figure D.2. Composition and characterization of lagoon sediments and island soil (Source: Wardlaw et al., 1991).

Table D.1. Quantitative estimates for the composition of bottom sediments.

Sediment-Type	Grain size (mm)	Average grain size (mm)	Sand (%)	Mud (%)
Granule-coarse-sand	0.5 - 2.0	1.25	52-67	6>
Granule-sand-mud	0.5-2.0	1.25	47-68	8.-24.
Sand	0.125 - 0.5	0.312	85	9>
Sand-mud	0.125 - 0.5	0.312	53-80	20-38
Muddy Sand	0.125 - 0.5	0.312	75-90	9.0-17.0
Mud	0.125 - 0.5	0.312	0-60	40<

Table D.2. Estimates of critical shear stresses and densities for different types of sediments in the lagoon

Sediment-Type	Critical shear stress (N/m2)	Density (kg/m3)
Granule-coarse-sand	1	2000
Granule-sand-mud	0.6	2000
Sand	0.6	1750
Sand-mud	0.2	1500
Muddy Sand	0.5	1700
Mud	0.15	1350
Average Grain Size for SPM	0.62 (mm)	
Average Density for SPM	1716.66 (kg/m^3)	

In the absence of site-specific measurements, the erosion coefficients were determined using the empirical expression for sand-mud mix sediment beds proposed by Perera et al. (2020). This approach utilized the sand and mud ratios in the bottom sediments of the lagoon (Table D.1) to estimate spatially distributed erosion coefficients for the model.

D.2.2 Characterization of Radionuclide Distribution in the Sediment Bed

As part of the model setup, the initial radionuclide concentrations in the sediment layer needed to be estimated at each model grid node. The radionuclide isopleth maps from AEC (1973) were interpolated at the model grid nodes to estimate the radionuclide concentrations in the lagoon sediment layer. The original data from the sources were processed using an average sediment thickness of 3.2 cm for the samples collected in the AEC survey (AEC, 1973) to compute the volumetric concentrations of selected radionuclides. Six radionuclides (^{241}Am, ^{207}Bi, ^{137}Cs, ^{152}Eu, ^{239}Pu, and ^{90}Sr) were included in the fate and transport modeling.

The estimated distributions of radionuclides in the bottom sediments for the current year 2015 and future year 2090 are shown in Figure D.3 to Figure D.8. The concentrations for 2015 and 2090 were estimated using the 1972 AEC survey data and correcting for radioactive decay during the intervening periods. In 2090, the concentrations of radionuclides with lower half-lives (e.g., ^{137}Cs) in the lagoon sediment will be substantially reduced.

D.2.3 Model Scenarios

FVCOM-ICM was setup to simulate the mobilization, fate, and transport of eroded bottom sediments. PNNL assumed that the bottom shear stresses are the main driving mechanism to erode and mobilize contaminated bottom sediments during extreme weather events such as storms. Therefore, the model setup included parameterizations for (1) erosion of the bottom sediments and their subsequent settling, (2) transport of suspended sediment-bound radionuclides in the lagoon and the surrounding ocean, and (3) radioactive decay. The other processes such as radionuclide exchange from groundwater and other terrestrial flows and dynamic recirculation of radionuclides already infiltrated into the marine food that contribute to the background radionuclide concentration were not considered in the current study due to the absence of reliable, site-specific data. Sediment erosion and settling is a dynamic process that occurs under normal tidal conditions. Therefore, a baseline model scenario was conducted for a 30-day period prior to the storms in both the current and future climates. The baseline scenario served as reference and provided initial conditions for simulating storm scenarios.

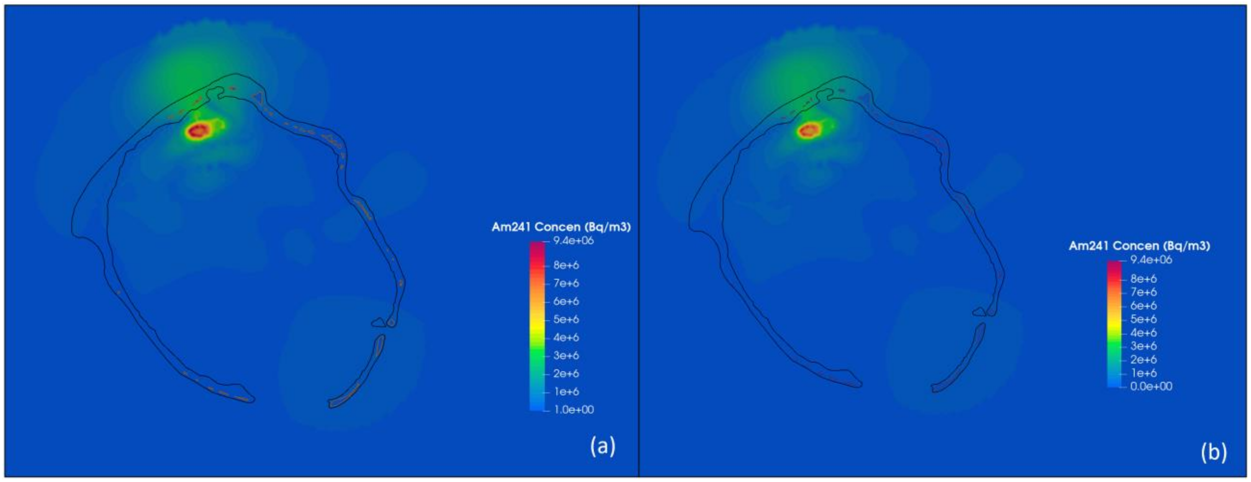

Figure D.3. Estimated distribution of ^{241}Am in the bottom sediment layer for (a) the current year 2015 and (b) the future year 2090 based on the data from AEC (1973).

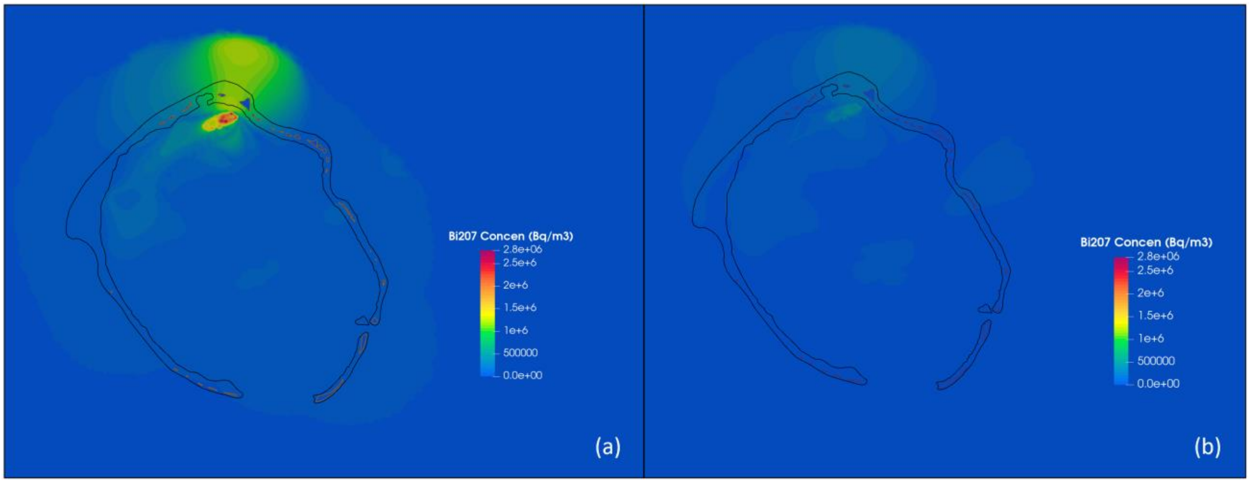

Figure D.4. Estimated distribution of ^{207}Bi in the bottom sediment layer for (a) the current year 2015 and (b) the future year 2090 based on the data from AEC (1973).

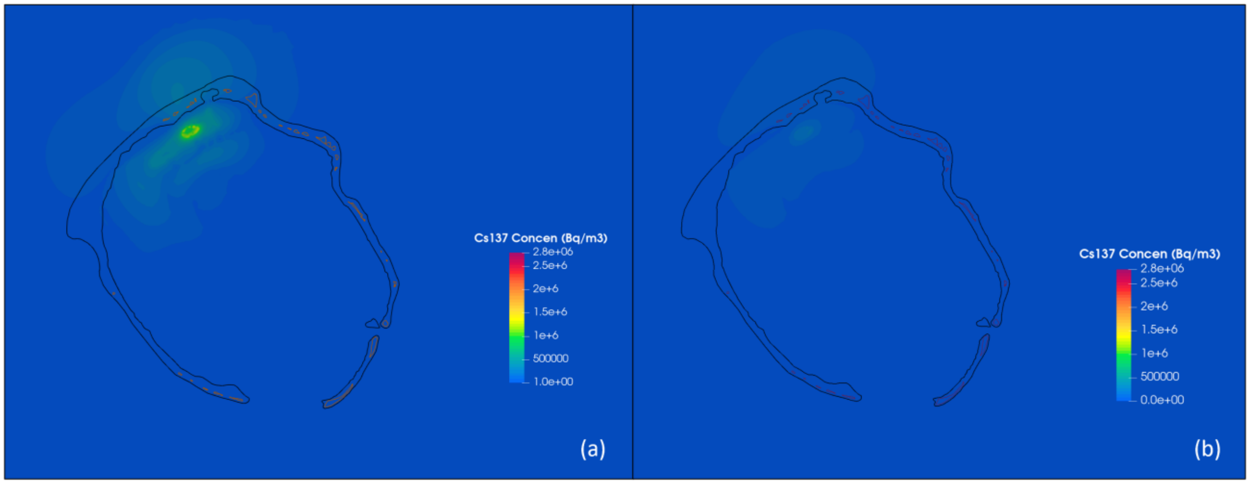

Figure D.5. Estimated distribution of ^{137}Cs in the bottom sediment layer for (a) the current year 2015 and (b) the future year 2090 based on the data from AEC (1973).

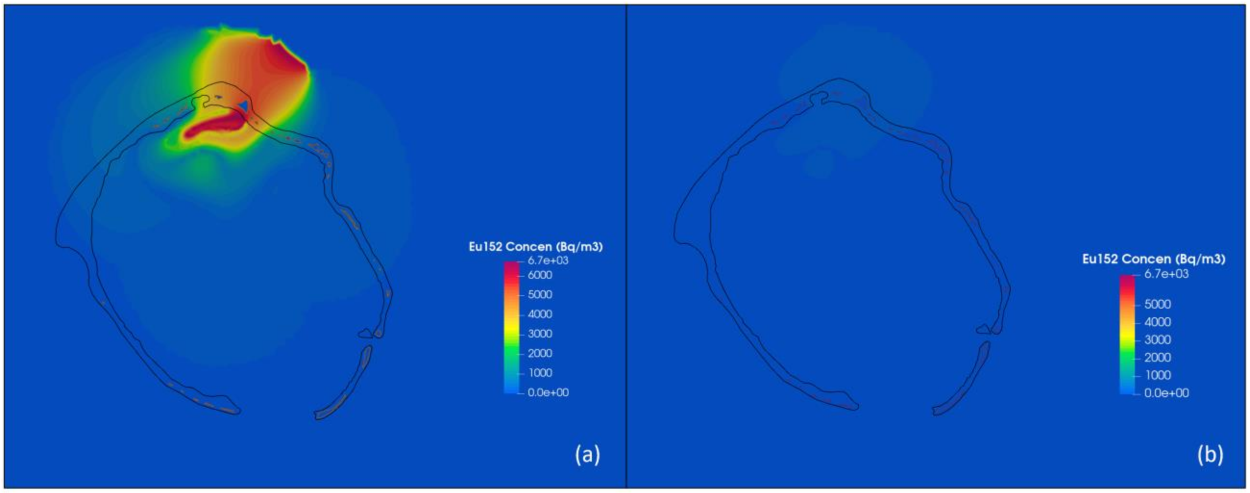

Figure D.6. Estimated distribution of ^{152}Eu in the bottom sediment layer for (a) the current year 2015 and (b) the future year 2090 based on the data from AEC (1973).

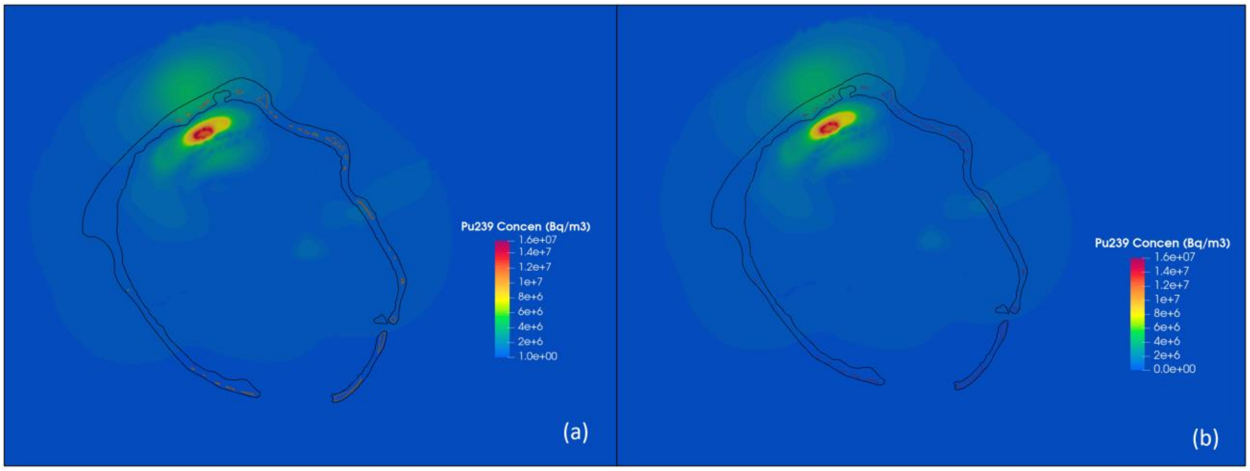

Figure D.7. Estimated distribution of ^{239}Pu in the bottom sediment layer for (a) the current year 2015 and (b) the future year 2090 based on the data from AEC (1973).

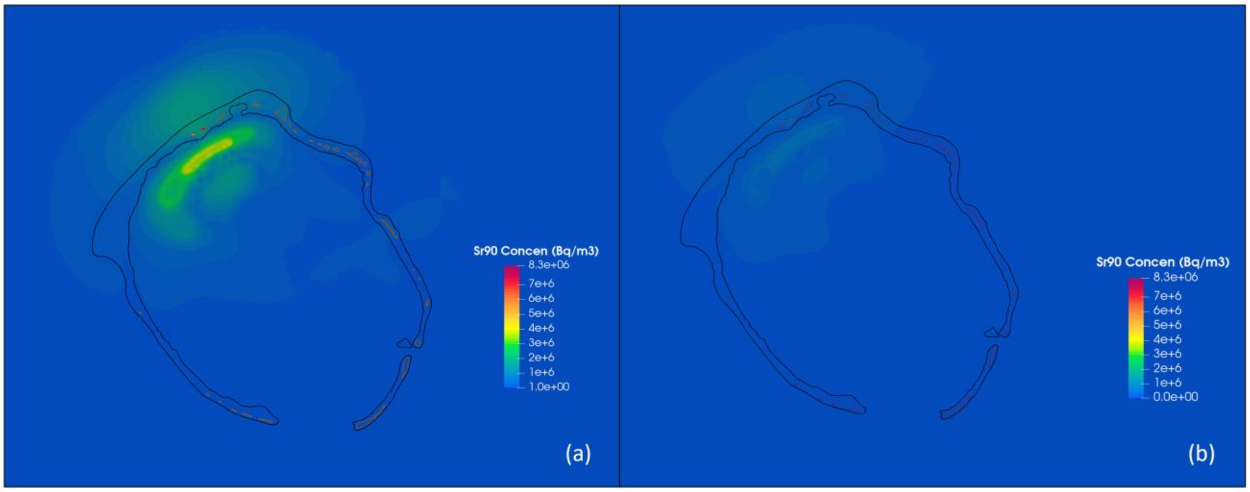

Figure D.8. Estimated distribution of ^{90}Sr in the bottom sediment layer for (a) the current year 2015 and (b) the future year 2090 based on the data from AEC (1973).

The mobilization, fate, and transport of radionuclides under the three WRF-ARW simulated storm scenarios (see Section 4.0 and Appendix B) were performed for a 30-day period individually for both current and future climate conditions. In addition, three model scenarios were also simulated for the future climate conditions with a different initial sediment bed radionuclide concentration which reflects the release of radioactive material from a hypothetical Runit Dome failure. In all model scenarios, the transport of radionuclides from the bottom sediments into the water column is governed by the erosion, suspension, and settling processes. The erosion coefficient (Eq. 1) and free settling velocity (Eq. 4) govern dynamics of the eroded sediments. Ideally, these parameters need to be determined empirically under site-specific conditions. In the absence of such studies, PNNL selected theoretical and literature-based values for the model simulations; however, there is significant uncertainty in the estimated parameter values. To achieve conservative estimates by maximizing the suspension of eroded bottom sediments in the water column, all model scenarios used maximum erosion coefficient (for pure sand beds) and the appropriate minimum free settling velocity from the literature values. Because significant uncertainty is associated with the parameter values of erosion coefficient and settling velocity, additional model simulations were conducted using Storm 3 (i.e., the strongest and closest storm) under current climate conditions to investigate the sensitivity of model predictions to values of erosion coefficient and settling velocity.

D.3 Model Results for Radionuclide Mobilization and Transport

FVCOM-ICM outputs the spatially and temporally varying concentration distributions of the selected radionuclides computed at each grid node of the 30 layers for a 30-day period at an hourly interval. The contour plots for the sample model results show the overall time-integrated extent of the radionuclide plumes in the bottom and surface layers of the water column. The plots depict the maximum concentrations estimated at each node during the 30-day period. Figure D.9 shows the maximum concentration distribution of ^{137}Cs in the surface layer of the lagoon and surrounding area during the 30-day period of baseline case for the current year and future year. The ^{137}Cs distribution patterns in both current and future years have similar overall extent. The differences seen between current and future years are mainly due to the fact that in the future year, the bottom sediment has lower ^{137}Cs concentration compared to the current year because of radioactive decay (Figure D.5).

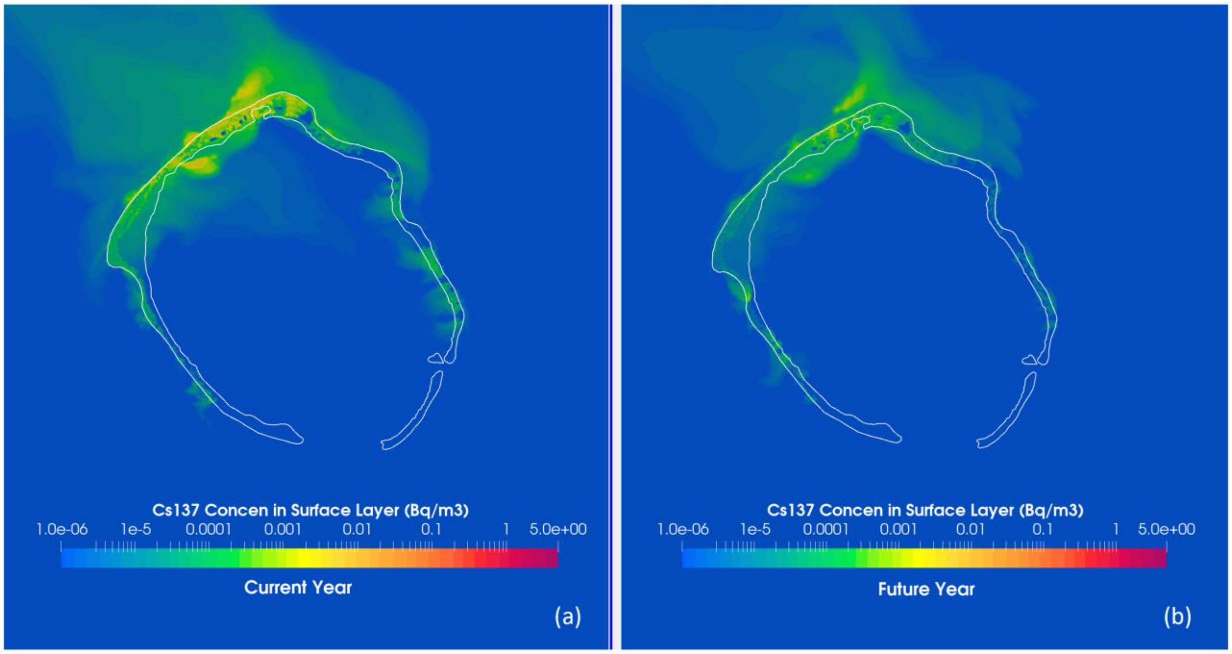

Figure D.9. Maximum ^{137}Cs concentration distribution in the surface layer for the baseline case in (a) current year 2015 and (b) future year 2090 (the color maps and contours in log scale).

Figure D.10 shows the maximum concentration distribution of ^{239}Pu in the surface layer for 2015 and 2090. Peak values for both current and future years are very similar due to slow decay of ^{239}Pu (Figure D.7). The differences partially reflect the differences in hydrodynamic conditions.

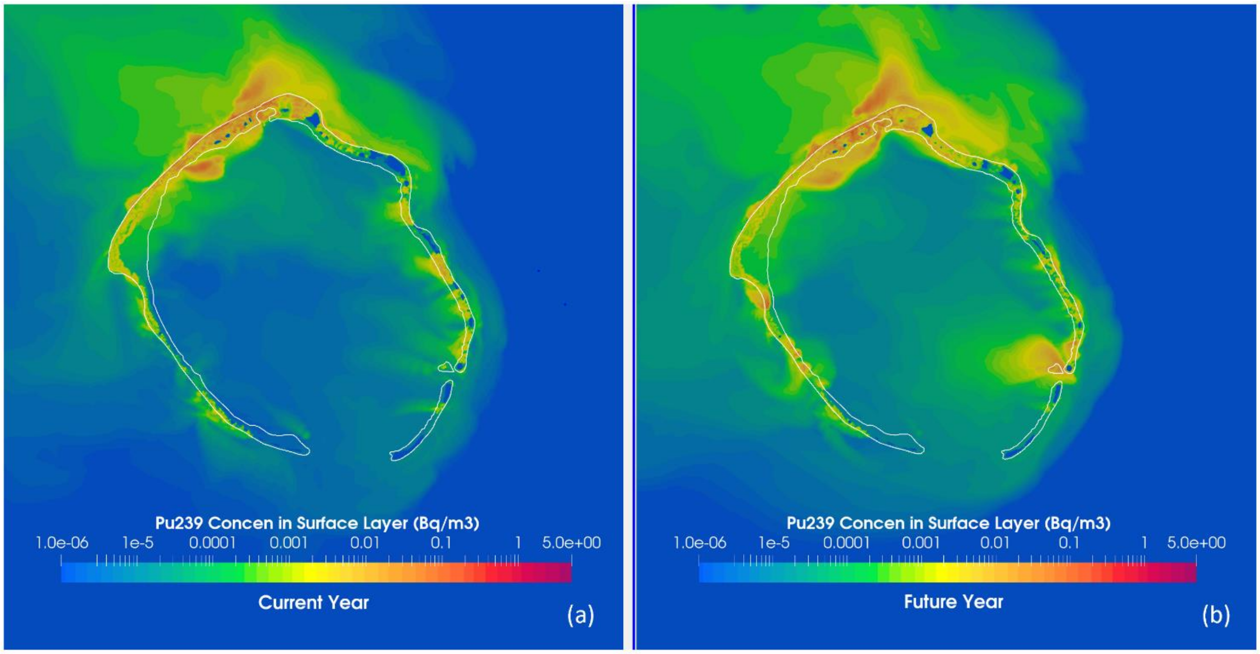

Figure D.10. The maximum ^{239}Pu concentration distribution in the surface layer for the baseline case (a) current year 2015 and (b) future year 2090 (the color maps and contours in log scale).

During storm events, the elevated wind-induced high bottom shear stresses caused higher levels of erosion, resulting in potentially high radionuclide concentrations in the water column. However, the compounded effect of wind-induced bottom shear intertwined with regular tides-driven bottom shear can generate highly non-linear combined effects. Figure D.11 shows the comparison between the ^{137}Cs distributions in the surface layer for current and future years. The peak concentration of ^{137}Cs for the current year is higher than the future year, which is partially due to the lower concentration of ^{137}Cs in the bottom sediments in future years because of radioactive decay. The other contributing factor for the significantly lower peak concentrations in the future compared to the current year is the substantial reduction in the intensity of Storm 1 in the future, resulting in a lower wind-induced shear on lagoon waters. The effect can be further compounded by the shifting of the path of Storm 1 away from the lagoon (Figure 15). A similar pattern of ^{137}Cs distribution in the bottom layer can be observed for current and future years (Figure 13). Despite being affected insignificantly by the decay process in future years, ^{239}Pu also shows noticeably low peak concentrations in the bottom layer for Storm 1 period (Figure D.13), which indicates the future distribution is greatly impacted by the weakening of the strength of Storm 1 in the future year.

In comparison to Storm 1, Storm 3 has higher strength, and the trajectories for both current and future years lie to the south of the atoll (Figure 15 and Figure 16). However, the lagoon waters can be substantially affected by the strong winds from Storm 3, as the atoll is within the radius of maximum wind. Figure D.14 and Figure D.15 show the peak concentrations of ^{137}Cs in the surface and bottom layers for Storm 3 periods of current and future years. They show a noticeable increase in peak concentration distributions, indicating a higher wind-induced erosion in Storm 3. Figure D.16 shows the peak concentrations of ^{239}Pu distribution in the bottom layer for Storm 3 period and a noticeable increase in peak concentration in comparison to Storm 1.

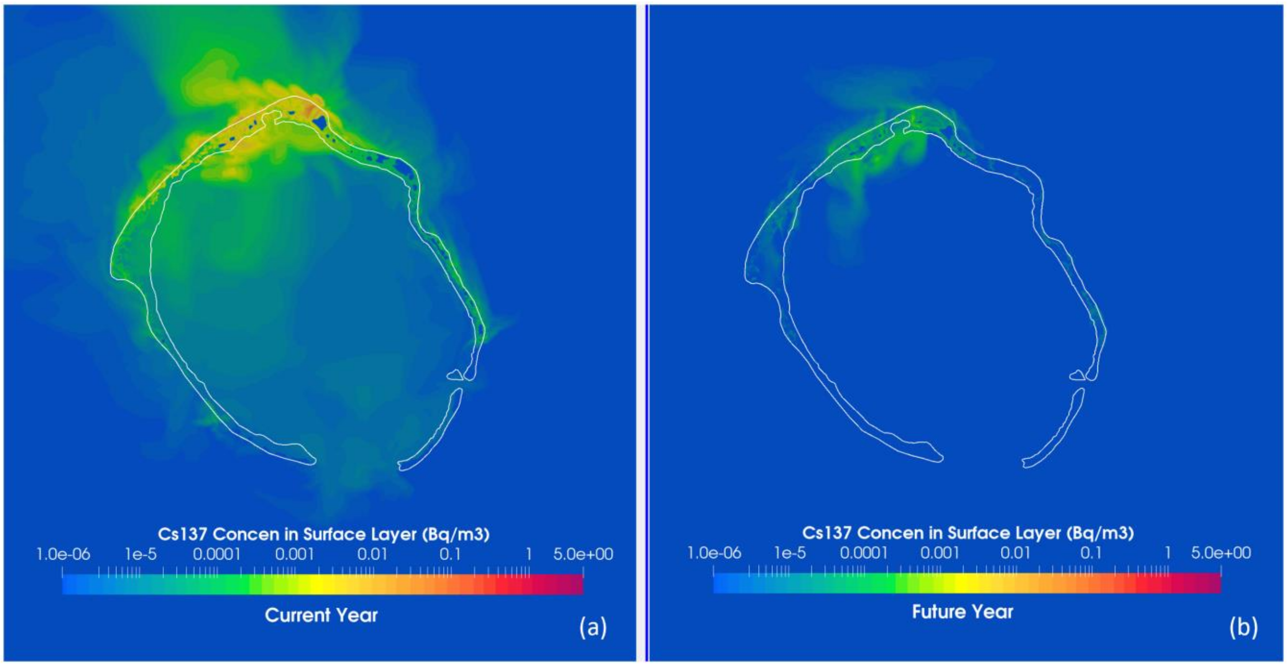

Figure D.11. The maximum ^{137}Cs concentration distribution in the surface layer for Storm 1 period of (a) the current year 2015 and (b) the future year 2090 (the color maps and contours in log scale).

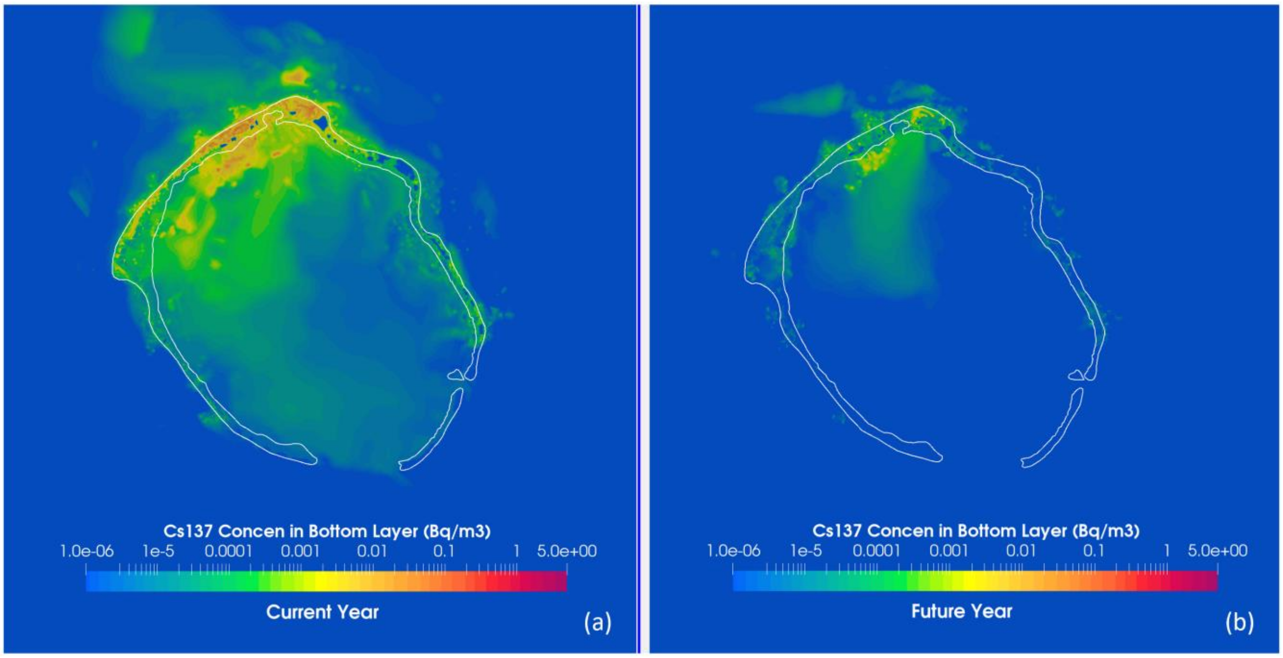

Figure D.12. The maximum ^{137}Cs concentration distribution in the bottom layer for Storm 1 period of (a) the current year 2015 and (b) the future year 2090 (the color maps and contours in log scale).

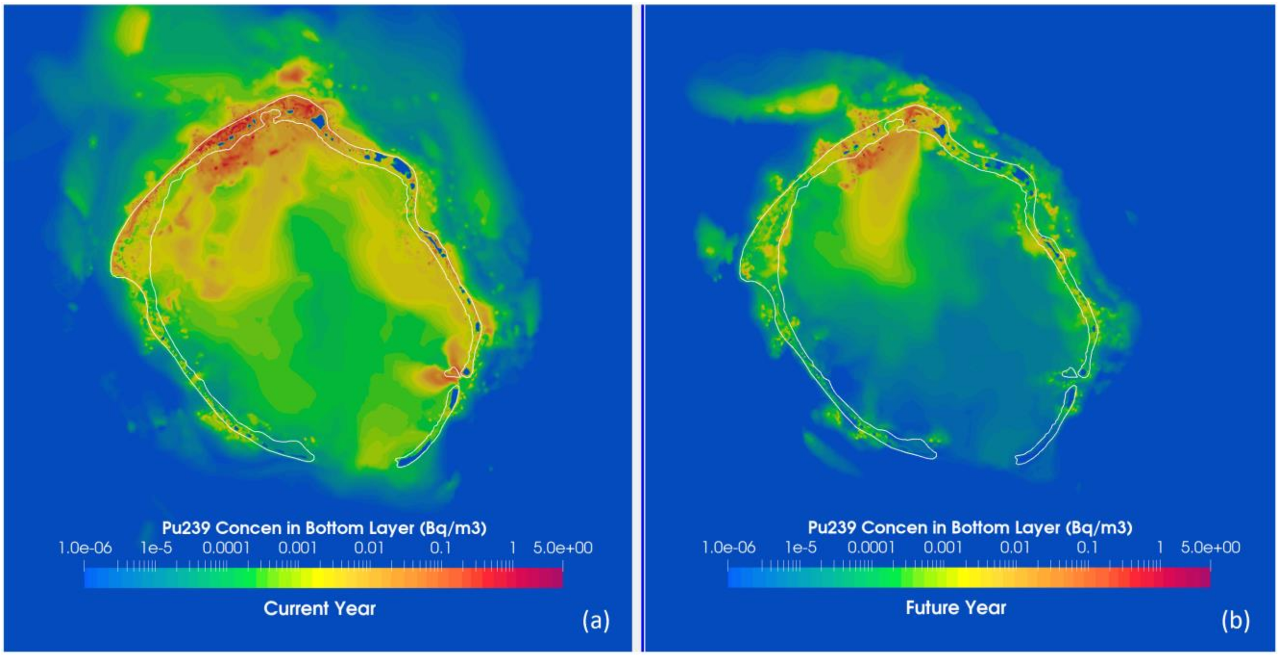

Figure D.13. The maximum ^{239}Pu concentration distribution in the bottom layer for Storm 1 period of (a) the current year 2015 and (b) the future year 2090 (the color maps and contours in log scale).

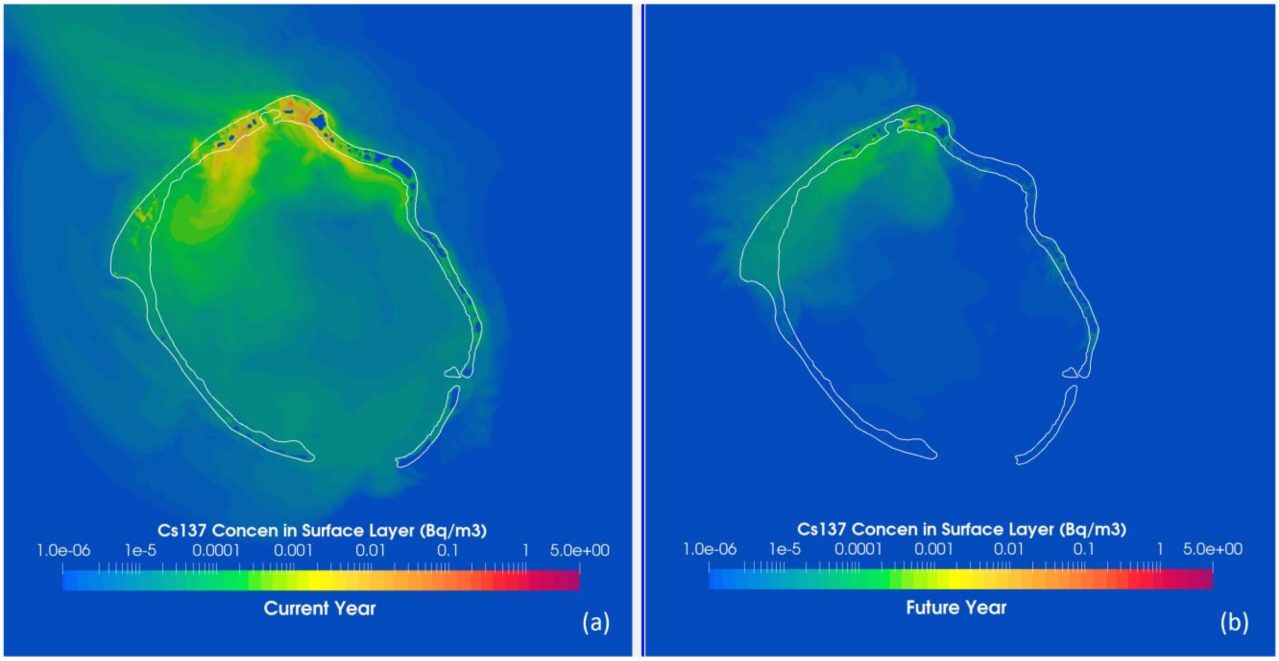

Figure D.14. The maximum ^{137}Cs concentration distribution in the surface layer for Storm 3 period of (a) the current year 2015 and (b) the future year 2090 (the color maps and contours in log scale).

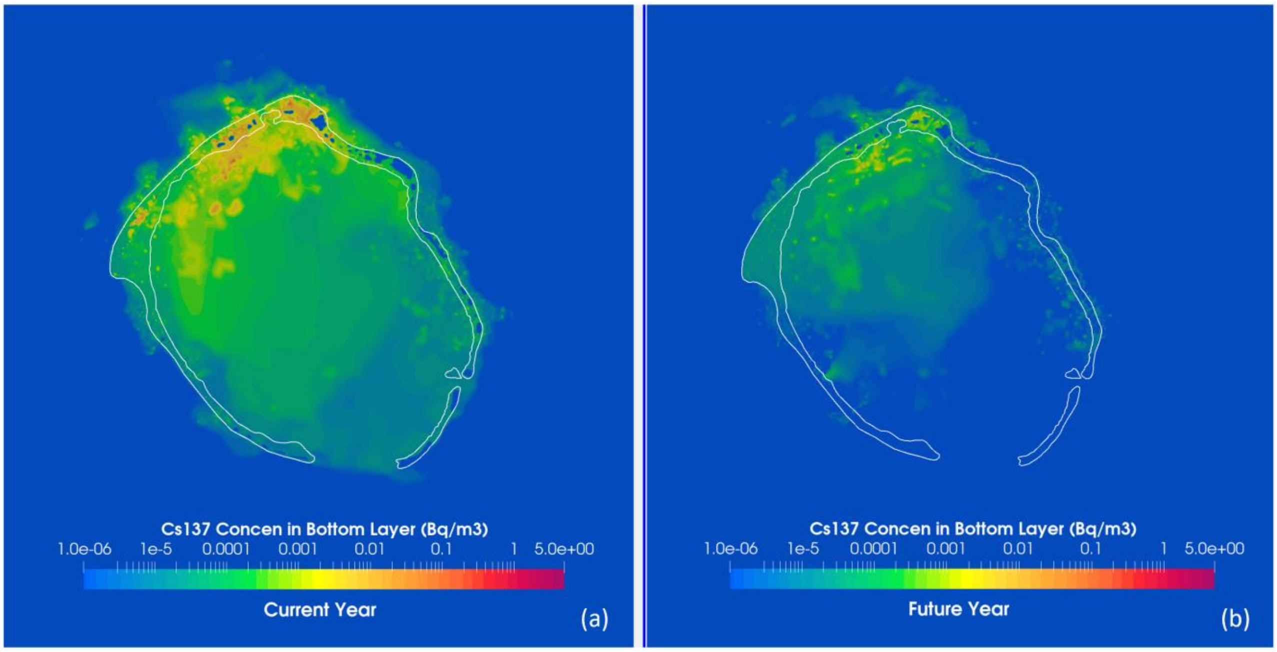

Figure D.15. The maximum ^{137}Cs concentration distribution in the bottom layer for Storm 3 period of (a) the current year 2015 amd (b) the future year 2090 (the color maps and contours in log scale).

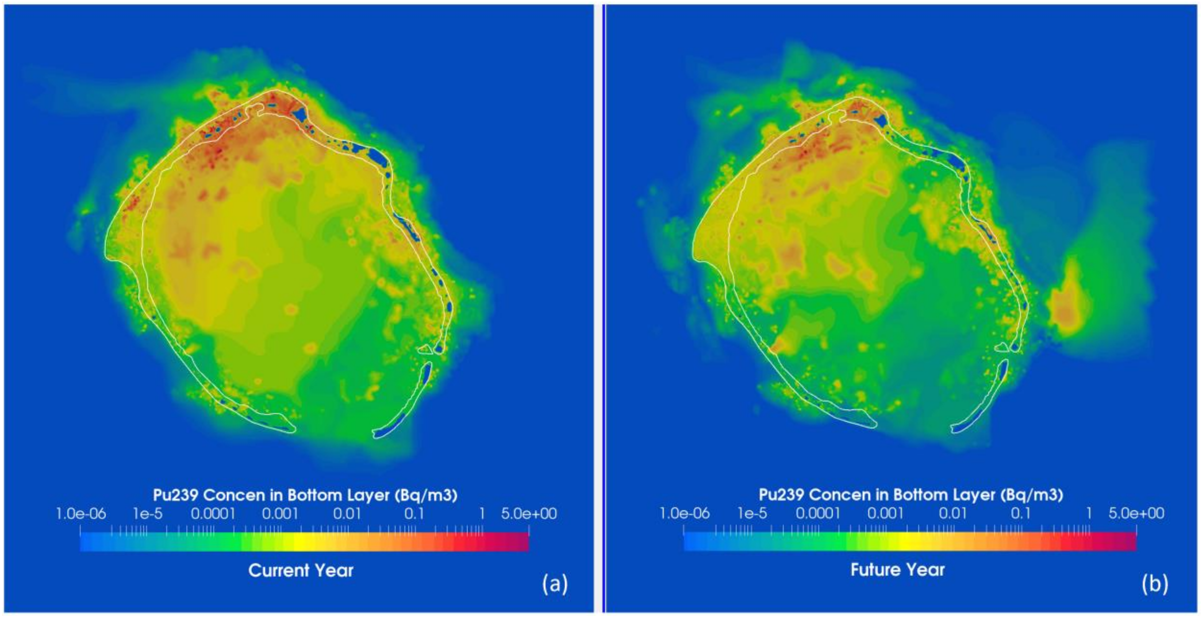

Figure D.16. The maximum ^{239}Pu concentration distribution in the bottom layer for Storm 3 period of (a) the current year 2015 and (b) the future year 2090 (the color maps and contours in log scale).

In comparison to Storms 1 and 3, Storm 2 is weaker in strength, and its trajectory lies significant distance distant away from the Enewetak Atoll. Figure D.17 shows the ^{239}Pu peak concentration distribution in the bottom layer for current and future years, which depicts relatively low peak concentrations spread in the lagoon compared to storm 1 and 3 (Figure D.13 and Figure D.16) caused by less wind shear-induced erosion.

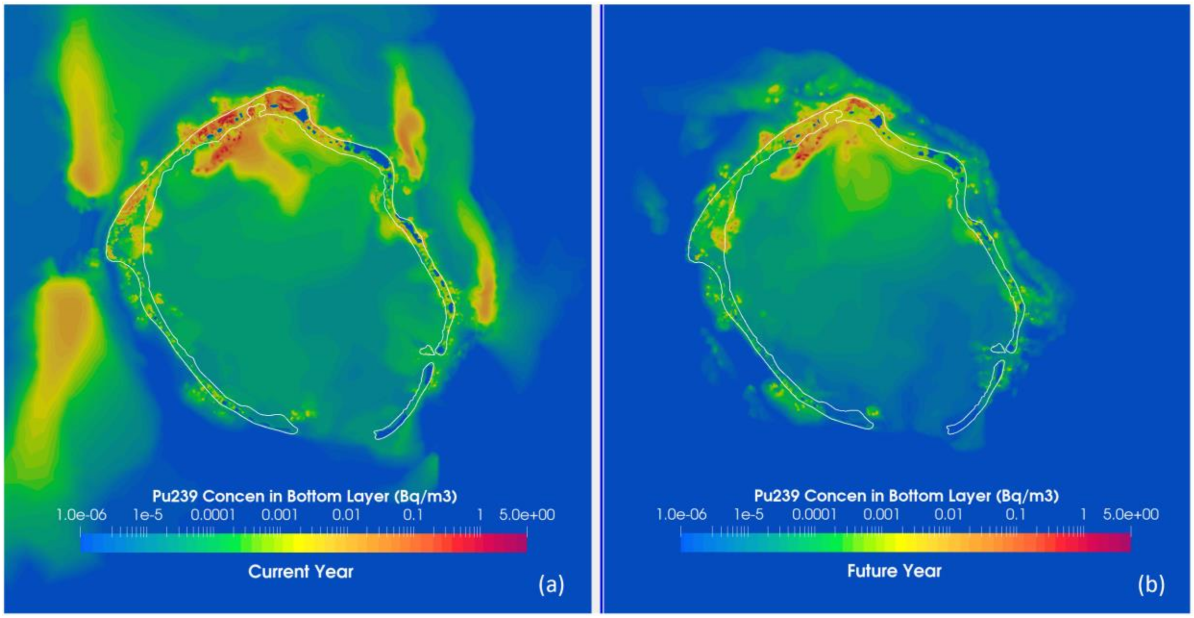

Figure D.17. The maximum ^{239}Pu concentration distribution in the bottom layer for Storm 2 period of (a) the current year 2015 (b) the future year 2090 (the color maps and contours in log scale).

Storm scenarios with the consideration of dome collapse under future climate conditions show noticeable differences in peak concentration distribution compared to the corresponding future storm scenarios without the dome collapse. Figure D.18 shows a peak concentration distribution of ^{239}Pu in the bottom layer for the Storm 3 period under future conditions with and without dome collapse. The future scenario with dome collapse shows much higher peak concentrations in the northern part of the lagoon and nearby islands. Also, the peak concentration pattern further shows an overall increase in peak concentrations inside the lagoon. The increase in the overall peak concentration can be attributed to the erosion of radionuclide inventory initialized in the lagoon bottom sediments near the Runit Dome, which were then dispersed toward the northern island and other parts of the lagoon.

The incremental concentrations from the eroded sediments around and nearby islands are important for the assessments of potential human exposure to radionuclide concentration. A potential exposure concentration for a selected island is estimated by spatial averaging of the nearby model nodes on the lagoon side of the island (Figure D.19). The temporal variation of the ^{137}Cs concentration distribution in the surface layer of the lagoon nearby Runit Island for the Storm 1 scenario is shown in Figure D.20. The ^{137}Cs concentration reaches a peak during the storm period when the effect of the wind shear from the storm is strongest and gradually diminishes within a 1–2 day period. However, the elevated concentration can linger for several days before the eroded sediment-bound radionuclides get flushed by currents and tides. Figure D.21 shows the temporal variation of spatially averaged ^{239}Pu concentration in the surface layer nearby Runit Island, which also shows a similar pattern as ^{137}Cs, although ^{239}Pu reaches a higher peak concentration.

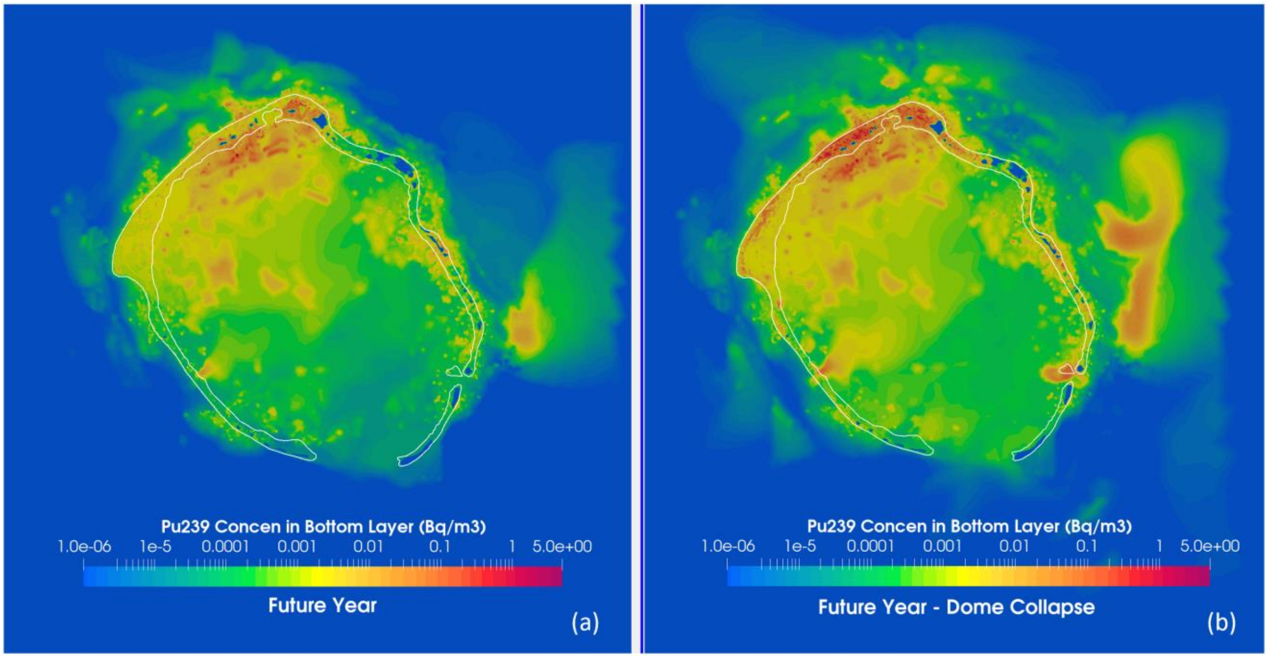

Figure D.18. The maximum ^{239}Pu concentration distribution in the bottom layer for Storm 3 period of (a) the future year 2090 and (b) the future year 2090 with dome collapse (the color maps and contours in log scale).

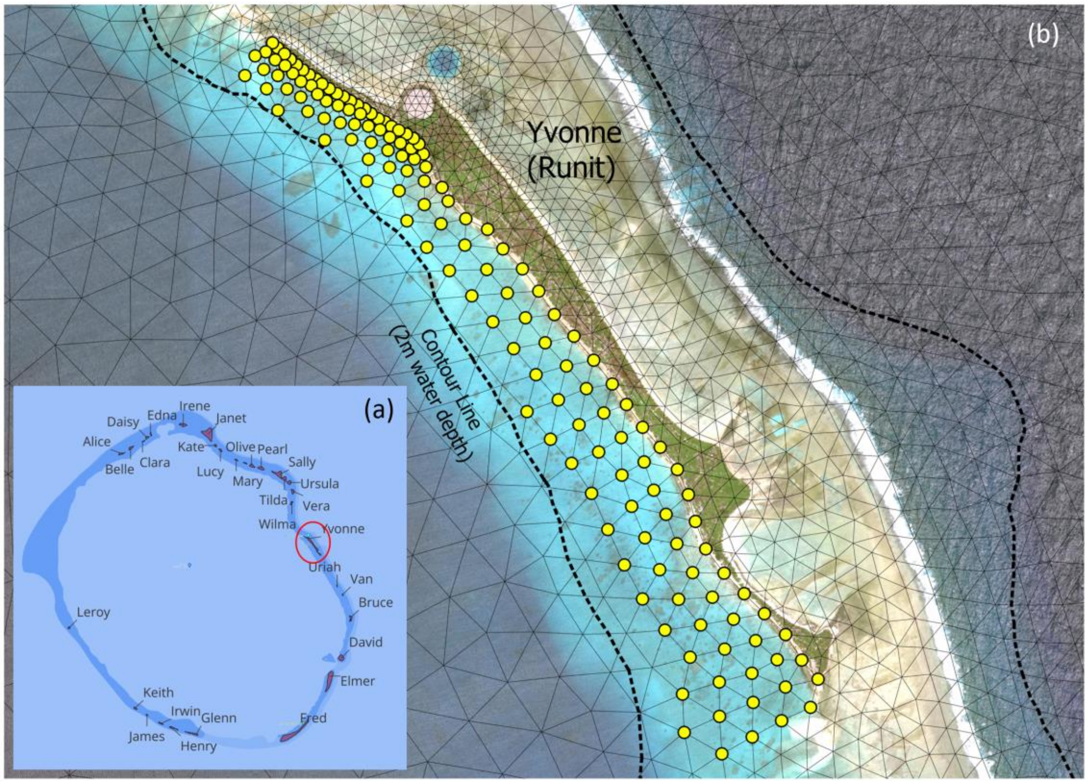

Figure D.19. (a) The island layout of the Enawetak Atoll. (b) Node selection for spatial averaging for estimating exposure concentration for Runit Island.

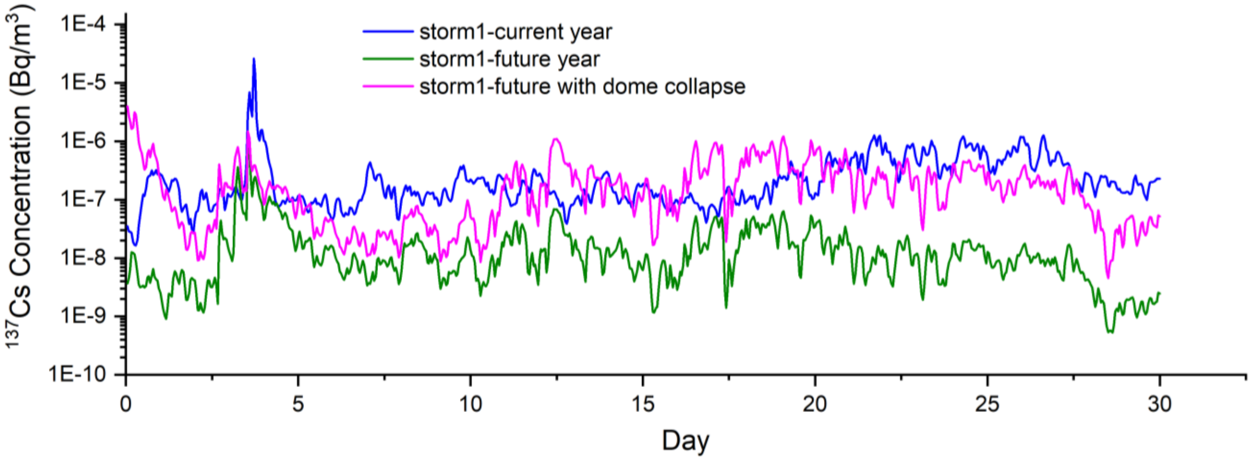

Figure D.20. Temporal variation of spatially averaged ^{137}Cs concentration in the surface layer near Runit Island for Storm 1 scenario.

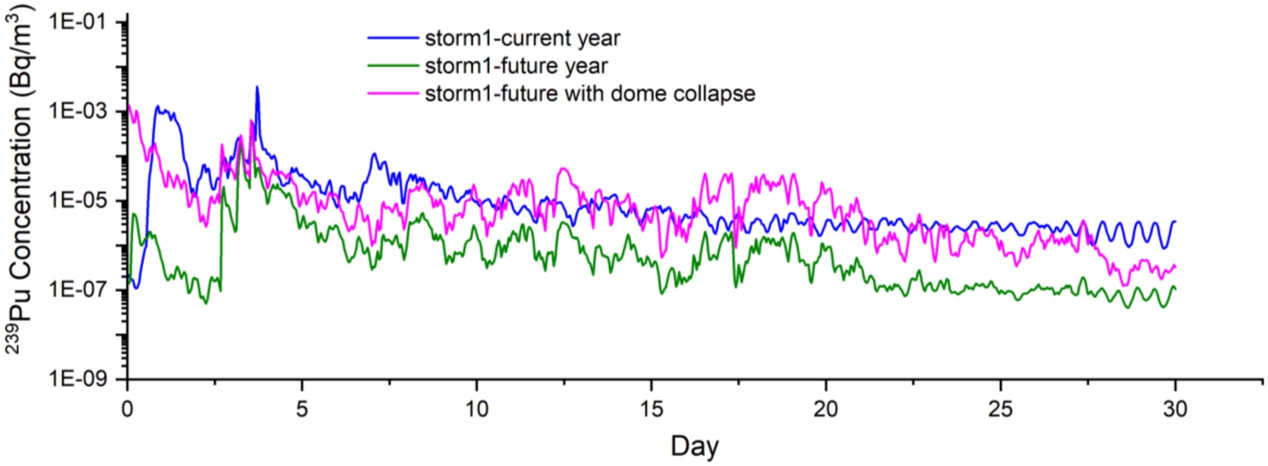

Figure D.21. Temporal variation of spatially averaged ^{239}Pu concentration in the surface layer near Runit Island for the Storm 1 scenario.

It should be noted that model results discussed previously used a sediment parameterization that theoretically maximizes the bottom erosion. This approach was adopted for the study as a conservative measure due to the absence of reliable data or field studies to determine the appropriate sediment parameterization, particularly the most sensitive two parameters: (1) erosion coefficient for bottom sediments (for pure sand); and (2) universal free settling velocity. The presented model results are estimated using an erosion coefficient of 2.6e-03 (kg m^{-2} s^{-1}) and a universal free settling velocity of 4.3E-05 m/s for a spherical particle. Hence, the current model results are contingent on the selection of these parameter values, and the model results may significantly vary for a different sediment parameterization. Figure D.22 demonstrates the sensitivity of the erosion coefficient and settling velocity on the erosion of the bottom sediment due to wind-induced shear during Storm 3 period of the current year. The sensitivity scenario 1 used an erosion coefficient that is ten times lower (i.e., 2.6e-05 kg m^{-2} s^{-1}) than the one used for the model scenario while maintaining the same settling velocity as in the model scenario. This results in a substantial reduction in the peak concentration, as depicted in the figure. The sensitivity scenario 2 further reduces the net erosion by increasing the free settling velocity substantially by using the maximum theoretical free settling velocity (i.e., 0.043 m/s) for a spherical sediment particle with average grain size (Table D.2) estimated for the lagoon bottom sediments. The effect of using a parameterization that minimizes the net erosion can be seen clearly in the Figure D.22 as it shows the sensitivity scenario 2 produces the lowest peak concentration for the lagoon domain.

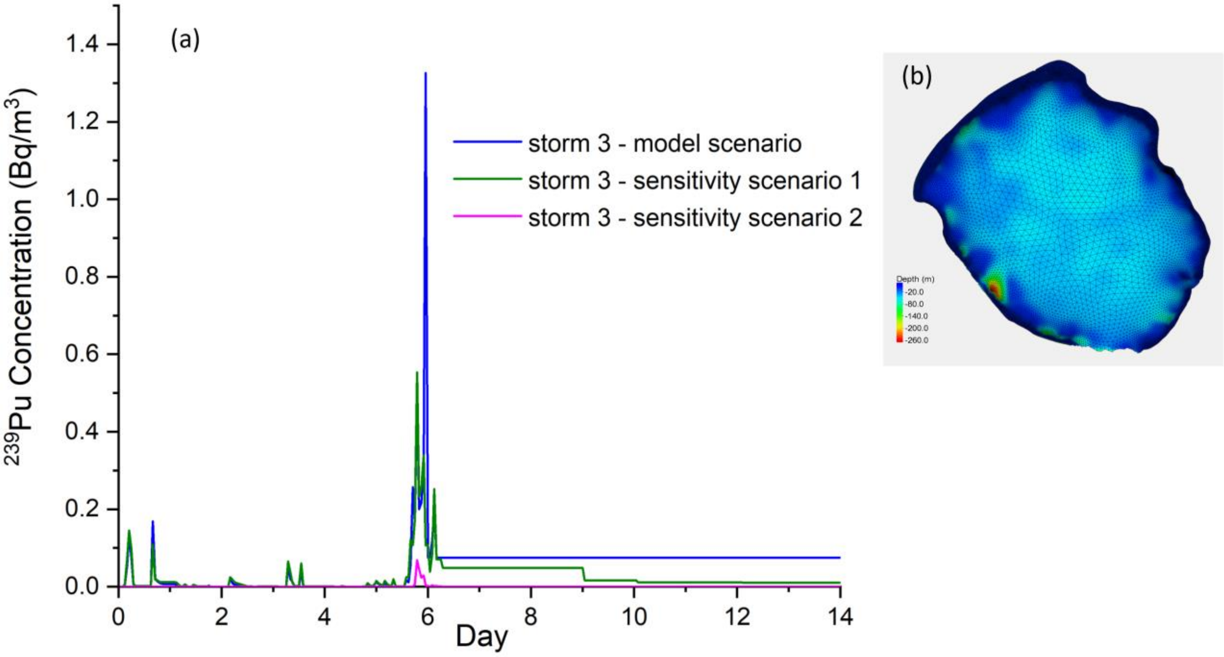

Figure D.22. (a) Comparison of temporal variations of maximum ^{239}Pu concentration in the surface layer of the lagoon during the period that the wind-induced shear from Storm 3 on the lagoon is strongest. All the scenario cases were tested for the current year. (b) Lagoon domain was considered for estimating the peak concentration.

Appendix E
Radiation Dose Assessment Approach

Of the 39 remaining islands of the Enewetak Atoll, only a few are large enough for residential use. These islands are Enewetak, Medren, Japtan, Bijere, Aomon, and Enjebi. However, most of the remaining islands may be used for visits, recreation, or harvesting food. Sufficient data exist to estimate direct external dose rates and concentrations of important radionuclides in foods that may be collected for each island. The RMI NWRS (Simon and Graham, 1995) includes information for 31 islands in the atoll. PNNL estimated radiation doses for residential islands and those that may be visited for food collection or recreation. The following sections present the approach, methods, and results of the PNNL radiation dose assessment. This assessment uses the ocean and sediment concentrations calculated by PNNL ocean modeling described in Section 4.0. PNNL evaluated dose to adults for a selected set of internal and external exposure pathways.

E.1 Generalized Exposure Scenario

The majority of the Enewetak population currently lives on a few of the southern-most islands. Previous inhabitants of Enjebi Island would like to return, and a few of the other islands could possibly support a few individuals or families. Many of the smaller islands could be useful for harvesting native plants or coconuts and as bases for near-island fishing.

To provide directly comparable dose/risk information island to island, a simple exposure scenario was developed and applied to every island, no matter whether it is large enough to support full-time residency. These nominal annual doses can be used to describe the current and possible future radiological conditions of each island. In actual future use, these full-time estimates could be prorated by actual occupancy times to obtain a reasonable approximation of dose.

The exposure scenario was applied only to adults (doses to children would differ, although not greatly). Individuals were assumed to reside on the island full time. An individual spends a portion of every day on the beach, another portion swimming or diving near the shore in the lagoon, and another portion in a small boat in the lagoon. People are exposed directly to gamma radiation from island soils, beach sands, and lagoon water. They inhale sea spray and resuspended dusts from the soil and beach. Individuals also eat plants and animals grown for food on the island. The diet is assumed to be all locally produced foods to maximize the potential ingestion exposure.

E.2 Radionuclides and Exposure Pathways

Radionuclides evaluated were those reported to be in the sediments or on the islands. These are ^{241}Am, ^{207}Bi, ^{60}Co, ^{137}Cs, ^{155}Eu, $^{239+240}$Pu, and ^{90}Sr. These radionuclides and the internal and external dose coefficients used in this assessment are shown in Table E.1Table 1. Details of nuclear tests performed at Enewetak Atoll (DOE 2015). Short-lived radionuclide progeny are assumed to be in equilibrium with the parent radionuclide (^{137}Cs/^{137m}Ba, ^{90}Sr/^{90}Y). Short-lived progeny are included in the dose coefficient of the parent radionuclide but external dose must be calculated for both parent and progeny. It should be noted that ^{137}Cs/^{137m}Ba has a branching ratio of 0.94, which has been explicitly incorporated into the dose calculations.

Table E.1. Radionuclides and adult dose coefficients used in the assessment.

Radionuclide	External Soil Dose Rate (Sv/hr per Bq/kg)	External Swimming Dose Rate (Sv/s per Bq/m^3)	Inhalation Dose (Sv/Bq)	Inhalation Class	Ingestion Dose (Sv/Bq)
^{241}Am	2.22E-12	1.20E-18	4.17E-05	M	2.04E-07
^{207}Bi	4.75E-10	1.46E-16	5.63E-09	M	1.27E-09
^{60}Co	8.59E-10	2.53E-16	3.07E-08	S	3.42E-09
^{137}Cs	1.83E-10	5.55E-17	4.67E-09	F	1.36E-08
^{152}Eu	3.64E-10	1.12E-16	6.96E-09	M	3.26E-10
$^{239+240}$Pu	1.48E-14	7.26E-21	5.01E-05	M	2.51E-07
^{90}Sr	2.54E-11	1.06E-18	2.39E-08	F	2.77E-08

^{137}Cs = ^{137}Cs + (^{137m}Ba * 0.94)
^{90}Sr = ^{90}Sr + ^{90}Y

Radionuclide concentrations in the various ocean layers and deposited in the sediments are key inputs to the dose calculations. Table E.2. Exposure pathways mapped to radionuclide concentrations in ocean and sediment maps the exposure pathways evaluated by PNNL to the source of radionuclides, either as island soils, lagoon water concentration, or as sediment concentration (which is also used for beach exposures).

Table E.2. Exposure pathways mapped to radionuclide concentrations in ocean and sediment.

Exposure Pathway	Radionuclide Source
Adult Human Exposure	
Seafood ingestion – pelagic fish, benthic fish, crustaceans, mollusks	Lagoon
Seawater spray inhalation	Lagoon
Island dust ingestion	Soil/Beach
External direct exposure	Soil/Beach
Locally produced terrestrial foods	Soil
Biota Exposure	
Internal dose - pelagic, algae, benthic, crustaceans, mollusks, coral	Lagoon
External dose – pelagic, coral, algae	Lagoon
- benthic, crustaceans, mollusks	Lagoon/Sediment

E.3 Calculating Internal Dose to Humans

Six internal dose assessment pathways were evaluated: ingestion of locally caught seafood; ingestion of locally produced crops; ingestion of locally raised animal products; inhalation of seawater spray; inhalation of dispersed island soil, and inhalation of coastal sediment. Methods for evaluating these pathways are included in the following sections.

E.3.1 Seafood Ingestion

Radiation dose from ingestion of seafood was evaluated for ingestion rates of locally produced foods taken from Robison and Phillips (1989) for twelve categories of consumed marine organisms. The ingestion rates for adults were used under the condition of imported food unavailable. The ingestion rates of each seafood type, and the necessary seawater-to-food transfer factors (TFs, taken from IAEA TRS-479) are given in Table E.3. Seafood ingestion rates and water-to-food concentration .

Table E.3. Seafood ingestion rates and water-to-food concentration ratios.

	Ingestion rate	CR data Bq/kg per Bq/L						
Seafood type	kg/yr	Am	Bi	Co	Cs	Eu	Pu	Sr
Reef fish	15.8	320	15	480	71	730	2500	11
Tuna	13.1	320	15	11000	79	730	190	38
Mahi Mahi	3.9	320	15	11000	79	730	190	38
Marine crabs	3.6	500	1000	33500	56	6900	120	78
Lobster	6.4	500	1000	3500	56	6900	120	78
Clams	10.6	9900	1000	5300	50	6900	650	88
Trochus (snail)	0.0	--	--	--	--	--	--	--
Tridacna (giant clam)	2.1	9900	1000	5500	50	6900	650	88
Jedrul (giant clam)	3.5	9900	1000	5500	50	6900	650	88
Octopus	8.9	9900	1000	5500	50	6900	1700	230
Turtle	3.2	320	15	480	71	730	2500	11
Turtle eggs (turtle)	3.2	320	15	480	71	730	2500	11

For each radionuclide or radionuclide parent/progeny pair the annual dose from seafood ingestion was calculated as follows:

$$Dose\ Rate\left(\frac{Sv}{year}\right) = IR\left(\frac{kg}{yr}\right)\ \times C\left(\frac{Bq}{L}\right) \times CR\left(\frac{Bq/kg}{Bq/L}\right) \times DC_{ingestion}\left(\frac{Sv}{Bq}\right)$$

where:

C = radionuclide concentration in ocean water (Bq/L)

IR = ingestion rate for each type of seafood (kg/yr)

CR = concentration ratio in seafood from water (L/kg)

$DC_{ingestion}$ = ingestion dose coefficient (Sv/Bq).

E.3.2 Terrestrial Food Crop Ingestion

Radiation dose from ingestion of locally produced foods was evaluated for the food types taken from Robison and Phillips (1989) and Robison et al. (1994) for 16 types of local plants, plus inadvertent ingestion of local soils. The ingestion rates for adults were used under the condition of imported food unavailable. The ingestion rates of each terrestrial food type, and the necessary soil-to-crop transfer factors (taken from IAEA TECDOC-1979) are given in Table E.4. Note that island soil data for the isotopes of Bi and Eu are unavailable, so the CR data are omitted.

Table E.4. Terrestrial plant ingestion rates for adults and soil-to-plant concentration ratios.

Plants	Ingestion rate	CR data Bq/kg per Bq/kg						
	kg/yr	Am	Bi	Co	Cs	Eu	Pu	Sr
Pandanus fruit	11.5	1.20E-05	x	1.30E-03	2.70E+00	x	8.70E-06	1.10E-02
Pandanus nuts	0.4	1.20E-05	x	1.30E-03	2.70E+00	x	8.70E-06	1.10E-02
Breadfruit	34.0	1.20E-05	x	1.60E-02	3.70E-01	x	7.00E-06	3.40E-02
Coconut juice	61.0	3.70E-05	x	0.31	4.30E+00	x	3.20E-05	1.70E-02
Coconut milk	22.2	3.70E-05	x	0.31	4.30E+00	x	3.20E-05	1.70E-02
Tuba/Jekero	0.0	--	--	--	--	--	--	--
Drinking coco meat	33.0	3.70E-04	x	3.1	4.30E+01	x	3.20E-04	1.70E-01
Copra meat	13.0	3.70E-04	x	3.1	4.30E+01	x	3.20E-04	1.70E-01
Sprouting coconut	22.3	3.70E-05	x	0.31	4.30E+00	x	3.20E-05	1.70E-02
Marsh cake (used coconut)	0.000	3.70E-04	x	3.1	4.30E+01	x	3.20E-04	1.70E-01
Papaya	4.9	1.20E-05	x	1.30E-03	2.70E+00	x	8.70E-06	1.10E-02
Squash	0.0	--	--	--	--	--	--	--
Pumpkin	1.0	1.20E-05	x	2.40E-02	3.4	x	8.50E-06	2.00E-01
Banana	0.1	1.20E-05	x	1.60E-02	3.70E-01	x	7.00E-06	3.40E-02
Arrowroot	17.3	1.20E-05	x	3.40E-01	6.20E-01	x	8.50E-06	2.20E+00
Citrus (used breadfruit)	0.037	1.20E-05	x	1.60E-02	3.70E-01	x	7.00E-06	3.40E-02
Soil	0.037	1.00E+00	1.00E+00	1.00E+00	1.00E+00	1.00E+00	1.00E+00	1.00E+00

For each radionuclide or radionuclide parent/progeny pair the annual dose from terrestrial plant ingestion was calculated as follows:

$$Dose\ Rate\left(\frac{Sv}{year}\right) = IR\left(\frac{kg}{yr}\right) \times Cs\left(\frac{Bq}{kg}\right) \times CR\left(\frac{Bq/kg}{Bq/kg}\right) \times DC_{ingestion}\left(\frac{Sv}{Bq}\right)$$

where:

Cs = radionuclide concentration in island soil (Bq/kg)

IR = ingestion rate for each type of plant crop (kg/yr)

CR = concentration ratio in plant crop from soil (Bq/kg per Bq/kg)

$DC_{ingestion}$ = ingestion dose coefficient (Sv/Bq).

E.3.3 Terrestrial Animal Product Ingestion

Radiation dose from ingestion of locally produced animal products was evaluated for the food types taken from Robison and Phillips (1989) for 11 types of local animal products. The ingestion rates for adults were used under the condition of imported food unavailable. The ingestion rates of each animal product type, and the necessary feed-to-animal-product transfer factors (taken from IAEA TRS-472 and GENII [Napier, 2012 and Snyder et al., 2012]) are given in Table E.5. Note that island soil data for the isotopes of Bi and Eu are unavailable, so the TF data are omitted.

Note that uptake in animals is predicated on the animals consuming local plants. To obtain an upper estimate of the potential radionuclide concentration in animal products, it was assumed that birds and chickens consume 0.1 kg/day of leaves of a plant represented by pandanus. Pigs are assumed to eat 5 kg/day of a similar plant. As a result, the equations for animal product concentrations include terms for plant concentration.

Table E.5. Terrestrial animal product ingestion rates for adults and feed-to-animal transfer factors.

Animals	Ingestion rate	TF data Bq/kg per Bq/day						
	kg/yr	Am	Bi	Co	Cs	Eu	Pu	Sr
Coconut crabs	4.6	0		0	2.6		0	0.12
Chicken muscle	5.7	0.006	x	0.97	2.7	x	0.003	0.02
" liver	3.2	0.006	x	0.97	2.7	x	0.003	0.02
" gizzard	0.6	0.006	x	0.97	2.7	x	0.003	0.02
Pork muscle	2.5	0.0005	x	0.00043	0.022	x	1.1E-06	0.0013
" kidney	0.0	--	--	--	--	--	--	--
" liver	1.2	5	x	0.00043	0.022	x	1.1E-06	0.0013
" heart	0.1	0.0005	x	0.00043	0.022	x	1.1E-06	0.0013
Bird muscle	4.8	0.006	x	0.97	2.7	x	0.003	0.02
" eggs	4.2	0.002	x	0.033	0.4	x	0.0012	0.35
Chicken eggs	7.5	0.002	x	0.033	0.4	x	0.0012	0.35

For each radionuclide or radionuclide parent/progeny pair the annual dose from terrestrial animal product ingestion was calculated as follows:

$$Dose\ Rate\left(\frac{Sv}{year}\right) = IR\left(\frac{kg}{yr}\right) \times Cs\left(\frac{Bq}{kg}\right) \times CR\left(\frac{Bq/kg}{Bq/kg}\right) \times CRA\left(\frac{Bq/kg}{Bq/kg}\right) \times IRA\left(\frac{kg}{yr}\right) \times DC_{ingestion}\left(\frac{Sv}{Bq}\right)$$

where:

Cs = radionuclide concentration in island soil (Bq/kg)

CR = concentration ratio in plant crop (pandanus) from soil (Bq/kg per Bq/kg)

IR = ingestion rate by people for each type of animal product (kg/yr)

CRA = uptake factor from feed to animal product (Bq/kg per Bq/day)

IRA = ingestion rate for plants by the animal (kg/yr)

$DC_{ingestion}$ = ingestion dose coefficient (Sv/Bq).

Note that feed-to-meat transfer factors do not exist in the literature for coconut crabs. For these only, a surrogate CRA was developed by this project based upon limited measurements of radionuclides in land crabs on Belle Island following the Nectar test in 1954 (Held 1957, UWFL-50).

E.3.4 Seawater Spray Inhalation

Members of the public may be exposed to airborne seawater spray and inhale this spray. The receptor location was taken to be anywhere on the island. The islands are small and experimental evidence indicates that the sea salt concentrations in air are essentially constant across the islands. Therefore, full-time exposure to sea spray is assumed (8,760 hours/year).

The seawater spray inhalation dose rate from particles suspended in air was calculated as follows:

$$Sea\ spray\ inhalation\ dose\ rate_{rn}\left(\frac{Sv}{year}\right) = C\left(\frac{Bq}{L}\right)\times t\left(\frac{h}{y}\right)\times IR\left(\frac{m^3}{h}\right)\times\left[ML_{equivalent}\left(\frac{L}{m^3}\right)\right]\times DC_{inhalation}\left(\frac{Sv}{Bq}\right)$$

where:

C = concentration in ocean water surface near beach (Bq/L)

t = time of exposure at beach (h/y)

IR = inhalation rate (m^3/hr)

$ML_{equivalent}$ = mass loading equivalent of particles in air (1.0 E-06 L/m^3)

$DC_{inhalation}$ = inhalation dose coefficient (Sv/Bq)

The “mass loading equivalent” parameter is the concentration of suspended ocean particles in air (Robison et al. 1994; Robison et al. 1979), with a value of 1×10^{-6} kg/m^3, where seawater density of 1.025 kg/L converts to units of L/m^3. The mass loading parameter is calculated as:

$$Mass\ laoding\ equivalent\left(\frac{L}{m^3}\right) = \frac{salt\ concentration\ in\ air}{salt\ concentration\ in\ seawater} = \left[35\left(\frac{\mu g}{m^3}\right)\times 10^{-6}\left(\frac{g}{\mu g}\right)\right]\Big/35\,\frac{g}{L} = 10^{-6}\left(\frac{L}{m^3}\right)$$

E.3.5 Resuspended Island Soil and Coastal Sediment Inhalation

Members of the public are assumed to inhale resuspended soil while on the island and dispersed coastal sediment while at the beach. For each radionuclide or radionuclide parent/progeny pair the annual dose from inhaling dusts was calculated as follows:

$$Sediment\ inhalation\ Dose\ Rate\left(\frac{Sv}{year}\right) = Cp_{sediment}\left(\frac{Bq}{kg}\right)\times t\left(\frac{h}{y}\right)\times IR\left(\frac{m^3}{h}\right)\times RS\left(\frac{kg}{m^3}\right)\times DC_{inhalation}\left(\frac{Sv}{Bq}\right)$$

where:

$Cp_{sediment}$ = radionuclide concentration in beach sediment or island soil (Bq/kg)

t = time spent at beach or in the island interior (h/y)

IR = inhalation rate, (0.92 m^3/h)

RS = resuspension factor of sediment in air, = 25 µg/m^3 = 2.5×10-9 kg/m^3

$DC_{inhalation}$ = inhalation dose coefficient (Sv/Bq).

The inhalation rate is set at 22 m^2/day or 0.92 m^2/hour. The mass loading of dust in air is set at 25 µg/m^3, which is a upper bound derived from measurements at Bikini Atoll (Robison et al., 1994; Robison et al., 1979).

The times spent exposed to airborne contaminants at the beach or in the island interior are the same as those assumed for external exposures at these locations, as listed in Appendix E.4.

E.4 Calculating External Dose to Humans

Four external dose pathways were evaluated: exposure to beach sand; exposure to island soils; external immersion dose while swimming; and exposure from the sea surface while boating. Methods for evaluating these pathways are included in the following sections.

The doses from external exposures are directly related to the amount of time spent at each location. For this analysis, full-time occupancy of an island for a full year is assumed to allow estimation of annual dose; however, the individual is assumed to engage in various activities in the island interior, on the beach, and in the near-shore lagoon water. The time distribution is shown in Table E.6.

Table E.6. Exposure times for island activities.

Exposure Pathway	Exposure Time (hours/year)
Swimming	365
Boating	720
Beach External/Inhalation	365
Island Soil External/Inhalation	7,310

E.4.1 External Exposure to Contaminants in Island Soil

Individuals are assumed to be exposed to contaminants in the soil while on the island. For each radionuclide, the annual dose from external exposure to radionuclides in the island soils was calculated as follows:

$$Soil\ Dose\ Rate\left(\frac{Sv}{year}\right) = Cp_{soil}\left(\frac{Bq}{m^3}\right) \times t\left(\frac{h}{y}\right) \times DC_{soil-infinite}\left(\frac{Sv \cdot m^3}{Bq \cdot s}\right) \times 3600\left(\frac{s}{h}\right)$$

where:

Cp_{soil} = radionuclide concentration in island soil (Bq/m^3)

t = time of exposure (hours/year)

$DC_{soil-infinite}$ = external soil dose coefficient, infinite volume (Sv/second per Bq/m^3).

E.4.2 Beach Sand External Exposure

Individuals are assumed to be exposed while standing on the beach; the exposure is to a narrow strip of sediment between the island interior and the water. For each radionuclide, the annual dose from external exposure was calculated as follows:

$$Beach\ Dose\ Rate\left(\frac{Sv}{year}\right) = Cp_{sediment}\left(\frac{Bq}{m^3}\right) \times SWF \times t\left(\frac{h}{y}\right) \times DC_{soil-infinite}\left(\frac{Sv \cdot m^3}{Bq \cdot s}\right) \times 3600\left(\frac{s}{h}\right)$$

where:

$Cp_{sediment}$ = radionuclide concentration in beach sediment (Bq/m^3)

SWF = Shore width factor, a parameter to account for the beach geometry (0.2)

t = time of exposure (hours/year)

$DC_{soil-infinite}$ = external soil dose coefficient, infinite volume (Sv/second per Bq/m^3).

E.4.3 Swimming/Diving External Exposure

Individuals may swim or dive for fish or seafood collection. For each radionuclide the annual dose from external exposure in the ocean surface water near the beach while swimming was calculated as follows:

$$Swimming\ Dose\ Rate\left(\frac{Sv}{year}\right) = C\left(\frac{Bq}{L}\right) \times t\left(\frac{h}{y}\right) \times DC_{immersion}\left(\frac{Sv \cdot m^3}{Bq \cdot s}\right) \times 1{,}000\left(\frac{L}{m^3}\right) \times 3600\left(\frac{s}{h}\right)$$

where:

C = radionuclide concentration in ocean surface near the beach (Bq/L)

t = time of exposure (hours/year)

$DC_{immersion}$ = external dose coefficient, water immersion (Sv/second per Bq/m^3).

E.4.4 Boating (Sea Surface) External Exposure

Individuals may travel via small boat from island to island or use a boat to support near-shore fishing. The dose rate in a boat at the surface of the water is effectively one-half of the dose rate from total immersion (swimming). For each radionuclide the annual dose from external exposure in the ocean surface while boating was calculated as follows:

$$Boating\ Dose\ Rate\left(\frac{Sv}{year}\right) = 0.5 \times C\left(\frac{Bq}{L}\right) \times t\left(\frac{h}{y}\right) \times DC_{immersion}\left(\frac{Sv \cdot m^3}{Bq \cdot s}\right) \times 1{,}000\left(\frac{L}{m^3}\right) \times 3600\left(\frac{s}{h}\right)$$

where:

C = radionuclide concentration in ocean surface of the 10×10 km region (Bq/L)

t = time of exposure (hours/year)

$DC_{immersion}$ = external dose coefficient, water immersion (Sv/second per Bq/m^3).

E.5 Calculating Dose to Lagoon Biota

Six types of marine biota were selected for evaluation of dose: benthic fish; pelagic fish; crustaceans; mollusks; macroalgae (seaweed); and coral. Benthic fish, crustaceans, and mollusks were considered bottom-dwelling organisms and exposed to the bottom layer of ocean and sediment; while pelagic fish, seaweed, and coral were considered to live more in the open water and exposed to the selected ocean water.

Internal and external dose rates to biota, in absorbed dose units of microGray per day (µGy/day), were calculated for all radionuclides. The internal and external dose coefficients for each of the specific biota types were taken from the ERICA 2.0 database (ERICA 2021). These coefficients are based on the methods of ICRP Publication 136 (2017) but include more specific types of biota, including the six marine organisms evaluated here. The dose coefficients include the contribution from short-lived progeny for ^{137}Cs/^{137}mBa and ^{90}Sr/^{90}Y.

E.5.1 Internal Dose to Marine Biota

The internal dose rate to all types of marine biota is dependent on the concentrations of radionuclides in the surrounding seawater, not the sediment, and was calculated using the following equation:

$$Biota\ Dose\ Rate_{internal}\left(\frac{\mu Gy}{day}\right) = C_{ocean}\left(\frac{Bq}{L}\right) \times CR\left(\frac{L}{kg}\right) \times DC_{int\_biota}\left(\frac{\mu Gy\ kg}{Bq\ h}\right) \times 24\left(\frac{h}{day}\right)$$

where:

C_{ocean} = radionuclide concentration in ocean water

CR = concentration ratio in marine biota from water (Bq/kg per Bq/L)

DC_{int_biota} = internal dose coefficient, biota-specific (µGy/hour per Bq/kg).

E.5.2 External Dose to Marine Biota

The external dose rate to all marine biota from surrounding ocean water was calculated using the following equation:

$$Biota\ Dose\ Rate_{ext\_ocean}\left(\frac{\mu Gy}{day}\right) = C_{ocean}\left(\frac{Bq}{L}\right) \times DC_{ext_{biota}}\left(\frac{\mu Gy\ kg}{Bq\ h}\right) \times 24\left(\frac{h}{day}\right) \div 1.025\left(\frac{kg}{L}\right)$$

where:

C_{ocean} = radionuclide concentration in ocean water (Bq/L)

DC_{ext_biota} = eternal dose coefficient, biota-specific (µGy/hour per Bq/kg)

1.025 kg/L = density of seawater.

The external dose rate to bottom-dwelling marine biota (benthic fish, crustaceans, mollusks) from ocean floor sediment was calculated using the following equation:

$$Biota\ Dose\ Rate_{ext\_sediment}\left(\frac{\mu Gy}{day}\right) = Cp_{sediment}\left(\frac{Bq}{kg}\right) \times DC_{ext\_biota}\left(\frac{\mu Gy\ kg}{Bq\ h}\right) \times 24\left(\frac{h}{day}\right)$$

where:

$Cp_{sediment}$ = radionuclide concentration in ocean floor sediment (Bq/kg)

DC_{int_biota} = internal dose coefficient, biota-specific (µGy/hour per Bq/kg).

The total external dose rate to bottom-dwelling marine biota was calculated considering these organisms to be at the interface of the ocean and sediment, where the dose rate is one-half that of the dose rate within the sediment plus one-half of that within the water.

$$Biota\ Dose\ Rate_{external}\left(\frac{\mu Gy}{day}\right) = 0.5\left[Biota\ Dose\ Rate_{ext\_ocean}\right] + 0.5\left[Biota\ Dose\ Rate_{ext\_sediment}\right]$$

E.6 Effects of Radioactive Progeny

In response to public comments, PNNL reconsidered all possible radionuclide decay chains that could increase the original dose estimated in the draft report. The steady state secular equilibrium of short-lived progenies, such as ^{137}Cs/^{137m}Ba and ^{90}Sr/^{90}Y, was implicitly considered in the parent radionuclides' dose coefficients. Short-lived radionuclides including ^{60}Co, ^{155}Eu, ^{207}Bi, ^{101}Rh, ^{102m}Rh, ^{125}Sb should have decayed to stable isotopes since measured during the 1972 AEC survey. There are two other decay chains that could generate appreciable amounts of long-lived radionuclides in the current (2015) and future (2090) years as shown below.

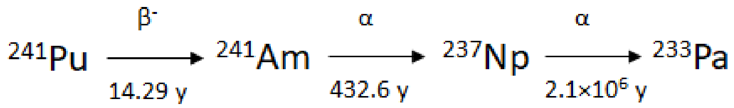

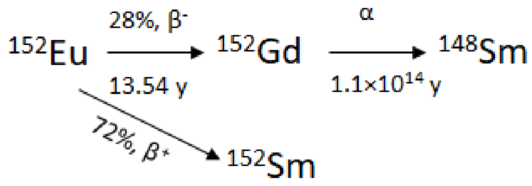

While ^{241}Pu was not detected during the AEC survey, Noshkin (1980) measured some ^{241}Pu in the Enewetak lagoon and estimated an inventory with an average value of 493 mCi/km^2 (18.2 GBq/km^2) in the lagoon sediments. Most of the ^{241}Pu should have decayed to ^{241}Am due to its relatively short half-life of 14.29 years. Noshkin (1980) estimated a 10% increase in ^{241}Am from decay of ^{241}Pu. Due to the relatively small contribution to overall ^{241}Am inventory and unavailability of detailed spatial data, PNNL did not model the ingrowth of ^{241}Pu to ^{241}Am for overall transport and dose calculations. However, PNNL incorporated available data for ^{241}Am activity in the top lagoon sediment from AEC (1973) and thus accounted for its contribution to overall dose.

PNNL evaluated the ingrowth of the progenies in these two chains. Due to very long half-lives, the progenies' activities are very small. Using Bateman equation (Bateman, 1910), PNNL estimated that the ^{241}Np ingrowth will be 0.0013% and 0.0034% of ^{241}Am inventory in 2015 and 2090, respectively. Similarly, the ingrowth of ^{152}Gd was also negligible—in the range of 10^{-13} times the ^{152}Eu inventory. Because the activities of these two progenies are small, the consequent dose will be insignificant and therefore does not affect the original results and conclusions.

Appendix F
Radiation Exposure Standards in the United States

Radiation dose is limited for members of the public by various national and state standards; the limits vary by situation as a result of varying legislative mandates. For operating nuclear facilities, the U.S. Nuclear Regulatory Commission requires its licensees to limit exposure to the public to 1 mSv (100 mrem) per year above natural background in 10 CFR 20.130 (NRC, 1991); DOE uses the same value (DOE, 2011). However, for decommissioned facilities released to the public for unrestricted use, the NRC requires that doses to an average member of the critical group not exceed 0.25 mSv (25 mrem) per year. Similarly, the NRC regulations for low-level radioactive waste disposal limit releases to the general environment to levels that would not cause dose to exceed 0.25 mSv/year (25 mrem/year) (NRC 2016). The U.S. Environmental Protection Agency (EPA) does not use dose-based standards; the EPA standards for radiation exposure tend to be risk-based. The EPA cleanup standards for radiologically contaminated areas range from a lifetime risk of 10^{-6} to 10^{-4}. This corresponds roughly to a maximum annual dose limit of about 0.12 mSv/year (12 mrem/year) (EPA 1997). Thus, U.S. regulations would limit radiation exposures to residents to within the range of 0.1 to 1 mSv/year (10–100 mrem/year).

Appendix G
Public Comments and Responses

Following publication of the draft report, PNNL solicitated comments from interested stakeholders. The public comment period began on September 28, 2023 and ended on November 15, 2023. The authors of the report carefully considered each comment and responded to them. Recommendations made in several comments were accepted by the authors and incorporated into the final report.

Table G.1. Public Comments and Responses

No.	Commentor and Affiliation	Comment	Response
1	April Brown, Marshallese Educational Initiative	According to the report: “The Congressional Act that authorized this study did not direct the study’s researchers to collect new data, so this study uses available information.” Using old data regarding contamination, skews the results of this current study and invalidates it’s results.	The report’s authors’ investigations confirm that older, publicly available, existing datasets are generally consistent with newer, publicly available, existing datasets. These investigations provide some confidence that the existing data is mostly representative of current conditions and that the use of existing data does not invalidate the study’s results. However, since this analysis was limited to the use of existing data, the report’s authors acknowledge uncertainties connected to the absence of new data collection efforts.
2	April Brown, Marshallese Educational Initiative	Accurate and up to date information must be utilized to provide an accurate assessment.	The report’s authors’ investigations confirm that older, publicly available, existing datasets are generally consistent with newer, publicly available, existing datasets. These investigations provide some confidence that the existing data is mostly representative of current conditions and that the use of existing data does not invalidate the study’s results. However, since this analysis was limited to the use of existing data, the report’s authors acknowledge uncertainties connected to the absence of new data collection efforts.
3	April Brown, Marshallese Educational Initiative	DOE has a history of downplaying the severity of radiation contamination and exposure. Testimony by atomic vets who built the dome detail how unauthorized dumps were made in the lagoon. A third party organization must study the dome, its contents, and the lagoon.	The report's authors acknowledge this comment. This study was directed by the U.S. Congress to focus on the potential impacts of climate change on the hazards posed to humans and the environment from radioactive contaminants and other toxins in the Enewetak Atoll. The report's authors utilized the best publicly available data sets to perform their research, and they address all sources, methods, and findings in the report.
4	Jon Barnett, University of Melbourne	This study has some significant limitations that should be clearly conveyed in its communication so that this is not understood to be a definitive assessment. These include: 1. That it is based on past research and not new research	The report’s authors acknowledge limitations of this study, and the report includes statements about research scope limitations. While this research resulted in new findings, PNNL's scope did not include new data collection.
5	Jon Barnett, University of Melbourne	2. That there is no information about radionuclides in the freshwater lens	This study’s scope was to evaluate and assess the risks associated with a potential increase in contamination levels caused by climate change. The impacts of climate change on contamination were studied through a short-time, extreme weather event that could be expected to result in mobilization and transport of contaminated lagoon sediments. While longer-term, slower radionuclide transport could occur via the groundwater pathway, sufficient data were not available to model such processes. Other

No.	Commentor and Affiliation	Comment	Response
			studies, including Buesseler et al. (2018) and Hamilton (2021), previously reported on radionuclide concentrations in groundwater, which are summarized in this report for completeness. The report’s authors did not consider the freshwater lens for either current or future climate because there was inadequate existing data for parametrizing a subsurface model coupled to hydrodynamic simulations. In addition, subsurface conditions under future climate may have substantial uncertainties, and this poses considerable difficulties for modeling efforts due to high uncertainties associated with future precipitation levels.
6	Jon Barnett, University of Melbourne	3. That the focus is on the risk of contamination from storms only, and not from slow-onset changes in sea-levels or freshwater lenses	This study’s scope was to evaluate and assess the risks associated with a potential increase in contamination levels caused by climate change. The impacts of climate change on contamination were studied through a short-time, extreme weather event that could be expected to result in mobilization and transport of contaminated lagoon sediments. While longer-term, slower radionuclide transport could occur via the groundwater pathway, sufficient data were not available to model such processes. The report’s authors did not consider the freshwater lens for either current or future climate because there was inadequate existing data for parametrizing a subsurface model coupled to hydrodynamic simulations. In addition, subsurface conditions under future climate may have substantial uncertainties, and this poses considerable difficulties for modeling efforts due to high uncertainties associated with future precipitation levels. The report’s authors considered sea-level rise, and they incorporated the elevated sea-level of 0.62 m in modeling the storms and hydrodynamic conditions under future climate; these details are described in the report.
7	Jon Barnett, University of Melbourne	4. That the study uses estimates, hypotheses and educated guesses, and not data, observations and field experiments from Enewetak, including: estimates (not data) about current radiation conditions; estimates of what future storm conditions may be like (not observations of what current storms are like); estimates of how radionuclides might move through the environment (not experiments and observations); and estimates of radiation doses to Enewetak Atoll’s humans, plants, and animals (and not observations of current doses). Estimates, hypotheses and educated guesses are only as good as the data that informs them, and there is no current data that informs them.	The commenter is correct that hypotheses are as strong at the data that informs them. The commentor is also correct that the research team did not perform direct radiation measurements or sampling. As directed by the U.S. Congress, the report’s authors utilized existing, publicly available data sets. However, the report’s authors’ investigations confirm that older, publicly available, existing datasets are generally consistent with newer, publicly available, existing datasets. These investigations provide some confidence that the existing data is mostly representative of current conditions and that the use of existing data does not invalidate the study’s results. The project focused on predictive modeling of impact of future climate (including severe storms) on the radiological contamination and consequent dose. The future storms are projected based on most severe historically observed storms using state-of-the-science climate modeling techniques. The ocean model

No.	Commentor and Affiliation	Comment	Response
			was provided with inputs of lagoon sediment data and the island soils data, both determined by field samples, to simulate the impact of climate driven ocean circulation on the radiological contamination and consequent dose. Hydrodynamic conditions for the ocean modeling were obtained from most recent, scientifically accepted global reanalyses. The input data for dose calculations also included information gathered from direct field samples of isotopes in the atoll island soils as part of the RMI Nationwide Radiological Study (Simon and Graham, 1991).
8	Jon Barnett, University of Melbourne	5. Regarding the past research, a clear statement about what classified sources of information exist, and if they were also used, is also necessary.	As directed by the U.S. Congress, the report's authors used existing, publicly available data sets to complete this study.
9	Jon Barnett, University of Melbourne	6. The finding that in the simulated release of waste from the Runit Dome local food consumption increased a person’s radiation dose by approximately 20 times above present, and to a level greater than most U.S. standards for health risk, should be highlighted in the summary.	The report's authors acknowledge this comment. Their finding regarding the 20-times dose increase is included within the report summary and conclusion.
10	Andrew Tompson, Lawrence Livermore National Laboratory	In general, the residual radionuclides produced by a nuclear detonation will be large in number, present in different isotopic abundances or physical forms dependent on the location of the device (underground, on or above a ground surface, in or proximate to water bodies, etc.), often short-lived, and may give rise to daughter products that may be relevant in an investigation. Some discussion of this in the context of Enewetak should be provided, albeit in brief. For example, two of the more prominent isotopes found in underground tests are tritium and 14C, which are of no lasting concern here, as they would largely be lost to the atmosphere to contribute to "bomb pulse" atmospheric signals. Thus, the source term you deal with here is a very specific subset of test related radionuclides.	As directed by the U.S. Congress, this study utilized existing, publicly available data for Enewetak Atoll. Existing information accounts for the fallout, decay, and movement of radionuclides that has occurred since the tests were conducted. Additional modeling to compute source term from the tests’ fallout is outside of the study’s scope.
11	Andrew Tompson, Lawrence Livermore National Laboratory	Understandably, the measurement campaigns you review must be heavily relied upon to characterize the source term as it exists today, but their limitations must be acknowledged. Admittedly, the data available to characterize radiologic contamination on surface solids (§2.1), in lagoon sediments (§2.2) or lagoon and ocean water (§2.3) or in the fill materials under Runit dome (Â§2.4) can be sparse (in number), scattered (in space), selective or incomplete (in terms of isotopes measured or considered), and presented in disparate terms or units (e.g., Bq/kg-soil, pCi/m3-water, pCi/g-soil, mCi/km2-lagoon surface....). This can make interpretation or inter-comparison of the information as a whole difficult. I would hope the discussions in Â§2.1 to Â§2.4 could be evened out and made more consistent in this respect.	The commenter is correct in highlighting challenges and limitations, such as sparseness and disparate terms or units, in the data. The report's authors addressed these items in two ways. First, while sparseness existed in the data set, the report’s authors used their best judgement in their selection of the dome inventory provided by NAS. The report’s authors also utilized the best available data to set up the ocean model and calculate the soil and marine doses. Second, this report includes unit conversions from US to SI units along with the report’s tables. While soil and sediment data were provided in Bq/g or Bq/kg; water concentrations were reported in Bq/m^3. Conversions of mCi/km^2 to Bq/m^2 and Bq/kg were provided in the table captions for lagoon sediments data.
12	Andrew Tompson, Lawrence Livermore National Laboratory	Please provide a data reference for the caption. Suggest using DOE/NV--209-REV 16 September 2015 (see next item) and adding it as a new reference.	The report has been revised to include the reference DOE/NV--209-REV 16 in the caption.
13	Andrew Tompson,	Suggest modifying entries in table to be	The report has been revised to include edits in

No.	Commentor and Affiliation	Comment	Response
	Lawrence Livermore National Laboratory	consistent with the current standard reference: DOE (2015). United States Nuclear Tests, July 1945 through September 1992, U.S. Department of Energy, National Nuclear Security Administration, Nevada Field Office, Las Vegas, NV (DOE/NV--209-REV 16 September 2015) Note that in this reference: (a) Dates and times are listed in GMT, which my differ from the date in your table (should be stated as local time if you leave it). (b) Lat and Long info differ slightly from your table	Table 1 and Figure 3 using DOE/NV--209-REV 16.
14	Andrew Tompson, Lawrence Livermore National Laboratory	You note that 43 tests were conducted on Eniwetok, although only 42 are listed in the table. The ROSE test is missing. Hardtack 1, ROSE, 15 kt., 06/02/1958 GMT 11.532600N, 162.342600 E, June 2, 1958 (GMT) 18:45:00.00 (GMT), Barge (Per DOE/NV--209-REV 16 September 2015)	The report has been revised to include the “ROSE” test, as suggested.
15	Andrew Tompson, Lawrence Livermore National Laboratory	HOLLY test yield listed as 5.9 kt in DOE/NV--209 Rev 16 (2015). Please correct. 5. SEQUOIA test yield listed as 5.2 kt in DOE/NV--209 Rev 16 (2015). Please correct.	The report has been revised to include edits in Table 1 and Figure 3 using DOE/NV--209-REV 16.
16	Andrew Tompson, Lawrence Livermore National Laboratory	Suggest listing all tests chronological order.	The report has been revised to order tests in chronological order, as suggested.
17	Andrew Tompson, Lawrence Livermore National Laboratory	Suggest using "Test" instead of "Shot"	The report has been revised to use the term “Test” instead of “Shot.”
18	Andrew Tompson, Lawrence Livermore National Laboratory	At the outset, it was not clear whether a control dose assessment was to be made (in the absence of climate change) to assess the changes imparted by climate change, but this seems apparent in the Chapter 5 introduction. This should be mentioned up front.	The Summary and Introduction of the report have been revised to state that a control dose assessment was made to assess the changes imparted by climate change.
19	Andrew Tompson, Lawrence Livermore National Laboratory	PP11, 12, Tables 2, 3 1. Please provide a fundamantal data reference for the captions 2. Please provide a listing of, or reference to the isotopic half lives, say before Table 7	The report was revised to include the following additional information: 1. A color key and sources for Table 2 and Table 3 are provided in the paragraph above Table 2.2 2. The NuDAT 2.3 database reference was added to the Table 7 caption and the report’s reference section.
20	Andrew Tompson, Lawrence Livermore National Laboratory	What is the point or utility of presenting groundwater concentrations? It seems groundwater is neglected in this document.	The report’s authors included groundwater concentrations data for completeness. The report’s authors limit additional use of groundwater concentrations due to limited existing, publicly available data sets on this topic and because they felt that additional exploration did not sufficiently align with the scope of this study. The characterization and evaluation of the radionuclide flux through groundwater is important to assess the current background level of contamination in the lagoon. However, the scope of the study was to evaluate and assess the risk associated with the incremental contamination level caused by impacts of climate change. Therefore, the authors investigated the impacts of climate change through a short-time, extreme weather event that could be expected to result in mobilization and transport of contaminated lagoon sediments. While longer-term, slower radionuclide transport could occur via the groundwater pathway, sufficient data were not available to model such processes. In that context, while the groundwater flux may play

No.	Commentor and Affiliation	Comment	Response
			a role in the collapse of the Runit Dome and seepage of contaminant flow into the lagoon for a prolonged period, a hypothetical severe scenario was used. The report's authors assumed the collapse of the dome, which resulted in an instantaneous release of all the contamination of the Runit Dome into the lagoon, as the worst-case scenario, which is appropriate for the risk assessment. Bounding the effects of groundwater flux did not alter the objective of assessing the incremental risk associated with future climate events.
21	Andrew Tompson, Lawrence Livermore National Laboratory	Table 16: What are the units of these data?	The report was revised to include Bq/g unit in Table 16.
22	Andrew Tompson, Lawrence Livermore National Laboratory	The approach does not seem to take into account the presence of fresh groundwater as a component of the radiologic source term or as a resource that could be impacted by climate change and/or provide another kind of exposure pathway. This is certainly a consideration in the Buesseler (2018) reference. Fresh groundwater is an important resource in low abundance (which makes it critical for an island population) and eligible for radiologic inputs from rainfall or sea wash across contaminated surface materials. Some of the references speak of groundwater under the dome or elsewhere; you cite data from Buesseler et al. (2018) in Table 9. The limited groundwater concentration data in the Dome (Table 14) show some fairly high values for soluble 137Cs (10,000 Bq/m3 = 270 pCi/L) or soluble 90-Sr (13,000 Bq/m3 = 351 pCi/L) which exceed US drinking water standards (200 and 8 pCi/L, respectively). Minimally, you should recognize or acknowledge it, even if your analysis excludes further consideration, and provide some kind of justification for doing so. Certainly, assuming the entire radiologic inventory under the dome is discharged into the lagoon is ONE way to handle this, but not the only way.	As stated in responses to Comment No. 5 and Comment No. 20, there is very limited characterization of groundwater concentrations available, including those in the freshwater lens. The characterization and evaluation of the radionuclide flux through groundwater is important to assess the current background level of contamination in the lagoon. However, the scope of the study was to evaluate and assess the risk associated with the incremental contamination level caused by impacts of climate change. Therefore, the authors investigated the impacts of climate change through a short-time, extreme weather event that could be expected to result in mobilization and transport of contaminated lagoon sediments. While longer-term, slower radionuclide transport could occur via the groundwater pathway, sufficient data were not available to model such processes. In that context, while the groundwater flux may play a role in the collapse of the Runit Dome and seepage of contaminant flow into the lagoon for a prolonged period, a hypothetical severe scenario was used. The report's authors assumed the collapse of the dome, which resulted in an instantaneous release of all the contamination of the Runit Dome into the lagoon, as the worst-case scenario, which is appropriate for the risk assessment. Bounding the effects of groundwater flux did not alter the objective of assessing the incremental risk associated with future climate events.
23	Andrew Tompson, Lawrence Livermore National Laboratory	Of the data you do have, what is the rationale for inclusion of specific isotopes in your models? Why do you exclude others? Abundance (low concentration) considerations? Half-life considerations? How do you account for areas where there are no data? No measurements taken or no radionuclides present? Could other radionuclides be present, but not measured for whatever reason? These issues should be discussed/recognized, as appropriate, as the logic here seems fairly arbitrary to me. For example, underneath Table 4, you mention that only 239, 241Am, 207Bi, 137Cs, and 152Eu will be retained in the model. Why not 241Pu, which had a high value in the table in the Noshkin report column? Why are other radionuclides presented in later discussions?	The report's authors acknowledge this comment and provide additional information on their thinking and decisions. Isotopes were selected on the basis of 1) limited measurements of the list of nuclides, 2) Nuclides with decay half-lives of less than 5 years were assumed to be decayed by 2015, and 3) Short-lived progeny in steady-state equilibrium with parents in any environmental medium (e.g., Y90, Ba137m). Radiological decay was only considered for inventory and isotope selection while environmental losses due to "washout" from the lagoon were not considered and thus the inventory is conservative. The commentor is correct in highlighting that Pu241 was not considered along with its ingrowth to Am241. Noshkin (1980) mentioned that only a 10% increase over present Am241

No.	Commentor and Affiliation	Comment	Response
			levels is expected at Enewetak from Pu241 decay and thus supports our statement that there was not significant amount of Pu241 in the lagoon sediment inventory. The report's authors incorporated existing Am241 data from AEC (1973) survey that should be reasonably close to the total inventory of Am241, including from Pu241 ingrowth. Spatial data of sediment laden radionuclides from AEC (1973) were interpolated to fill the areas which had no data. The report includes a review of existing data from previous studies, including lagoon water samples and crater samples, in Chapter 2 Section 3. These data were not used as inputs for model assessment.
24	Andrew Tompson, Lawrence Livermore National Laboratory	Tables 7 and 8 make references to the immediate daughter products of 90Sr (90Y) and 137Cs (137mBa)? These daughters have very short half-lives, but is there an assumption that they will always exist in some kind of secular equilibrium (regardless of the matrix of the parent?) What is the rationale here? If you are going to consider daughter products, why not consider the chain 241Pu (14.3 y) --> 241Am (432.6y) --> 237Np (2.14E6 y)? The first two isotopes are measured in the content presented in Table 4, so which not address this connection? You say on p18 "only a minor amount was observed", but is that because it was not looked for? 241Pu is abundant in tabulated underground test inventories (https://www.osti.gov/biblio/1242909). What about the 237Np daughter product?	The report's authors' rationale begins with the fact that short-lived radionuclide progeny are assumed to be in equilibrium with the parent radionuclide in any environmental medium (137Cs/137mBa, 90Sr/90Y). Short-lived progeny are included in the dose coefficient of the parent radionuclide but external dose was calculated for both parent and progeny. Am241 ingrowth from Pu241 is about less than 10% of existing Am241 inventory and therefore Pu241 decay chain was not considered. Am241 would generate Np237 during future years but was not originally considered. In response to this comment, the authors performed an estimate of the amount of Np237 expected to be present in 2015 and 2090. The amount of Np237 would be small in 2015 and 2090 (about 0.001% and 0.003% of the starting Am241 amount). Therefore, Np237's contribution to radiation dose in 2015 and 2090 would be insignificant. The report has been revised to include this information.
25	Andrew Tompson, Lawrence Livermore National Laboratory	Could a groundwater-based circulation through the Runit debris be considered as a potential release/ failure mechanism?	The report's authors did not have access to adequate, existing, publicly available historical or current data or the resources to conduct a groundwater-based circulation modeling effort. The seepage water (from precipitation or storm surge overtopping) through the surrounding ground of the Runit Dome may go through the dome sediments and contaminate the groundwater. However, determining whether such seepage water and associated erosion can result from the collapse of the dome requires an extensive modeling covering the subsurface, integrity of the structure, fluid-structure interaction accompanied by a fragility analysis. The authors note that the hypothetical collapse of the dome and release of its content is a bounding scenario.
26	Andrew Tompson, Lawrence Livermore National Laboratory	Figure 9: If you are taking a fixed mass of RNs and distributing them over an area, what aspect of the calculation yields a gradient in the apparent concentrations? What is the physical argument? It seems arbitrary.	The report's authors acknowledge this comment and provide additional information regarding Figure 9. Figure 9 shows a concentration gradient towards the beach waters from the dome. Although the mass has been distributed evenly at each node of the selected area, the associated concentrations decline on average as the distance increases from the source. The report's authors' rationale behind the even distribution of mass was prompted by the

No.	Commentor and Affiliation	Comment	Response
			complex and indeterministic nature of the spread area of sediments due to the hypothesized instantaneous collapse of the dome. By doing so, the report authors expected the release of more contaminant material into the waters of the lagoon (useful in risk assessment context) while maintaining a realistic concentration gradient in the spread area. The length of the spread area was selected as the distance to the intersection of the plume centerline and the -2m isodepth contour which was also the criteria for deciding receptor points for dose calculation.
27	Andrew Tompson, Lawrence Livermore National Laboratory	In the Buesseler (2018) citation, estimates of 237Cs and 239 fluxes from the lagoon are made using a water residence time argument (see specifically §4.5 in that reference). Are you in a position to verify the fluxes or residence times in the citation using your hydrodynamic model?	The report's authors acknowledge this comment and provide additional information on their modeling assessment. As part of the modeling assessment, the report's authors conducted a flushing study for the lagoon using a numerical dye by coupling the simulated hydrodynamics, which was validated with tide data. The flushing time, which is analogous to water renewal time, is commonly defined as the time it takes to replenish the water in a basin with exchange flow through the open boundaries of that basin/lagoon. A common way to express flushing time is via e-folding flushing time which is the time it takes to reduce the average concentration in the basin/lagoon to 37% of the original concentration of the contaminant/pollutant. This flushing time may be analogous to the residence time estimated by Buesseler (2018), which is 16 days. The report's authors' estimates show the e-folding flushing time for the lagoon is around 30 days. This time length closely matches with the residence time of 28 days reported by Atkinson et al. (1981), which was based on a box model and considered the currents and hydrodynamic circulation inside the lagoon.
28	Andrew Tompson, Lawrence Livermore National Laboratory	Consider the information and analyses in: Storlazzi, C.D., et al., 2017, The Impact of Sea-Level Rise and Climate Change on Department of Defense Installations on Atolls in the Pacific Ocean (RC-2334): U.S. Geological Survey Administrative Report for the U.S. Department of Defense Strategic Environmental Research and Development Program, 121 p.	The report's authors acknowledge this comment. Stortlazzi et. al. (2017) utilized sea level rise of 0.6 m (RCP4.5), 1.5 m (RCP8.5) and 2.0 m (RCP8.5+icesheet collapse) for the year of 2085 from CMIP5 simulations. The report authors used 0.62 m under the high emissions scenario following a report by Pacific Climate Change Science Program (PCCSP, 2011), which was produced by a collaboration between PCCSP and RMI National Weather Service Office.
29	Elise Burt	The impacts of global warming will impact the people and environments of many nations.	The report's authors acknowledge this comment. This study was directed by the U.S. Congress to focus on the potential impacts climate change on the hazards posed to humans and the environment from radioactive contaminants and other toxins in the Enewetak Atoll.
30	Elise Burt	In the newspaper "Notice from Public Comment", it is stated that the "DOE remains remains committed to fulfilling the United States' commitments regarding the health and safety of the people of the Marshall Islands…." Nowhere are those commitments stated. The US certainly has not kept the health and safety of the Marshallese people nor those of our US Veterans who were involved in the testing of the so called cleanup. In fact the Marshallese people were used as test subjects when they were allowed to return to their home islands. Only lies have been told about the safety	The report's authors acknowledge this comment. This study was directed by the U.S. Congress to focus on the potential impacts of climate change on the hazards posed to humans and the environment from radioactive contaminants and other toxins in the Enewetak Atoll. The report's authors' ocean model encompasses the entire RMI region, but the authors limited the radionuclides assessment to Enewetak Atoll to align with the project scope. The report's authors utilized the best publicly available data sets to perform their research, and they address all sources, methods, and findings in the report.

No.	Commentor and Affiliation	Comment	Response
		considerations used by our soldiers involved in the cleanup and those exposed to the testing. I recently read an article regarding fallout from the 1945 atomic test "Trinity" that covered 46 states, Canada and Mexico. That test was "only" 18.6kilotons of energy released as compared with the Operation Castle tests of48,200 kilotons. What about the effects on all the surrounding islands? My family and I lived on Kwajalein along with numerous friends. Arkansas, our current home, is also the home of many Marshallese. While I recognize that this report is only covering the Runit dome, so much more needs to be done.	The report titled United States Nuclear Tests – July 1945 through September 1992 (DOE 2015) is considered the currently accepted standard for test information within the scientific community. This report outlined all the tests, including the test type, yield, and location. In this report, DOE-NV reported multiple tests within Operation Castle. One of these tests, "Nector," occurred in the Enewetak Atoll. "Nector" had a yield of 1.69 Mt (1690 kt). Radiological surveys (AEC 1973; Busselar 2016) showed significant fallout and deposition in the Mike crater.

Final Report

Pacific Northwest National Laboratory

902 Battelle Boulevard
P.O. Box 999
Richland, WA 99354
1-888-375-PNNL (7665)

www.pnnl.gov